Structures and Aggregation Behavior of Ion Pair Catalysts

Dissertation

Zur Erlangung des Doktorgrades der Naturwissenschaften

(Dr. rer. Nat.)

An der Fakultät für Chemie und Pharmazie

Der Universität Regensburg

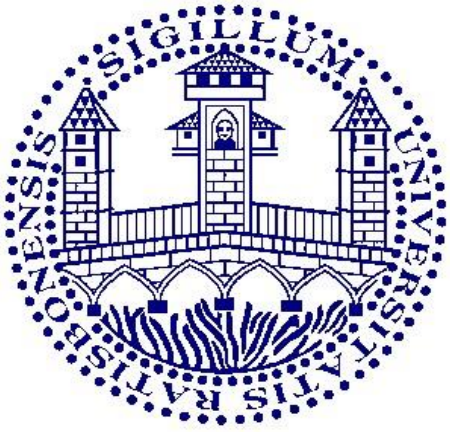

vorgelegt von

Maximilian Franta

aus Hof

im Jahr **2024**

Die vorliegende Dissertation beruht auf Arbeiten, die zwischen November 2020 und Juli 2024 im Arbeitskreis von Professorin Dr. Ruth M. Gschwind am Institut für Organische Chemie der Universität Regensburg durchgeführt wurden.

Promotionsgesuch eingereicht am: 30.07.2024

Die Arbeit wurde angeleitet von: Prof. Dr. Ruth M. Gschwind

Promotionsausschuss:

Vorsitzender: Apl. Prof. Dr. Rainer Müller

1. Gutachterin: Prof. Dr. Ruth M. Gschwind

2. Gutachter: Prof. Dr. Werner Kremer

3. Prüferin: Prof. Dr. Julia Rehbein

なにもなかった

Meiner Familie

„If we lose credibility just by admitting fault, then we didn´t have any in the first place.“

- Issho

Contents

1. Introduction 1
1.1. Aggregation in Ion pair Catalysis 1
1.2. Pyridinamide Ion Pairs 2
1.3. Chiral Phosphoric Acids 3
1.3.1. Features of Chiral Phosphoric Acids 3
1.3.2. Mechanistic Insights 4
1.4. Outline 6
1.5. References 10
2. Ternary Complex in Brønsted Acid Catalysis – Unexpected Weak Steric Limitation Leads to a Broad Structural Space 15
2.1. Abstract 16
2.2. Introduction 16
2.3. Results and Discussion 21
2.3.1. Model Systems and Experimental Setup 21
2.3.2. Structural Space 22
2.3.3. Accessing the Ternary Complex 28
2.3.4. Conformational Investigations 30
2.4. Conclusion 34
2.5. References 35
2.6. Supporting Information 39
2.6.1. Analytical Methods 39
2.6.1.1. NMR Spectrometer Data 39
2.6.1.2. Pulse Sequences and Parameters 39
2.6.2. Materials and Chemicals 41
2.6.2.1. Solvents 41

2.6.2.2. Chemicals 41
2.6.2.3. Synthesis of Imines 42
2.6.2.4. Synthesis of Hantzsch Ester Derivate 3b 43
2.6.3. NMR Investigations 44
2.6.3.1. Substrate Scope 44
2.6.3.2. General Procedure for Sample Preparation (GPSP) 47
2.6.4. Chemical Shift Assignment 48
2.6.4.1. Assignment Strategy 48
2.6.5. Exclusion of Other Species 54
2.6.6. General Features of Ternary Complex 58
2.6.6.1. Binary vs. Ternary Complex 59
2.6.7. Structural Space 60
2.6.7.1. [3:3] Dimer 61
2.6.7.2. 2:1:1 Dimeric Species 64
2.6.7.3. Additional Species 66
2.6.8. Binding Constant 68
2.6.9. Diffusion Ordered Spectroscopy (DOSY) 71
2.6.10. NOE Analysis of Conformers 73
2.6.10.1. TRIFP 1a/2a/HE 3b 74
2.6.10.2. [3:3] Dimer with OMe-CPA 1b 79
2.6.11. Appendix 81
2.6.11.1. NMR Screening - ^{1}H- NMR Spectrum of Each Sample 81
2.6.11.2. NMR Spectra of TRIFP 1a/2a/HE 3b 94
2.6.11.3. NMR Spectra of TRIFP 1a/*E*-2a/HE 3b 101
2.6.11.4. NMR Spectra of OMe-CPA 1b/2a/HE 3b 102
2.6.12. Acknowledgements 106
2.6.13. References 107

3. Dimeric Pathway in Chiral Phosphoric Acid Catalysis — A General Feature? 109
3.1. Abstract 110
3.2. Introduction 111
3.3. Results and Discussion 114
3.3.1. Model Systems 114
3.3.2. NMR Investigations on CPA/CPA/Imine Formation 115
3.3.3. Dimeric Pathway in CPA Catalysis 120
3.3.4. Ion Supported Dimer Formation 122
3.4. Conclusion 125
3.5. References 126
3.6. Supporting Information 129
3.6.1. Analytical Methods 129
3.6.1.1. NMR Spectrometer Data 129
3.6.1.2. Pulse Sequence and Parameters 129
3.6.1.3. Chiral HPLC 130
3.6.2. Materials and Chemicals 131
3.6.2.1. Solvents 131
3.6.2.2. Chemicals 131
3.6.2.3. Synthesis of Imines 132
3.6.3. NMR Investigations 134
3.6.3.1. Substrate Scope 134
3.6.3.2. General Procedure for Sample Preparation (GPSP) 134
3.6.3.3. Investigated Systems 135
3.6.4. Dimeric Species NMR Investigations 137
3.6.4.1. Steric Influence 137
3.6.4.2. Electronic Influence 139

3.6.4.3. Ratio between Monomeric and Dimeric Species 141
3.6.5. DOSY Results 142
3.6.6. CPA-Catalyzed Transfer Hydrogenation of Imines 145
3.6.6.1. General Procedure for CPA-Catalyzed Transfer Hydrogenation of Imines with Hantzsch-Ester 3 (GP II) 145
3.6.7. HPLC Investigations 151
3.6.8. Appendix 152
3.6.8.1. NMR Spectroscopy 152
3.6.8.2. HPLC Chromatograms 170
3.6.9. Acknowledgments 207
3.6.10. References 207
4. Highly Nucleophilic Pyridinamide Anions in Apolar Organic Solvents due to Asymmetric Ion Pair Association 209
4.1. Abstract 210
4.2. Introduction 211
4.3. Results and Discussion 213
4.3.1. Conductivity 213
4.3.2. DOSY NMR 214
4.3.3. Kinetics 216
4.4. Conclusion 223
4.5. References 224
4.6. Supporting Information 227
4.6.1. NMR Spectroscopy 227
4.6.1.1. Sample Preparation for NMR Spectroscopy 227
4.6.1.2. Diffusion Ordered Spectroscopy (DOSY) 227
4.6.1.3. CAC Sandwich-Model 233
4.6.1.4. ACA Sandwich-Model 239

4.6.1.5. Importance of the Ultrasonic Bath during NMR Sample Preparation ... 243
4.6.2. Acknowledgments ... 246
4.6.3. References ... 246
4.7. Additional Findings ... 247
4.7.1. Model Systems ... 247
4.7.2. Aggregation Trends ... 248
4.7.3. Solvent Effects ... 255
4.7.4. NMR Spectroscopy ... 257
4.7.5. References ... 258
5. Conclusion ... 259
6. Eidesstattliche Versicherung ... 268

1. Introduction

1.1. Aggregation in Ion pair Catalysis

In the realm of chemical reactions, the interactions between substrates, catalysts and solvents play a pivotal role for reactivity and selectivity.[1] Especially intermolecular interactions can lead to various aggregation ranging from simple dimers to more intricate higher-order assemblies.[2–6] These aggregates can both enhance and alter reaction pathways, leading to different reactivity or selectivity of the reaction.[7–10] Hence, understanding the complex interplay between aggregation behavior and reaction outcome has emerged as a fundamental area of research across various fields in chemistry.

In this context, among other intermolecular interactions the formation of ion pair aggregates has received a lot of attention in the past decade.[11–14] The driving force behind their formation is the electrostatic interaction between positive and negative charged species.[15] The influence of such ion pair aggregates on reaction behavior are multifaceted. For example, these aggregates can serve as reservoirs of reactive intermediates, effectively modulating their reactivity and stability[16,17] or encapsulate reaction partners which can shield the substrates from the bulk solvent, creating unique microenvironments that deviate from conventional solution-phase chemistry.[18–20] Thus, ion pair aggregates can impact the overall reaction rate and selectivity by changing the local concentration of reactants within the aggregate. This localization effect can lead to enhanced interactions between substrates, promoting specific reaction pathways while inhibiting others.[7,21]

Due to their influence on reactivity and selectivity, the understanding of ion pair formation is key for reaction design. In the past, ion pair aggregation was primarily attributed to electrostatic interactions, leading to solvent separated ion pairs (SSIP) or contact ion pairs (CIP).[22,23] However, recent studies of ion pair catalysts revealed that intermolecular interactions, such as London-Dispersion and hydrogen bonds, can support these electrostatic interactions to form more complex and stable aggregates.[21] Therefore, this thesis explores the influence of both electrostatic interactions as well as supporting intermolecular interactions on ion pair aggregation. Thereby, the new catalyst class of pyridinamide ion pairs is investigated for their electrostatic interactions, while the

structural space and mechanism of chiral phosphoric acids (CPAs) are studied for a further advance in the understanding of this catalyst class. To elucidate the complex interactions in such aggregates, advanced spectroscopic techniques and computational methods are employed. The insights derived from these studies not only shed light on fundamental aspects of ion pairs but also pave the way for reaction design.

1.2. Pyridinamide Ion Pairs

Pyridinamide ion pairs were discovered only recently and demonstrated a huge potential in organocatalysis. Previously, neutral pyridine derivatives have been dominating the field of Lewis basic organocatalysts. Especially, 4-dimethylaminopyridine (DMAP)[24,25] and 9-azajulolidine (TCAP)[26–28] are widely used due to their high performance, latter still being one of the most reactive Lewis basic organocatalysts to this day. The reactivity of pyridine based organocatalysts is known to result from the electron-donating substituents attached to the pyridine. Therefore, in the progress of further increasing the catalytic activity, anionic substituents were employed. Here, the Zipse group introduced pyridinyl amide ion pairs as organocatalysts (see Figure 1.1).[13]

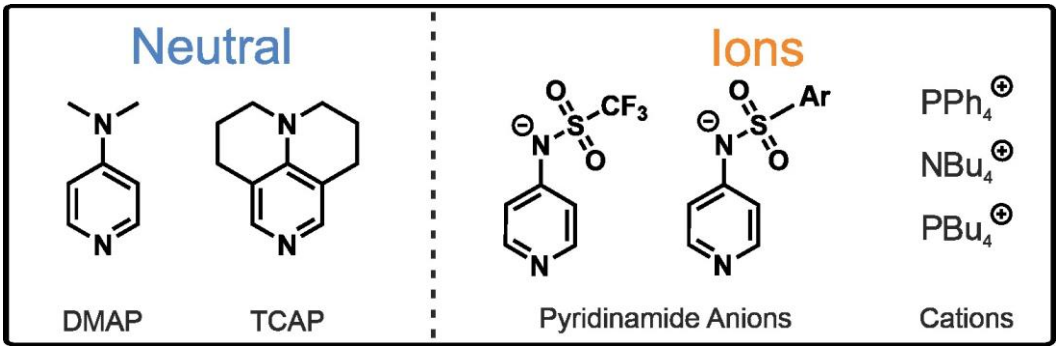

Figure 1.1 Neutral and anionic pyridine derivates used as Lewis base organocatalysts. DMAP and TCAP are shown on the left as prominent examples of neutral pyridine-based catalysts. On the right, some exemplary pyridinamide based ion pair catalysts are depicted.

In general, the reactivity of these ion pair catalysts originates from the anion. However, due to the nature of free ions in apolar organic solvents, normally unreactive ion pairs are formed at concentrations relevant for synthesis, which would diminish the catalytic activity. However, pyridinamide ion pairs are able to outperform TCAP and DMAP in several reactions.[13,29] Thus, instead of the expected 1 to 1 ion pair formation other processes have to be involved to provide the high nucleophilicities observed. Understanding the electrostatic interactions and resulting aggregation behavior of these

ions could enable new design options for ion pair catalysts and could expand the application to further reactions.

1.3. Chiral Phosphoric Acids

The field of Chiral phosphoric Acids (CPAs) originated in 2004 through the pioneering work of Akiyama *et al.*[30] and Terada *et al.*[31], who independently developed a method to utilize CPAs as catalysts in Mannich-type reactions. Soon after, the groups of List[32] and Rueping[33] demonstrated the possibilities of CPAs as catalysts with high enantioselectivities by applying them to other reactions such as transfer hydrogenations of imines. Thereafter, CPAs became a prominent catalyst class and the applicability to various reactions was further investigated. Thereby, among others reaction procedures for Friedel-Craft reactions,[34,35] Ene-type reactions,[36] Strecker-reactions,[37] cycloadditions[38] and cyclizations[39] were developed to use the enormous potential of CPAs.

1.3.1. Features of Chiral Phosphoric Acids

CPAs possess remarkable features due to their unique structural characteristics. Typically, CPAs are based on a BINOL (1,1'-binaphthyl-2,2'-diyl) backbone which is renowned for its axial chirality. The induced stereoselectivity in reactions originates from the attached 3,3´-substituents at the naphthyl-rings. Here, a huge variety of 3,3´-substituents has been tested to adjust the CPA to the reaction of interest.[40–43] Commonly used substituents are substituted phenyl rings e.g. TRIP (3,3'-bis(2,4,6-triisopropylphenyl)-1,1'-binaphthyl-2,2'diyl hydrogen phosphate)[32] and TRIFP (3,3'-bis(3,5-bis (trifluoromethyl)phenyl)-1,1'-binaphthyl-2,2'diyl hydrogen phosphate)[33] or a triphenylsilyl-group (TiPSY: 3,3'-bis(triphenylsilyl)-1,1'-binaphthyl-2,2'diyl hydrogen phosphate)[44]. These 3,3´-substituents primarily differ in size and the flexibility of the phenyl group, for which Goodman *et al.* established two parameters to describe these steric properties of the 3,3´-substituents.[45] On the one hand, the rotational barrier of the 3,3´-substituent and on the other hand, A Remote Environment Angle: AREA (θ), to describe the size of the binding pocket. Besides the 3,3´-substituents, another key feature stems from the dual functionality generated by the Brønsted acidic PO - H and the Brønsted basic P=O groups which are responsible for the variety of catalyzed reactions. The acidic PO - H group serves as an electrophile scavenger, while the Brønsted basic

phosphoryl oxygen acts as a hydrogen bond or proton acceptor, facilitating concerted activation of nucleophiles (see Figure 1.2).

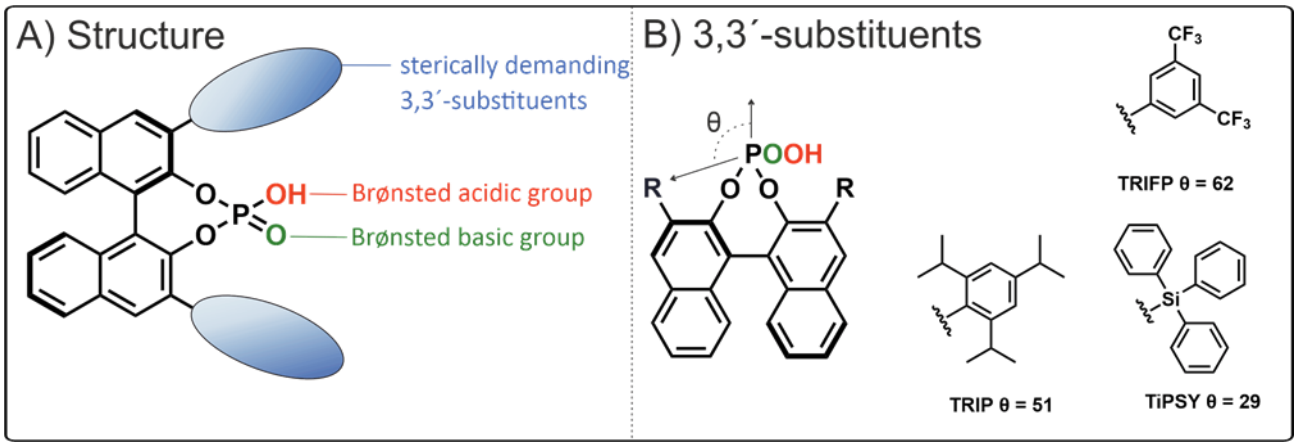

Figure 1.2 A) Structure of CPAs with all key features highlighted. In the center of a CPA both the Brønsted acidic (red) as well as the Brønsted basic (green) groups are located. The 3,3´-substituents which lead to the confined arrangement to induce the stereoselectivity are limiting the binding pocket (blue). B) The influence of the 3,3´-substituents described by the AREA (θ) value.[45] Huge substituents lead to small θ values which indicates a small binding pocket and higher steric limitations and vice versa.

The combination of the axial chirality of the BINOL backbone, the unique 3,3'-substituent arrangement, and the dual functional groups make CPAs versatile tools for controlling stereochemistry and promoting a diverse array of chemical reactions. Thus, making them to one of the most prominent catalysts in asymmetric organocatalysis.[1,43,46]

1.3.2. Mechanistic Insights

Due to the success of CPAs in organocatalysis, mechanistic studies have been of huge interest to optimize reaction conditions and improve the already astonishing enantioselectivities. For that purpose, the CPA-catalyzed transfer hydrogenation of imines with Hantzsch Ester (HE) as hydrogenation agent was established as a model system. The underlying reaction mechanism for this model system was initially proposed by Rueping *et al.*[33] and later confirmed and further elucidated by computational studies[47,48] as well as in-depth NMR investigations[21,49–52].

In this proposed catalytic cycle, the initial step describes the formation of a binary complex between the CPA and the imine which are connected *via* an ion pair assisted hydrogen bond.[21,53] Mechanistic studies focused on this binary complex and revealed several new details about this reaction step. Among other findigs, an *E*/*Z*-isomerization was revealed during step A in which the binary complex is formed.[47] Further computational and

experimental studies revealed that the reaction proceeds *via* a *Z*-imine transition state which was then used to improve the reaction.[47,54] In the next step, the HE attaches to the binary complex through an additional hydrogen bond between the Brønsted basic P=O group of the CPA and the N-H group of the HE. Thereafter, the hydride transfer from the HE leads to the chiral product and the CPA is restored by the pyridinium salt (see Figure 1.3, left).

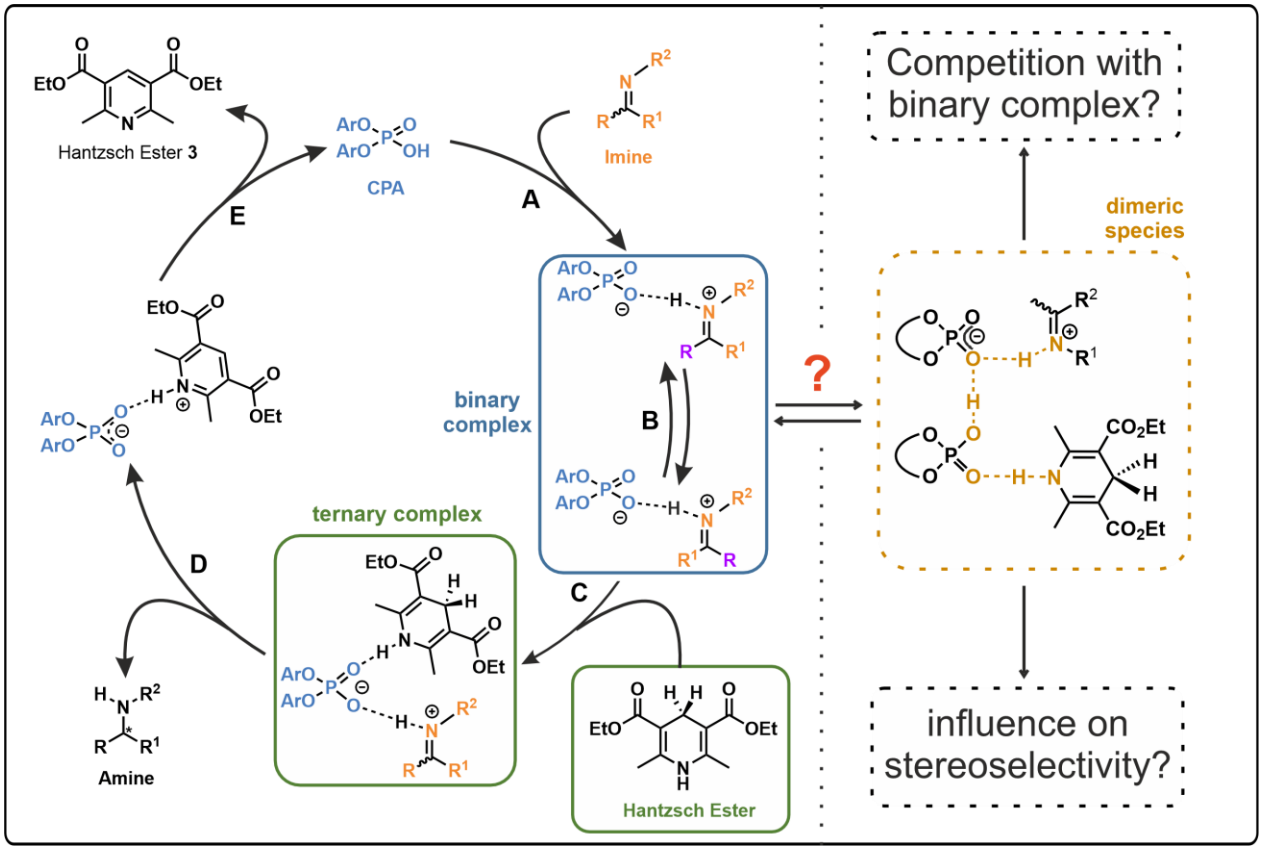

Figure 1.3 Catalytic cycle of the CPA-catalyzed transferhydrogenation of imines with HE as hydrogenation agent. Besides this acknowledged mechanism a possible secondary pathway including a dimeric species was observed. Here, further studies could reveal if this species is a general feature in CPA-catalysis. This could then lead to an optimization of stereoselectivity in case and influence on the stereoselectivity is observed due to the dimeric species or even a competition between both pathways.

Although the first report about CPAs dates back almost two decades, a complete understanding with a simple prediction model still remains elusive. Until now, experimental studies of CPAs are still only possible by investigating the binary complex due to the poor solubility of the HE.[55] Nevertheless, even this first reaction step may not be completely understood yet. Only recently, a possible dimeric species consisting of a hydrogen bond bridged CPA dimer with each CPA binding to either a substrate or the HE was revealed by Niemeyer *et al.* for the transfer hydrogenation of quinolines.[7] This

revelation opens up new possibilities in case this dimeric species is observed as a general feature in CPA-catalyzed reactions and could possibly change the entire reaction optimization (see Figure 1.3, right).

Besides the binary complex, only theoretical calculations have been able to establish models for the proposed ternary complex of CPAs.[45,56–59] These calculations also postulated a complex data-driven prediction model for a broad substrate scope.[58] However, these models could have never been validated by experimental studies which are for now only based on the binary complex. Experimentally, it has just recently become possible to analyze a ternary complex for the first time. Here, chiral disulfonimides (DSIs) were used instead of CPAs and demonstrated a possibility to access the ternary complex also with CPAs.[55] Due to the lack of experimental data on the ternary complex of CPAs, experimental access seems to be key to validate or optimize established theoretical models and could even open up new possibilities for reaction design in CPA catalysis.

1.4. Outline

This thesis delves into the complex aggregation behavior in ion pairs catalysis, aiming to elevate our understanding to a new level. On the one hand, ion pair aggregation driven by purely electrostatic interactions is investigated using pyridinamide ion pair catalysts. Here, diffusion-ordered spectroscopy (DOSY) NMR measurements are conducted and combined with conductivity and nucleophilicity studies from a collaboration. This joint investigation seeks to elucidate the underlying aggregation behavior, which is responsible for the remarkable reactivity observed within this catalyst class. On the other hand, aggregation trends of a combination of electrostatic and intermolecular interactions are investigated thoroughly for the CPA-catalyzed transfer hydrogenation of imines. Here, the primary focus lies on the study of late reaction intermediates as well as higher aggregates of both the binary and the ternary complex of CPAs. Therefore, special 1D and 2D multinuclear NMR experiments were used as central tool to identify such new species. These studies should elevate our understanding of ion pair aggregation in catalysis and change our view on the significance of potential side-species.

Chapter 2 focused on achieving experimental access of late intermediates in the CPA-catalyzed transfer hydrogenation of imines. Prior experimental studies of CPAs only resolved around the binary complex and were unable to give a general prediction model

for reaction design.[51,52,60] Only, complex data-driven models were able to establish prediction models for the stereoselectivity of CPA-catalyzed reactions,[61] but experimental data of late intermediates is missing till this date to validate and optimize these models or even give a simple prediction model itself. Therefore, to investigate late intermediates of CPAs, an NMR screening at 180 K was conducted using combinations of 5 CPAs, 7 imines, and a Hantzsch Ester (HE) derivative, which improves the solubility of the HE at low temperatures. Here, for the first time the ternary complex of CPAs was identified by experimental methods. Thereafter, two model systems were selected for further investigation of the ternary complex. Due to the complexity of the system, with multiple exchanging species and conformers, additional pulse sequences from Bio-NMR had to be applied to small molecules to obtain detailed structural information. These investigations revealed a variety of hydrogen bond species, which indicates a broad structural space for the ternary complex. Besides the 1:1:1 ternary complex, the 2:1:1 ternary complex of the dimeric species was identified and validated the previously calculated structures.[62] Additionally, a yet unknown [3:3] dimeric species consisting of two ternary complexes was revealed by NMR which has not been considered in prior calculations.[61] Furthermore, three different conformers were calculated for the CPA/*E*-imine/HE ternary complex which were validated by NMR spectroscopy. These results demonstrated that despite the sterically hinderance of the 3,3´-substituents, especially in later intermediates, a broad conformational and structural variety is still observed.

In chapter 3, the CPA-catalyzed transfer hydrogenation of imines was selected as a model system to investigate if dimeric CPA/CPA species are a general feature in CPA-catalyzed reactions and its following implications on the reaction selectivity. Therefore, low temperature NMR spectroscopy was employed using a 2:1 stoichiometry of CPA to imine instead of the typical 1:1 stoichiometry to force the formation of possible dimers. To reveal potential electronic and steric trends, a total of 7 CPAs and 13 imines were screened. Besides NMR spectroscopy, high pressure liquid chromatography (HPLC) was used to determine the enantioselectivity of the reaction when adjusting the reaction conditions towards a possible dimerization. Although the NMR studies confirmed the existence of a 2:1 dimer at 180 K and revealed formation trends based on electronic and steric properties of the CPA and imine, no similar effect on stereoselectivity as with quinolines was observed for a wide range of reaction conditions. Thus, a dimeric pathway

can be ruled out as a general feature of CPA catalysis but must be considered for special reactions like the transfer hydrogenation of quinolines.

In chapter 4, a class of ion pair catalysts was investigated in regard of their aggregation and the resulting influence on the reactivity. The Zipse group introduced pyridinamide based ion pair catalysts, which showcased their potential in ion pair catalysis over neutral organocatalysts by outperforming the widely utilized 4-dimethylaminopyridine (DMAP) and 9-azajulodine (TCAP).[13] Due to their success, they became a prime example to study ion pair formation and its influence on reactivity. The observed reactivity was contrary to the expected ion pair formation of an unreactive 1:1 ion pair which should have led to diminished reactivity especially at higher concentrations relevant for synthesis. To investigate this behavior, DOSY-NMR measurements of 7 different pyridinamide catalysts in 4 different solvents were performed within a concentration range of 0.001 mM to 5 mM. These results were then combined with conductivity measurements, calculations and nucleophilicity parameters, measured by the benzhydrylium method of Prof. Herbert Mayr.[26,63,64] This combination of methods allowed unprecedent insights into ion pair formation and showcased its general potential for mechanistic studies. Thereby, DOSY revealed so called “sandwich” complexes which were crucial for the correct interpretation of the conductivity and nucleophilicity data. These complexes are asymmetric associations consisting of either 2 cations and 1 anion or vice versa. Thus, these findings resolve the limitation of ionic compounds forming less reactive 1:1 adducts and pave the way for catalyst design.

In summary, this thesis presents NMR-spectroscopic studies of ion pair aggregation and their transfer to synthetic applications. The main focus lays on chiral phosphoric acids as a catalyst class. Here, the ternary complex of CPAs was experimentally investigated. Despite the steric limitations of CPAs, especially considering larger aggregates such as ternary complexes, a broad structural space including a dimeric 2:1:1 ternary complex and a yet unknown [3:3] dimer was revealed. In addition, three different conformers for the ternary complex were identified by a combination of calculations and NMR spectroscopy. Furthermore, a secondary dimeric reaction pathway was ruled out as a general characteristic of CPAs. Although a dimer formation was observed by low temperature NMR investigations, it was not possible to apply these findings on the reaction. Various conditions were investigated, but for none a significant change in enantioselectivity as observed with quinolines was detected. Besides CPAs,

pyridinamide based ion pair catalysts were investigated in regard of their ion pair formation trends. Here, NMR measurements in collaboration with conductivity and nucleophilicity measurements enabled a deeper mechanistic understanding by revealing higher ion pair aggregates. Thus, this thesis demonstrates that higher aggregates can be an important feature in ion pair catalysis due to their common appearance and proven impact on the reaction. Hence, the mechanistic understanding of ion pairs in catalysis is key to control and improve the reaction outcome. This thesis laid the foundation for future reaction design studies by providing experimental access to late reaction intermediates in CPA catalysis. Furthermore, a new combination of methods was established for in-depth studies of ion pairs which enables better and more detailed studies of ion pairing trends in the future.

1.5. References

[1] M. Mahlau, B. List, *Angew. Chem. Int. Ed.* **2012**, *52*, 518–533.

[2] E. Bergin, *Annu. Reports Prog. Chem. - Sect. B* **2012**, *108*, 353–371.

[3] P. Song, H. Wang, *Adv. Mater.* **2020**, *32*, 1–12.

[4] M. C. Etter, *Acc. Chem. Res.* **1990**, *23*, 120–126.

[5] W. Saenger, *Principles of Nucleic Acid Structure*, Springer Science & Business Media, **2013**.

[6] P. D. U. Bornscheuer, *USB-Stick*, RÖMPP, **2008**.

[7] D. Jansen, J. Gramüller, F. Niemeyer, T. Schaller, M. C. Letzel, S. Grimme, H. Zhu, R. M. Gschwind, J. Niemeyer, *Chem. Sci.* **2020**, *11*, 4381–4390.

[8] N. Berg, S. Bergwinkl, P. Nuernberger, D. Horinek, R. M. Gschwind, *J. Am. Chem. Soc.* **2021**, *143*, 724–735.

[9] E. Powell, W. Xu, *Proc. Natl. Acad. Sci. U. S. A.* **2008**, *105*, 19012–19017.

[10] D. P. Goronzy, M. Ebrahimi, F. Rosei, Arramel, Y. Fang, S. De Feyter, S. L. Tait, C. Wang, P. H. Beton, A. T. S. Wee, et al., *ACS Nano* **2018**, *12*, 7445–7481.

[11] J. F. Brière, S. Oudeyer, V. Dalla, V. Levacher, *Chem. Soc. Rev.* **2012**, *41*, 1696–1707.

[12] M. R. Antonio, M. Nyman, T. M. Anderson, *Angew. Chem. Int. Ed.* **2009**, *48*, 6136–6140.

[13] J. Helberg, T. Ampßler, H. Zipse, *J. Org. Chem.* **2020**, *85*, 5390–5402.

[14] D. Qian, J. Sun, *Chem. Eur. J.* **2019**, *25*, 3740–3751.

[15] Y. Marcus, G. Hefter, *Chem. Rev.* **2006**, *106*, 4585–4621.

[16] G. Krishna, J. Schulte, B. A. Cornell, R. J. Pace, P. D. Osman, *Langmuir* **2003**, *19*, 2294–2305.

[17] M. Salehi, S. J. Johnson, J. T. Liang, *Langmuir* **2008**, *24*, 14099–14107.

[18] K. D. Ristroph, R. K. Prud'homme, *Nanoscale Adv.* **2019**, *1*, 4207–4237.

[19] L. Yang, X. Song, T. Gong, K. Jiang, Y. Hou, T. Chen, X. Sun, Z. Zhang, T. Gong, *Drug Deliv.* **2018**, *25*, 388–397.

[20] D. H. Leung, R. G. Bergman, K. N. Raymond, *J. Am. Chem. Soc.* **2006**, *128*, 9781–9797.

[21] N. Sorgenfrei, J. Hioe, J. Greindl, K. Rothermel, F. Morana, N. Lokesh, R. M. Gschwind, *J. Am. Chem. Soc.* **2016**, *138*, 16345–16354.

[22] L. L. Chan, J. Smid, *J. Am. Chem. Soc.* **1968**, *90*, 4654–4661.

[23] K. Müller-Dethlefs, P. Hobza, *Chem. Rev.* **2000**, *100*, 143–167.

[24] S. Singh, G. Das, O. V. Singh, H. Han, *Org. Lett.* **2007**, *9*, 401–404.

[25] Q. Shi, Z. C. Tan, Y. Y. Di, B. Tong, Y. S. Li, S. X. Wang, *J. Chem. Eng. Data* **2007**, *52*, 941–947.

[26] M. R. Heinrich, H. S. Klisa, H. Mayr, W. Steglich, H. Zipse, *Angew. Chem. Int. Ed.* **2003**, *42*, 4826–4828.

[27] R. Tandon, T. Unzner, T. A. Nigst, N. De Rycke, P. Mayer, B. Wendt, O. R. P. David, H. Zipse, *Chem. Eur. J.* **2013**, *19*, 6435–6442.

[28] A. Tamaki, S. Kojima, Y. Yamamoto, *J. Org. Chem.* **2016**, *81*, 8710–8721.

[29] S. H. Dempsey, A. Lovstedt, S. R. Kass, *J. Org. Chem.* **2023**, *88*, 10525–10538.

[30] T. Akiyama, J. Itoh, K. Yokota, K. Fuchibe, *Angew. Chem. Int. Ed.* **2004**, *43*, 1566–1568.

[31] D. Uraguchi, M. Terada, *J. Am. Chem. Soc.* **2004**, *126*, 5356–5357.

[32] S. Hoffmann, A. M. Seayad, B. List, *Angew. Chem. Int. Ed.* **2005**, *44*, 7424–7427.

[33] M. Rueping, E. Sugiono, C. Azap, T. Theissmann, M. Bolte, *Org. Lett.* **2005**, *7*, 3781–3783.

[34] D. Uraguchi, K. Sorimachi, M. Terada, *J. Am. Chem. Soc.* **2004**, *126*, 11804–11805.

[35] G. B. Rowland, E. B. Rowland, Y. Liang, J. A. Perman, J. C. Antilla, *Org. Lett.* **2007**, *9*, 2609–2611.

[36] M. Terada, K. Soga, N. Momiyama, *Angew. Chem. Int. Ed.* **2008**, *47*, 4122–4125.

[37] M. Rueping, E. Sugiono, C. Azap, *Angew. Chem. Int. Ed.* **2006**, *45*, 2617–2619.

[38] P. Jiao, D. Nakashima, H. Yamamoto, *Angew. Chem.* **2008**, *120*, 2445–2447.

[39] M. Rueping, W. Ieawsuwan, A. P. Antonchick, B. J. Nachtsheim, *Angew. Chem. Int. Ed.* **2007**, *46*, 2097–2100.

[40] M. Terada, *Synthesis (Stuttg).* **2010**, 1929–1982.

[41] T. Akiyama, *Chem. Rev.* **2007**, *107*, 5744–5758.

[42] K. Saito, K. Horiguchi, Y. Shibata, M. Yamanaka, T. Akiyama, *Chem. Eur. J.* **2014**, *20*, 7616–7620.

[43] D. Parmar, E. Sugiono, S. Raja, M. Rueping, *Chem. Rev.* **2014**, *114*, 9047–9153.

[44] R. I. Storer, D. E. Carrera, Y. Ni, D. W. C. MacMillan, *J. Am. Chem. Soc.* **2006**, *128*, 84–86.

[45] J. P. Reid, J. M. Goodman, *J. Am. Chem. Soc.* **2016**, *138*, 7910–7917.

[46] T. Akiyama, K. Mori, *Chem. Rev.* **2015**, *115*, 9277–9306.

[47] L. Simón, J. M. Goodman, *J. Am. Chem. Soc.* **2008**, *130*, 8741–8747.

[48] T. Marcelli, P. Hammar, F. Himo, *Chem. Eur. J.* **2008**, *14*, 8562–8571.

[49] J. Greindl, J. Hioe, N. Sorgenfrei, F. Morana, R. M. Gschwind, *J. Am. Chem. Soc.* **2016**, *138*, 15965–15971.

[50] N. Lokesh, J. Hioe, J. Gramüller, R. M. Gschwind, *J. Am. Chem. Soc.* **2019**, *141*, 16398–16407.

[51] M. Melikian, J. Gramüller, J. Hioe, J. Greindl, R. M. Gschwind, *Chem. Sci.* **2019**, *10*, 5226–5234.

[52] K. Rothermel, M. Melikian, J. Hioe, J. Greindl, J. Gramüller, M. Žabka, N. Sorgenfrei, T. Hausler, F. Morana, R. M. Gschwind, *Chem. Sci.* **2019**, *10*, 10025–10034.

[53] M. Fleischmann, D. Drettwan, E. Sugiono, M. Rueping, R. M. Gschwind, *Angew. Chem. Int. Ed.* **2011**, *50*, 6364–6369.

[54] P. Renzi, J. Hioe, R. M. Gschwind, *J. Am. Chem. Soc.* **2017**, *139*, 6752–6760.

[55] M. Žabka, R. M. Gschwind, *Chem. Sci.* **2021**, *12*, 15263–15272.

[56] L. Simón, J. M. Goodman, *J. Org. Chem.* **2010**, *75*, 589–597.

[57] J. P. Reid, J. M. Goodman, *Chem. Eur. J.* **2017**, *23*, 14248–14260.

[58] J. P. Reid, M. S. Sigman, *Nature* **2019**, *571*, 343–348.

[59] C. B. Santiago, J. Y. Guo, M. S. Sigman, *Chem. Sci.* **2018**, *9*, 2398–2412.

[60] N. Sorgenfrei, J. Hioe, J. Greindl, K. Rothermel, F. Morana, N. Lokesh, R. M. Gschwind, *J. Am. Chem. Soc.* **2016**, *138*, 16345–16354.

[61] A. Milo, A. J. Neel, F. D. Toste, M. S. Sigman, *Science (80-.).* **2015**, *347*, 737–743.

[62] D. Jansen, J. Gramüller, F. Niemeyer, T. Schaller, M. C. Letzel, S. Grimme, H. Zhu, R. M. Gschwind, J. Niemeyer, *Chem. Sci.* **2020**, *11*, 4381–4390.

[63] H. Mayr, *Tetrahedron* **2015**, *71*, 5095–5111.

[64] T. A. Nigst, J. Ammer, H. Mayr, *J. Phys. Chem. A* **2012**, *116*, 8494–8499.

2. Ternary Complex in Brønsted Acid Catalysis – Unexpected Weak Steric Limitation Leads to a Broad Structural Space

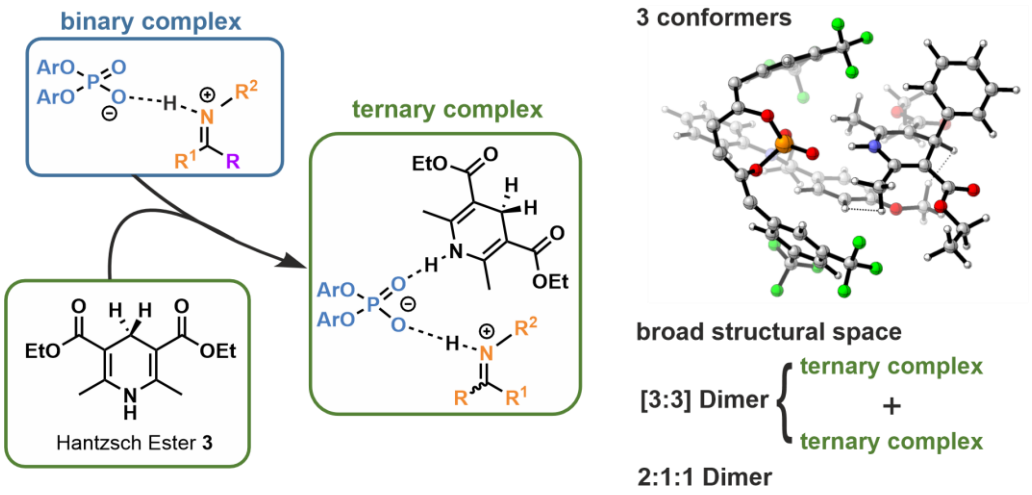

Maximilian Franta, Aryaman Pattanaik, Wagner Menezes da Silva, Kumar Motiram-Corral Prof. Dr. Julia Rehbein, Prof. Dr. Ruth M. Gschwind

To be submitted

A) NMR measurements for system screening and initial NMR investigations were performed by Maximilian Franta. The chemical shift assignment and conformer analysis was done by Maximilian Franta. The manuscript was mainly written by Maximilian Franta, assisted by Wagner Menezes da Silva. B) NMR pulse sequence adaptation was done by Kumar Motiram-Corral and Wagner Menezes da Silva. C) All theoretical calculations were performed by Aryaman Pattanaik, in assistance of Prof. Dr. Julia Rehbein. Aryaman Pattanaik and Prof. Dr. Julia Rehbein assisted in interpretation of data and writing and proof-reading of the manuscript. D) Prof. Dr. Ruth M. Gschwind contributed to conceptualization of the project, design of experiments, interpretation of data, writing and proof-reading of the manuscript and provided funding.

Preliminary version - text and Figures may differ from the manuscript.

2.1. Abstract

In ion pair catalysis, the last intermediate structures prior to the stereoselective transition states are of special importance for predictive models due to the high isomerization barrier between *E*- and *Z*- substrate double bonds connecting ground and transition state energies. However, in prior experimental investigations of chiral phosphoric acids (CPA) solely the early intermediates could be investigated while the key intermediate remained elusive. In this study, the first experimental structural and conformational insights into ternary complexes with CPAs are presented using a special combination of low temperature and relaxation optimized NMR spectroscopy. Combined NMR investigations and theoretical calculations revealed three conformers of the ternary complex, of which one is also closely resembling the previously calculated transition states. In addition, a 2:1:1 ternary complex as well as an unprecedent [3:3] dimeric species consisting of two ternary complexes was revealed. Given the importance of the ground state energies for the transition state interpretation in ion pair catalysis we believe that the presented experimental insight into the structural and conformational variety of the ternary complexes is key to the future development of predictive models in ion pair catalysis.

2.2. Introduction

The detection and identification of late reaction intermediates is pivotal for an in-depth understanding of mechanisms and thus predicting the reaction outcome. However, accessing these intermediates through experimental and computational methods often proves to be challenging. Especially for the BINOL (1,1′-binaphtol) derived chiral phosphoric acids (CPA), which have emerged as a prominent catalyst class with excellent stereoselectivities over the past decades,[1–12] late intermediates have been experimentally elusive until now. Due to their remarkable success in organocatalysis, extensive theoretical and analytical studies have already been conducted.[13–20] In contrast, despite years of effort, experimental studies have only been able to investigate early intermediates such as the binary complex (see Figure 2.1A, blue). The important last intermediate prior to the stereoselective step had been inaccessible due to solubility issues of the hydrogenation agent as well as the complexity of the systems. Only theoretical calculations have been capable of establishing models for transition states and were able to derive complex data-driven prediction models.[21,22]

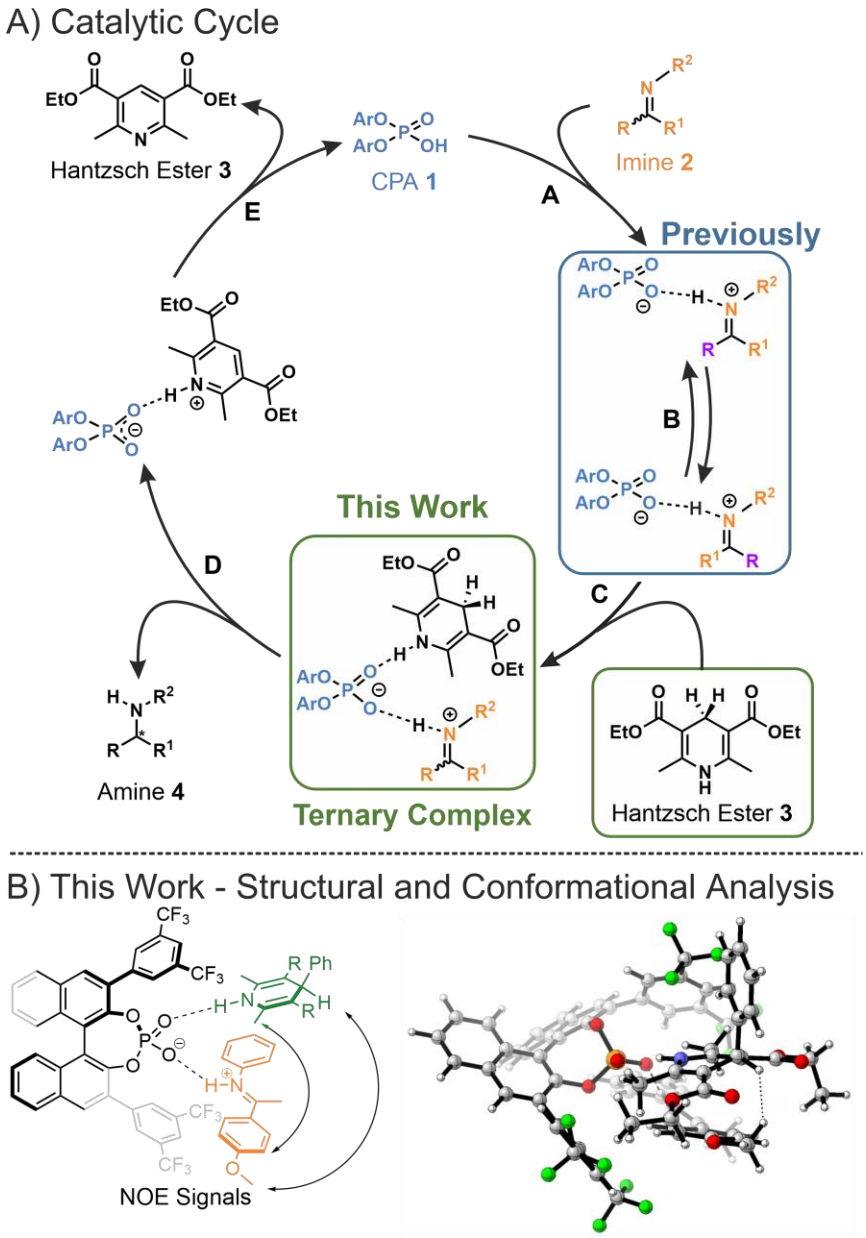

Figure 2.1 A) Proposed catalytic cycle for the CPA-catalyzed transfer hydrogenation of imines. Prior studies elucidated structural details of the binary complexes but the ternary complexes remained elusive for nearly a decade. B) In this work, we accessed the ternary complex by using a HE derivate which is soluble even at 180 K needed for NMR investigations. The gathered measurements were used for a structural and conformational analysis in collaboration with computational methods.

Nevertheless, despite the challenges associated with identifying reaction mechanisms involving hydrogen bonds and ion pair character,[23,24] experimental studies combined with calculations have provided a plethora of valuable insights into the early intermediates of the catalytic cycle originally proposed by Rueping *et al.* (see Figure 2.1A).[25] Among them, an *E*/*Z*-isomerization was revealed during step A in which a binary complex is formed *via* a hydrogen bond-assisted ion pair between CPA and imine.[17,24,26,27] In addition, the 3,3´-substituents were found to play a crucial role for controlling the

stereoselectivity.[25,28–34] To classify the influence of the 3,3´-substituents, Goodman *et al.* introduced two parameters: proximal sterics described by the rotational barrier of the 3,3´-substituent and the cone angle AREA (θ) of the binding pocket.[13] Furthermore, Goodman *et al.'s* computations postulated four distinct stereochemical arrangements for the CPA/imine binary complex[13], which were later experimentally confirmed by NMR studies.[30,31] Of these four calculated conformations, two are corresponding to an *E*-imine species (Type I *E* and Type II *E*) and two to a *Z*-imine species (Type I *Z* and Type II *Z*), with Type I and Type II differing in the arrangement of the imine to the binaphthyl moiety of the CPA. Notably, one of each imine isomer leads to the correct enantioselectivity (Type I *E* and Type II *Z*).

Besides the structural investigations of the binary complex, the aggregation behavior of CPAs was extensively investigated. Despite the strong hydrogen bonds and sterically hinderance of the 3,3´-substituents, a variety of structural arrangements could be possible due to the ion pair character of CPAs. Such aggregates could influence reactivity and selectivity by enabling new reaction pathways or serve as off-cycle equilibria. Indeed, several higher aggregates were identified by NMR spectroscopy.[30,35] On the one hand, an off-cycle [2:2] dimeric species was revealed consisting of two binary complexes which enclose the imines in between two CPAs.[30] Similar $[CPA/imine]_2$ dimers are also observed using *N*-(ortho-hydroxyaryl) imines which lead to a bidentate binding that might contribute to the high stereoselectivity with these substrates.[36] On the other hand, a 2:1 CPA/CPA/imine dimer was discovered with quinolines as substrate, for which calculations proposed that the quinoline forms a hydrogen bond to one CPA while the Hantzsch ester (HE) attaches to the second CPA.[37] Here, experiments showed an inversion in stereoselectivity in comparison to the classic monomeric pathway induced by a secondary dimeric pathway.[35]

For now however, prediction models are based on theoretical calculations of the energetically most probable monomeric CPA/imine/HE transition states.[14,15,38,39] Even in the case of monomeric reaction pathways the high activation barrier of the substrate double bond is expected to create a special importance of the relative energies of the last, the ternary intermediate prior to the stereoselective step. Usually, only the relative transition state energies must be considered. In case of a slow *E*/*Z*- isomerization the ground state energies of the last intermediate have to be taken into account, since *E*- and *Z*- pathways are mainly decoupled.[24] Hence, the structures, the conformations and the

potential aggregation of the elusive ternary complexes are of special interest for predictive models and the rational understanding of ion pair catalysis with CPAs.

However, experimentally advancing the ternary complexes with CPAs deemed extremely challenging due to additional exchange processes which cause line broadening and shorten the transverse relaxation times (T2), worsening the resolution and signal intensities of 2D NMR spectra. Hence, our group performed studies of the ternary complex featuring a BINOL-derived chiral disulfonimide (DSI) catalyst, which is closely related to CPAs but better accessible for NMR measurements. Here, the first insights into the aggregation behavior of ternary complexes were provided based on NMR spectroscopy.[40] Subsequently, we transferred this knowledge to CPAs and showed in a London-Dispersion study for the first time that ternary complexes of CPAs can also be detected by NMR spectroscopy.[41] In consequence, the focus of our NMR investigations shifted towards the ternary complex of CPAs for more in-depth details on its structure and aggregation behavior. Nevertheless, structural and conformational investigation were still elusive based on standard methods for small molecules. Therefore, NMR methods for proteins could be used which are optimized for short T2 relaxation times and slow tumbling.[34] Both are crucial in mechanistic studies of ternary complexes of CPAs, especially at low temperatures which also push the system in the slow tumbling regime.

Thus, the aim of this study is to provide easy experimentally access to the late intermediates of CPAs using NMR spectroscopy. Therefore, we employed the ^{15}N HSQC-NOESY pulse sequence under optimized NMR conditions for our systems, thereby enhancing sensitivity and yielding more comprehensive data for in-depth investigations. Based on this approach, the structural and conformational variety of ternary complexes with CPAs was investigated for the first time. The structural space was especially examined in relation to previously reported structures, such as the 2:1 dimeric species. Here, we observed the 2:1:1 ternary complex for the first time and confirmed that the HE forms a hydrogen bond to the second CPA, as proposed by calculations.[35] Furthermore, an unprecedent [3:3] dimeric species was revealed in which imine and HE are enclosed by two CPAs leading to the first observed additional separated hydrogen bond signal of the HE. Besides the structural investigations, the first conformational analysis of the 1:1:1 ternary complex of CPAs was conducted by NMR spectroscopy combined with calculations revealing three conformers. Notably, the most stable conformer also closely resembles the calculated transition states, thereby validating these for the first time

experimentally. This structural and conformational variety of late intermediates in CPA catalysis was not unraveled in prior theoretical studies, underscoring the crucial role of experimental studies in deepening our comprehension of complex structures' conformational space.

2.3. Results and Discussion

2.3.1. Model Systems and Experimental Setup

In order to investigate transfer hydrogenation reactions of CPAs the last intermediates prior to the stereoselective step/transition state, 25 ternary complexes comprised of different CPA **1**/imine **2**/HE **3** combinations were screened in a 1:1:1 stoichiometry at 180 K (see Figure 2.2). This low temperature is crucial to slow down exchange processes and enables the detection of hydrogen bonds. Therefore, we used dichloromethane (DCM) as solvent which combines low temperature accessibility, excellent NMR prop-erties of the complexes and very high ion pair formation trends. In prior attempts of accessing the ternary complex by NMR spectroscopy, the poor solubility of the HE **3a** at 180 K as well as product formation during the sample preparation hindered any structure elucidation for several years. In the study of DSIs,[40] the HE derivate **3b** with a phenyl-group, substituting one of the hydrogen atoms distant from the binding site, was successfully employed to improve solubility and to reduce reactivity. Also, for complexes with CPAs the HE derivate **3b** proved itself to be superior to **3a** and allowed us to investigate the ternary complex with concentrations of up to 50 mM in a 1:1:1 stoichiometry of CPA **1**/ imine **2**/ HE **3**. In addition, both the imine **2** and HE **3** were ^{15}N-labelled (^{15}N spin number = ½) for an easier identification of hydrogen bonds between the CPA **1** and imine **2** (PO^--H-N^+) and between the CPA **1** and HE **3** (PO-H-N) due to their doublet splitting. Different CPAs 1a-f and imines 2a-g were selected with varying steric and electronic properties due to their significant influence on the NMR properties of the complexes observed in prior studies. The screening of 25 systems revealed some general characteristics of the formation of ternary complexes. Despite the steric hinderance of the 3,3´-substituents, the ternary complex was detected for each CPA (see SI 2.6.11). It also revealed that CPAs with a relatively high AREA (θ) value and low rotational barrier,[13] such as TRIFP **1a** (AREA (θ) = 4.03; rotation barrier = 2.02kcal mol^{-1}) and OMe-CPA **1b**, result in sharper spectral lines, better suited for NMR investigations and a higher formation trend of ternary complexes.

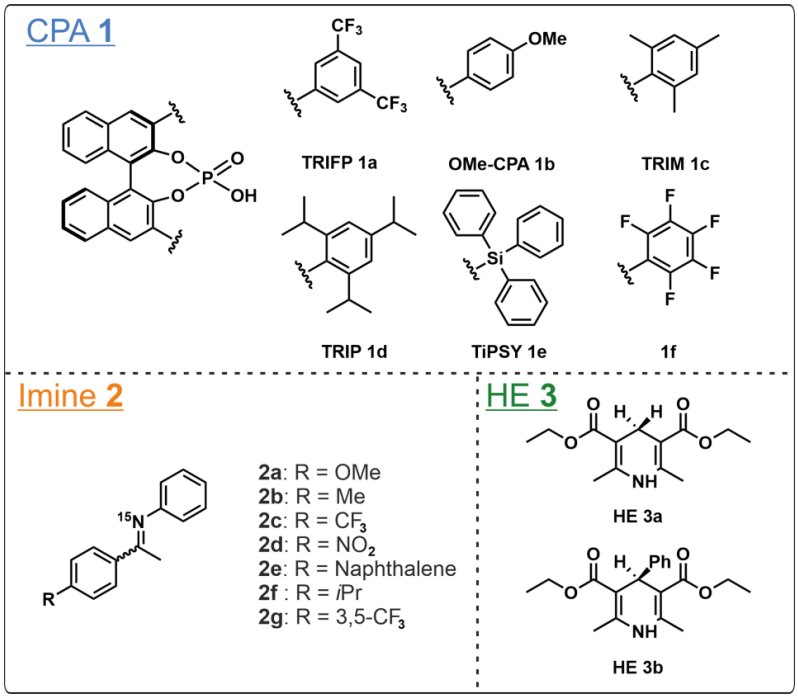

Figure 2.2 Model compounds used in the screening for ternary complexes comprised of (R)-CPAs 1, imines 2 and HE 3. 25 combination of imines 2a-g with CPAs 1a-f and HE 3b were screened.

The combination of TRIFP **1a**/ **2a**/HE **3b** showed the best NMR properties (high ternary complex formation, acceptable line widths, CF_3 groups for ^{1}H-^{19}F-HOESY) and was therefore selected as model system. Besides the hydrogen bond signals of the ternary complex, additional yet unknown signals were observed in the hydrogen bond area of the ^{1}H-spectrum during system screening. Here, one signal pattern of two doublets was observed in several systems, which hinted towards a potential new aggregate of the ternary complex. To study these signals, CPA **1b** with a *p*-methoxy-phenyl as 3,3´-substituent (OMe-CPA **1b**) was selected as second model system as it showed the highest preference of this new species out of all screened systems.

2.3.2. Structural Space

First, the hydrogen bond area in the ^{1}H-spectrum (from 9 to 19 ppm) of TRIFP **1a**/**2a**/HE **3b** was evaluated to identify the ternary complex (see Figure 2.3). While the presence of a ternary complex is indicated by a new CPA/HE hydrogen bond signal (9.05 ppm) only one signal set for the CPA/imine hydrogen bond (two doublets, one for each imine isomer) is observed suggesting a fast exchange of the binary and ternary complex on the NMR timescale even at 180 K. This was corroborated by a chemical shift mapping in which both signals of the binary complex are high-field shifted upon the addition of HE **3b** to the system of TRIFP **1a**/**2a** (see Figure 2.3B and SI 3.7). Similarly,

only one CPA/HE signal is observed for the ternary complexes in all 1H 15N correlation spectra. This indicates that this signal is an averaged HE **3b** signal of both *E*- and *Z*-ternary complexes as well as the free HE. Hence, these species are also in fast exchange. Additionally, further analysis of the CPA/imine hydrogen bonds shows that the CPA/Z-imine signal is further highfield shifted (-0.27 ppm) than the CPA/E imine (-0.16 ppm). From the fitting of the chemical shift mapping data the binding constants were calculated showing that 3b is only weakly bound to the binary complex (*Z*-**2a**: K_a=22.2; *E*-**2a**: K_a=19.8) similar to the situation in DSIs.[40]

For quinolines complexes with dimeric catalysts structures were found to influence the stereoselectivity,[35] therefore next the potential presence of catalyst dimers in the ternary complexes was tested. So far, exclusively the binary complex of the 2:1 dimer has been experimentally investigated, supported by calculations that proposed the HE forms a hydrogen bond to the second CPA (see Figure 2.3C). However, so far, there has been no experimental evidence whether the HE binds to the second CPA or to the same CPA as the substrate. Therefore, a 2:1:1 stoichiometry of TRIFP **1a**/**2a**/HE **3b** was used to force the system into this dimeric species (which is not observed in a 1:1:1 stoichiometry) and to investigate the binding behavior of the HE in this complex. In accordance with the 2:1 binary complex signal pattern, two singlets representing the CPA **1**/CPA **1** (PO--H--OP) hydrogen bonds of both imine isomers and two doublets for the CPA **1**/CPA **1**/imine **2** (PO--H--N) hydrogen bonds of both imine isomers were detected (see Figure 2.3C, purple). In addition, for the first time a signal for the hydrogen bond between HE and CPA in such a **1a**/**1a**/**2a**/**3b** complex was detected (see Figure 2.3C, green). Similar to the 1:1:1 ternary complex, a fast exchange process between 2:1:1 complexes with and without HE **3b** was observed and corroborated by a chemical shift mapping (see SI 2.6.7.2). Moreover, the chemical shift mapping revealed a significantly higher shift for the CPA/CPA (PO--H--OP; up to 0.38 ppm) hydrogen bond signals compared to the CPA/CPA/imine signals (PO--H—N; up to -0.08 ppm). This observation indicates that the chemical environment of the CPA **1**/CPA **1** hydrogen bond is more impacted by the addition of the HE **3b** than the CPA **1**/CPA **1**/imine **2** hydrogen bond. This finding supports Grimme et al.s calculations in which the substrate is attached to one CPA while the HE is attached to the other CPA of the dimer.[35,37] Thus, this is the first time the 2:1:1 complex is experimentally detected and chemical shift mapping indicates that imine and Hantzsch ester bind to different catalyst molecules.

Next, the structural space of the 1:1:1 ternary complex was further investigated. In prior studies, no additional structures of ternary complexes were considered.[15,41] However, in all 25 screened systems multiple additional hydrogen bond signals were detected. Considering the remarkable impact of the dimeric pathway with quinolines which was only detected as a small populated species by NMR,[35] the elucidation of such additional late reaction intermediates could be crucial for any prediction model.

Besides a singlet at approximately 18 ppm (see Figure 2.4A, purple), which appeared in most systems and seems to be related to a CPA aggregate $[CPA]_n$, an additional signal pattern was observed regularly, twice even as the major species (see SI 2.6.7.1). For these investigations, the OMe-CPA **1b**/**2a**/HE **3b** system was selected as model system due to a high formation of this species (see Figure 2.4A, blue) In general, both signals are doublets and appear together indicating that they belong to the same species. To identify the underlying hydrogen-bonded substrates of each signal, samples were compared in which either the imine **2a** or the HE **3b** was ^{15}N-labelled. Thereby, the signal at 13.77 ppm (blue) was identified as a [CPA/imine] hydrogen bond which was later elucidated as an *E*-imine species by EXSY correlations (see Figure 2.4B). Furthermore, the signal at 9.98 ppm was identified as a [CPA/HE] hydrogen bond (see SI 2.6.7.1). This is the first time that an additional separate hydrogen bond signal is observed as in prior studies only averaged signals for the HE **3b** were detected due to fast exchange processes.[40,41] Therefore, the exchange processes of this new species have to be slowed down which indicates a locked system that hinders the HE **3b** from a fast exchange with the binary and ternary complexes.

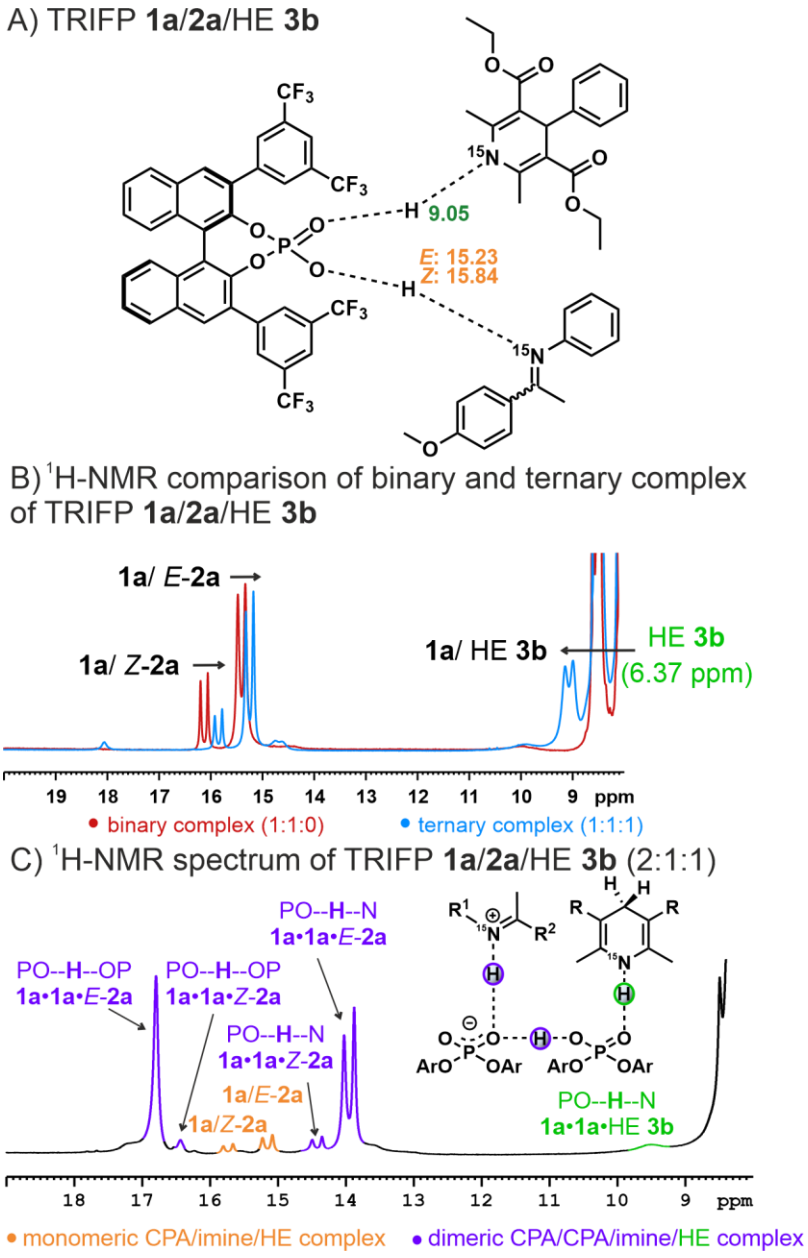

Figure 2.3 A) Structure of the ternary complex of TRIFP 1a/2a/HE 3b with the proton chemical shifts of the hydrogen bond signals. B) ^{1}H-NMR spectrum comparison of the binary (red, 1:1:0 stoichiometry, 40 mM, CD_2Cl_2, 180K) and the ternary complex (blue, 1:1:1 stoichiometry, 40 mM, CD_2Cl_2, 180K) of the system TRIFP 1a/2a/ HE 3b. Upon addition of the HE 3b, a high-field shift of both CPA/imine hydrogen bond signals is observed. C) ^{1}H-NMR spectrum of the TRIFP 1a/2a/ HE 3b system in a 2:1:1 stoichiometry (40:20:20 mM, CD_2Cl_2, 180K). This sample demonstrated that also for the dimeric 2:1 species (purple) it is possible to form a complex with the HE 3b.

Besides these initial observations, the [CPA **1b**/*E*-**2a**] hydrogen bond signal is high field shifted in comparison to other CPA/imine hydrogen bond signals (see Figure 2.4A). Similar chemical shifts were previously reported only for a [2:2] dimer of two CPAs that lock two imines between them, which also occurred exclusively as an *E*-imine species.[30] Considering the integral ratio of 1:1, the same amount of [CPA/*E*-imine] hydrogen bonds as [CPA/HE] hydrogen bonds within this complex (see Figure 2.4A). Hence, a first

assumption would be a [3:3] dimer consisting of two ternary complexes (CPA/imine/HE=**3**) where the CPAs enclose both imine **2a** and HE **3b** (see Figure 2.4C). To validate that the signals correspond to a dimeric species, dilution experiments were performed. Here, a significant decrease in both [3:3] dimer signals was observed compared to the hydrogen bond signals of the binary/ternary complex (see SI 2.6.7.1), supporting the [3:3] dimer hypothesis. Furthermore, the uniform decrease of both the [CPA/imine] as well as the [CPA/HE] hydrogen bond signals supports the observation that both are related to the same complex. Next, diffusion ordered spectroscopy (DOSY) measurements were conducted for validation of a higher aggregation (see SI 2.6.9). For DOSY evaluation, the hydrogen bond signals cannot be used, so other well-separated signals, such as the OMe-group signals for CPA **1b**, were utilized. However, for these signals, the exchange between binary/ternary complexes must be considered which results in an averaged signal set for the aliphatic and aromatic signals for the proposed [3:3] dimer. Hence, using these signals for DOSY results in an averaged volume of all species for each substrate, rather than the volume of one specific complex. For comparison purposes, separate samples with a 1:1 stoichiometry were measured for the binary complex and for HE **3b** alone. Here, a volume of 1625 Å^3 was determined for the binary complex and 506 Å^3 for HE **3b**. Combining these values yields an estimated volume of 2131 Å^3 for the ternary complex. However, the average volume of all CPA species inside the 1:1:1 sample is 2331 Å^3, significantly exceeding the estimated volume of the ternary complex (2131 Å^3). Thus, a higher aggregate must be responsible for this significant increase in volume, which also supports the [3:3] dimer hypothesis. Besides NMR experiments, calculations were performed to verify a [3:3] dimer. Despite separate hydrogen bond signals, the exchange processes identified by EXSY signals prevent a NOESY analysis of the [3:3] dimer due to its similarities to the ternary complex, making it difficult to differentiate NOE correlations clearly. Nevertheless, calculations resulted in a [3:3] structure that encloses imine **2a** and HE **3b** which supports the initial assumption of a locked system based on the additional separated hydrogen bond signal for HE **3b** (for further details see SI 2.6.10.2). Thus, the [3:3] dimer model is supported by both computations as well as NMR data, including the integral ratio of approximately 1:1 of the [CPA **1b**/*E*-**2a**] to [CPA **1b**/HE **3b**] hydrogen bond signals, chemical shifts, DOSY and dilution experiments (for further discussion see SI 2.6.7.1).

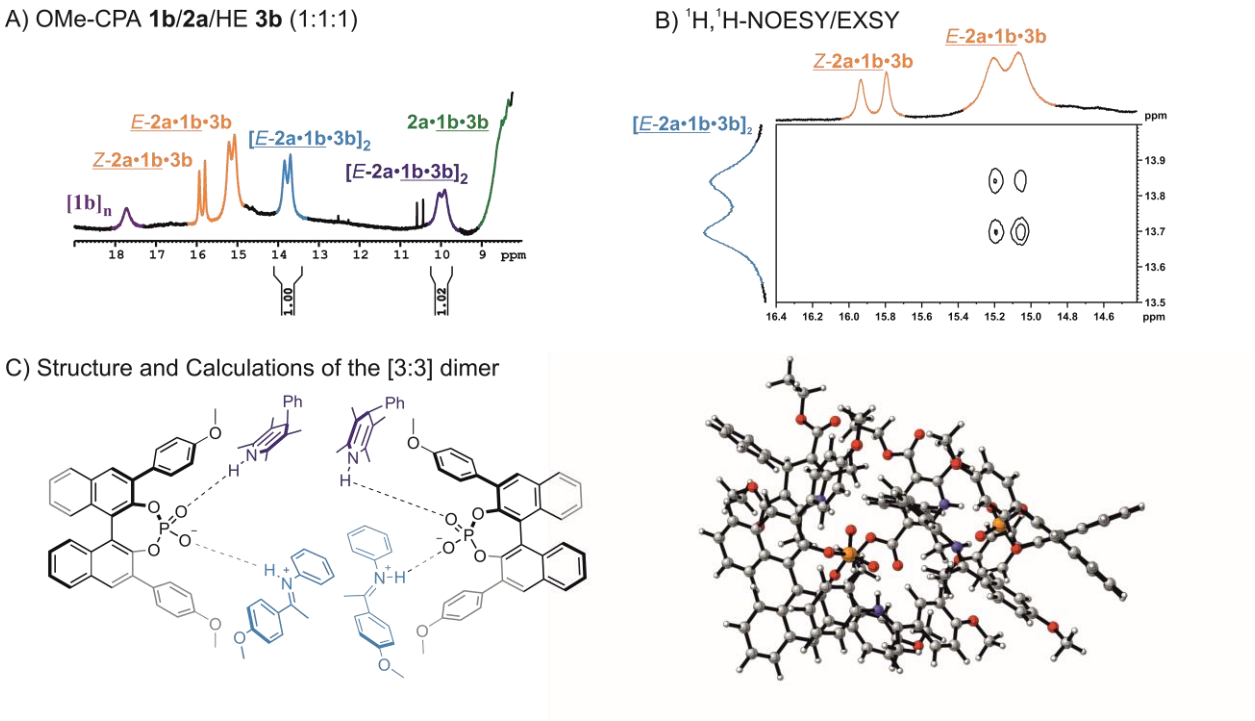

Figure 2.4 A) The ^{1}H-NMR spectrum of the OMe-CPA 1b/2a/3b system (1:1:1 stoichiometry, 40 mM, CD_2Cl_2, 180 K). The hydrogen bonds between CPA 1/imine 2 (orange) and CPA 1/3b (green) can be assigned to the ternary complex. The $[CPA]_n$ aggregate is highlighted in pink. Additionally, two new hydrogen bond signals are observed ($[E\text{-}2a/1a/3b]_2$ in blue; $[E\ 2a/1b/3b]_2$ in purple; the respective hydrogen bond is underlined), which can be identified as a [3:3] dimeric species consisting of two ternary complexes. B) One part of the ^{1}H-^{1}H NOESY/EXSY of this system is displayed showing the exchange between the [3:3] dimer and the 1b/E-2a hydrogen bond signal which reveals the [3:3] dimer as an E-imine species. C) Schematic display of the [3:3] dimer (left) and calculated structure of the [3:3] dimer.

In conclusion, we were able to experimentally confirm the ternary complex with CPAs by NMR spectroscopy. Beyond the mere formation of the ternary complex, we were also for the first time able to identify two higher aggregates as late intermediates: a 2:1:1 dimeric species and a previously unknown [3:3] dimeric species consisting of two ternary complexes.

2.3.3. Accessing the Ternary Complex

Next, we conducted the first experimental analysis of the structural arrangement of ternary complexes with CPAs. Here, we focused on the 1:1:1 ternary complex of our model system TRIFP **1a**/**2a**/HE **3b**. Other species were not analyzed because no system was observed during screening that exclusively contained either the 2:1:1 complex or the [3:3] dimer, preventing an in-depth NOE analysis due to exchange processes. For the classic approach known from the binary complexes, ^{1}H,^{31}P-HMBC is used as a starting point for the chemical shift assignment of any CPA structures. This method provides information about the central region of the ternary complex and the connection of all substrates. However, in the TRIFP **1a**/**2a**/HE **3b** system binary and ternary complexes are in fast chemical exchange even at 180 K resulting in signal broadening and reduced chemical shift resolution. These exchange processes are particularly pronounced in the phosphorus dimension resulting in poor chemical shift resolution in ^{1}H,^{31}P-HMBC spectra which deems the classic approach infeasible. Therefore, a variety of NMR methods were tested and finally optimized to enable a new approach for the chemical shift assignment. Here, especially the center of the ternary complex which consists of a PO^{-}-H-N^{+} (CPA/imine) and PO-H-N (CPA/HE) hydrogen bond was of interest. The possibility of ^{15}N-labelling both imine **2a** as well as the HE **3b** moved ^{15}N-2D-NMR spectra into the focus. At 180 K, the CPA/Imine/HE system is in the slow-tumbling regime, making the NMR pulse sequences commonly employed in protein studies suitable for our purposes. The ^{15}N-HSQC-NOESY experiment, utilizing the pulse sequence from the Bruker® library hsqcetgpnosp with adiabatic pulses, is a method applied in protein research. It combines two robust NMR techniques: the ^{15}N HSQC (heteronuclear single quantum coherence) and the NOESY (nuclear Overhauser effect spectroscopy). In the ^{15}N HSQC component, correlations between nitrogen and proton nuclei within proteins are observed, providing

insights into the chemical environment. Conversely, the NOESY component detects NOE effects, uncovering interactions between nearby nuclear spins.

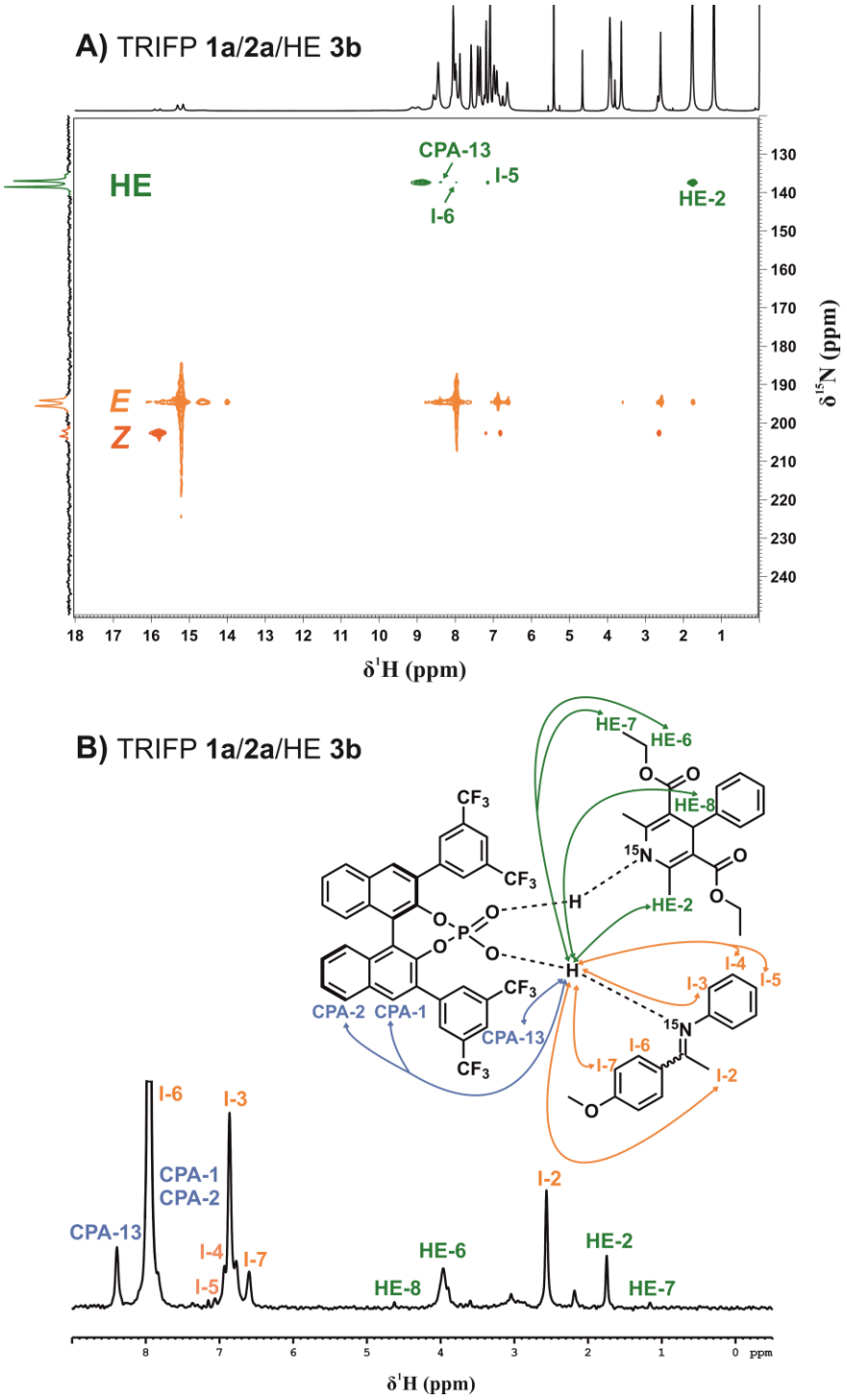

Figure 2.5 A) ^{15}N-HSQC-NOESY spectrum of TRIFP 1a/2a/ HE 3b (1:1:1 stoichiometry, 40 mM, CD_2Cl_2, 180K). Separated rows for the CPA/E-imine (orange), CPA/Z-imine (red) and CPA/HE (green) hydrogen bonds can be observed. B) Single rows can be displayed as 1D spectra for more detailed information to reveal the structural environment of each hydrogen bond, here exemplary displayed for the CPA/E-imine hydrogen bond (δ (^{15}N)=195 ppm).

These interactions offer valuable distance constraints, aiding in the determination of a protein's three-dimensional structure. By integrating these techniques, the ^{15}N HSQC-NOESY experiment yields comprehensive structural details about the CPA/Imine/HE (see Figure2.5A). With this pulse sequence a reduced number of cross-signals is detected in comparison to ^{1}H-^{1}H NOESY, which minimizes signal overlapping significantly. The higher sensitivity of the ^{15}N HSQC-NOESY compared to the ^{1}H NOESY is primarily attributed to the significantly longer T2 relaxation times of ^{15}N signals relative to ^{1}H signals. This characteristic reduces magnetization loss during the evolution period (τ), thereby preserving more signal and resulting in enhanced sensitivity. This phenomenon is already known[42,43] and has been used in the studies of hydrogen bonding of different systems.[44–48]

The use of one-dimensional rows of this spectrum, at the ^{15}N frequency of interest, offers an enhanced method for observing inter- and intramolecular contacts (Figure 5B). Moreover, detailed knowledge about the center of the ternary complex and hydrogen bond site can be obtained. Thus, based on the initial screening, optimized sample preparation, ^{15}N-HSQC-NOESY and the selection of the TRIFP **1a**/**2a**/HE **3b** system which has the better chemical shift resolution, after initial attempts by our group[40,41] it is for the first time possible to achieve detailed structural information of the ternary complex.

The new approach for the chemical shift assignment enables unambiguous structural investigations of the ternary complex, applicable across a wide range of substrates for the first time. The resulting chemical shift assignments establish the basis for conformational investigations of the ternary complex of CPAs which were previously beyond reach.

2.3.4. Conformational Investigations

So far, there has been no comprehensive conformational analysis of 1:1:1 ternary complexes of CPAs. Hence, we aimed to elucidate their conformational space based on established NMR methods, which allowed us to access the ternary complex, and by including theoretical calculations. Therefore, we employed our TRIFP **1a**/ **2a**/ HE **3b** model system to utilize ^{1}H,^{19}F-HOESY in addition to ^{1}H,^{1}H NOESY and 15N HSQC-NOESY. Additionally, the 1:1:1 ternary complex is the major populated species in this system, thus no other species are interfering with our NOE analysis. Nevertheless, the fast exchange between binary and ternary complexes, which is still present at 180 K,

must be considered for a NOE interpretation. This leads to a challenging NOE analysis as only interactions involving HE **3b** can be considered, given that HE **3b** is not associated with the binary complex. Despite these limitations, a clear distinction between the calculated conformers is feasible by focusing on the distinct HE **3b** NOE correlations, that are unique for each respective conformer in comparison to the others. This confined assessment of exclusively the distinct HE **3b** NOE correlations within the extensive NOE network is crucial, since most signals involve contributions from several conformers, preventing the unambiguous assignment to a single conformer. Initial analysis of the HE 3b NOE network, however, proved elusive, suggesting the presence of multiple conformers for the 1:1:1 ternary complex. As a result, a valid interpretation of the NMR data is only qualitatively attainable and must be supported by theoretical calculations.

Thus, an initial conformational search was performed by using CREST[49] which uses meta-dynamics.[50] The B97-D[51] functional combined with def2-SVP[52] basis set was used for geometry optimization and frequency analysis in ORCA 5.0.3 software package.[53] The global and local minimum energy structures were confirmed by 3n-6 non-zero positive normal modes. To adapt the experimental conditions of 180 K and CD_2Cl_2 all the calculations were performed in CPCM model[54] with the di-electric constant ε=16.20. For further improvement of the electronic energies of the conformers, hybrid functionals were also used for better comparison. These calculations resulted in eight conformers, of which only the three lowest-energy conformers, with a cutoff at +4.5 kcal/mol relative to the lowest-energy conformer, were considered (see Figure 2.6). Based on these conformers, the beforementioned NMR approach of ^{1}H,^{1}H NOESY and ^{15}N HSQC-NOESY was utilized and further corroborated by ^{1}H,^{19}F HOESY spectra.

First, the lowest energy conformer C1 with a face-to-face arrangement of **2a** and HE **3b** inside the binding pocket of TRIFP **1a** was analyzed by NMR spectroscopy. Especially NOE correlations of the HE **3b** proton (chemical shift: 4.66 ppm, referred to as *HE-8*) which is neighboring the phenyl-group are indispensable as the arrangement of this proton to the imine and CPA is significantly different for all conformers. For C1 *HE-8* is close to the methoxy-group of the imine. In addition, the methyl-groups of the HE **3b** are in close proximity to the *p*-methoxy-phenyl ring of the imine. Both correlations are uniquely observed for C1 and confirmed by NOESY (see Figure 2.6, left). In conformer C2 (+3.4 kcal/mol relative to C1), a similar arrangement to C1 is observed with both substrates positioned inside the binding pocket of TRIFP **1a**, but the imine is slightly

flipped. This results in a distinct close proximity of the *N*-phenyl-moiety of the imine to HE **3b** (*HE-8*), which is proven by NOE correlations (see Figure 2.6, middle). Hence, both C1 and C2 can be experimentally validated and clearly distinguished. Comparing both structures with the Type I *E* and Type II *E* structures of the binary complex shows similarities of both C1 and C2 to the Type I *E* structure indicating that both could originate from this conformation. Furthermore, the third conformer C3 (relative energy to C1: +2.6 kcal/mol) is also observed by the NOE network. Contrary, C3 is similar to Type II *E* with a flipped imine inside the binding pocket and further differs from C1 and C2 as the HE **3b** is positioned outside the binding pocket. The latter results in distinct interactions between *HE-8* and the BINOL-backbone of TRIFP **1a** which are detected by NOESY (see Figure 2.6, right). Thus, not only a broad structural space with three confirmed complexes but also a conformational space with three different conformers was identified. Considering the utilization of a phenyl-substituted HE **3b**, which is more sterically demanding than commonly employed HE **3a**, even more conformers could be observed using HE **3a**. These results demonstrate that the steric limitations of the 3,3´-substituent do not limit the aggregation of ternary complexes as much as one would expect.

To investigate if only one or more of these conformers could be reactive, the computed conformers were analyzed for possible reaction pathways. Here, for conformers C1 and C2 the reactive hydrogen atom of the HE **3b** was found to be close enough to the N=C bond to proceed the reaction in the respective stereoselectivity which is observed for (*R*)-TRIFP **1a**. In addition, comparing conformer C1 with previously computed transition states for this reaction reveals several similarities.[38] In particular, the face-to-face arrangement of imine **2a** and HE **3b** exists in both C1 as well as the postulated transition states for TRIFP **1a**.[14] Therefore, it is likely that the transition states arise from conformer C1, which is the first experimental validation of the ternary complex prior to the transition states. Additionally, conformer C2 depicts another reactive structure, which also leads to the correct stereoselectivity. Despite C2 having a relatively higher energy than C1 (+ 3.57 kcal/mol), the fact that C2 is populated even at 180 K demonstrates that it cannot be disregarded for the prediction models of the reaction which typically is performed at 303 – 333 K.[25,28] Contrary to C1 and C2, in conformer C3 the HE **3b** is positioned outside of the binding pocket. Due the resulting distance between imine **2a** and HE **3b**, an immediate reaction is not possible. Despite being an unreactive conformer, identifying C3 contributes to the understanding of sterically demanding CPAs (e.g. TRIP **1d**, TiPSY **1e**).

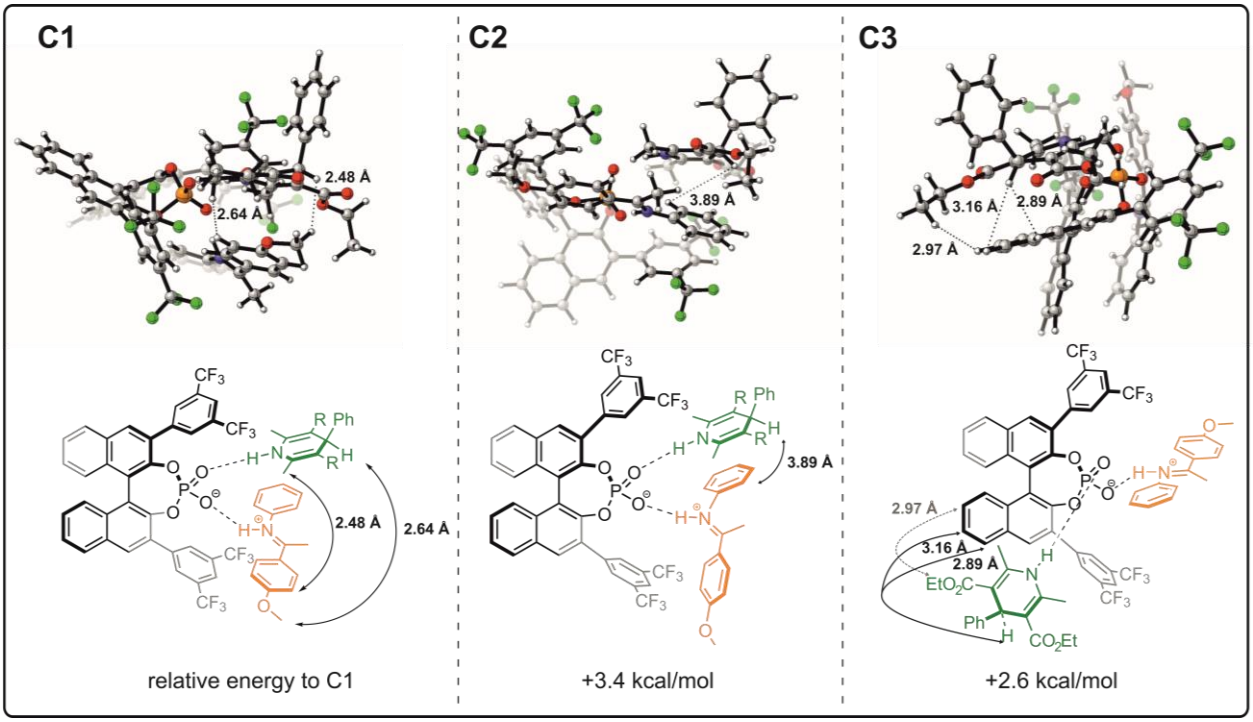

Figure 2.6 Conformational Analysis of the ternary complex. Three conformers were computed and validated by NMR spectroscopy. All three conformers coexist, with energetic stability decreasing in the following order: C1>C3>C2. C1 and C2 are reactive in this state, while for C3 rearrangements are necessary to lead to a hydrogenation of the imine. The conformers are validated by distinct NOE cross signals of the HE 3b. All distinct NOE correlations are depicted for each conformer in the structure below the 3D structure.

Normally, the presence of a plethora of structures would be expected to decrease stereoselectivity. However, despite detecting multiple additional hydrogen bond signals in TRIP **1d** and TiPSY **1e** systems, both are two of the most prominent CPAs with the highest selectivity.[28,29] However, considering C3, it is reasonable to assume that due to the steric constraints of these CPAs, multiple structures could be formed in which the HE is outside of the binding pocket. Consequently, these structures would not affect stereoselectivity as they are unreactive, despite being detectable by NMR spectroscopy.

In summary, the combination of computations and NMR spectroscopy revealed a broad conformational space consisting of three conformers. Among them, two conformers have an arrangement of imine **2a** to HE **3b** that could facilitate the reaction. Despite the non-reactive arrangement of conformer C3, identifying this conformer contributed to the understanding of the hydrogen bond signals of sterically more demanding CPAs. In addition, the first experimental validation of the previously calculated transition states was achieved as conformer C1 of the ternary complex was found to closely resemble the transition states.

2.4. Conclusion

While CPAs have been under scientific investigations due to their tremendous success in organocatalysis for almost a decade, experimental investigations have struggled to provide insights into later reaction steps. Until now, the binary complex of CPAs has been the main focus for any experimental studies. While these studies have yielded crucial insights, the development of an experimental prediction model for stereoselectivities based on these early intermediates remains a formidable challenge. Consequently, attention has shifted towards investigating subsequent reaction intermediates, which are anticipated to bear greater resemblance to the transition state.

Therefore, in this study we conducted the first experimental structural and conformational analysis of ternary complexes with CPAs. First, we took advantage of the T2 relaxation properties of the TRIFP 1a/ 2a/ HE 3b model system and employed the 15N HSQC NOESY pulse sequence with the appropriate acquisition parameters to investigate the ternary complex. By combining this method with standard 2D NMR spectra, an extensive structural and conformational space was revealed. Thereby, we identified not only the ternary complex of CPAs, but also a novel [3:3] dimeric species consisting of two ternary complexes, as well as a dimeric 2:1:1 ternary complex. Accessing the 2:1:1 ternary complex also confirmed the proposed calculated structures experimentally for the first time. These revelations showcase that despite the sterically hinderance of CPAs, higher aggregates are still formed in later reaction steps and should be considered in prediction models. Besides the structural investigations, we combined theoretical calculations and NMR spectroscopy to obtain and analyze conformers of the 1:1:1 ternary complex. Here, three different conformers were observed of which two could lead to a reactive transition state. One of these two even closely resembles the previously calculated transition states and therefore provides the first experimental validation for them.

In summary, a new approach to access the ternary complex of CPAs has been established. Based on this approach, a new [3:3] dimer and a ternary 2:1:1 complex was revealed along with a broad conformational space. Considering the significance of ground state energies for interpreting the transition states in ion pair catalysis, the presented experimental insights into the structural and conformational diversity of ternary complexes could be crucial for the future development of predictive models in ion pair catalysis.

2.5. References

[1] M. Sickert, F. Abels, M. Lang, J. Sieler, C. Birkemeyer, C. Schneider, Chem. Eur. J. **2010**, 16, 2806–2818.

[2] Q. X. Guo, H. Liu, C. Guo, S. W. Luo, Y. Gu, L. Z. Gong, J. Am. Chem. Soc. **2007**, 129, 3790–3791.

[3] T. Akiyama, J. Itoh, K. Yokota, K. Fuchibe, Angew. Chem. Int. Ed. **2004**, 43, 1566–1568.

[4] D. Uraguchi, M. Terada, J. Am. Chem. Soc. **2004**, 126, 5356–5357.

[5] D. Uraguchi, K. Sorimachi, M. Terada, J. Am. Chem. Soc. **2004**, 126, 11804–11805.

[6] G. B. Rowland, E. B. Rowland, Y. Liang, J. A. Perman, J. C. Antilla, Org. Lett. **2007**, 9, 2609–2611.

[7] M. Rueping, A. P. Antonchick, T. Theissmann, Angew. Chem. Int. Ed. **2006**, 45, 6751–6755.

[8] P. Jiao, D. Nakashima, H. Yamamoto, Angew. Chem. **2008**, 120, 2445–2447.

[9] Q. Yin, S. G. Wang, S. L. You, Org. Lett. **2013**, 15, 2688–2691.

[10] M. Rueping, T. Theissmann, M. Stoeckel, A. P. Antonchick, Org. Biomol. Chem. **2011**, 9, 6844–6850.

[11] M. Yamanaka, J. Itoh, K. Fuchibe, T. Akiyama, **2007**, 6756–6764.

[12] A. G. Woldegiorgis, X. Lin, Beilstein J. Org. Chem. **2021**, 17, 2729–2764.

[13] J. P. Reid, J. M. Goodman, J. Am. Chem. Soc. **2016**, 138, 7910–7917.

[14] L. Simón, J. M. Goodman, J. Am. Chem. Soc. **2008**, 130, 8741–8747.

[15] J. P. Reid, M. S. Sigman, Nature **2019**, 571, 343–348.

[16] J. Greindl, J. Hioe, N. Sorgenfrei, F. Morana, R. M. Gschwind, J. Am. Chem. Soc. **2016**, 138, 15965–15971.

[17] N. Sorgenfrei, J. Hioe, J. Greindl, K. Rothermel, F. Morana, N. Lokesh, R. M. Gschwind, J. Am. Chem. Soc. **2016**, 138, 16345–16354.

[18] R. Maji, S. C. Mallojjala, S. E. Wheeler, Chem. Soc. Rev. **2018**, 47, 1142–1158.

[19] M. Duan, C. D. Díaz-Oviedo, Y. Zhou, X. Chen, P. Yu, B. List, K. N. Houk, Y. Lan, Angew. Chem. Int. Ed. **2022**, 61, 1–7.

[20] D. Parmar, E. Sugiono, S. Raja, M. Rueping, Chem. Rev. **2014**, 114, 9047–9153.

[21] C. B. Santiago, J. Y. Guo, M. S. Sigman, Chem. Sci. **2018**, 9, 2398–2412.

[22] L. Simón, J. M. Goodman, J. Org. Chem. **2010**, 75, 589–597.

[23] M. Žabka, R. Šebesta, Molecules **2015**, 20, 15500–15524.

[24] P. Renzi, J. Hioe, R. M. Gschwind, J. Am. Chem. Soc. **2017**, 139, 6752–6760.

[25] M. Rueping, E. Sugiono, C. Azap, T. Theissmann, M. Bolte, Org. Lett. **2005**, 7, 3781–3783.

[26] J. E. Johnson, N. M. Morales, A. M. Gorczyca, D. D. Dolliver, M. A. McAllister, J. Org. Chem. **2001**, 66, 7979–7985.

[27] L. Simón, J. M. Goodman, J. Org. Chem. **2011**, 76, 1775–1788.

[28] S. Hoffmann, A. M. Seayad, B. List, Angew. Chem. Int. Ed. **2005**, 44, 7424–7427.

[29] R. I. Storer, D. E. Carrera, Y. Ni, D. W. C. MacMillan, J. Am. Chem. Soc. **2006**, 128, 84–86.

[30] M. Melikian, J. Gramüller, J. Hioe, J. Greindl, R. M. Gschwind, Chem. Sci. **2019**, 10, 5226–5234.

[31] N. Lokesh, J. Hioe, J. Gramüller, R. M. Gschwind, J. Am. Chem. Soc. **2019**, 141, 16398–16407.

[32] I. Harden, F. Neese, G. Bistoni, Chem. Sci. **2023**, 14, 10580–10590.

[33] S. Panda, P. Ghorai, Angew. Chem. Int. Ed. **2023**, 62, DOI 10.1002/anie.202306179.

[34] E. Naulin, M. Lombard, V. Gandon, P. Retailleau, E. Van Elslande, L. Neuville, G. Masson, J. Am. Chem. Soc. **2023**, 145, 26504–26515.

[35] D. Jansen, J. Gramüller, F. Niemeyer, T. Schaller, M. C. Letzel, S. Grimme, H. Zhu, R. M. Gschwind, J. Niemeyer, Chem. Sci. **2020**, 11, 4381–4390.

[36] J. Gramüller, P. Dullinger, D. Horinek, R. M. Gschwind, Chem. Sci. **2022**, 13, 14366–14372.

[37] R. Mitra, H. Zhu, S. Grimme, J. Niemeyer, Angew. Chem. Int. Ed. **2017**, 56, 11456–11459.

[38] D. Yepes, F. Neese, B. List, G. Bistoni, J. Am. Chem. Soc. **2020**, 142, 3613–3625.

[39] L. Simón, J. M. Goodman, J. Am. Chem. Soc. **2009**, 131, 4070–4077.

[40] M. Žabka, R. M. Gschwind, Chem. Sci. **2021**, 12, 15263–15272.

[41] J. Gramüller, M. Franta, R. M. Gschwind, J. Am. Chem. Soc. **2022**, 144, 19861–19871.

[42] D. Stefanatos, S. J. Glaser, N. Khaneja, Phys. Rev. A **2005**, 72, 062320.

[43] N. Khaneja, J.-S. Li, C. Kehlet, B. Luy, S. J. Glaser, Proc. Natl. Acad. Sci. **2004**, 101, 14742–14747.

[44] R. M. Gschwind, M. Armbrüster, I. Z. Zubrzycki, J. Am. Chem. Soc. **2004**, 126, 10228–10229.

[45] Y. Toyama, I. Shimada, J. Magn. Reson. **2019**, 304, 62–77.

[46] A. Liu, A. Majumdar, W. Hu, A. Kettani, E. Skripkin, D. J. Patel, J. Am. Chem. Soc. **2000**, 122, 3206–3210.

[47] A. Dallmann, B. Simon, M. M. Duszczyk, H. Kooshapur, A. Pardi, W. Bermel, M. Sattler, Angew. Chem. Int. Ed. **2013**, 52, 10487–10490.

[48] R. Fiala, J. Czernek, V. Sklenář, J. Biomol. NMR **2000**, 16, 291–302.

[49] P. Pracht, F. Bohle, S. Grimme, Phys. Chem. Chem. Phys. **2020**, 22, 7169–7192.

[50] S. Grimme, J. Chem. Theory Comput. **2019**, 15, 2847–2862.

[51] S. Grimme, J. Comput. Chem. **2006**, 27, 1787–1799.

[52] F. Weigend, R. Ahlrichs, Phys. Chem. Chem. Phys. **2005**, 7, 3297–3305.

[53] F. Neese, Wiley Interdiscip. Rev. Comput. Mol. Sci. **2022**, 12, 1–15.

[54] V. Barone, M. Cossi, J. Phys. Chem. A **1998**, 102, 1995–2001.

2.6. Supporting Information

2.6.1. Analytical Methods

2.6.1.1. NMR Spectrometer Data

For all NMR spectroscopic measurements on model systems a Bruker Avance III HD 600 MHz spectrometer with a TBI (Triple resonance broadband inverse) 5 mm triple resonance broadband inverse probe with 19F-selective channel (TBI-F) with z gradient and BVT unit was used. The temperature of the spectrometer was regulated by a BVT 3900 unit and liquid nitrogen. Furthermore, samples for the characterization of in this work synthesized imines were measured on a Bruker Avance III HD 400 MHz spectrometer equipped with 5 mm BBO BB-1H/D probe head with Z-Gradients. Spectrometer control and spectra processing was performed by Bruker Software TopSpin 3.2 PL 7. For data processing, preparation and presentation Microsoft Excel, ChemBioDraw 19.0 and CorelDraw 2022.

Chemical shifts of ^{1}H and ^{13}C were referenced to TMS or the solvent. The heteronuclei ^{15}N and ^{31}P were referenced, employing $\nu(X) = \nu(TMS) \cdot \Xi reference / 100\ \%$ according to Harris et al.[1] The following frequency ratios and reference compounds were used: $\Xi(^{15}N) = 10.132912$ (lq. NH_3) and $\Xi(^{31}P) = 40.480742$ (H_3PO_4).

2.6.1.2. Pulse Sequences and Parameters

Standard pulse sequences from the Bruker pulse sequence catalogue (zg, zg30, etc.) have been used. For all ^{1}H-NMR spectra a sweep width of 22 ppm with an offset at 10 ppm were used. For ^{31}P spectra the sweep width was 40 ppm with the offset at 5 ppm and for ^{15}N a sweep width of 508 ppm with the offset at 200 ppm was used. Furthermore, the following acquisition parameter have been used:

^{1}H-NMR: Pulse program zg30, Relaxation delay = 2.00 s, Acquisition time = 2.48 s, SW = 22 ppm, TD = 66 K, ns = 1 – 64;

^{13}C NMR: Pulse program: zgpg30, Relaxation delay = 2.00 s, Acquisition time = 0.80 s, SW = 270.0 ppm, TD = 66k, NS = 1k – 4k;

^{15}N NMR: Pulse program: zg30; Relaxation delay = 3.00 s, Acquisition time = 1.06 s; SW = 508 ppm, TD = 66 K; NS = 1K – 4K;

^{31}P-NMR: Pulse program: zgpg30; Relaxation delay = 3.00 s, Acquisition time = 4.5 s, SW = 40.0 ppm, TD = 66k, NS = 256 - 512;

2D-^{1}H,^{1}H NOESY: Pulse program: noesygpph; Relaxation delay = 4.00 s, mixing time (D8) = 80-300 ms; NS = 8-16, TD = 4096; increments = 512-1024;

2D-^{1}H,^{1}H COSY: Pulse program: cosygpqf; Relaxation delay = 5.00 s, NS = 4-16, TD = 4096; increments = 512;

2D-^{1}H,^{13}C HSQC: Pulse program: hsqcedetgpsisp2.3; Relaxation delay = 3.75 s, $^{1}J_{XH}$ = 145 Hz; NS = 8-12, TD = 4096; increments = 512;

2D-^{1}H,^{13}C HMBC: Pulse program: hmbcgplpndqf; Relaxation delay = 3.90 s, $^{1}J_{XH}$ = 145 Hz, J_{XH}(long range) = 10 Hz; NS = 14-22, TD = 4096; increments = 512 - 1024;

2D-^{1}H,^{31}P HMBC: Pulse program: inv4gplrndqf; Relaxation delay = 6.00 s, NS = 16, TD = 4096; increments = 256 - 512;

2D-^{1}H,^{15}N HMBC: Pulse program: inv4gplrndqf; Relaxation delay = 4.00 s, delay for evolution of long range couplings (D6) = 20.00 ms; NS = 8-10, TD = 4096; increments = 256;

^{1}H DOSY: Relaxation delay = 2.00 s, NS = 16-128, TD = 66k, increments = 20, Diffusion time delay = 45.0 ms, gradient strength 5-95% linear, gradient pulse: 1.0 – 1.3 ms;

2D-^{1}H,^{15}N HSQC-NOE: Pulse program: hsqcetgpnosp, Relaxation delay = 3.00 s, NS = 8, TD = 66k, increments = 20, Diffusion time delay = 45.0 ms, gradient strength 5-95% linear, gradient pulse: 2.9 – 7.5 ms.

2.6.2. Materials and Chemicals

2.6.2.1. Solvents

Deuterated solvents were purchased from Deutero or Sigma Aldrich. Deuterated and non-deuterated dichloromethane (DCM) were refluxed over CaH_2 under Argon atmosphere and distilled and stored over activated molecular sieves (3Å).

2.6.2.2. Chemicals

(*R*)-TRIFP **1a**, (*R*)-OMe-CPA **1b**, TRIM **1c**, TRIP **1d**, TiPSY **1e** were purchased at abcr. All synthesized imines were stored in a desiccator over anhydrous $CaCl_2$ or inside a glove box. Chemical necessary for the synthesis of the ^{15}N-enriched Hantzsch Ester (HE) **3a** and Hantzsch Ester derivate **3b** were purchased from Sigma Aldrich and stored in the glovebox. The imine was synthesized from ^{15}N-enriched aniline and the respective acetophenone-derivate which were both purchased from Sigma Aldrich.

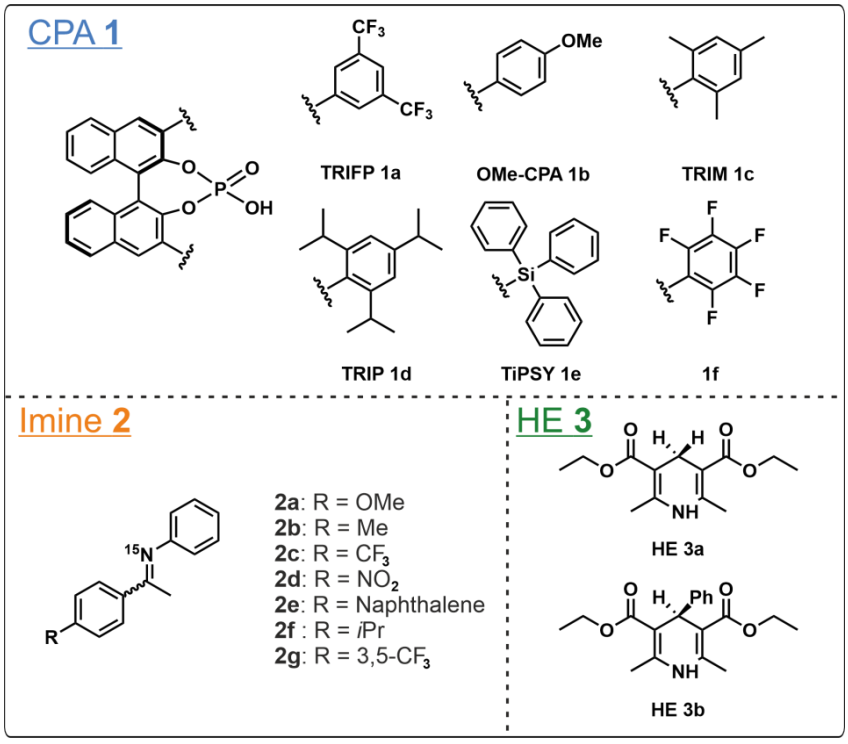

Figure S 2.1 Chiral Phosphoric Acids (CPAs) 1, imines 2, HE 3 used for NMR investigations in this study.

2.6.2.3. Synthesis of Imines

The imine was prepared as described in literature.[2] The characterization of the in this work synthesized imines was performed on Bruker Avance 400 MHz-Spectrometer with a 5mm BBO BB-1H/D probe head with Z-Gradients.

General Procedure for the synthesis of imines GP I [2,3]

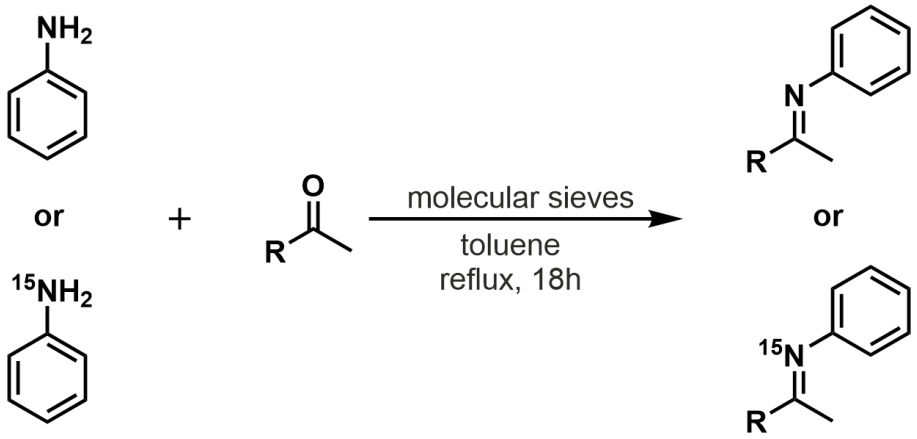

Molecular sieve (4 Å pore size, 3-5 g) was put into a 50 mL Schlenk flask and dried with a heat gun at 400°C for 30 min under reduced pressure. Aniline or Aniline (98% ^{15}N) (15.0 mmol, 1.40 g, 1.40 mL, 1.0 eq), the respective ketone (19.5 mmol, 1.3 eq.) and 25 mL anhydrous toluene were added under Argon flow. To this setup a reflux condenser was added under Argon flow and further flushed with Argon for 3 min. A drying tube, which was filled with $CaCl_2$, was attached to the reflux condenser and the solution was subsequently refluxed for 18 h. Afterwards, the heating bath was removed and the reaction mixture was allowed to cool down before being filtrated. Thereupon, the solvent was removed under reduced pressure to give a yellow solid, which was recrystallized in methanol 3-5 times to give the pure respective imine.

^{15}N-labeled Aniline was used for the synthesis to enable further investigations by NMR spectroscopy.

All substrates (**2a** – **2c**) were prepared according to literature following GP I. All NMR spectra match with the literature reports.[3–6] ^{15}N labeled imines were synthesized analogously and the NMR spectra matched with the literature reports.[4]

2.6.2.4. Synthesis of Hantzsch Ester Derivate 3b

Hantzsch ester **3b** (^{15}N-diethyl 2,6-dimethyl-4-phenyl-1,4-dihydropyridine-3,5-dicarboxylate) was synthesized according to literature using ^{15}N-labeled $^{15}NH_3$ (aq.).[7]

Benzaldehyde (2.0 mL, 20 mmol), ethyl acetoacetate (5.0 mL, 40 mmol, 2 eq.) and $^{15}NH_3$ (14 M aq., 2.0 mL, 140 mmol, 7 eq.) were freshly distilled and subsequently stirred under reflux for 4 h. Then the mixture was cooled down and solidified. The resulting solid was dissolved in DCM (20 mL) and washed with saturated aq. NaCl (20 mL). After separation of the organic phase and drying with $MgSO_4$, the solvent was evaporated under reduced pressure, yielding crude HE **3b** as a yellow solid (~ 6 g, 91 % yield). Subsequently, the yellow solid was triturated with petroleum ether/EtOAc under reflux, filtered while hot, and washed with petroleum ether, resulting in the pure pale-yellow solid HE **3b** (67% yield after crystallization, >99% ^{15}N based on ^{1}H NMR integration).

^{1}H NMR (400 MHz, $CDCl_3$): δ 7.24 – 7.31 (m, 2H), 7.16 – 7.23 (m, 3H), 7.10 – 7.14 (m, 2H), 5.67 (d, $^{1}J_{NH}$ = 92.7 Hz), 4.99 (s, 1H), 4.08 (AB part of ABX_3, J_{AB} = 10.8 Hz, J_x = 7.1 Hz , 4H), 2.32 (d, $^{3}J_{NH}$ = 3.0 Hz, 6H), 1.22 (X part of ABX_3, J_x = 7.1 Hz, 6H).

^{13}C NMR (101 MHz, $CDCl_3$): 167.6 (d, J = 3.0 Hz), 147.7 (CqAr), 143.8 (d, J = 12.0 Hz, Cq), 128.0 (CHAr), 127.8 (CHAr), 126.1 (CHAr), 104.2 (d, J = 1.7 Hz, Cq), 59.7 (CH2), 39.6 (d, J = 1.5 Hz, CH), 19.5 (d, J = 2.2 Hz, CH3), 14.2 (CH_3).

^{15}N NMR (41 MHz, $CDCl_3$): δ 131.8 (dsept, J = 92.8 Hz, 3.1 Hz).

2.6.3. NMR Investigations

2.6.3.1. Substrate Scope

Based on our previous studies on CPAs, we know that the electronic and steric properties of both CPA **1** and imine **2** play a crucial role for the spectral properties of the investigated system, especially the combination of the respective properties of CPA **1** and imine **2**. Therefore, we conducted a broad system screening of 25 different CPA/imine combinations to identify the combination of both which leads to the best NMR properties.

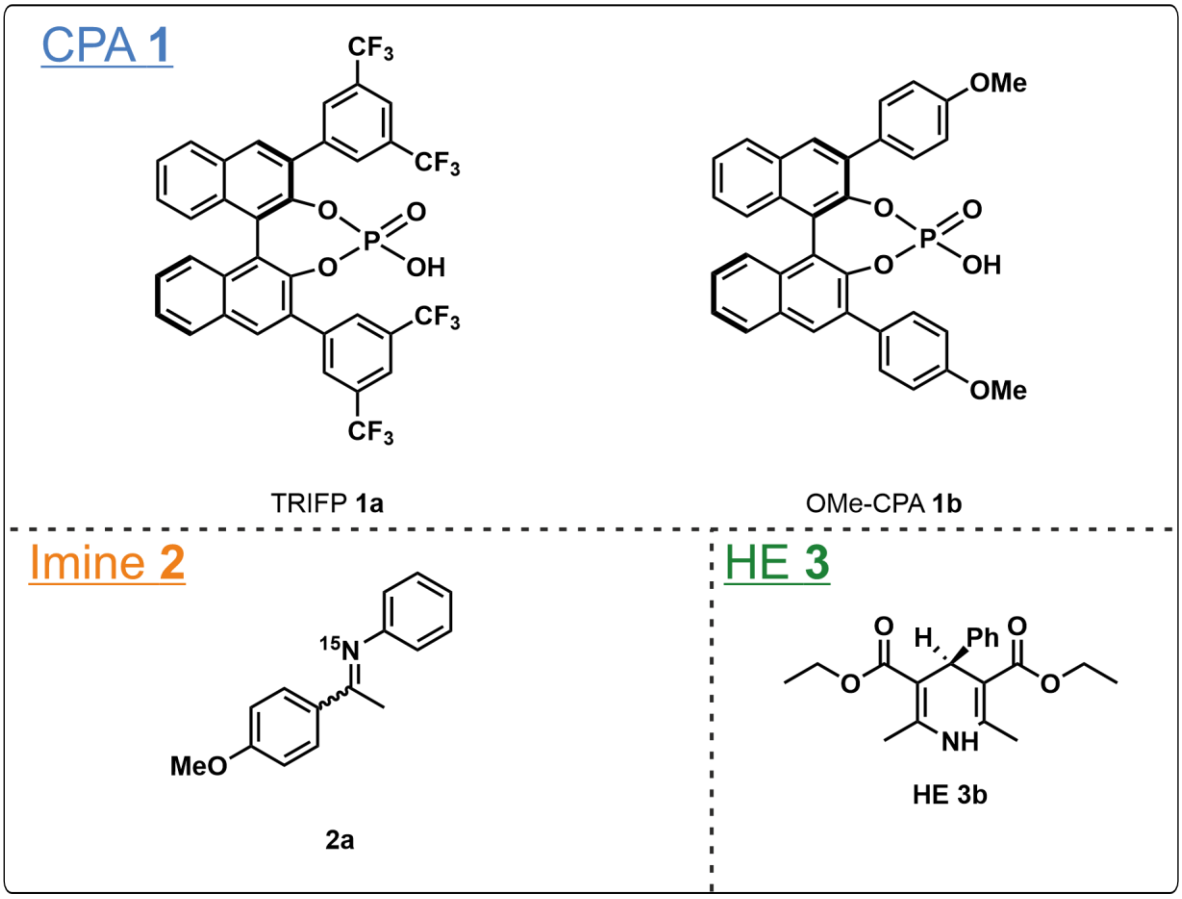

Figure S 2.2 CPAs 1, imine 2b and HE 3b used as model system substrates for NMR investigations in this study.

Table S 2.1 List of investigated samples with selected model systems by NMR spectroscopy (600MHz, CD_2Cl_2, 180K).

Sample Nr.	System	Concentration CPA **1** [mM]	Concentration imine **2** [mM]	Concentration HE **3** [mM]
1	**1a•2a•3b**	40	40	40
2	**1a•2a•3b** *E-only*	40	40	40
3	**1a•2a•3b** *Z-enhanced*	40	40	40

4	**1a•2a•3b** *2:1 dimer*	100	50	50
5	**1b•2a•3b**	40	40	40
6	**1a•3b**	25	-	25
7	**2a•3b**	-	25	25
8	**1b**	25	-	-
9	**1b•2a**	40	40	-
10	**3b**	-	-	25

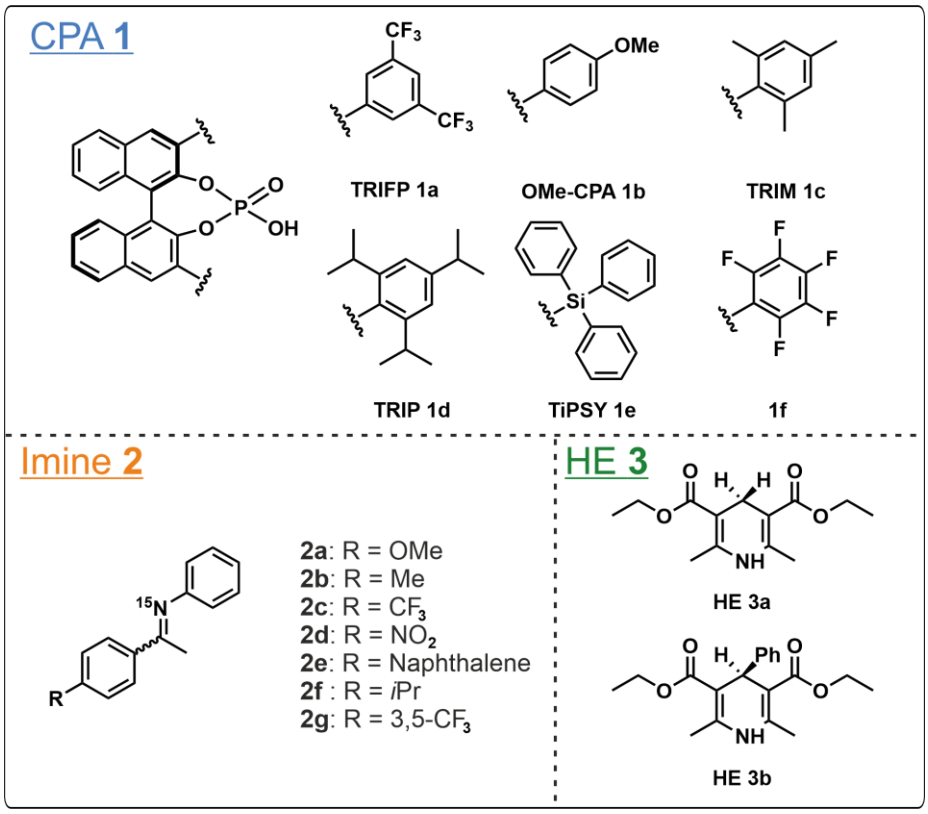

Figure S 2.3 CPAs 1, imines 2 and HE 3 used for screening by NMR spectroscopy.

Table S 2.2 List of samples of all additionally screened systems to select the model systems for this study (1:1:1 stoichiometry, 600MHz, CD_2Cl_2, 180K).

Sample Nr.	System	Concentration CPA **1** [mM]	Concentration imine **2** [mM]	Concentration HE **3** [mM]
11	**1a•2a•3b**	40	40	40
12	**1a•2b•3b**	40	40	40
13	**1a•2c•3b**	40	40	40
14	**1a•2d•3b**	40	40	40
15	**1a•2e•3b**	40	40	40
16	**1a•2f•3b**	40	40	40
17	**1a•2g•3b**	40	40	40
18	**1b•2a•3b**	40	40	40
19	**1b•2b•3b**	40	40	40
20	**1b•2c•3b**	40	40	40

21	**1b•2d•3b**	40	40	40
22	**1c•2a•3b**	40	40	40
23	**1c•2b•3b**	40	40	40
24	**1c•2c•3b**	40	40	40
25	**1c•2d•3b**	40	40	40
26	**1c•2e•3b**	40	40	40
27	**1d•2a•3b**	40	40	40
28	**1d•2b•3b**	40	40	40
29	**1d•2c•3b**	40	40	40
30	**1d•2e•3b**	40	40	40
31	**1d•2f•3b**	40	40	40
32	**1e•2b•3b**	40	40	40
33	**1e•2c•3b**	40	40	40
34	**1e•2e•3b**	40	40	40
35	**1f•2a•3b**	40	40	40

2.6.3.2. General Procedure for Sample Preparation (GPSP)

One stock solution each was prepared for the ^{15}N-labeled imine **2** (50 mM) and ^{15}N-labeled Hantzsch Ester **3** (50 mM) in dry CD_2Cl_2 (*d*-DCM). The CPA **1** (25-50 mM, 1-2 eq.) was directly weighed in an NMR tube, which was subsequently dried with a heat gun at 140 °C for 30 min under reduced pressure (CPAs are often delivered with residual moisture, thus the heating process is necessary to remove remaining traces of water). After heating the tube was cooled down to room temperature and evacuated and flushed with Argon three times. Out of each stock solution 0.3 mL were added to the NMR tube as well as TMS atmosphere as reference (0.5 mL). Thereupon, the tube was closed and sealed with parafilm and stored in the fridge at -80 °C or used immediately.

All samples used in this work were prepared following this procedure and are listed in Table S2.1 and Table S2.2.

E-only Samples

A stock solution with the ^{15}N-labeled imine **2** (50 mM) in dry CD_2Cl_2 (*d*-DCM) was prepared and cooled down to -80°C. Another stock solution for the ^{15}N-labeled **3** (50 mM) in dry CD_2Cl_2 (*d*-DCM) was prepared and also cooled down to -80°C. The CPA **1** (25 mM) was directly weighed in an NMR tube, which was subsequently dried with a heat gun at 140 °C for 30 min under reduced pressure. The tube was evacuated and flushed with Argon three times and also cooled down to -80°C. Out of each stock solution 0.3 mL were taken and added to the pre-cooled NMR tube. In addition, TMS atmosphere (0.5 mL) was added to the NMR tube as a reference. Thereupon, the tube was closed and sealed with parafilm under continuous cooling and immediately investigated by NMR spectroscopy at -80°C.

2.6.4. Chemical Shift Assignment

2.6.4.1. Assignment Strategy

Normally, $^{1}H,^{31}P$-HMBC spectra are used as a starting point for any chemical shift assignment of CPA/imine complexes due to the easily accessible information about the center of the complexes that can be obtained. However, due to various exchange processes within and in between ternary and binary complexes, the ^{31}P signals appear very broad and overlapped. Hence, in the $^{1}H,^{31}P$-HMBC no signals at all can be observed anymore. Besides ^{31}P, ^{15}N can also be used to obtain information about the hydrogen bonds. The two ^{1}H-signals of the hydrogen-bonded proton I1 were assigned to the *E*- and *Z*-complexes based on prior studies and known NOE contacts with the CPA.[4,7,8] Based on this assignment, the respective ^{15}N chemical shift of the nitrogen atoms were identified with the $^{1}H,^{15}N$-HMBC spectrum. However, in the $^{1}H,^{15}N$-HMBC only very few cross signals can be observed out of which only one can be unambiguously assigned to I2 (see FigureS2.4). Additionally, one cross signal for the hydrogen bond with HE **3b** is observed to a proton at 1.76 ppm. However, as no reference is available it cannot be differentiated between HE 2 and HE 7 yet.

TRIFP **1a** systems represent a unique scenario in which $^{1}H,^{19}F$-HOESY spectra can be employed which provide further insights (see FigureS2.5). In the $^{1}H,^{19}F$-HOESY all surrounding hydrogen atoms of the 3,3´-substituents can be observed. Here, the same signals as in the $^{1}H,^{15}N$-HMBC are detected again (2.60 ppm for I2, 1.76 ppm for HE 2 or HE 7). In addition, signals with a ^{1}H chemical shift of 1.19 ppm, 3.64 ppm, 3.93 ppm and 4.66 ppm are observed. With this information both CH_3-groups of the HE **3b** can be assigned by combining these observations with $^{1}H,^{1}H$-COSY data, which also confirmed the signal at 3.93 ppm as HE 6. Subsequently, the signal at 3.64 ppm can be assigned to the methoxy-group I8 of the imine, which is confirmed by $^{1}H,^{13}C$-HMBC. Furthermore, a ^{1}H chemical shift of 4.66 ppm is assumed to correspond to HE 8 after assigning I8 and HE6. This assumption is proven by NOE correlation to the already assigned HE 2, HE 6, HE 7 and later also to the phenyl-ring of HE **3b** (HE 9-11).

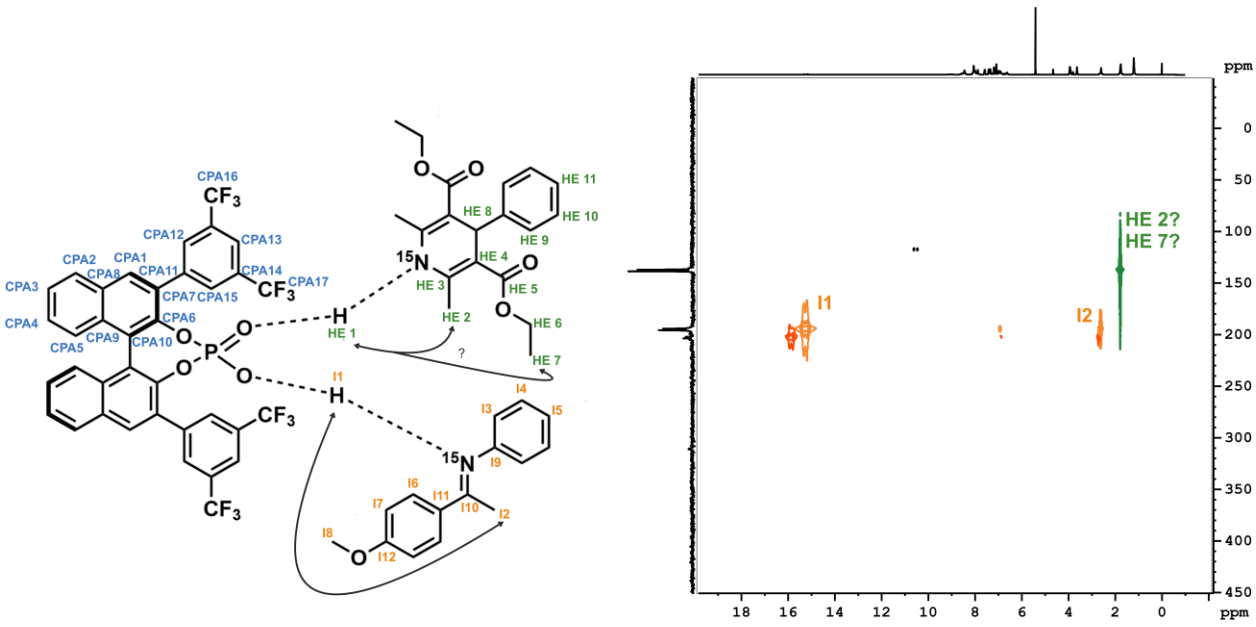

Figure S 2.4 $^{1}H,^{15}N$-HMBC of TRIFP 1a/2a/HE 3b (right, 1:1:1 stoichiometry, 40 mM, 600MHz, CD_2Cl_2, 180K) depicting the cross signals with I 2 and either HE 2 or HE 7. TRIFP 1a/E-2a is marked in orange, TRIFP 1a/Z-2a is marked in red and TRIFP 1a//HE 3b is marked in green. The structure with corresponding $^{1}H,^{15}N$-HMBC relations (arrows) is displayed on the left.

Also, first information about the CPA can be obtained. Based on the intensity of the signals at 7.86 ppm and 8.45 ppm these signals should correspond to CPA 12 and CPA 13 respectively as smaller distances are depicted as higher intensity in NOESY/HOESY spectra. For both signals no COSY relations can be observed, supporting the initial assumption. In addition, $^{1}H,^{1}H$-NOESY cross signals between both are observed but only for 7.86 ppm cross signals to other aromatic protons are detected. Combining $^{1}H,^{1}H$-COSY, $^{1}H,^{1}H$-TOCSY, $^{1}H,^{13}C$-HSQC, $^{1}H,^{13}C$-HMBC with these NOE correlations confirms the suggested assignment of CPA 12 (7.86 ppm) and CPA 13 (8.45 ppm). As a result of this assignment, a network of signals can be examined by 2D NMR spectra which can only be related to the BINOL-backbone additionally supporting the assignment of CPA 12 and CPA 13 and lead to a full assignment of all hydrogen atoms of the CPA. The same can be achieved for the imine **2a** and the HE **3b** from the assigned signals. For the imine **2a**, the ketone-part can be fully assigned using $^{1}H,^{13}C$-HMBC and $^{1}H,^{1}H$-NOESY cross signals of the methoxy-group I8. The remaining *N*-phenyl moiety can then be assigned based on $^{1}H,^{13}C$-HSQC, $^{1}H,^{13}C$-HMBC and $^{1}H,^{1}H$-NOESY cross signals with I2. To double check the assignment $^{1}H,^{1}H$-COSY and $^{1}H,^{1}H$-TOCSY are considered. For HE **3b** only the phenyl-ring is not assigned yet which can also be achieved by $^{1}H,^{13}C$-HSQC, $^{1}H,^{13}C$-HMBC and $^{1}H,^{1}H$-NOESY cross signals with HE 3-8.

All quaternary carbons can be assigned by ^{1}H,^{13}C-HSQC, ^{1}H,^{13}C-HMBC from the surrounding assigned protons/carbons. Then, HE 8 can finally be unambiguously confirmed by ^{1}H,^{13}C-HMBC correlations with HE 3 and HE 4. Hence, starting with ^{1}H,^{19}F-HOESY enables an assignment of all three substances: CPA, imine and HE.

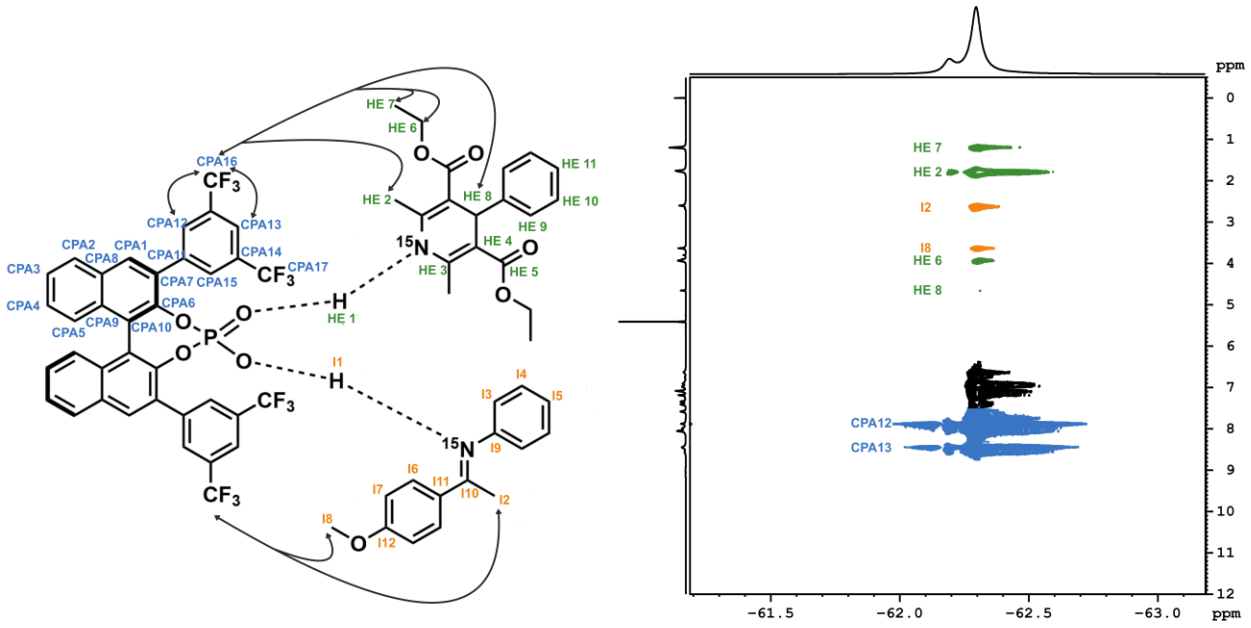

Figure S 2.5 ^{1}H,^{19}F-HOESY of TRIFP 1a/2a/HE 3b (right, 1:1:1 stoichiometry, 40 mM, 600MHz, CD_2Cl_2, 180K) depicting the cross signals of the CF^3-groups of TRIFP 1a. Cross signals to TRIFP 1a are marked in orange, cross signals to 2a are marked in orange, cross signals to 3b are marked in green. The structure with corresponding ^{1}H,^{19}F-HOESY relations (arrows) is displayed on the left.

However, if ^{1}H,^{19}F-HOESY spectra are not accessible which is the case for all other commonly used CPAs, such as TRIM **1c** (3,3'-bis(2,4,6-trimethylphenyl)-1,1'-binaphthyl2,2'diyl hydrogen phosphate), TRIP **1d** (3,3'-bis(2,4,6-triisopropylphenyl)-1,1'-binaphthyl-2,2'diyl hydrogen phosphate), and TiPSY **1e** (3,3'- bis(triphenylsilyl)-1,1'-binaphthyl-2,2'diyl, this assignment strategy is not possible. Therefore, we applied ^{15}N-HSQC-NOESY to get a new starting point for the assignment of each substrate. This method even derives significantly more information about all three substrates than ^{1}H,^{19}F-HOESY when examining the individual rows of each ^{15}N-chemical shift separately (see FigureS2.6). Again, HE 2 and HE 6-8 are observed which can be assigned similarly as in the ^{1}H,^{19}F-HOESY assignment strategy. The remaining HE **3b** signals can then also be assigned by combining ^{1}H,^{1}H-COSY, ^{1}H,^{1}H-TOCSY, ^{1}H,^{13}C-HSQC, ^{1}H,^{13}C-HMBC and ^{1}H,^{1}H-NOESY as described above. For imine **2a**, different signals can be observed. In contrast to ^{1}H,^{19}F-HOESY, the methoxy-group I8 is not detected. However, most other imine signals can be directly observed by ^{15}N-HSQC-NOESY. Checking and combining

the information derived by $^{1}H,^{1}H$-COSY and $^{1}H,^{1}H$-TOCSY spectra for these signals, leads to an unambiguous assignment of the aromatic protons of the imine, which is further supported by $^{1}H,^{13}C$-HSQC, $^{1}H,^{13}C$-HMBC and $^{1}H,^{1}H$-NOESY. Subsequently, the methoxy-group I8 can be assigned based on $^{1}H,^{1}H$-NOESY cross signals to I7. The assignment of CPA 12 and CPA 13 of TRIFP **1a** is similar to the above described assignment strategy as the ^{15}N-HSQC-NOESY results in the same information as the $^{1}H,^{19}F$-HOESY and enables the full assignment of the BINOL-backbone. For other CPAs, depending on the 3,3´-substituent, different assignment strategies have to be employed. For example, OMe-CPA **1b** has a distinct methoxy-group at the 3,3´-substituent which shows cross signals to the CPA/imine nitrogen leading to a starting point for the CPA assignment.

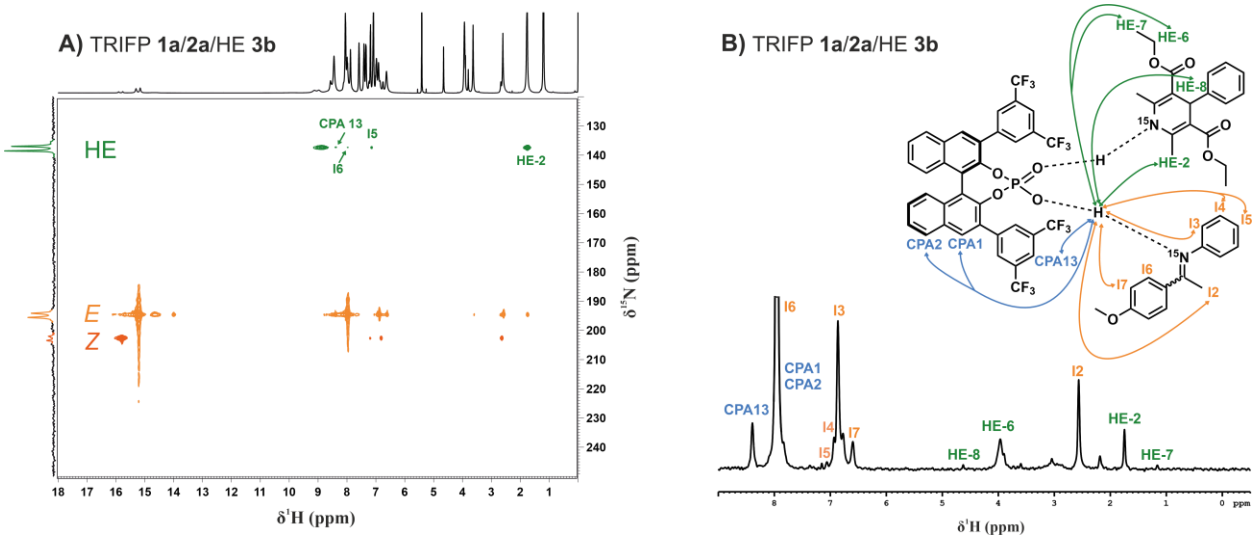

Figure S 2.6 ^{15}N-HSQC-NOESY spectrum of TRIFP 1a/2a/ HE 3b (1:1:1 stoichiometry, 40 mM, CD_2Cl_2, 180K). Separated rows for the TRIFP 1a/E-2a (orange), TRIFP 1a/Z-2a (red) and TRIFP 1a/HE 3b (green) hydrogen bonds can be observed. B) Single rows can be displayed as 1D spectra for more detailed information to reveal the structural environment of each hydrogen bond, here exemplary displayed for the TRIFP 1a/E-2a hydrogen bond. Cross signals to TRIFP 1a are marked in orange, cross signals to 2a are marked in orange, cross signals to 3b are marked in green.

TRIFP 1a/*E*-2a/HE 3b Assignment

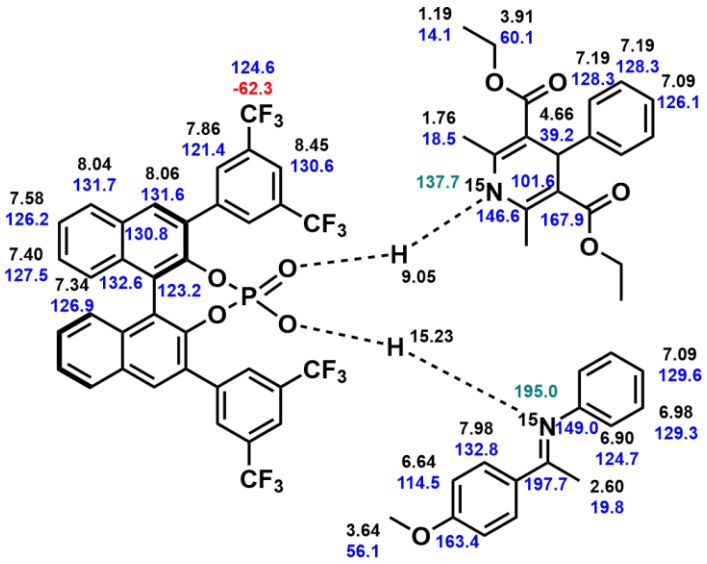

OMe-CPA 1b/*E*-2a/HE 3b Assignment

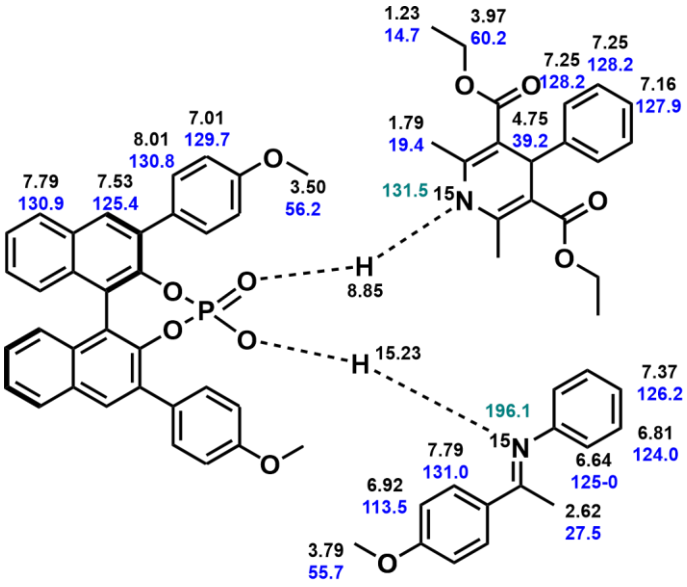

OMe-CPA 1b /*Z*-2a/HE 3b Assignment

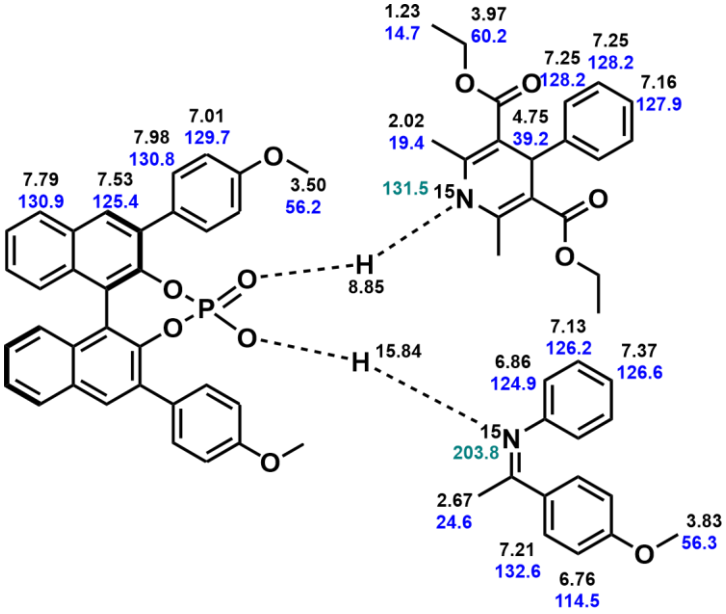

2.6.5. Exclusion of Other Species

To confirm the association of the hydrogen bond signals of the ternary complex and exclude other possibilities, separate samples containing TRIFP **1a**/HE **3b** or **2a**/HE **3b** were evaluated and compared (see FigureS2.7 and FigureS2.8).

First, HE **3b** was measured alone. Here, the NH-hydrogen can be seen at 6.71 ppm (green). After addition of the imine **2a** this signal shifts slightly to 7.03 ppm (green). Upon further addition of the CPA (TRIFP **1a**) the signal shifts significantly to 9.05 ppm (green). Similarly, a shift of the aliphatic signals of HE **3b** can be observed. HE-1 (skin tone) is shifting from HE **3b** solo at 4.03 ppm to 3.93 ppm in the ternary complex. HE-2 (pink) is shifting from HE **3b** solo at 1.26 ppm to 1.19 ppm in the ternary complex. HE-3 (orange) is shifting from HE **3b** solo at 2.30 ppm to 1.76 ppm in the ternary complex. Hence, HE-3 shifts further in high-field direction in comparison to HE-1 and HE-2 which is corresponding with the distance to the hydrogen bonded NH. For both the HE **3b** and **2a**/HE **3b** sample, a different set of chemical shifts compared to the ternary complex can be observed. Also, the CPA/imine/HE hydrogen bond signal for HE **3b** is displayed as a doublet when both substances are ^{15}N labeled, or as a singlet when only the imine is ^{15}N labeled, indicating that the imine is not participating. Therefore, an imine/HE complex contribution can be excluded for the ternary complex similar to the DSIs.

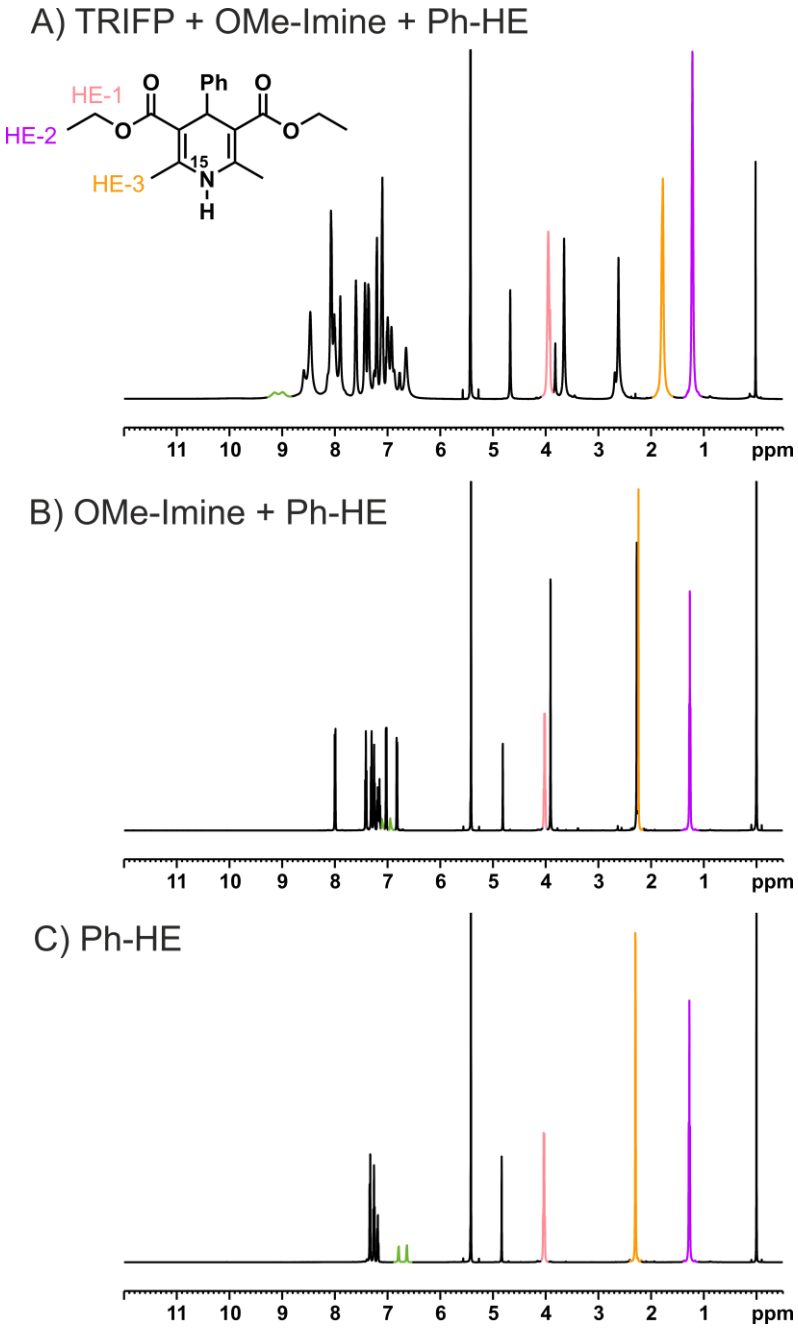

Figure S 2.7 Comparison of different samples to validify the CPA/HE hydrogen bond of the ternary complex. A) TRIFP 1a/2a/HE 3b (1:1:1 stoichiometry, 40 mM, 600MHz, CD_2Cl_2, 180K). B) 2a/HE 3b (1:1 stoichiometry, 25 mM, 600MHz, CD_2Cl_2, 180K). C) HE 3b (25 mM, 600MHz, CD_2Cl_2, 180K). The NH hydrogen atom of the HE 3b is marked in green. In addition, the aliphatic signals of HE 3b are also colored corresponding to the molecule shown on the top left.

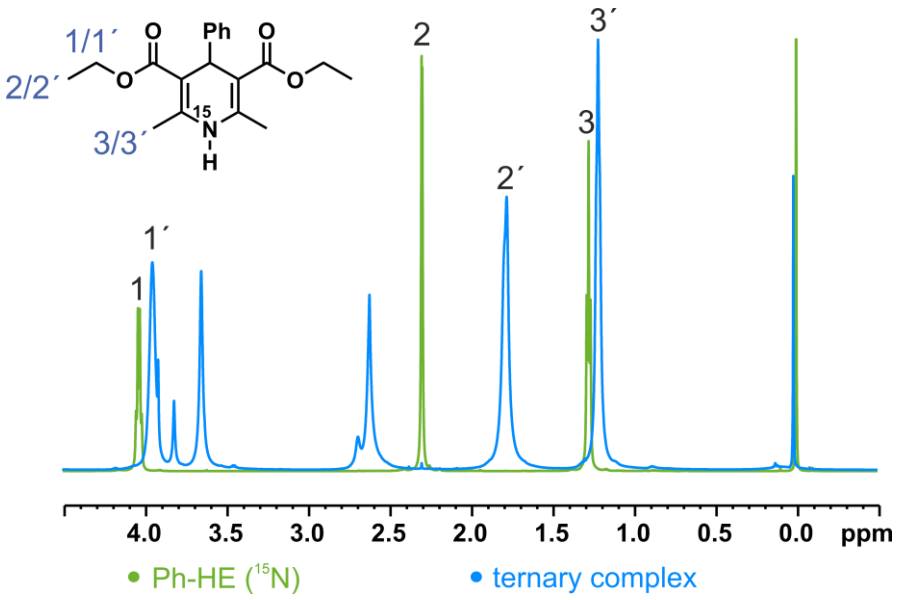

Figure S 2.8 Comparison of the aliphatic signals of HE 3b when measured alone (green, 25 mM, 600MHz, CD_2Cl_2, 180K) and in the ternary complex of TRIFP 1a/2a/HE 3b (blue, 1:1:1 stoichiometry, 40 mM, 600MHz, CD_2Cl_2, 180K). A high-field shift can be observed for all signals upon addition of TRIFP 1a and 2a, which is even more pronounced when the respective hydrogen atom is closer to the hydrogen bonded NH.

In addition, a sample with TRIFP **1a** and HE **3b** was investigated to exclude a simple CPA/HE species being responsible for the observed hydrogen bond signals of the HE **3b**. Here, a doublet was detected at 6.37 ppm which vanishes upon addition of the imine to form the ternary complex (see Figure S2.9). The CPA/HE hydrogen bond of the ternary complex is not observed in the TRIFP **1a**/HE **3b** sample. This additionally supports, that a CPA/HE species can be excluded for the signal at 9.05 ppm.

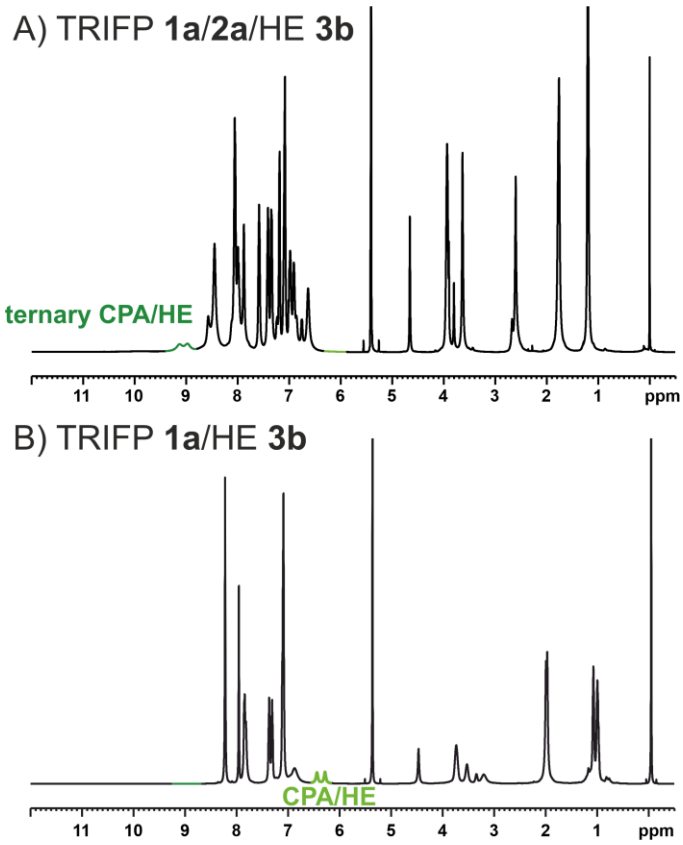

Figure S 2.9 Comparison of different samples to validify the CPA/HE hydrogen bond of the ternary complex. A) TRIFP 1a/2a/HE 3b (1:1:1 stoichiometry, 40 mM, 600MHz, CD_2Cl_2, 180K). B): TRIFP 1a/HE 3b (1:1, 40 mM, 600MHz, CD_2Cl_2, 180K). The CPA/HE hydrogen bond of the ternary complex does not appear in the other sample, excluding a simple CPA/HE species. Also, the observed hydrogen bond signal in B) vanishes in A), excluding a contribution to the NOE correlations.

Additionally, to rule out the possibility that the Overhauser effects originate from binary complexes (CPA/HE or imine/HE), we investigated the respective 1:1 mixtures. The combination of TRIFP **1a** and Hantzsch ester **3b** showed a shift of the NH-group of the HE **3b** to 6.37 ppm in comparison to a sample with only the HE **3b**. This signal of the TRIFP **1a**/HE **3b** complex vanished upon the addition of imine in a 1:1:1 mixture (see Figure2.9A). Therefore, the binary complex of TRIFP **1a** and HE **3b** is in slow exchange with the ternary complex, and the corresponding binding constant for ternary complex formation is significantly higher than the binding of the Hantzsch ester to the catalyst, similarly to DSI complexes.[7] Thus, any contribution to the Overhauser effects in the ternary complex can be unambiguously eliminated.

The formation of the complex between imine **2a** and HE **3b** in the ternary complex mixture is improbable due to the considerably higher acidity of the CPA. Indeed, a 1:1 mixture of imine **2a** and HE **3b** exhibited sharp ^{1}H-NMR signals with a distinct set of chemical shifts

compared to the ternary complex. Once again, this rules out the contribution of the imine/HE complex to the intermolecular NOEs observed in the ternary mixtures.

As stated above, the ternary complexes are in fast exchange with the binary complexes, in which rotation can occur due to the large binding pocket of the catalyst, even with intact hydrogen bonds.[9] Even within CPA complexes featuring strong hydrogen bonds, hydrogen bond switching can take place, which is fast on the NMR timescale. To eliminate any potential impact of these processes in the binary complexes on the structure determination of the ternary complex, interactions exclusively with the Hantzsch ester were interpreted.

2.6.6. General Features of Ternary Complex

CPA **1**: All CPAs are symmetric along the C2 axis, only the 3,3'-substituents are not symmetric and have distinct signals for the aromatic protons, carbons or e.g. for TRIFP **1a** two distinct 3,5-CF_3 groups due to the restricted rotation along the main substituent axis.

Imine **2**: For the CPA/imine hydrogen bond one set of signals for *E*-complex and one set of signals for Z-complex can be observed. In contrast to the binary complex, the CPA/imine hydrogen bond signals are slightly high-field shifted but no separate hydrogen bond signal for the ternary complex is detected. This indicates a fast exchange between both complexes leading to one signal set. Furthermore, according to the Steiner-Limbach curve and the results of the binary complex, this high-field shift of the hydrogen bonds reveal a weaker hydrogen bond and hence, a stronger ion pair character.[8] The additional chemical exchange leads to worse line broadening and worse resolution of ^{15}N- and ^{31}P-NMR spectra for the ternary complex samples in comparison to the binary complex samples to the point that no ^{1}H,^{31}P-HMBC signals can be detected and only a few ^{1}H,^{15}N-HMBC signals are observed. Both imine isomers show NOE correlations to the HE **3b**, which are used to analyze the conformers. However, only for the *E*-isomer species enough signals are detected for a full chemical shift assignment and conformer analysis. Despite of sharper ^{1}H signals of the *Z*-isomer species, which should benefit 2D spectra, due to the lower population only a few signals can be unambiguously identified which hinders deeper analysis of the *Z*-species.

HE **3b**: For the CPA/HE hydrogen-bonded species only one set of signals is observed. The ternary complex is confirmed by ^{15}N-HSQC-NOESY spectra in which NOE correlations between the CPA/imine hydrogen bond and HE **3b** are detected. The same is observed for the CPA/HE hydrogen bond to imine **2a**.

2.6.6.1. Binary vs. Ternary Complex

In the hydrogen bond area of the ternary complex, only one set of signals for the CPA/imine hydrogen bond is detected. This indicates a fast exchange between binary and ternary complex, as otherwise two separate signal sets would have to be observed in the 1:1:1 sample of the ternary complex. This is supported by a chemical shift mapping of these signal upon addition of the HE **3b** to the binary complex (see FigureS2.17).

Comparing the CPA/imine hydrogen bonds of the binary and ternary complex, reveals a high-field shift of the hydrogen bonds upon addition of the HE **3b** (see FigureS2.10). Exemplary for TRIFP **1a**/**2a**/HE **3b**, for the CPA/*Z*-imine hydrogen bond a high-field shift from 16.11 ppm (binary complex) to 15.84 ppm (ternary complex) is observed, while for the CPA/*E*-imine hydrogen bond a high-field shift from 15.39 ppm (binary complex) to 15.23 ppm (ternary complex) is observed. In general, based on the Steiner-Limbach curve this indicates a weakening of the hydrogen bond upon addition of the HE.[8]

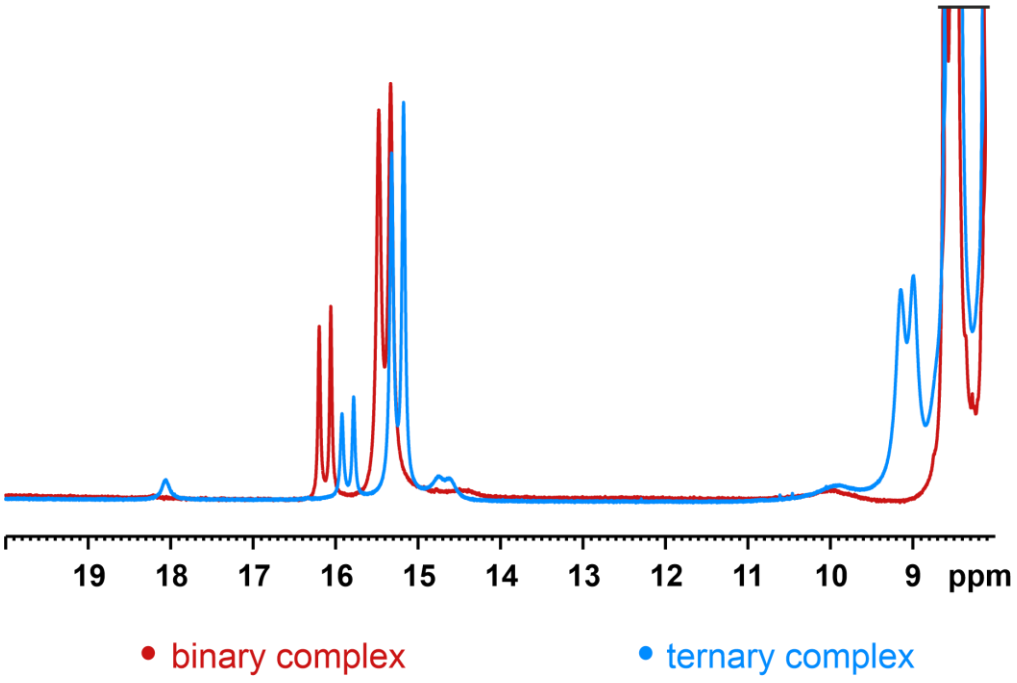

Figure S 2.10 Comparison of the binary complex with TRIFP 1a/2a (red; 1:1 stoichiometry, 40mM) and the ternary complex (blue; 1:1:1 stoichiometry, 40 mM, 600MHz, CD_2Cl_2, 180K).

2.6.7. Structural Space

Besides the ternary complex, other hydrogen-bonded species can be observed in the hydrogen bond area of the ^{1}H-spectrum of all screened systems, which vary in population depending on the system (see Figure S2.11).

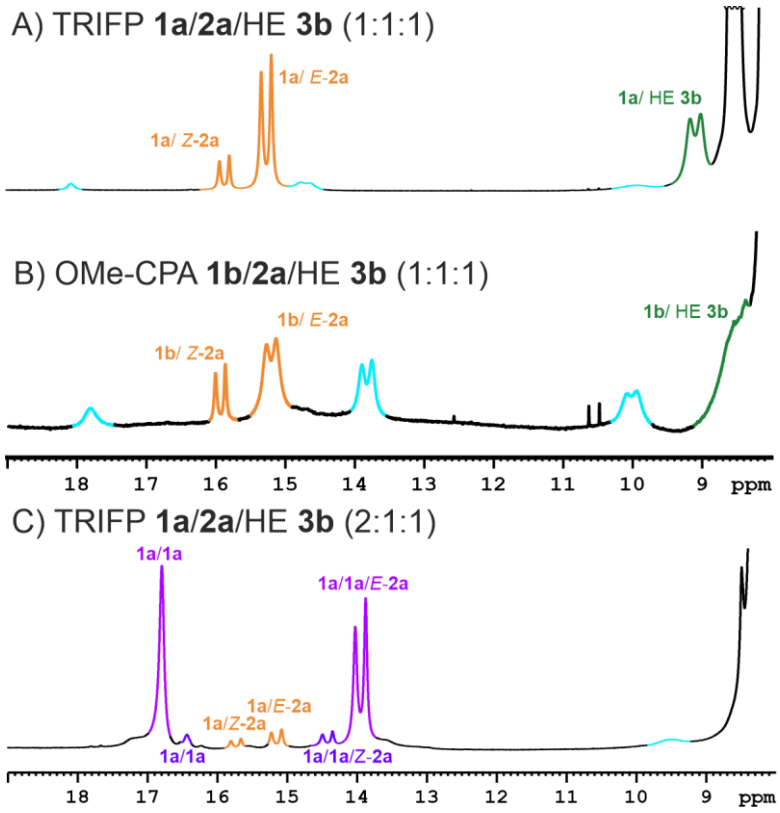

Figure S 2.11 ^{1}H-spectrum of the ternary complex of TRIFP 1a/2a/HE 3b (1:1:1 stoichiometry, 600MHz, CD_2Cl_2, 180K). All additional hydrogen bond signals are colored in light blue. B) ^{1}H-spectrum of the ternary complex of TRIFP 1b/2a/HE 3b (1:1:1 stoichiometry, 600MHz, CD_2Cl_2, 180K). All additional hydrogen bond signals are colored in light blue (see SI 2.6.7.1). C) ^{1}H-spectrum of the of TRIFP 1a/2a/HE 3b in a 2:1:1 stoichiometry (stoichiometry, 600MHz, CD_2Cl_2, 180K). The dimeric species is marked in pink (CPA/CPA/E-imine) or purple (CPA/CPA/Z-imine), with each having one singlet for the CPA/CPA hydrogen bond and one doublet for the CPA/CPA/imine hydrogen bond, which are in a 1:1 integral ratio (see SI 2.6.7.2).

2.6.7.1. [3:3] Dimer

Next to the hydrogen bond signals of the ternary complex (orange), an additional marginal populated hydrogen-bonded species (blue) can be observed in the TRIFP **1a**/**2a**/HE **3b** system (see FigureS2.9). Here, their contribution to NOESY spectra can be neglected due to their extremely low population even compared to the *Z*-imine species, for which a NOE analysis was already only partly possible. These signals are higher in population in the second model system of OMe-CPA **1b**/**2a**/HE **3b** and can also be observed in various other CPA/imine/HE systems. A total of three additional hydrogen bond signals can be seen, one singlet and two doublets.

Further investigations were deducted to investigate the origin of these unknown signals. Comparing all systems of TRIFP **1a** with several different imines **2a-g** revealed that the low-field shifted singlet (18.04 ppm) stays at the same chemical shift in all system. Only upon using a different CPA, the singlet shifts indicating its dependency solely on the CPA. Noteably, this signal only appears upon addition of the imine, which might be attributed to an interplay of stabilization between the different species.10 Given the data and limited experimental access to this species, we assume that this system stems from a phosphoric acid aggregate.

For further investigations of the new hydrogen bond signals observed in the ^{1}H-spectra samples, the OMe-CPA **1b**/**2a**/HE **3b** system was used due to a higher population of these hydrogen bond species in comparison to TRIFP **1a**/**2a**/HE **3b** (see FigureS2.12). Samples with either a ^{15}N-labeled or unlabeled imine **2a** were measured to reveal the respective species. Here it was shown that the doublet at 13.76 ppm is corresponding to an [CPA/imine] **2a** hydrogen bond while the doublet at 9.99 ppm is related to a [CPA/HE **3b**] species (see FigureS2.12).

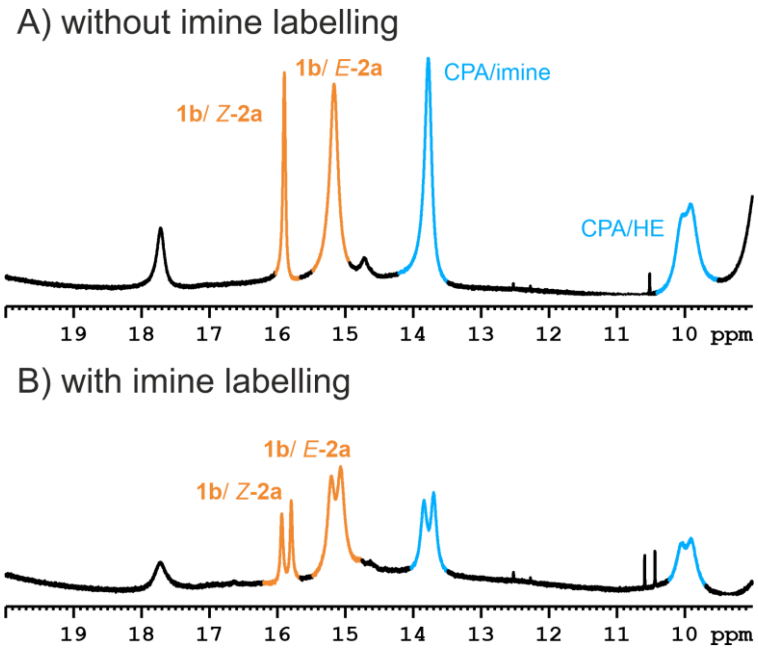

Figure S 2.12 A) ^{1}H-spectrum of the ternary complex of 1b/2a/HE 3b. Here, imine 2a is not ^{15}N-labeled, HE 3b is ^{15}N-labeled (1:1:1 stoichiometry, 600MHz, CD_2Cl_2, 180K). B) ^{1}H-spectrum of the ternary complex of 1b/2a/HE 3b. Both imine 2a and HE 3b are ^{15}N-labeled (1:1:1 stoichiometry, 600MHz, CD_2Cl_2, 180K).

Although a separate set of hydrogen bonds is detected, the CPA **1b** and imine **2a** signals have an averaged signal set with the binary and ternary complexes due to exchange processes. This indicates a locked system similar to the previously reported [2:2] dimeric species consisting of two binary complexes.[10] Also, for the [2:2] dimer, the signals were characteristically more high-field shifted than the CPA/imine hydrogen bonds of the binary complex similarly to the newly observed CPA/imine hydrogen bond signal. In addition, the integral ratios of the hydrogen bond signals in the ^{1}H-NMR spectrum gave a ratio of 1:1 of the CPA/imine signal to the CPA/HE signal. From this a first hypothesis of a [**3**:**3**] dimeric species consisting of two ternary complexes (CPA/imine/HE=**3**) was developed.

This [3:3] dimer was then further investigated by dilution experiments and diffusion ordered spectroscopy (DOSY). Diluting a 40 mM sample to a 20mM or a 10 mM sample demonstrated that these signals are corresponding to a dimeric species and again showed that both doublets belong to the same species as both were diminishing at the same rate (see FigureS2.13).

In contrast, the relative population of the 1b/E-2a/3b hydrogen bond signal of the ternary complex is increasing with smaller concentration. This observation can be explained by

the decrease of the [3:3] dimer which releases E-imine complexes only. Hence, the relative population of the E-imine species of the ternary complex is increasing in comparison to the other species.

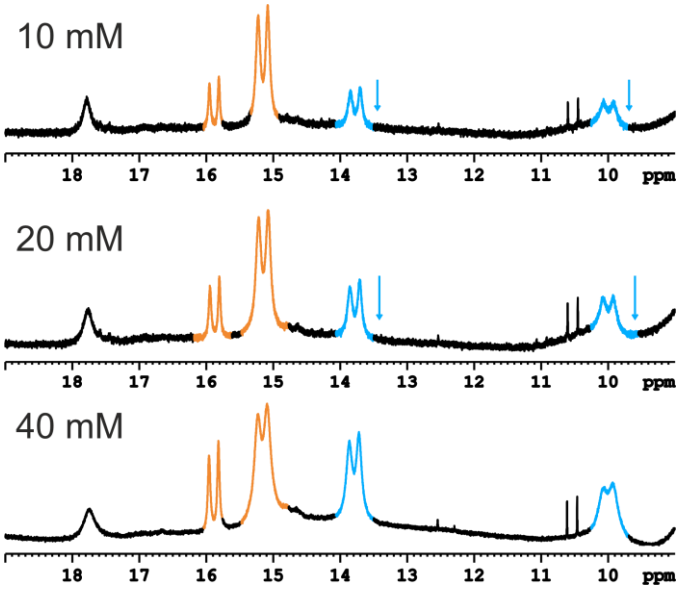

	Relative Integrals				
Concentration / mM	**1b/1b**	*Z*-2a•1b•He 3b	*E*-2a•1b•3b	[*E*-2a•1b•HE 3b]$_2$	Sum
40	0.091 ↑	0.18 ↑	0.3 ↓	0.43 ↑	1.00
20	0.089 ↑	0.14 ↑	0.55 ↓	0.22 ↑	1.00
10	0.081 ↑	0.12 ↑	0.65 ↓	0.15 ↑	1.00

The arrows in the table indicate wheter the relative integral increases or decreases with increasing concentration

Figure S 2.13 ^{1}H-spectrum of the ternary complex of 1b/2a/HE 3b (1:1:1 stoichiometry, 600MHz, CD_2Cl_2, 180K). The sample was diluted from bottom to top starting at 40 mM to 20 mM to 10 mM. The signals of the [3:3] dimeric species (blue) diminished each time in comparison to the ternary/binary complex hydrogen bond signal indicating a dimeric species. In the table below, the relative integrals of each hydrogen bond signal are listed by using the sum of the integrals. The integrals were obtained using Mestrenova® 14.3.3 with linear baseline correction. The spectra were processed using the Bernstein Polynomial Fit (polynomial order: 3), with baseline correction applied to the zoomed region.

DOSY experiments (for details, refer to SI 3.9) further confirmed the presence of larger aggregate species, as indicated by the significantly higher volumes calculated from the diffusion coefficients compared to those of the binary complex and the anticipated volume of the ternary complexes (refer to Table S3.3). CPA **1b** exhibits a volume of 2331 Å^3 in the **1b**/**2a**/HE **3b** sample (1:1:1 stoichiometry). Since this volume represents the average volume of all CPA species, it significantly surpasses the volume of the binary complex (1625 Å^3). Moreover, when calculating the volume of the ternary complex by adding the measured volume of the free HE **3b** to the binary complex (1625 Å^3 + 506 Å^3 = 2131 Å^3),

the determined value for the CPA in the 1:1:1 **1b**/**2a**/HE **3b** sample still significantly exceeds this value. This is notable considering that the ternary complex is expected to be smaller than 2131 Å³ because the HE **3b** is located inside the binding pocket of the CPA next to the imine **2a**. Additionally, based on the binding constant of the ternary complex (see SI chapter 2.6.8), only a small percentage of the CPA should populate the ternary complex. This would result in a partial increase of the calculated volume due to the exchange with the binary and ternary complex. Hence, the volume of 2331 Å³ is a significant increase in comparison to both binary and ternary complex hinting towards bigger aggregate.

In addition, a sample with only CPA **1b** was investigated revealing a volume of 1748 Å³. This relatively high volume is a result of the dimerization behavior of CPAs. Nevertheless, this demonstrates that even for a CPA/CPA-dimer only a volume of 1748 Å³ can be determined.

Hence, a by far larger aggregate than the ternary complex or a single CPA-dimer must be responsible for the significant increase in volume from 1625 Å³ to 2331 Å³. This again supports the proposed [3:3] dimeric species.

2.6.7.2. 2:1:1 Dimeric Species

Based on these results, we tried to investigate if other dimeric structures such as the 2:1 dimeric species are also observed as ternary complex. Here, a characteristic singlet for the CPA/CPA hydrogen bond along with a doublet for the CPA/CPA/imine hydrogen bond should be detected for each imine isomer. Similar to the ternary complex an additional CPA/CPA/HE hydrogen bond signal is expected upon addition of the HE **3b**, in case of a dimeric CPA/CPA/imine/HE complex.[11] To investigate the 2:1 dimeric species, a sample with a 2:1:1 stoichiometry of TRIFP **1a**/**2a**/HE **3b** was prepared and measured at 180 K to force the system into a possible CPA/CPA/imine/HE.

Here, the above described typical pattern for the dimeric species was clearly observed for both the *Z*- and *E*- imine isomers (see Figure S2.11 C). Nevertheless, similar to the high-field shift of the 1:1:1 ternary complex, a slight high-field shift of the dimeric species CPA/imine signals is observed when comparing those with a 2:1 sample (CPA/imine) without HE **3b** (TRIFP **1a**/*Z*-**2a**: -0.15 ppm; TRIFP **1a**/*E*-**2a**: -0.12 ppm). Furthermore, the CPA/CPA hydrogen bond signals are shifting towards low-field upon addition of the

HE **3b** (for TRIFP **1a**/TRIFP **1a**/*Z*-**2a**: +0.26 ppm; for TRIFP **1a**/TRIFP **1a**/*E*-**2a**: +0.30 ppm) and a new low populated signal is detected in the CPA/HE hydrogen bond region (9-10 ppm). Given the increasingly complex spectra, a chemical shift mapping is the most effective method for confirming the formation of a ternary complex. Therefore, a chemical shift mapping was performed starting from a 2:1:0 stoichiometry of CPA:imine:HE and adding HE **3b** in 0.5-2 eq. relative to the imine. Here, a clear shift of all mentioned signals was observed with increasing HE **3b** concentration (see FigureS2.14). Hence, although not present in a 1:1:1 stoichiometry, the dimeric CPA/CPA/imine/HE complex can be observed using a 2:1:1 stoichiometry.

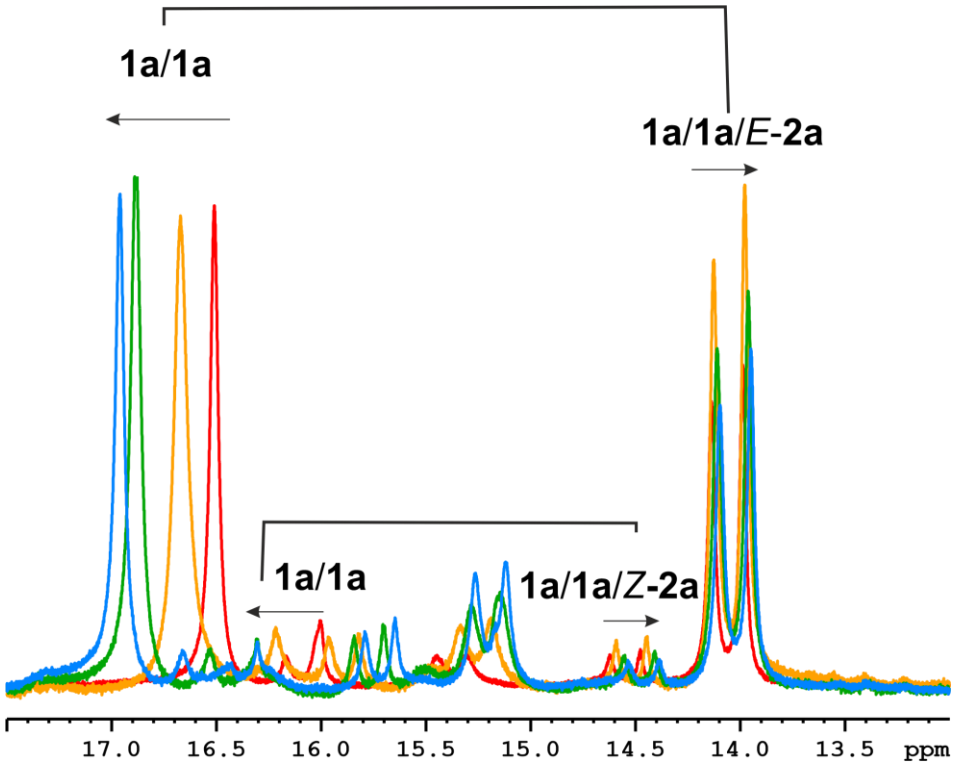

Figure S 2.14 ^{1}H-NMR chemical shift mapping of the hydrogen bond signals of the dimeric species upon addition of 0-2 eq. HE 3b (600MHz, CD_2Cl_2, 180K). A general high-field shift is observed for the CPA/CPA/imine hydrogen bonds upon addition of the HE 3b, while a low-field shift is observed for the CPA/CPA hydrogen bonds (order: red, orange, green, blue).

2.6.7.3. Additional Species

Furthermore, also for other CPAs the structural space was investigated. Especially the sterically more hindered TRIP **1d** and TiPSY **1e** were assumed to have a smaller structural space. Astonishingly the opposite trend was observed. While for TRIM **1c** a relatively similar structural space to TRIFP **1a** and **1b** was found (see FigureS2.15A), in samples containing TRIP **1d** and TiPSY **1e** a lot of additional hydrogen bond signals were detected. For all TRIP **1d** systems a plethora of signals was detected in the region of 14.5-16.0 ppm (see FigureS2.15B). For TiPSY **1e** highly populated species are observed in a chemical shift range of 10.0-12.0 ppm with imine **2b** which is not the case for any other system (see FigureS2.15C). However, none of these signals could be assigned as no signals were observed by 2D-NMR. Nonetheless, these results again demonstrate that steric limitations are by far less significant for the structural space of the ternary complex than anticipated based on the steric hinderance.

In this context, especially the combination of TiPSY **1e** with **2e**, which also has a sterically hindering substituent with its naphthalene group at the ketone-part of the imine, showed that a steric limitation seems to play no role for the ternary complex as well as the [3:3] dimer. Here, again a high population of the [3:3] dimeric species is detected (see FigureS2.16, blue).

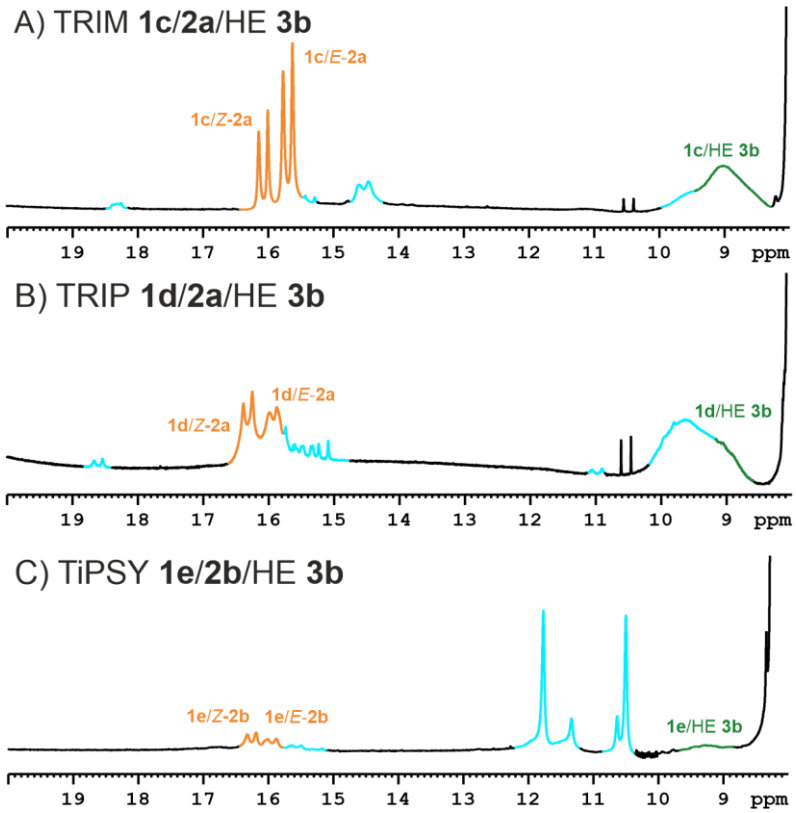

Figure S 2.15 A) ^{1}H-spectrum of the ternary complex of TRIM 1c/2a/HE 3b. B) ^{1}H-spectrum of the ternary complex of TRIP 1d/2a/HE 3b. C) ^{1}H-spectrum of the of TiPSY 1e/2a/HE 3b in a 2:1:1 stoichiometry (1:1:1 stoichiometry, 600MHz, CD_2Cl_2, 180K). All additional hydrogen bond signals are colored in light blue.

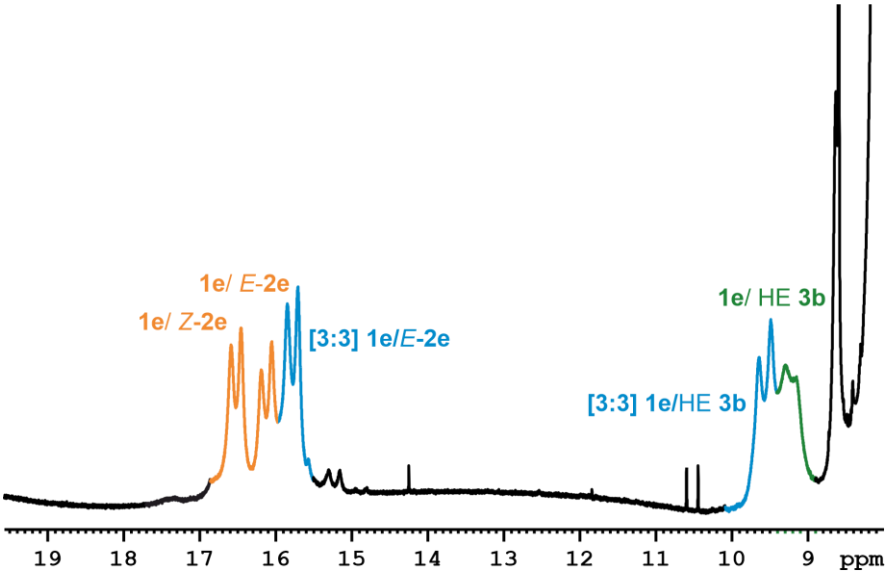

Figure S 2.16 ^{1}H-spectrum of the ternary complex of TiPSY 1e/2e/HE 3b (1:1:1 stoichiometry, 600MHz, CD_2Cl_2, 180K). All additional hydrogen bond signals are colored in blue.

2.6.8. Binding Constant

To investigate the binding of HE **3b** to the binary complex TRIFP **1a**/**2a**/HE **3b**, the following approach was employed for chemical shift mapping using NMR spectroscopy and binding isotherms:

An NMR sample was prepared with TRIFP **1a** (20 mM) and imine **2a** (20 mM) following **GPSP** but without the addition of HE **3b**, which corresponds to a sample of the binary complex. Then ^{1}H and ^{1}H,^{13}-HSQC NMR spectra were recorded at 180 K. Subsequently, the sample was equilibrated at room temperature, and HE **3b** (0.5 eq.) was added under argon and NMR spectra were recorded again. This procedure of adding Hantzsch ester equivalents (0.5 – 10 eq.) to the sample was repeated.

The spectra were calibrated to TMS and the chemical shifts monitored. The most significant changes were observed for the CPA/*Z*-**2a** hydrogen bond. These changes were manually fitted in an Excel spreadsheet to a binding isotherm fitting curve corresponding to a 1:1 binding model:[12,13]

$$\Delta\delta = \Delta\delta_{max}\frac{([P_T] + [L_T] + K_d) - \sqrt{([P_T] + [L_T] + K_d)^2 - 4[P_T][L_T]}}{2[P_T]}$$

Both the dissociation constant K_d and maximum chemical shift difference $\Delta\delta_{max}$ (representing the assumed “ternary complex” chemical shift) values were fitted iteratively.

[P_T]: Describes the concentration of the binary complex (“protein”) and was set to 20 mM, which is constant over all measurements.

[L_T]: Describes the total HE **3b** concentration (“ligand”), which was determined by integration of the ^{1}H-NMR spectra relative to the imine signals.

The K_d and δ_f values from selected chemical shift changes were fitted in Dynafit using 1:1 binding model.[14]

In general, the signals of the CPA/*Z*-**2a** showed a significantly larger high-field shift than the CPA/*E*-**2a** (see FigureS2.17). Fitting the chemical shift mapping revealed a binding constant of K_d = 22.2 indicating a weak binding of the HE **3b** to the binary complex. Despite the fact that the absolute chemical shift differences for the CPA/*E*-**2a** hydrogen bond between ternary and binary complex are significantly smaller than the respective

CPA/*Z*-**2a** hydrogen bond, the nearly linear change suggests a weaker binding of the *E*-complex.

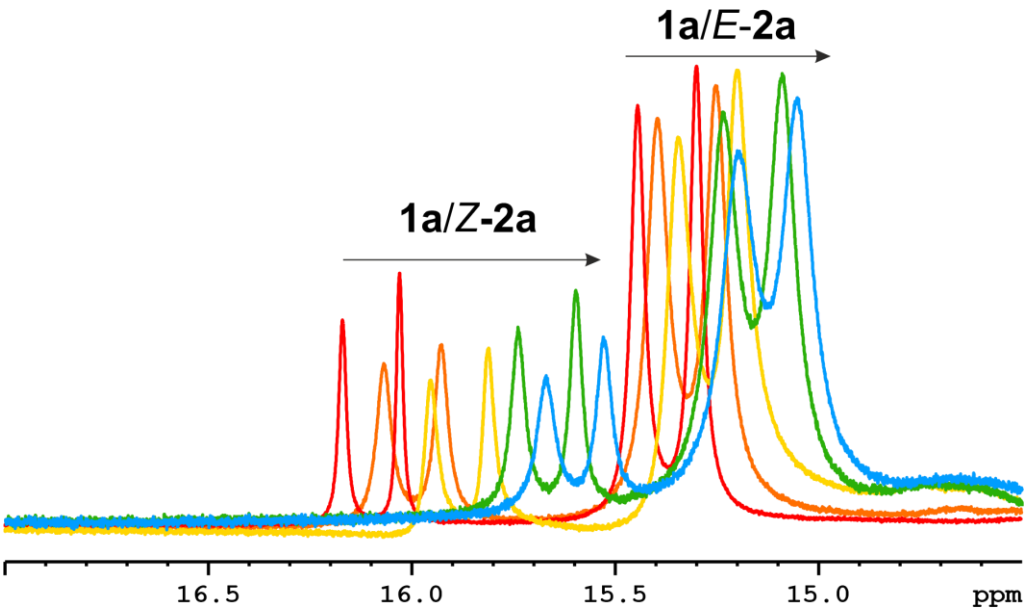

Figure S 2.17 ^{1}H-NMR chemical shift mapping of the TRIFP 1a/Z-2a (left) and TRIFP 1a/E-2a (right) hydrogen bond signals upon addition of 0-10 eq. HE 3b (600MHz, CD_2Cl_2, 180K). A general high-field shift is observed upon addition of the HE 3b (order: red, orange, yellow, green, blue).

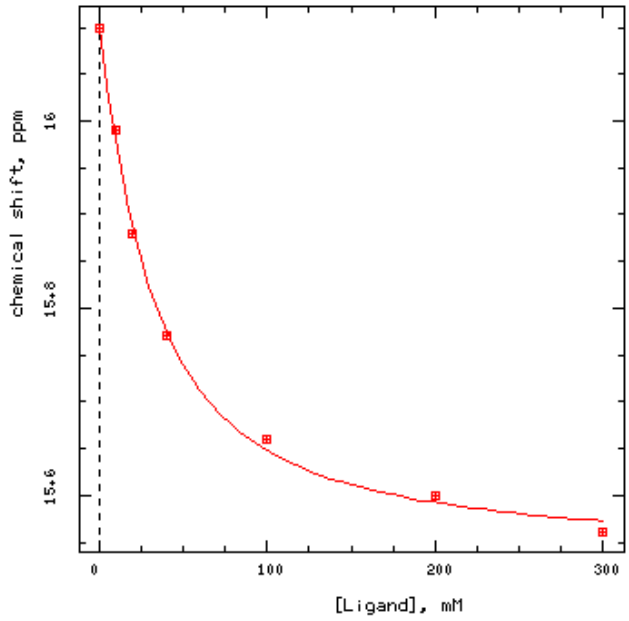

Figure S 2.18 TRIFP 1a/Z-2a hydrogen bond signal binding isotherm (7 titration points). K_d = 22.2 ± 1.8 mM; $\Delta\delta_{max}$= 15.524 ppm; K_a = 1 / K_d = 45.05 M^{-1}.

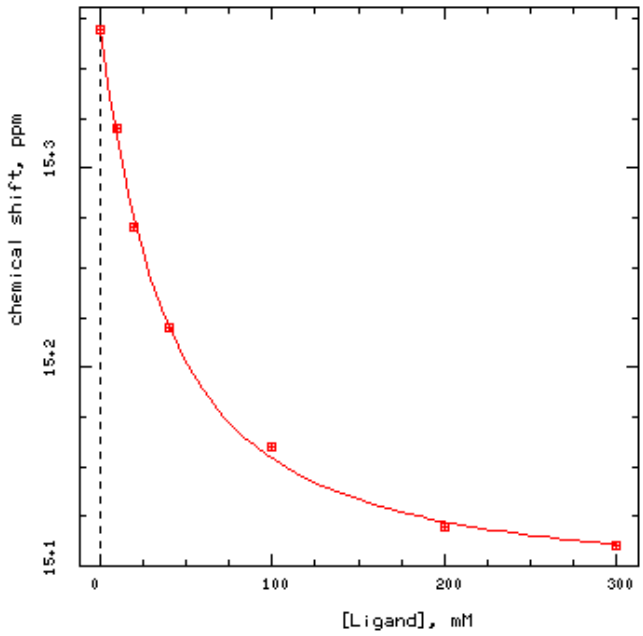

Figure S 2.19 TRIFP 1a/E-2a hydrogen bond signal binding isotherm (7 titration points). K_d = 19.8 ± 3.9 mM; $\Delta\delta_{max}$= 15.099 ppm, K_a = 1 / K_d = 50.50 M^{-1}.

2.6.9. Diffusion Ordered Spectroscopy (DOSY)

Diffusion ordered NMR spectroscopy (DOSY) experiments were performed using a Bruker Avance III HD 600 MHz spectrometer with a TBI (Triple resonance broadband inverse) 5 mm CPPBBO 1H/19F-BB or 1H/31P-BB probe head with Z-gradient and BVT unit was used. The temperature of the spectrometer was regulated by a BVT 3900 unit and liquid nitrogen. All measurements were performed at 298 K. Temperature was certified by internal NMR calibration samples from Bruker®. NMR Data was processed, evaluated, and plotted with TopSpin 3.2 software. Further analysis of the measurements was performed with Microsoft Excel (Version 16.0.10359.20023 64 Bit).

All DOSY measurements were performed with the convection suppressing DSTE (double stimulated echo) pulse sequence developed by Jerschow and Müller in a pseudo 2D mode.[15] Therefore, TMS was added to the sample and used as reference for the ^{1}H chemical shifts and for temperature as well as the viscosity of the solvent. For the measurement a set of 4 dummy scans and 8-32 scans was used for all samples. A relaxation delay of 3.5 s was used for all samples. The diffusion time delay was set to 40 ms and the gradient pulse lengths (p30, SINE.100 pulse shape) were optimized for each species to give a sigmoidal signal decay for varying gradient strengths between 5% and 95%. Optimal pulse lengths of 1.0 – 1.3 ms were used at 298 K for TMS and the formed aggregates. For each species, 32 spectra with linear varying gradient strength from 5% to 95% were measured. For integration, all separated signals were used for each substrate. Thereby, no line broadening occurred for increased gradient strengths.

The signal intensities of these groups in the DOSY spectra were classically analyzed as a function of the gradient strength by the in Bruker TopSpin 3.2 included software T1/T2 relaxation package by employing the Stejskal-Tanner equation.[16] Based on the obtained translational diffusion coefficients, the hydrodynamic radii of the analytes r_H were estimated following the Stokes-Einstein equation (S6), with D_i = self-diffusion coefficient k = Boltzmann constant, T = temperature, η = viscosity of the sample, c = correcting factor, F = shape factor:[17]

$$D_i = \frac{k_B T}{F c \pi \eta r_H} \qquad \text{(S1)}$$

The shape factor *F* was set to 1 for a spherical shape. The semi-empirical modification by Chen (S7) was used to calculate the correction factor *c*. Therefore, a from literature known value for the radius of the corresponding solvent was used ($r_{CD_2Cl_2}$ = 2.46 Å[18]).[20]

$$c_{Chen} = \frac{6F}{1 + 0.695\ (\frac{r_{solv}}{r_{ref}})^{2.234}} \tag{S2}$$

Viscosity calibration of the derived D_i values was performed with literature known values for the radii of TMS (r_{ref} = 2.96 Å, calculated from hard-sphere increments[19]) and the experimentally determined diffusion coefficient D_{ref} of TMS, which is determined individually for each sample.

$$\eta\ [kg/ms] = \frac{kT\ (1 + 0.695\ \left(\frac{r_{solv}}{r_{ref}}\right)^{2.234})}{6\pi D_{ref}\ r_{ref}} \tag{S3}$$

After including all correction and calibration equations in the Stokes equation (S6), the equation was rearranged for the hydrodynamic radii r_H (S9). The corresponding volumes V_A were calculated with the assumption of a spherical shape.

$$D = \frac{kT\ (1 + 0.695\ \left(\frac{r_{solv}}{r_{ref}}\right)^{2.234})}{6\pi\eta r_H} \tag{S4}$$

The experimental self-diffusion coefficients D_i, the viscosity corrected hydrodynamic radii r_H and the resulting volumes V_A of all samples are depicted in Table S3.3. TMS was used as viscosity reference in each sample separately with the variation in its experimental diffusion coefficients reflecting the different viscosities depending on the substrate concentration. The average D_i values were derived by using all baseline separated signals that were referring to the same species. As stated above the hydrodynamic values and the volumes are viscosity corrected and therefore the only values, which can be directly compared with each other (see Table S2.3).

Table S 2.3 Experimental self-diffusion coefficients D_i, viscosity corrected hydrodynamic radii r_H and resulting volumes V_A of various 1b/2a/3b combinations (40 mM). TMS was used as viscosity reference for the experimental self-diffusion coefficients D_i to allow for a comparison of hydrodynamic radii r_H and resulting volumes V_A. The corresponding self-diffusion coefficients D_i of TMS are given for each sample. Entry 1-5: SW = 22 Hz, O1P = 10.0 ppm, gradient strength 5-95% linear. Samples were measured at room temperature.

Entry	Species	Diffusion coefficient D_i [$m^2.s^{-1}$]	Hydrodynamic radius r_H [Å]	Volume V_A [$Å^3$]
1	OMe-CPA **1a** *TMS*	7.12E-10 2.48E-09	7.47	1748
2	**2a** *TMS*	1.53E-09 2.42E-09	3.97	262
3	HE **3b** *TMS*	1.26E-09 2.68E-09	4.94	506
4	OMe-CPA **1b**/ **2a** *TMS*	6.81E-10 2.30E-09	7.28	1625
5	OMe-CPA **1b**/ **2a** /HE **3b** *TMS*	3.11E-10 1.21E-09	8.23	2331

2.6.10. NOE Analysis of Conformers

The calculated conformers were compared to the NMR data, especially the NOE signals. For this analysis, only NOE correlations of the HE **3b** can be used. This is a result of the fast exchange of binary and ternary complexes leading to an averaged signal set for both the CPA **1** and the imine **2a**. Therefore, a distinction between both complexes is not feasible, but the HE **3b** signals can be unambiguously assigned to the ternary complex. The [3:3] dimer does also not interfere with this analysis, as for the TRIFP **1a** system the [3:3] species is negligible populated and does not result in any observable NOESY signals, simplifying the analysis.In addition, in the OMe-CPA **1b** system a separate signal set for the HE **3b** is detected indicating a slow exchange on the NMR timescale. Hence, the HE **3b** NOE signals can be interpreted without restrictions.

In addition, to distinguish between various conformers only the distinct NOE correlations for each conformer can be used. This means, the calculated conformers were first analyzed regarding the distances between HE **3b** and the CPA **1** as well as imine **2a**. Next, these findings were compared between all conformers and for each conformer distinct close distances between CPA/HE and imine/HE were noted. These close distances should be observable in NOESY spectra and therefore reveal if the analyzed conformers are existing or not. Contrary, calculated long distances between CPA/HE or imine/HE cannot be used. In case of such distinct long distances, a signal for other conformers with shorter distances would still be observed, making any evaluation

inaccessible. Hence, although a huge NOE network is detected, only very few signals can be used to identify the conformers. Nevertheless, this confined assessment of only the distinct NOEs is indispensable since most signals involve contributions from at least two conformers, preventing the unambiguous identification of a single conformer.

2.6.10.1. TRIFP 1a/2a/HE 3b

The system TRIFP **1a**/**2a**/HE **3b** was selected as model system for the conformer analysis due to a high population of the ternary complex in comparison to other species as well as sharper signals which lead to better NOESY resolution. Here, especially the *E*-imine **2a** complex was used due to its higher population which enabled a full chemical shift assignment. After excluding various conformers based on the NOESY spectra, three conformers were left which are supported by NOE correlations. The three lowest energy conformers (C1, C2, C3) and their respective NOE cross signals are displayed below (S20-S23). Other from calculations expected correlations are also observed between **1a**/HE **3b** and **2a**/HE **3b** but are not shown here, because they are not distinct for the respective conformer.

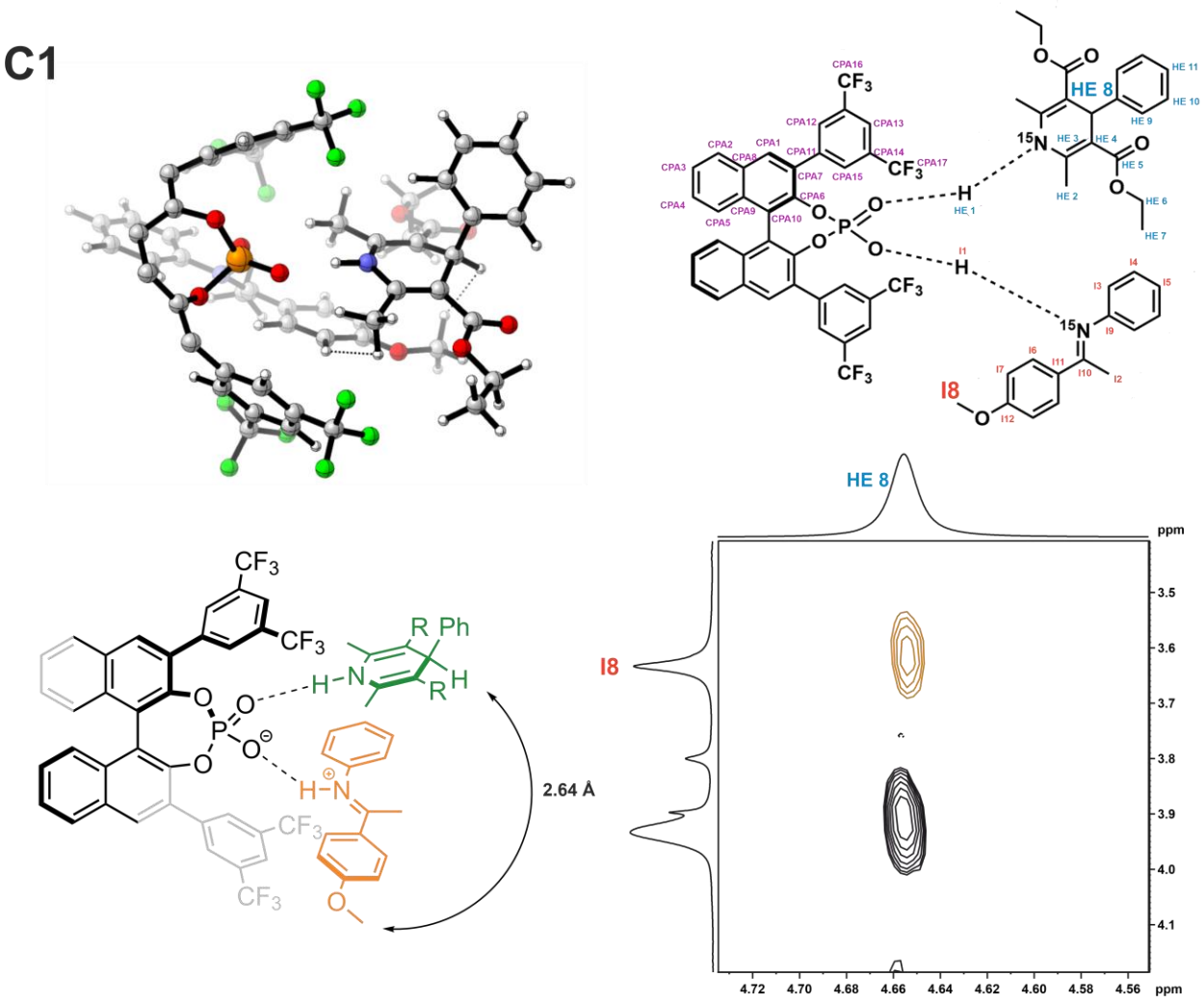

Figure S 2.20 Conformer 1 NOE analysis. Left right corner the calculated conformer C1 is displayed. One of the distinct signals for this conformer is the NOE correlation between the HE 3b hydrogen atom at 4.66 ppm with the OMe-group of the imine 2a at 3.64 ppm.

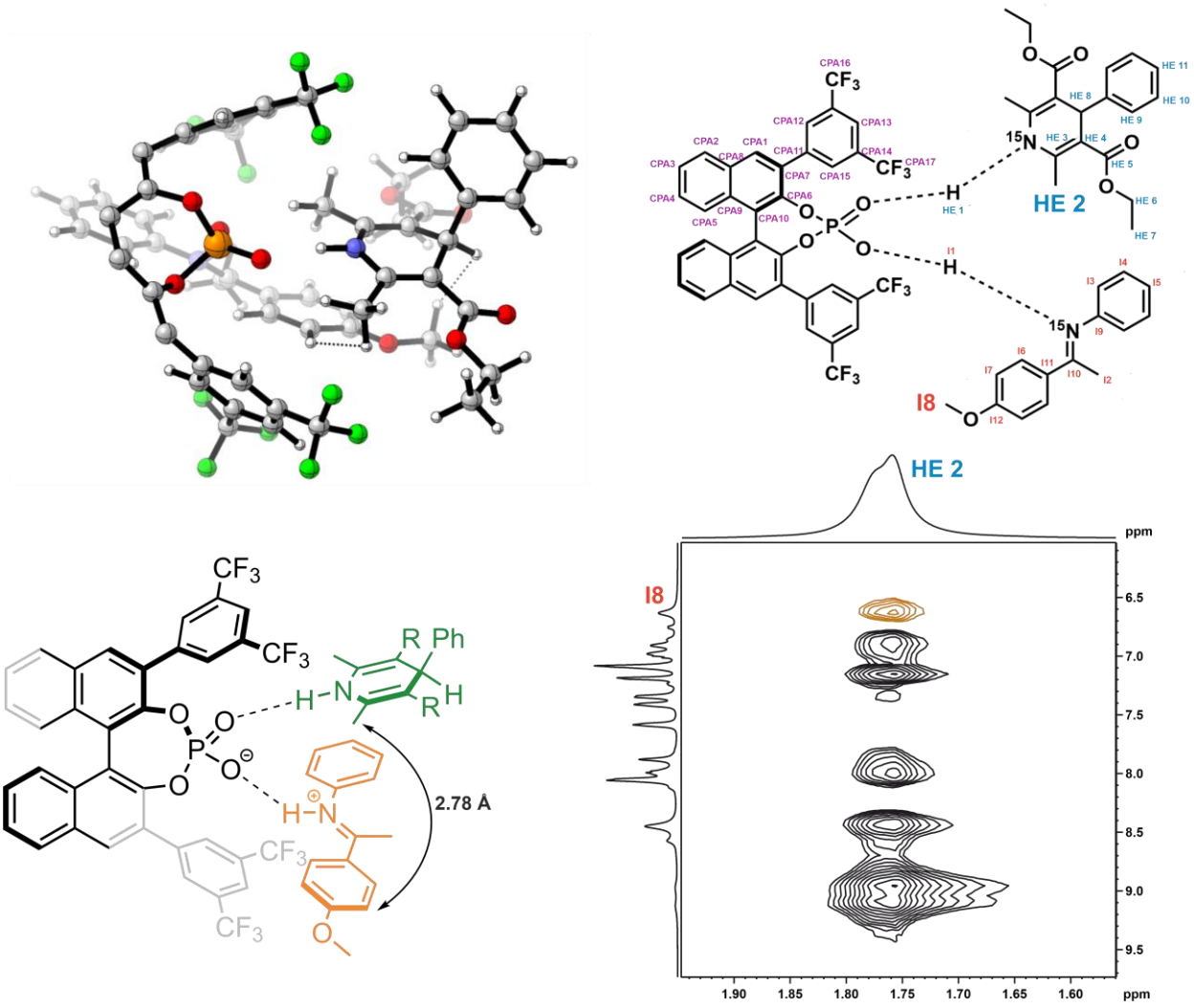

Figure S 2.21 Conformer 1 NOE analysis. Left right corner the calculated conformer C1 is displayed. One of the distinct signals for this conformer is the NOE correlation between the HE 3b CH_3-group at 1.76 ppm with the p-OMe-phenyl-ring of the imine at 6.64 ppm.

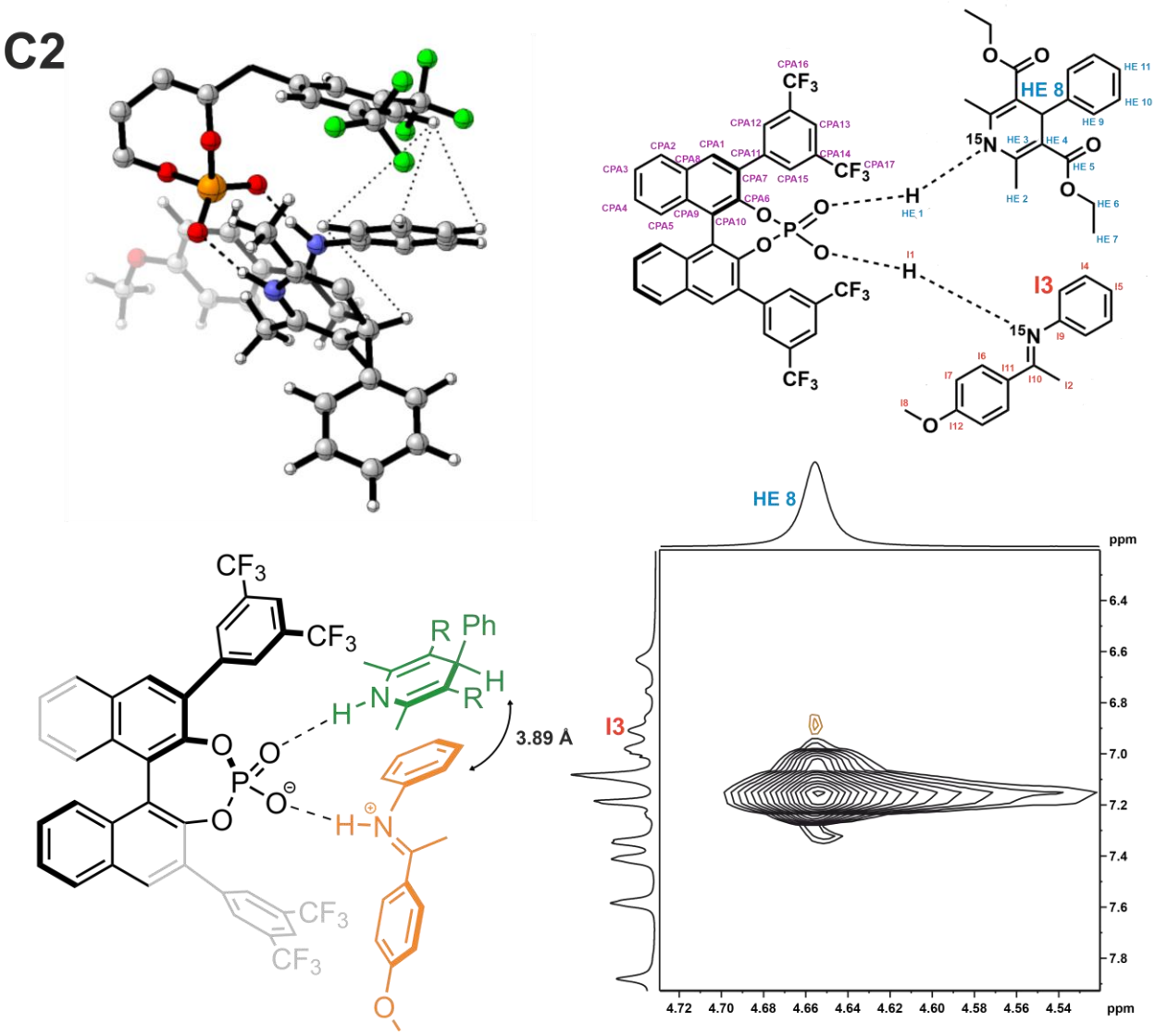

Figure S 2.22 Conformer 2 NOE analysis. Left right corner the calculated conformer C2 is displayed. One of the distinct signals for this conformer is the NOE correlation between the HE 3b hydrogen atom at 4.66 ppm with the phenyl-group of the imine at 6.90 ppm.

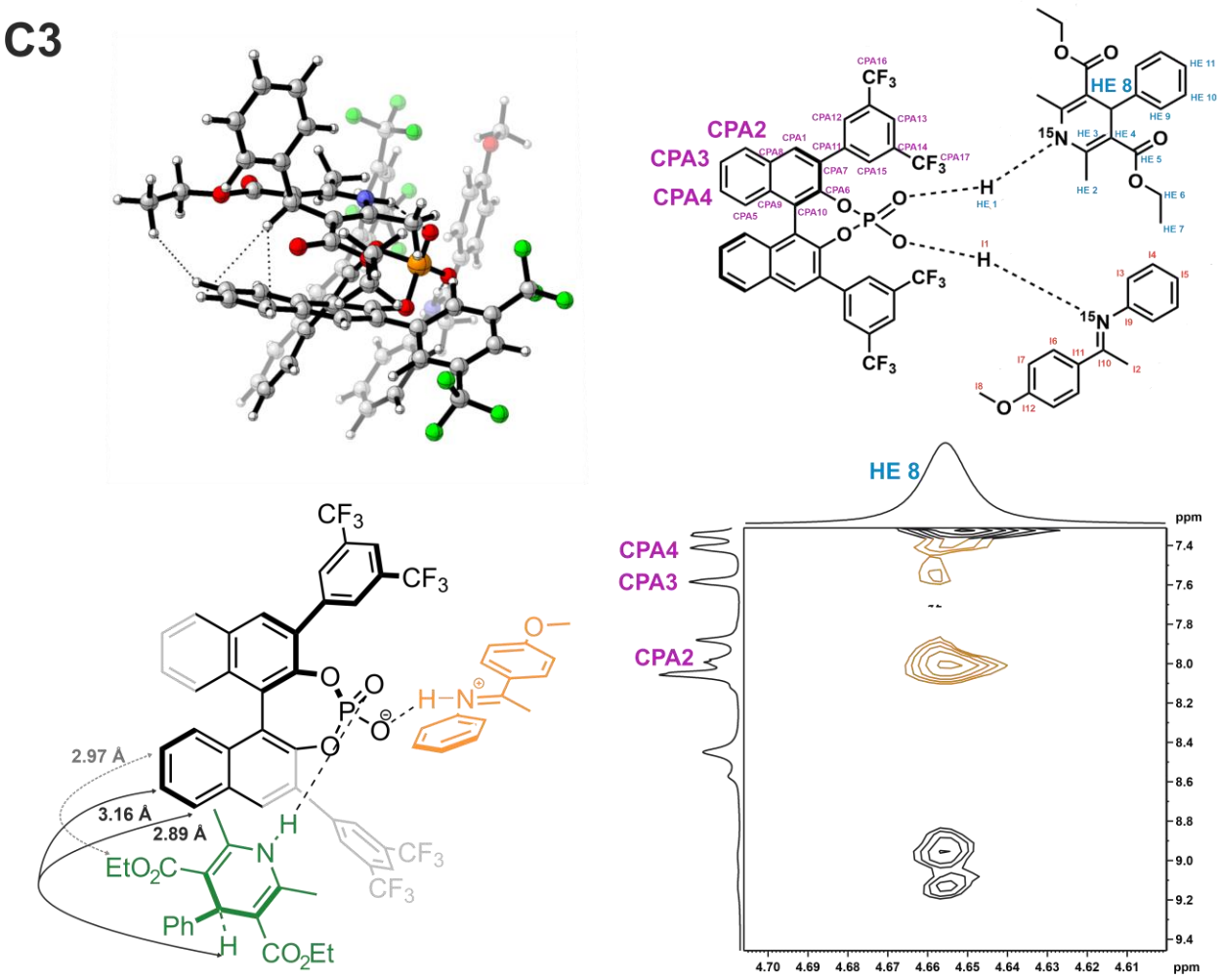

Figure S 2.23 Conformer 3 NOE analysis. Left right corner the calculated conformer C3 is displayed. The distinct signals for this conformer are the NOE correlation between the HE 3b hydrogen atom at 4.66 ppm with the BINOL-backbone.

2.6.10.2. [3:3] Dimer with OMe-CPA 1b

For the analysis of the [3:3] dimer, the second model system OMe-CPA 1b/2a/HE 3b was selected due to its high population. Here, nearly a 1:1 ratio between the population of the hydrogen bond signals of the binary/ternary complex and those of the [3:3] dimer. In addition, in this system a clearly observable separate signal set was detected for HE **3b** for the [3:3] species (see FigureS2.24-25). However, in NOESY/EXSY spectra exchange processes with the binary and ternary complexes are still observed. Therefore, the calculated structures of the [3:3] dimer were compared with the ternary complexes to find distinct NOE interactions which could still be interpreted but both are too similar to differ.

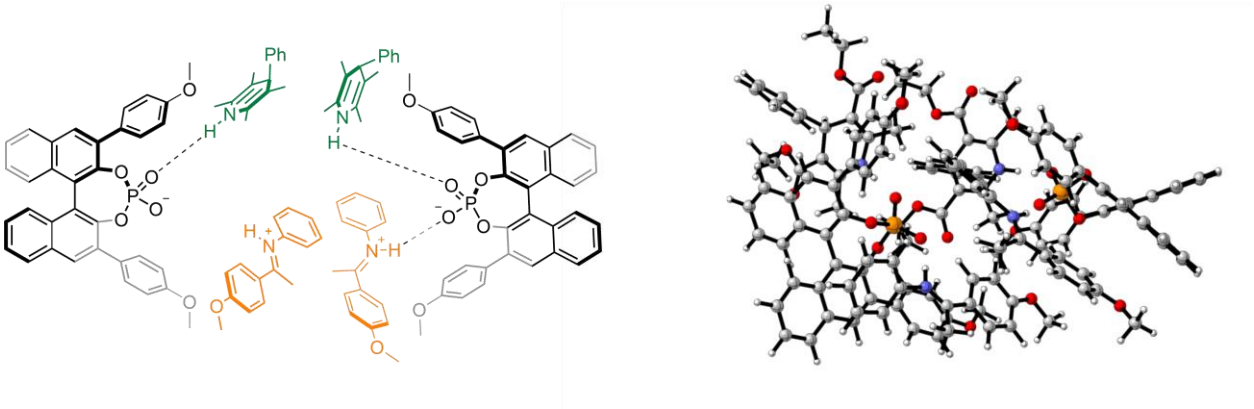

Figure S 2.24 Scheme of the [3:3] dimeric species (left). Calculated structure of the [3:3] dimeric species (right).

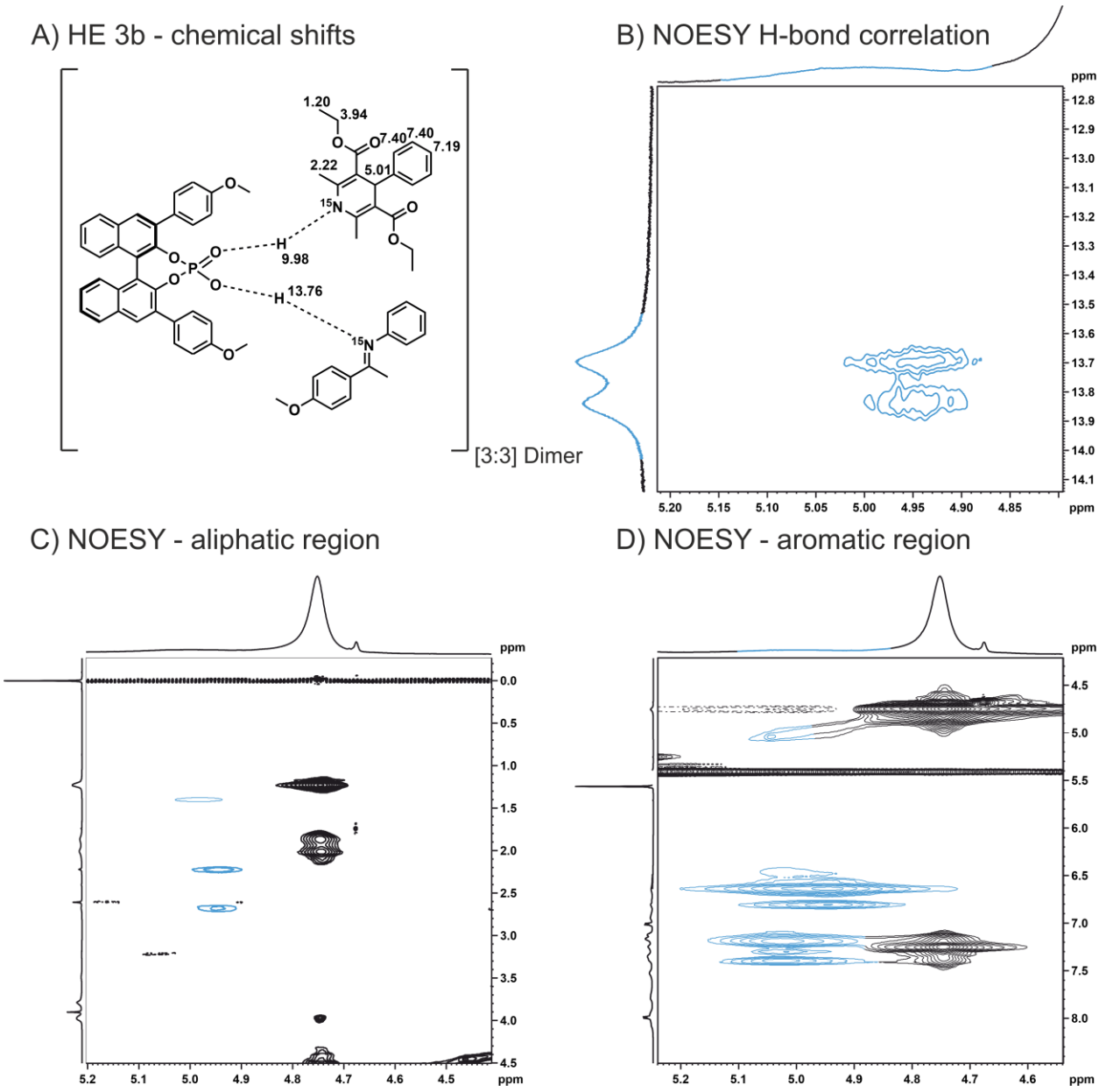

Figure S 2.25 A) Chemical Shift assignment for the separate signal set of the HE 3b. B) ^{1}H-^{1}H NOESY spectrum with focus on the NOE correlation of the H-bond to the HE 3b. C) ^{1}H-^{1}H NOESY spectrum with a zoom on the NOE correlation of the HE 3b signal at 5.01 ppm in the aliphatic region. D) ^{1}H-^{1}H NOESY spectrum with a zoom on the NOE correlation of the HE 3b signal at 5.01 ppm in the aromatic region.

2.6.11. Appendix

2.6.11.1. NMR Screening - ^{1}H- NMR Spectrum of Each Sample

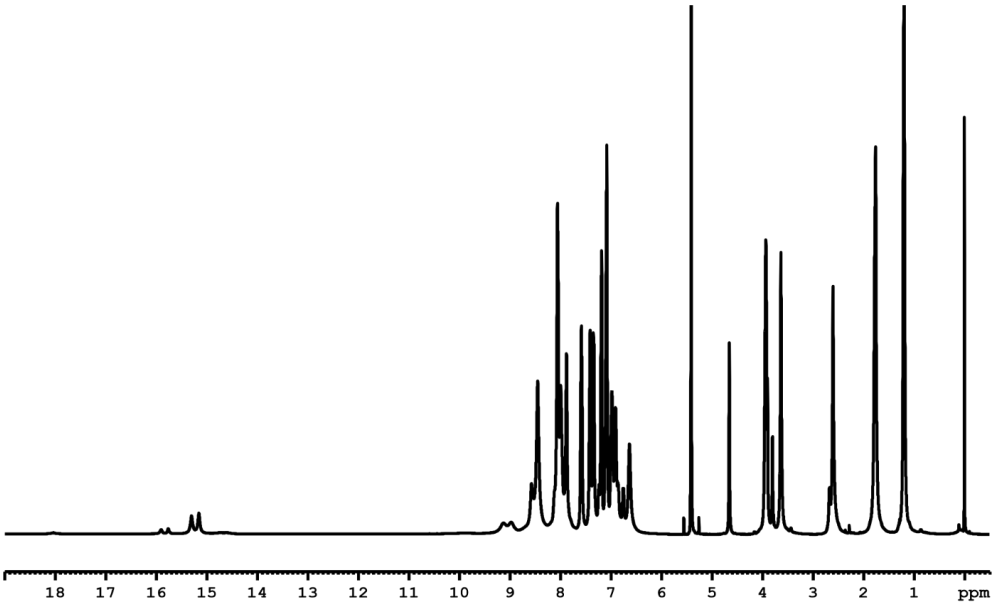

^{1}H-spectrum of the ternary complex of TRIFP 1a/2a/HE 3b (1:1:1 stoichiometry, 600MHz, CD_2Cl_2, 180K).

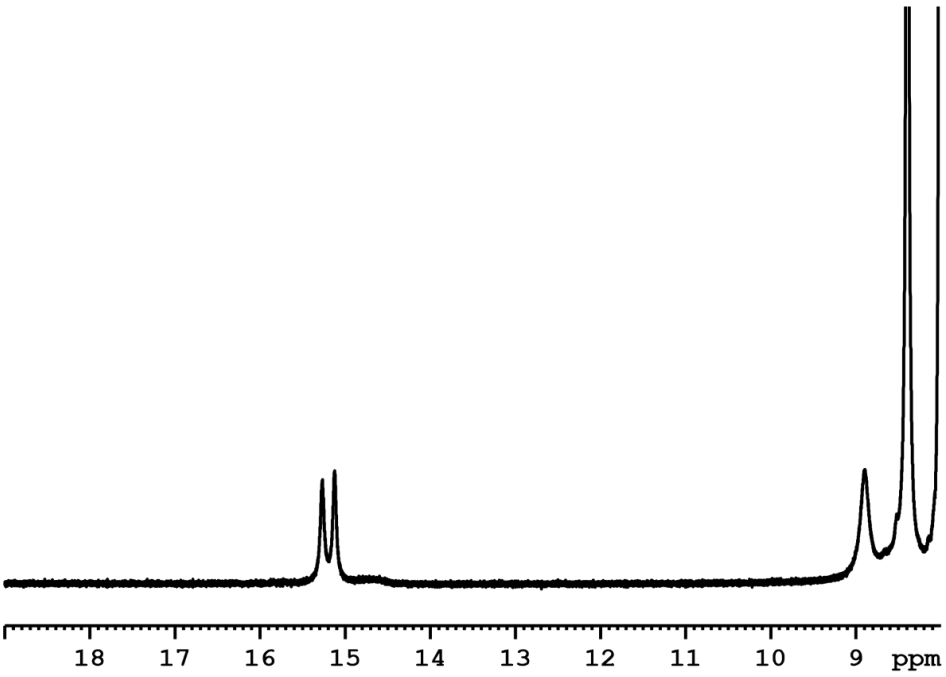

E-only sample: Hydrogen bond area of the ^{1}H-spectrum of the ternary complex of F 1a/E-2a/HE 3b (1:1:1 stoichiometry, 600MHz, CD_2Cl_2, 180K).

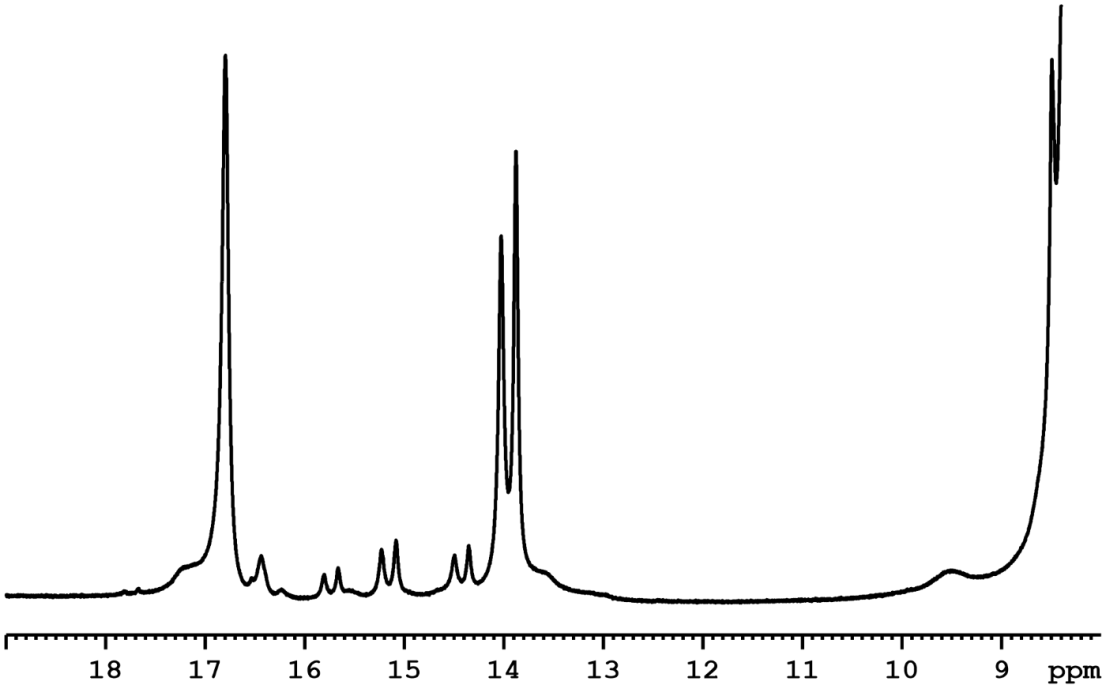

Hydrogen bond area of the ^{1}H-spectrum of the ternary complex of TRIFP 1a/2a/HE 3b (2:1:1 stoichiometry, 600MHz, CD_2Cl_2, 180K).

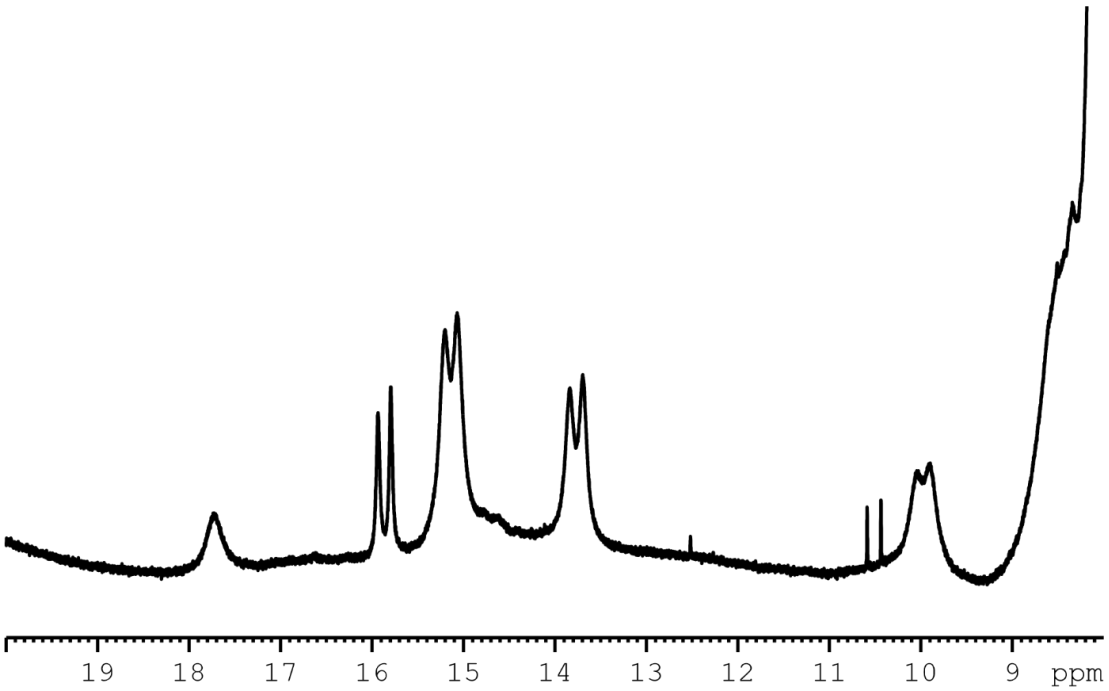

Hydrogen bond area of the ^{1}H-spectrum of the ternary complex of OMe-CPA 1b/2a/HE 3b (1:1:1 stoichiometry, 600MHz, CD_2Cl_2, 180K).

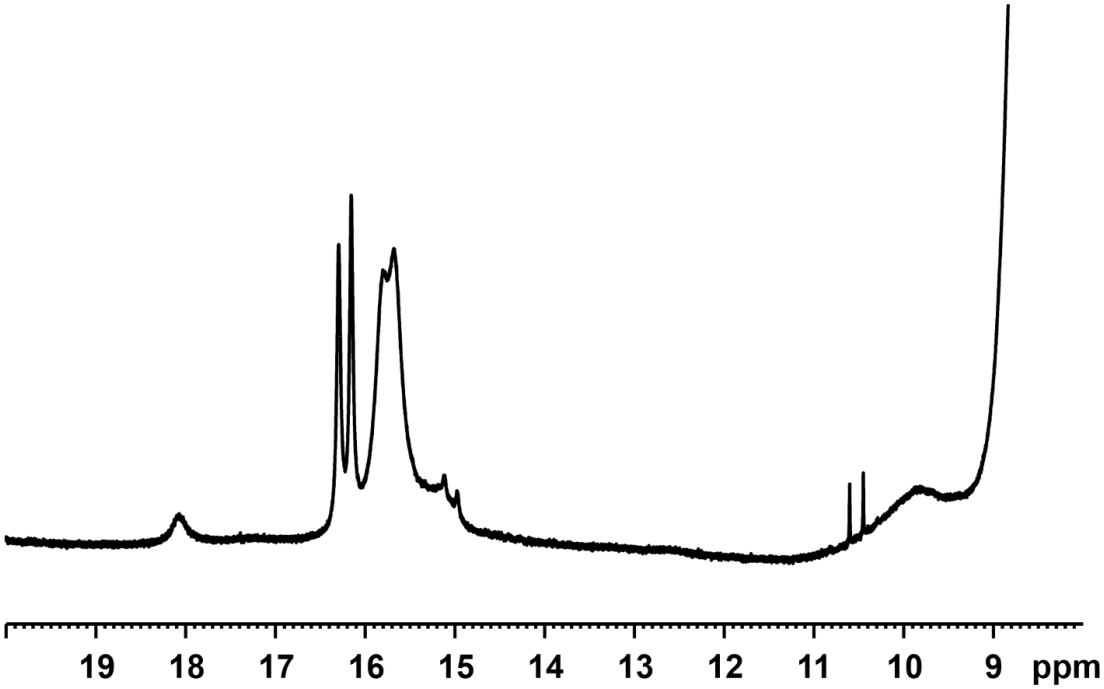

Hydrogen bond area of the ^{1}H-spectrum of the ternary complex of TRIFP 1a/2b/HE 3b (1:1:1 stoichiometry, 600MHz, CD_2Cl_2, 180K).

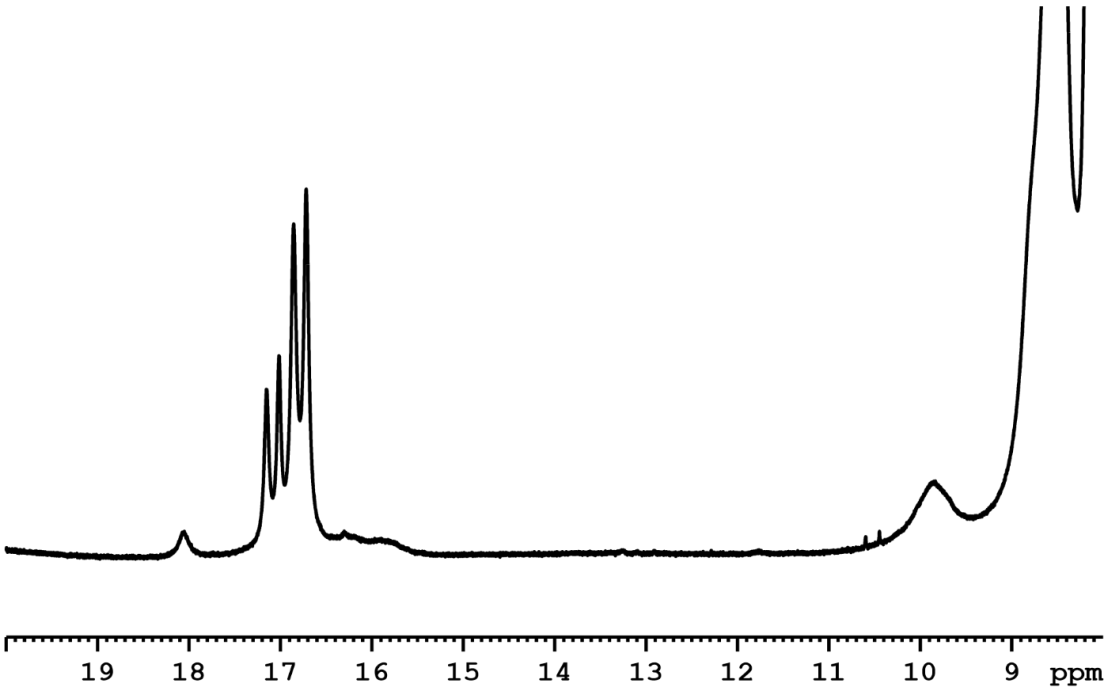

Hydrogen bond area of the ^{1}H-spectrum of the ternary complex of TRIFP 1a/2c/HE 3b (1:1:1 stoichiometry, 600MHz, CD_2Cl_2, 180K).

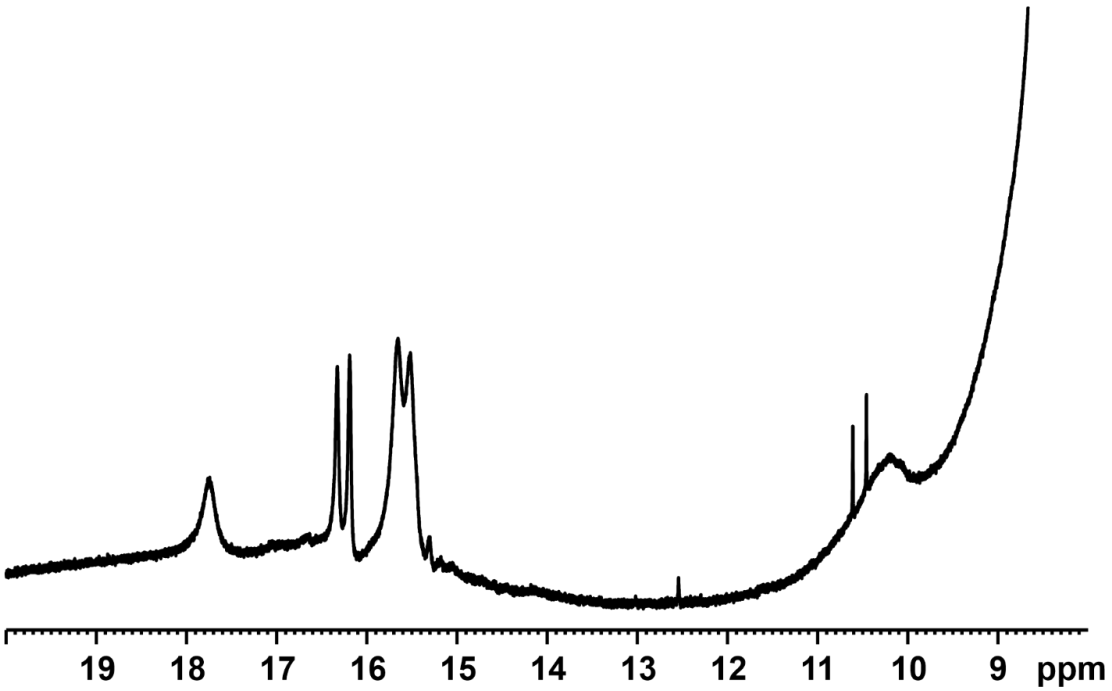

Hydrogen bond area of the ^{1}H-spectrum of the ternary complex of OMe -CPA 1b/2b/HE 3b (1:1:1 stoichiometry, 600MHz, CD_2Cl_2, 180K).

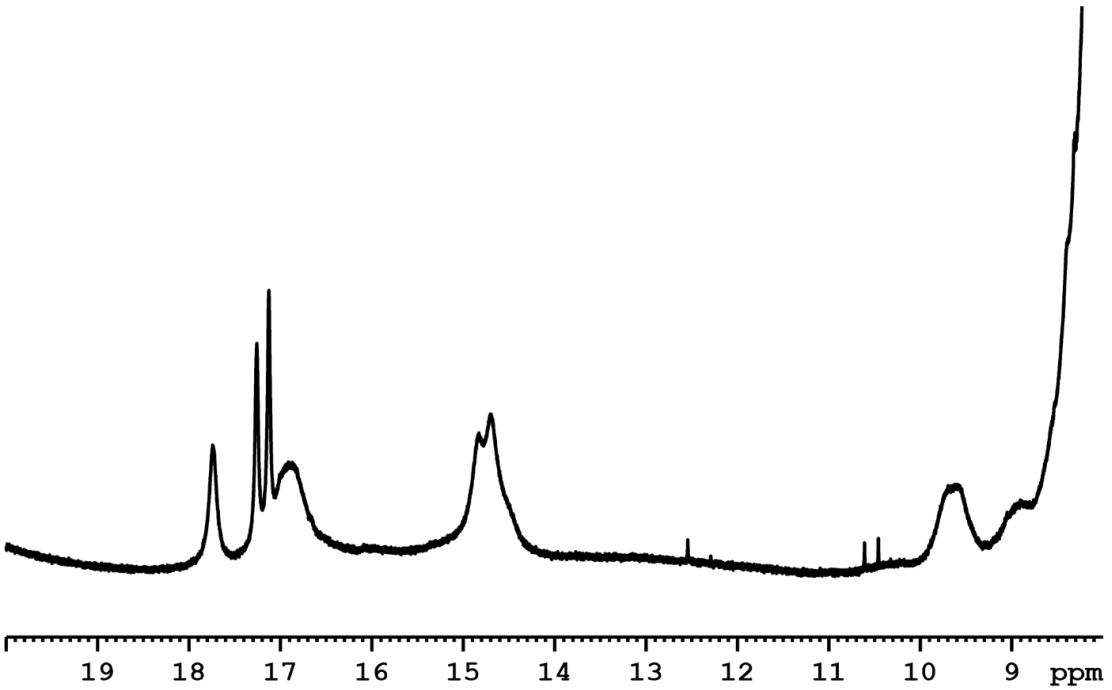

Hydrogen bond area of the ^{1}H-spectrum of the ternary complex of OMe -CPA 1b/2c/HE 3b (1:1:1 stoichiometry, 600MHz, CD_2Cl_2, 180K).

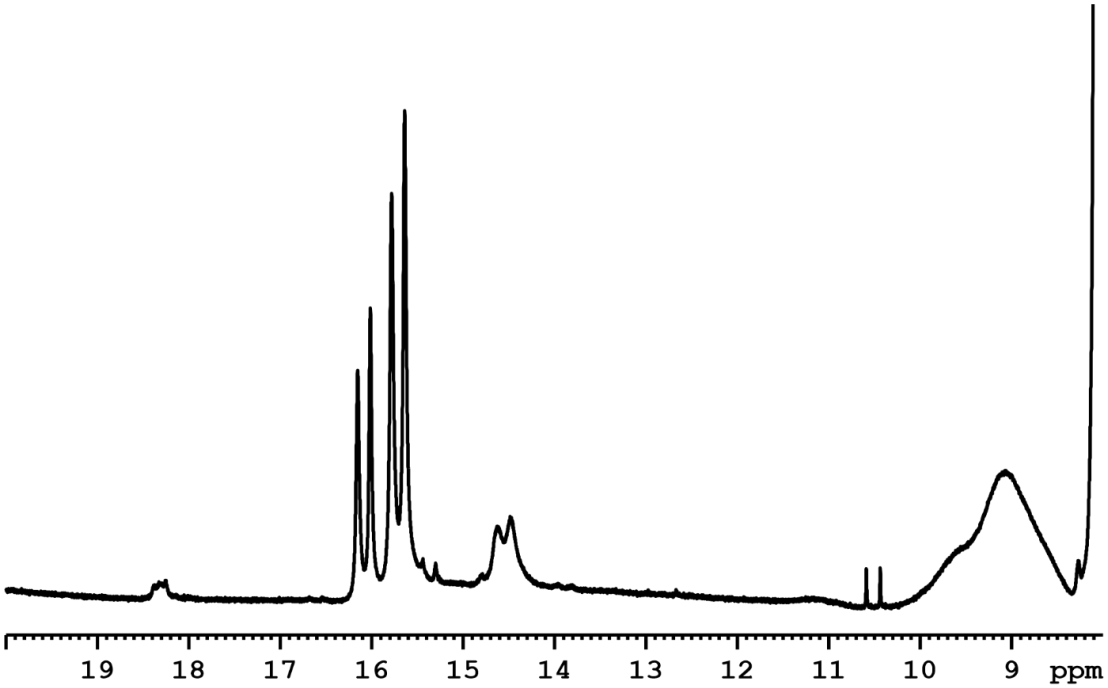

Hydrogen bond area of the ^{1}H-spectrum of the ternary complex of TRIM 1c/2a/HE 3b (1:1:1 stoichiometry, 600MHz, CD_2Cl_2, 180K).

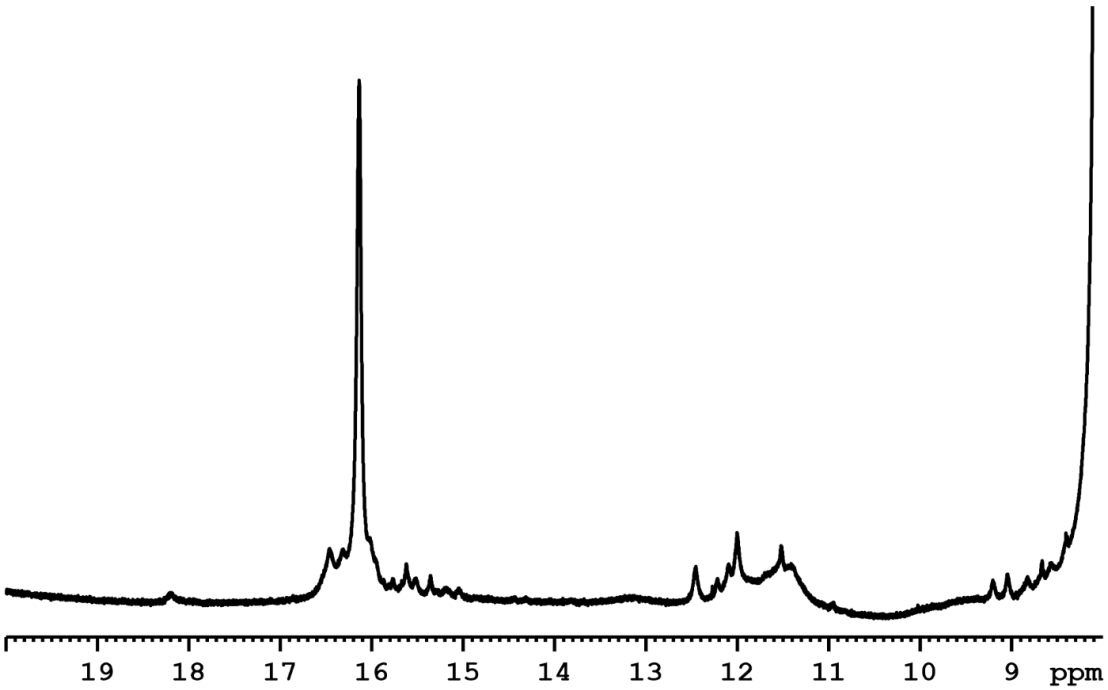

Hydrogen bond area of the ^{1}H-spectrum of the ternary complex of TRIM 1c/2b/HE 3b (1:1:1 stoichiometry, 600MHz, CD_2Cl_2, 180K).

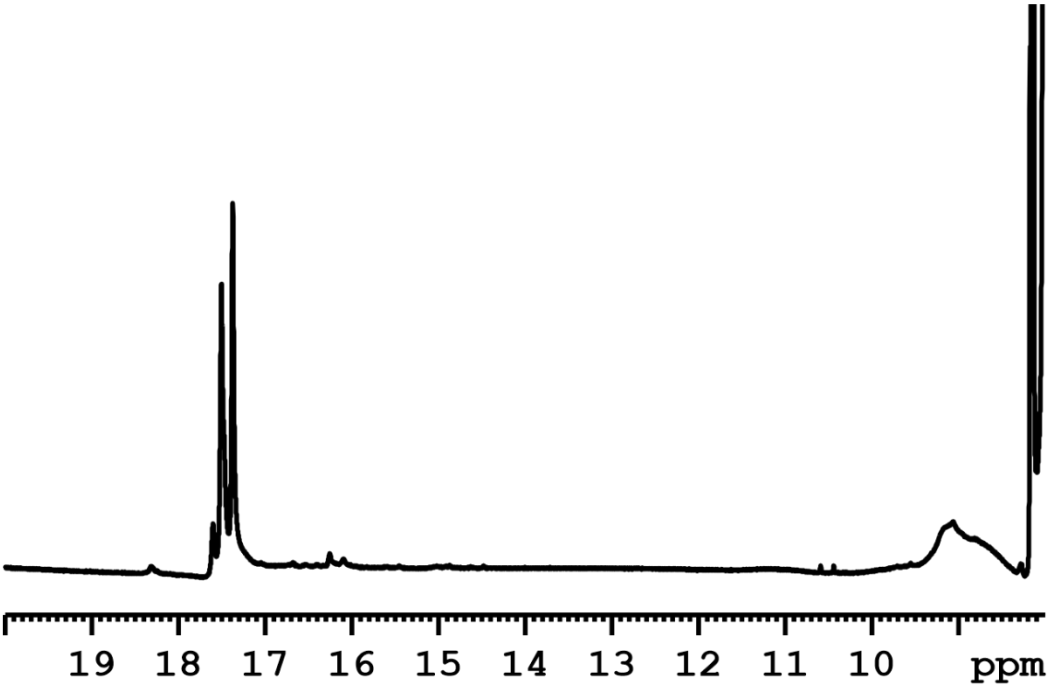

Hydrogen bond area of the ^{1}H-spectrum of the ternary complex of TRIM 1c/2c/HE 3b (1:1:1 stoichiometry, 600MHz, CD_2Cl_2, 180K).

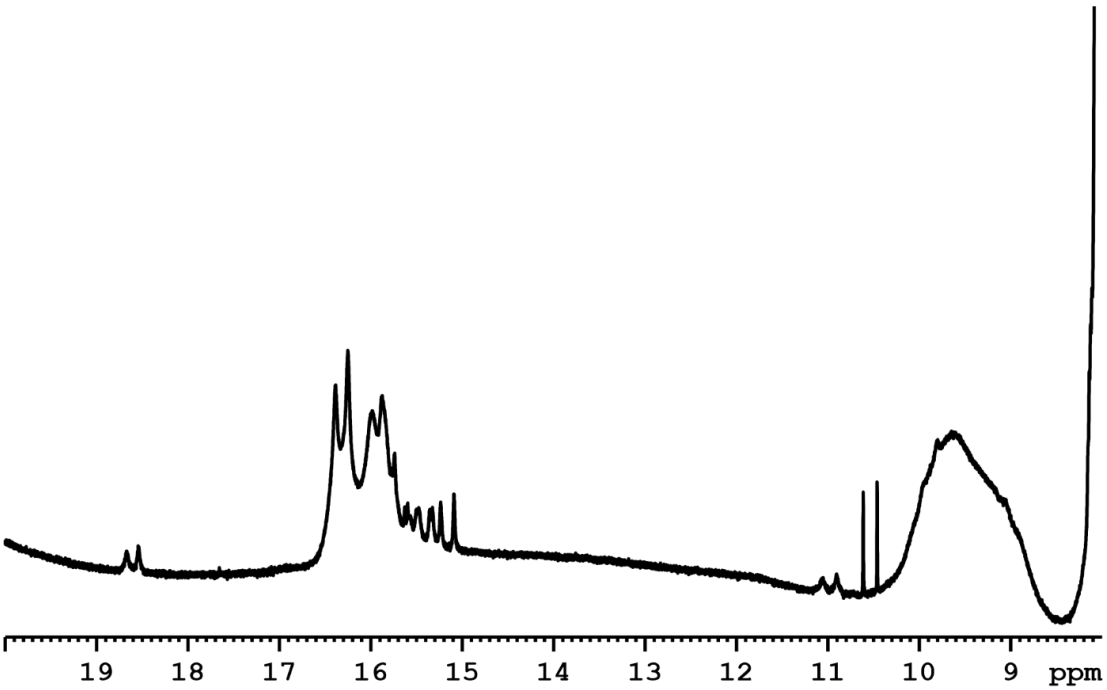

Hydrogen bond area of the ^{1}H-spectrum of the ternary complex of TRIP 1d/2a/HE 3b (1:1:1 stoichiometry, 600MHz, CD_2Cl_2, 180K).

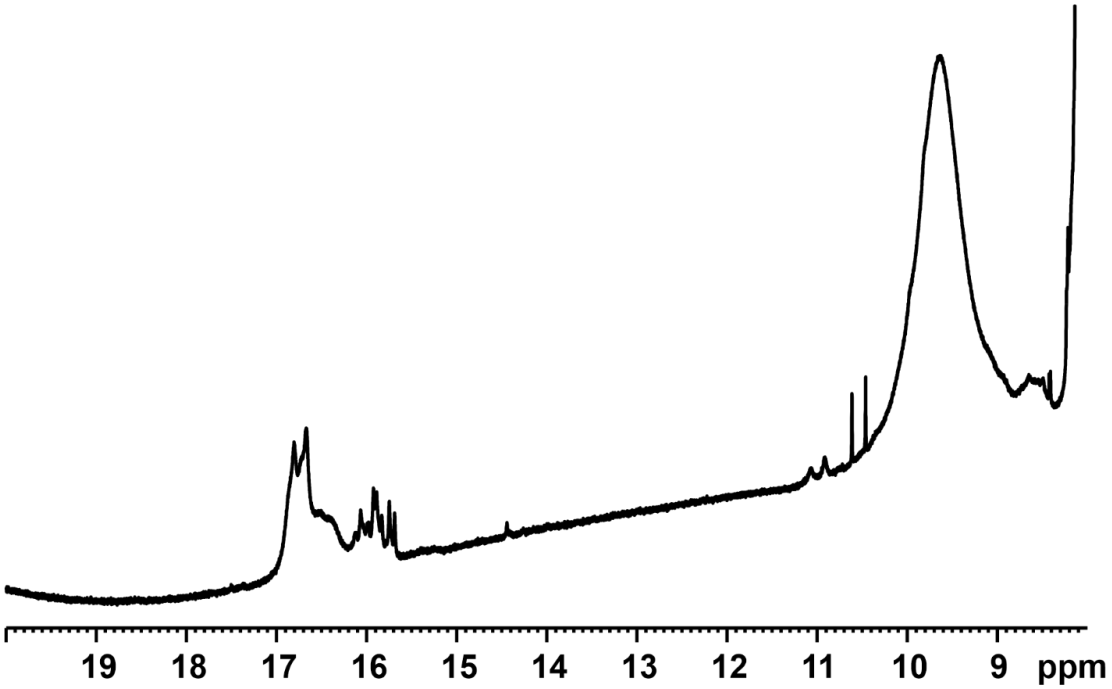

Hydrogen bond area of the ^{1}H-spectrum of the ternary complex of TRIP 1d/2b/HE 3b (1:1:1 stoichiometry, 600MHz, CD_2Cl_2, 180K).

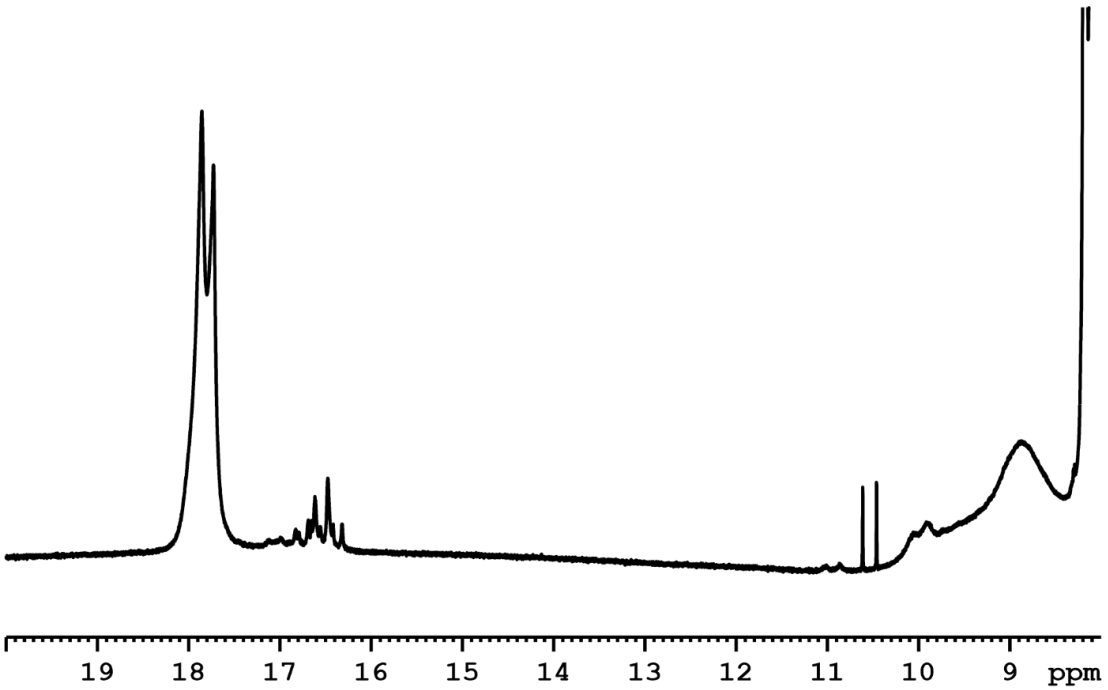

Hydrogen bond area of the ^{1}H-spectrum of the ternary complex of TRIP 1d/2c/HE 3b (1:1:1 stoichiometry, 600MHz, CD_2Cl_2, 180K).

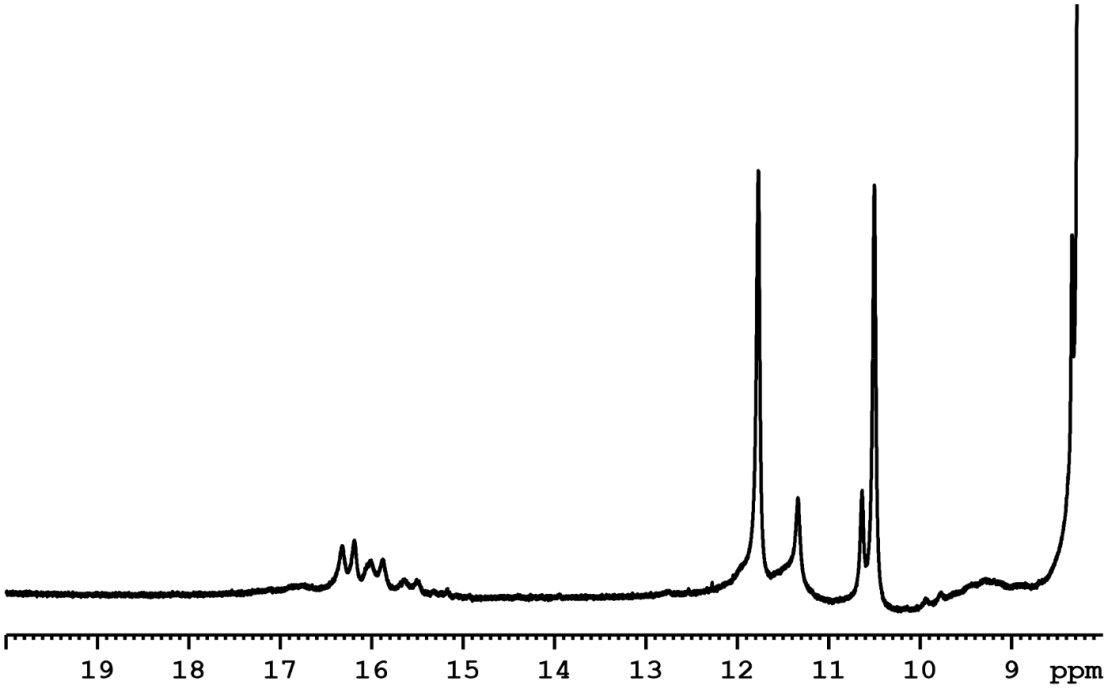

Hydrogen bond area of the ^{1}H-spectrum of the ternary complex of TiPSY 1e/2b/HE 3b (1:1:1 stoichiometry, 600MHz, CD_2Cl_2, 180K).

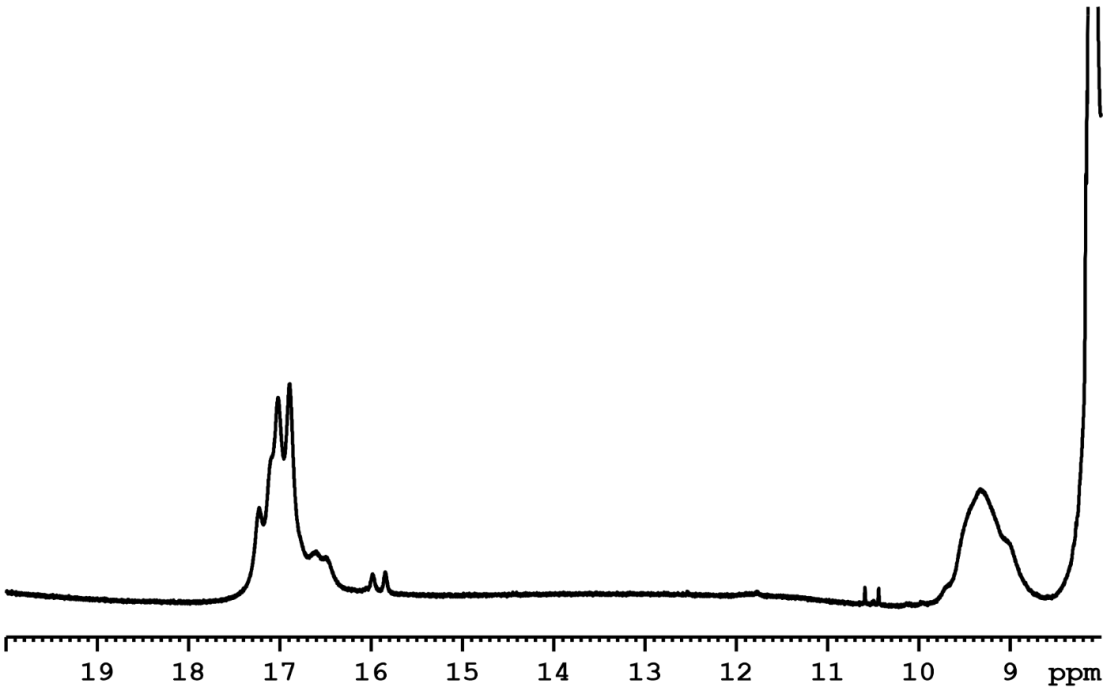

Hydrogen bond area of the ^{1}H-spectrum of the ternary complex of TiPSY 1e/2c/HE 3b (1:1:1 stoichiometry, 600MHz, CD_2Cl_2, 180K).

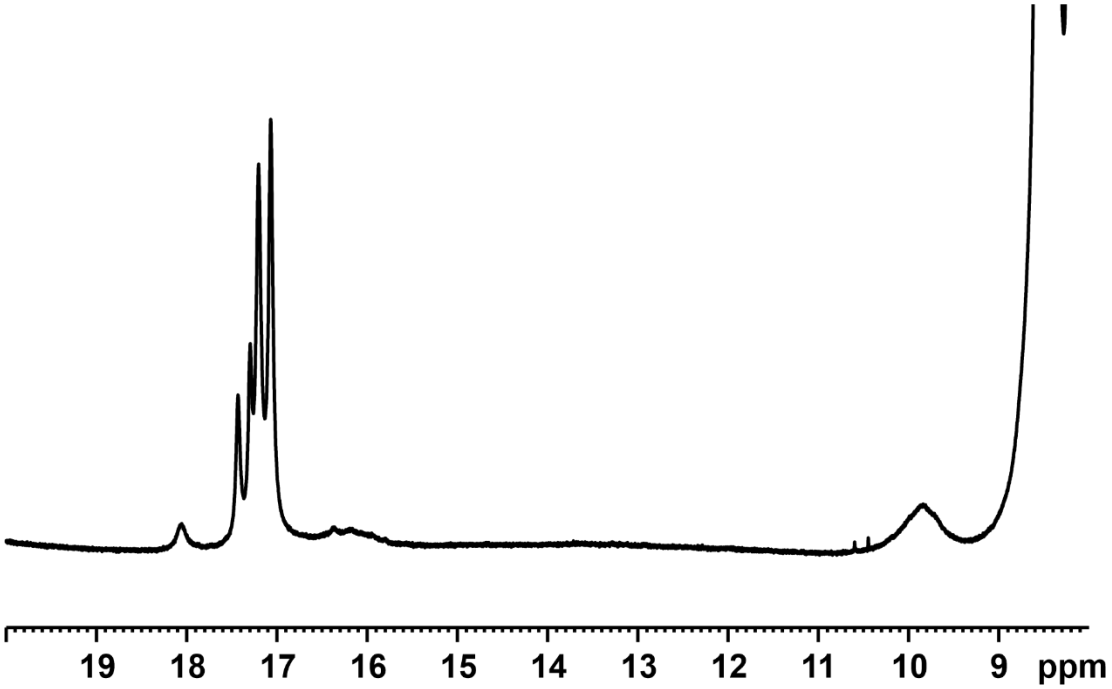

Hydrogen bond area of the ^{1}H-spectrum of the ternary complex of 1a/2d/HE 3b (1:1:1 stoichiometry, 600MHz, CD_2Cl_2, 180K).

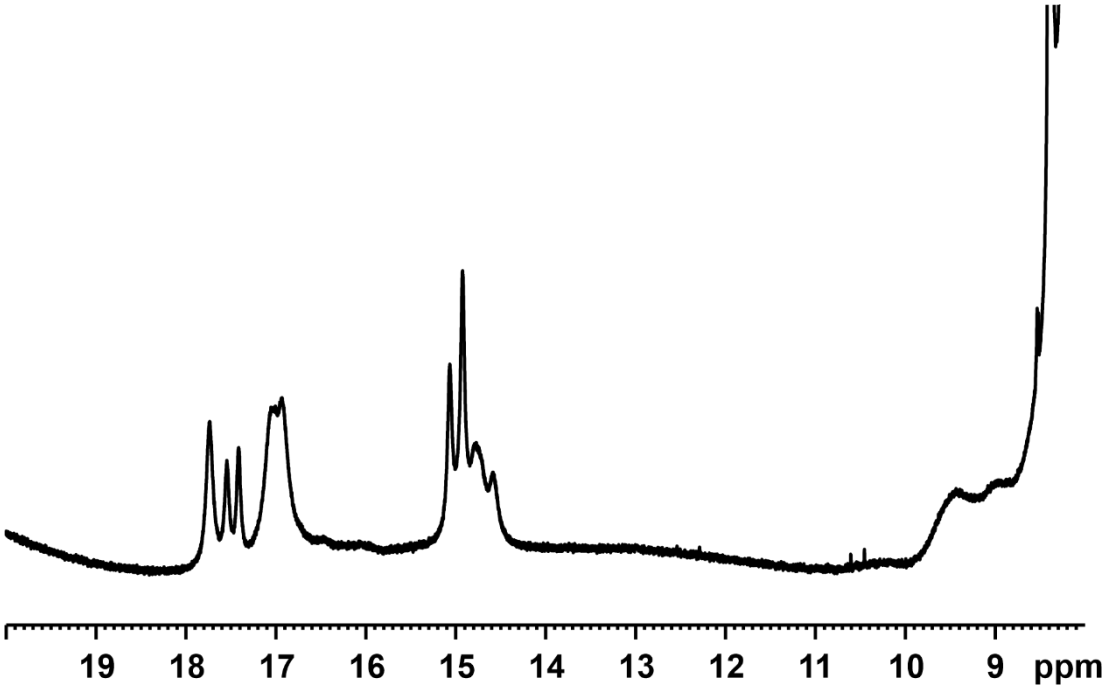

Hydrogen bond area of the ^{1}H-spectrum of the ternary complex of 1b/2d/HE 3b (1:1:1 stoichiometry, 600MHz, CD_2Cl_2, 180K).

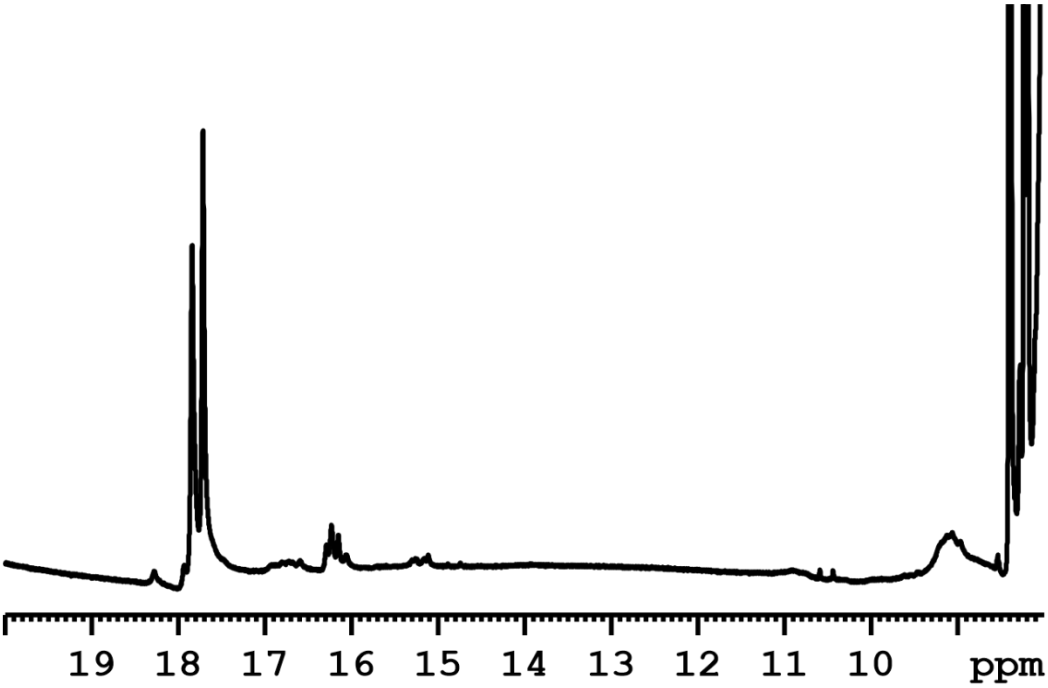

Hydrogen bond area of the ^{1}H-spectrum of the ternary complex of 1c/2d/HE 3b (1:1:1 stoichiometry, 600MHz, CD_2Cl_2, 180K).

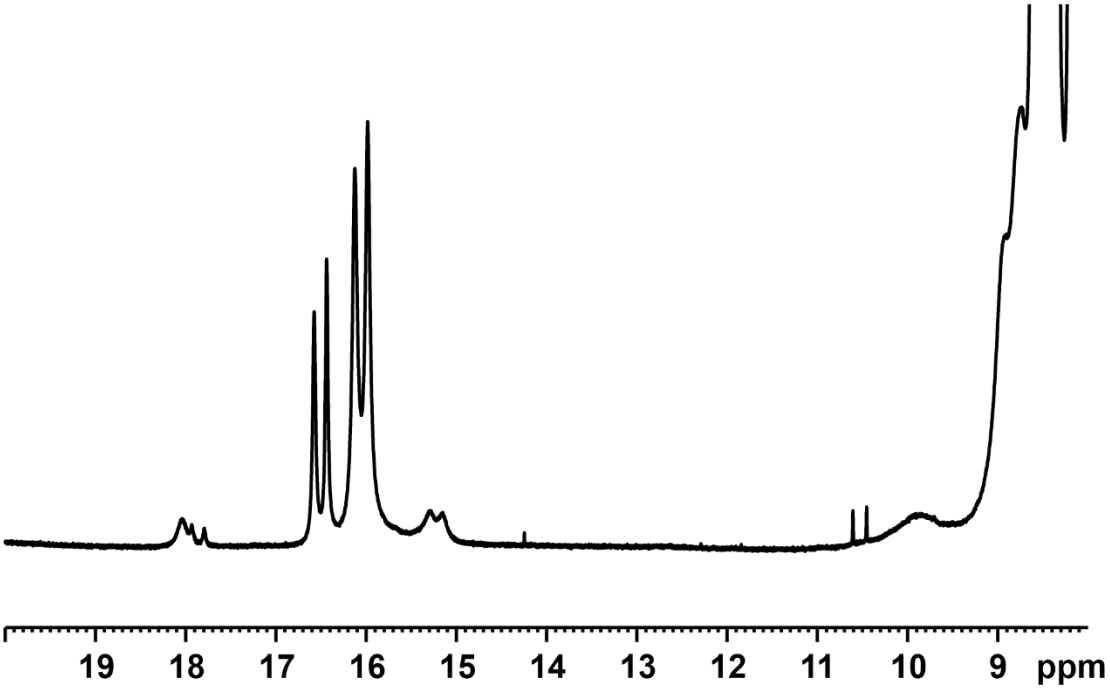

Hydrogen bond area of the ^{1}H-spectrum of the ternary complex of 1a/2e/HE 3b (1:1:1 stoichiometry, 600MHz, CD_2Cl_2, 180K).

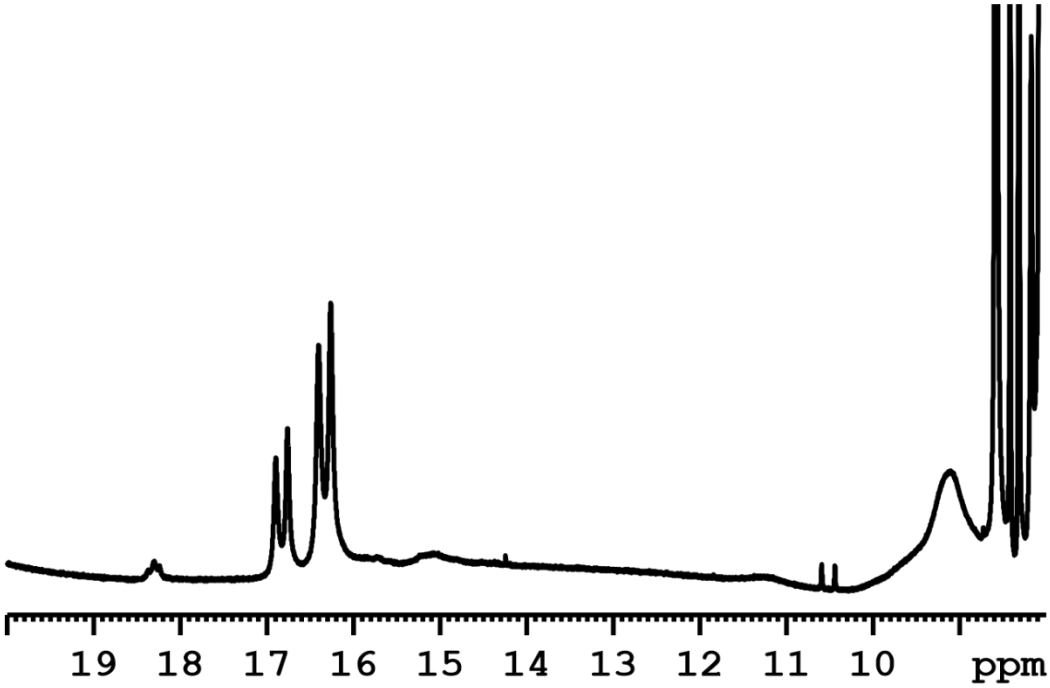

Hydrogen bond area of the ^{1}H-spectrum of the ternary complex of 1c/2e/HE 3b (1:1:1 stoichiometry, 600MHz, CD_2Cl_2, 180K).

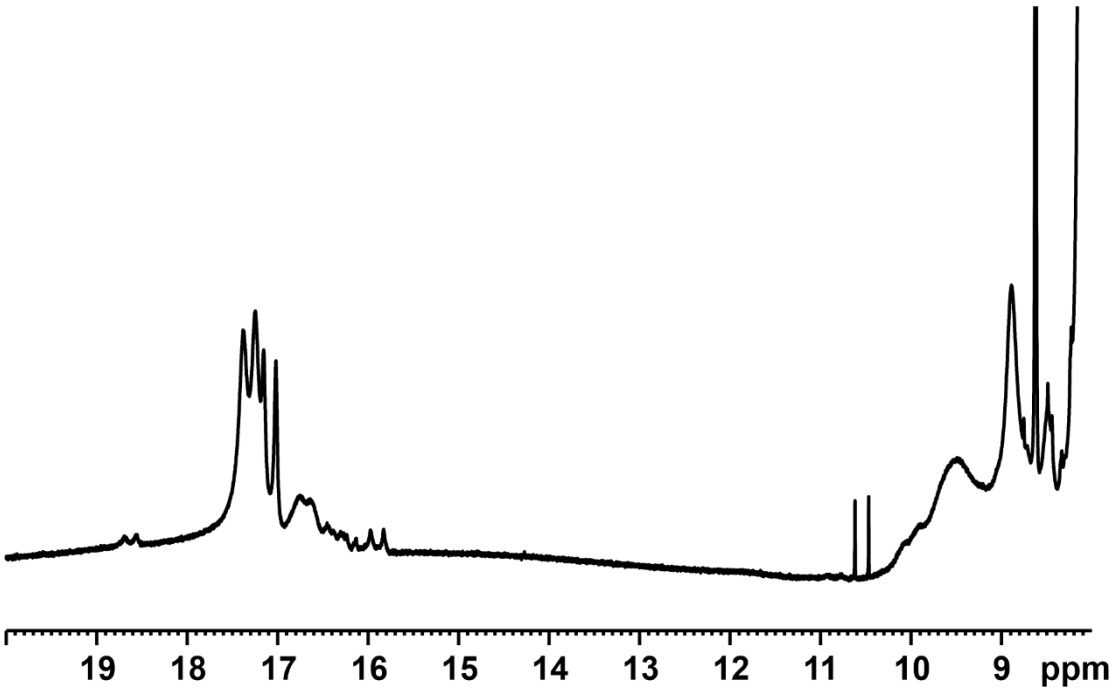

Hydrogen bond area of the ^{1}H-spectrum of the ternary complex of 1d/2e/HE 3b (1:1:1 stoichiometry, 600MHz, CD_2Cl_2, 180K).

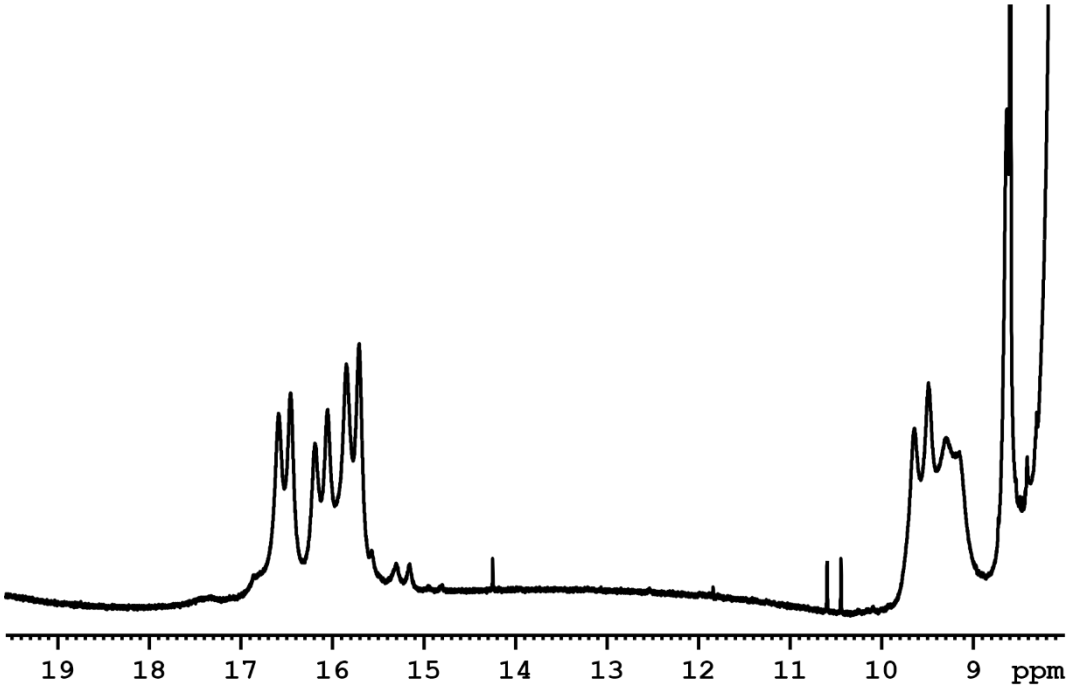

Hydrogen bond area of the ^{1}H-spectrum of the ternary complex of 1e/2e/HE 3b (1:1:1 stoichiometry, 600MHz, CD_2Cl_2, 180K).

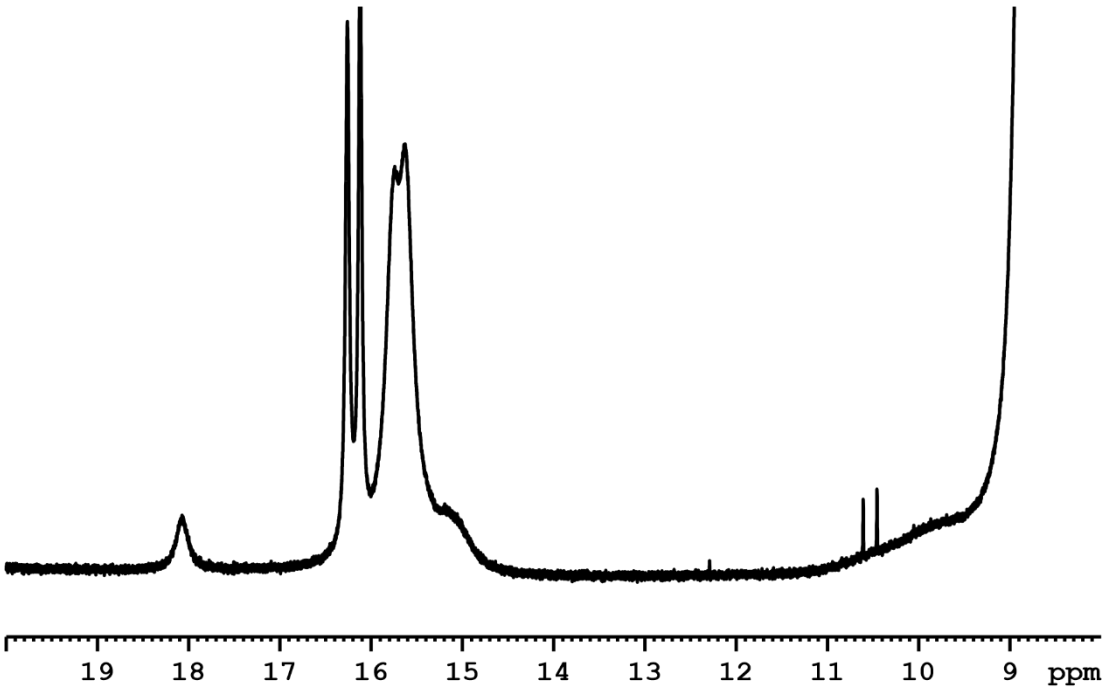

Hydrogen bond area of the ^{1}H-spectrum of the ternary complex of 1a/2f/HE 3b (1:1:1 stoichiometry, 600MHz, CD_2Cl_2, 180K).

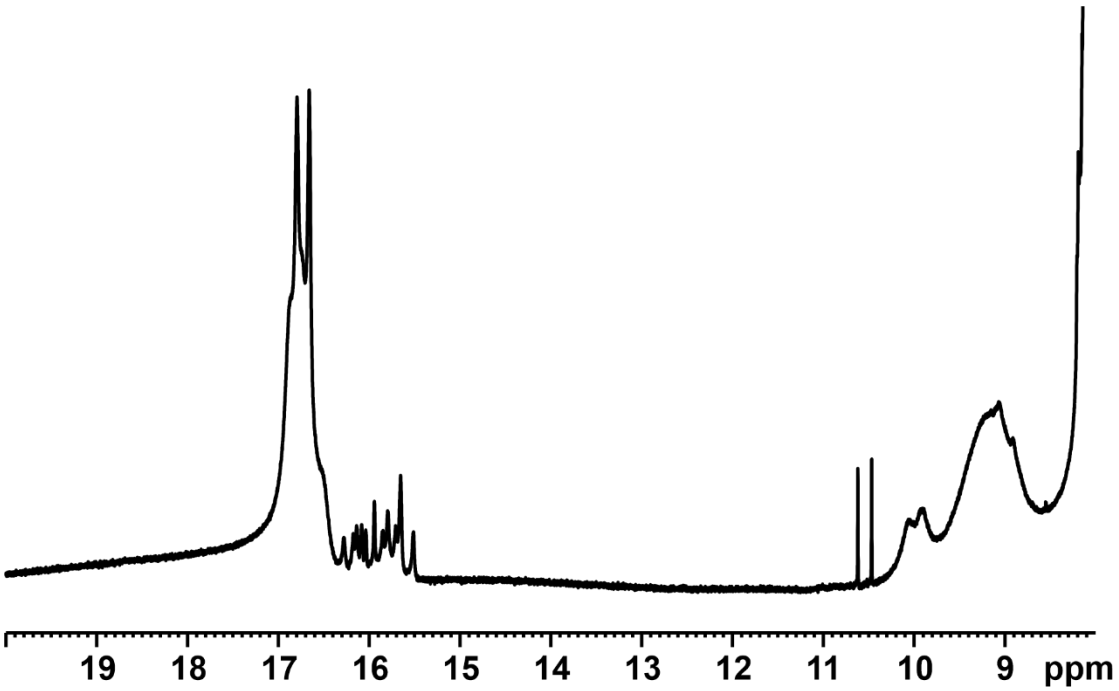

Hydrogen bond area of the ^{1}H-spectrum of the ternary complex of 1d/2f/HE 3b (1:1:1 stoichiometry, 600MHz, CD_2Cl_2, 180K).

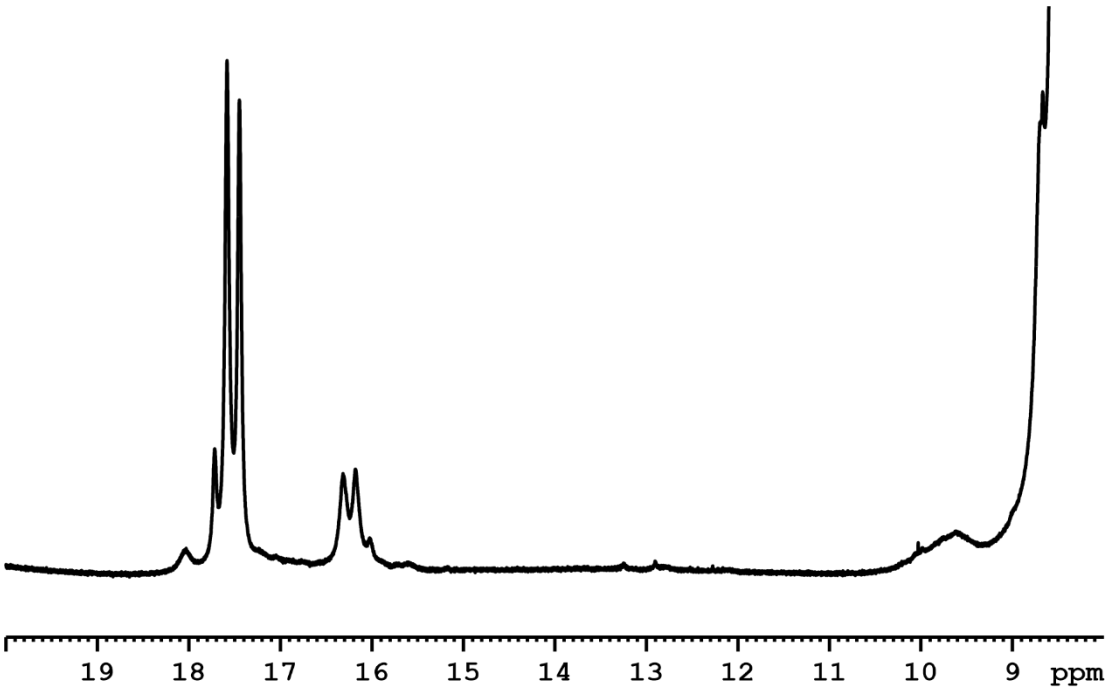

Hydrogen bond area of the ^{1}H-spectrum of the ternary complex of 1a/2g/HE 3b (1:1:1 stoichiometry, 600MHz, CD_2Cl_2, 180K).

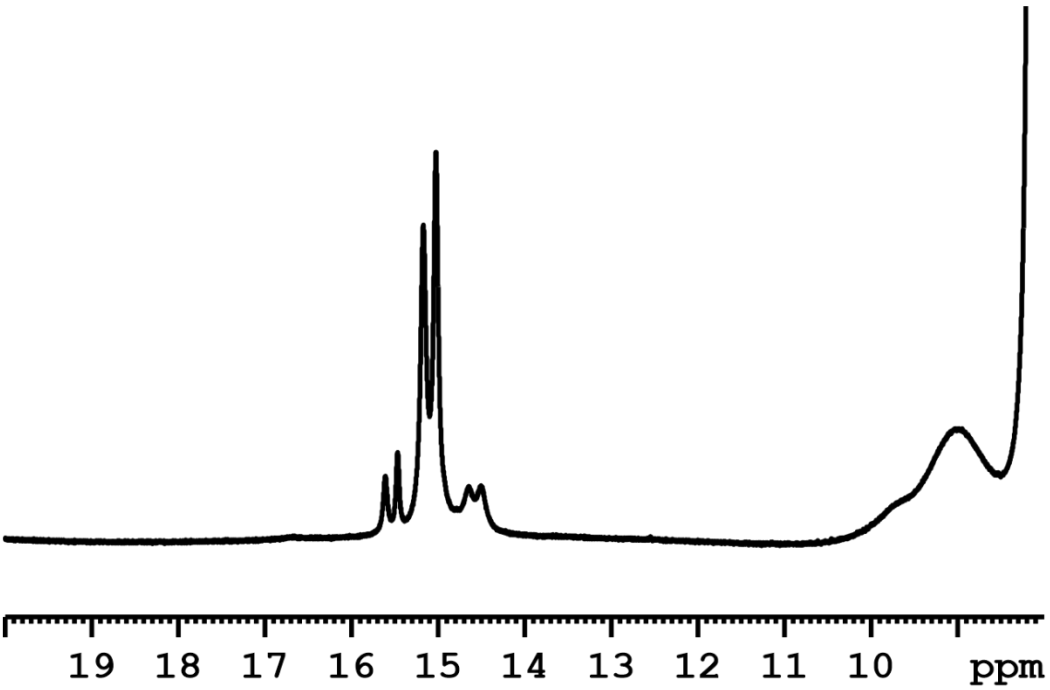

Hydrogen bond area of the ^{1}H-spectrum of the ternary complex of 1f/2a/HE 3b (1:1:1 stoichiometry, 600MHz, CD_2Cl_2, 180K).

2.6.11.2. NMR Spectra of TRIFP 1a/2a/HE 3b

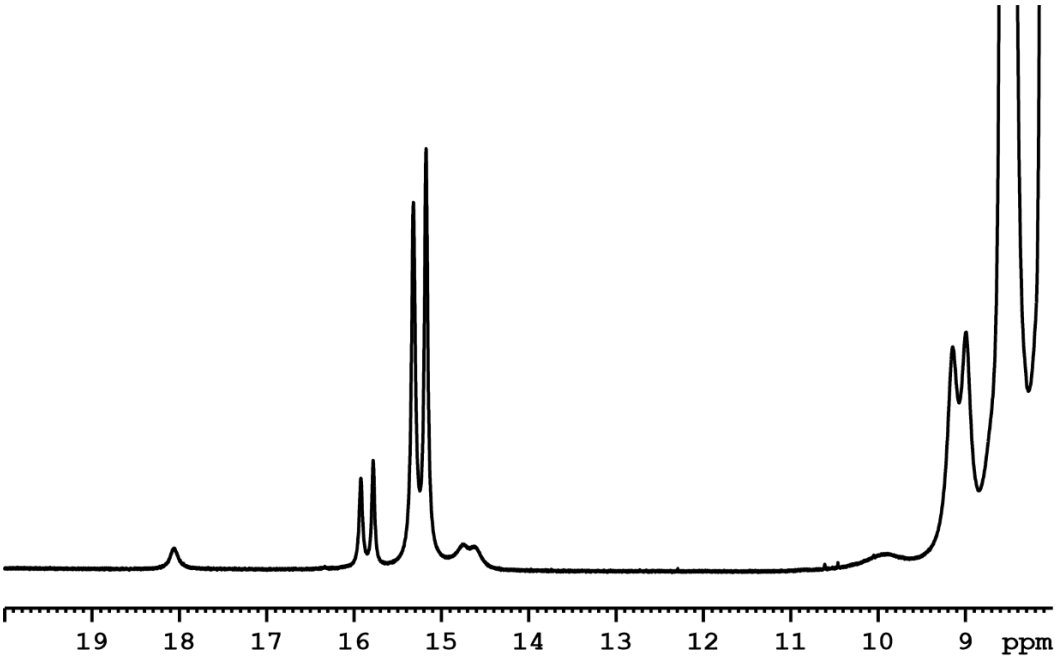

Hydrogen bond area of the ^{1}H-spectrum of the ternary complex of TRIFP 1a/2a/HE 3b (1:1:1 stoichiometry, 600MHz, CD_2Cl_2, 180K).

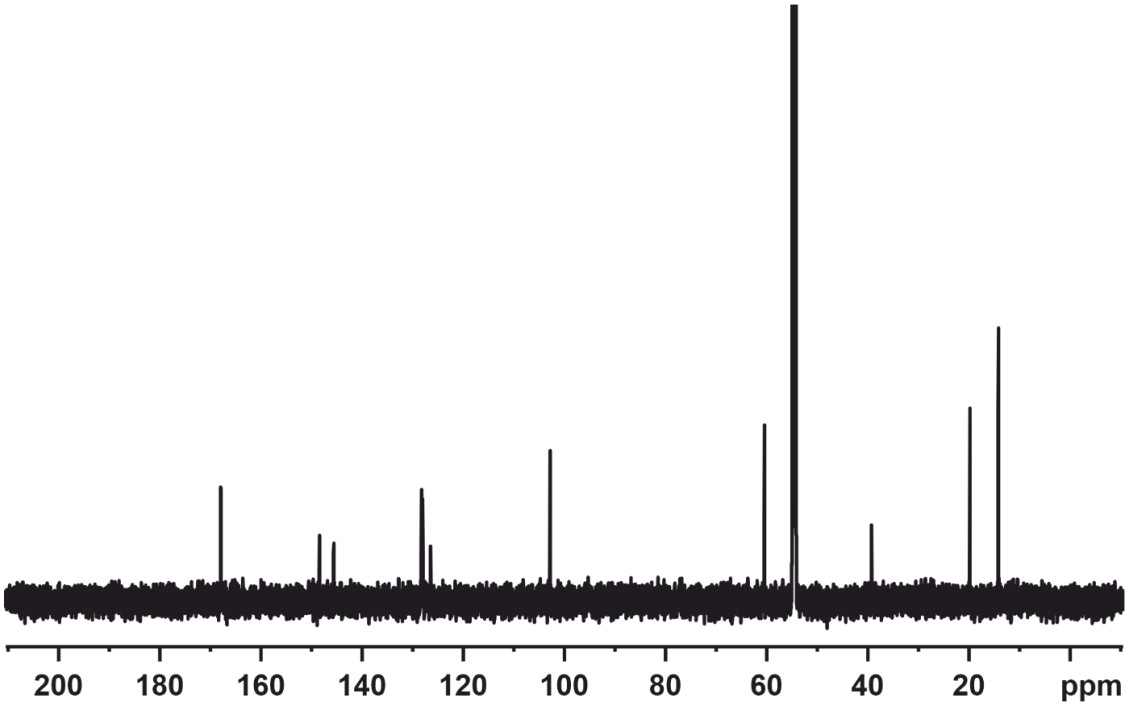

^{13}C-spectrum of the ternary complex of TRIFP 1a/2a/HE 3b (1:1:1 stoichiometry, 600MHz, CD_2Cl_2, 180K).

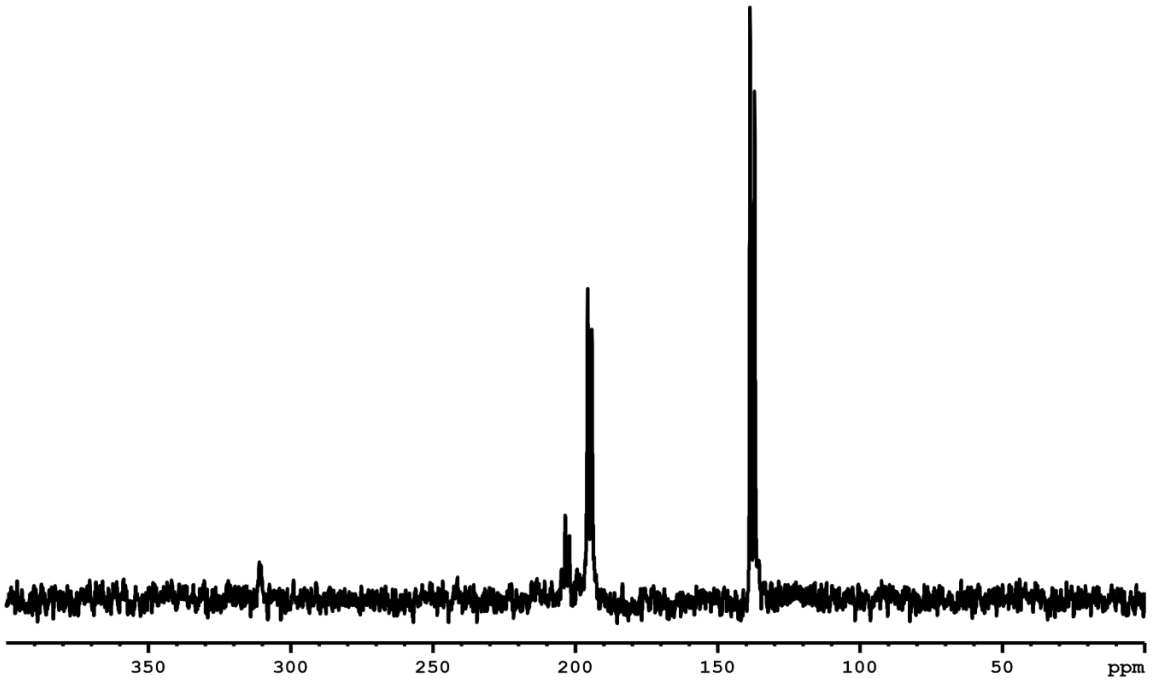

^{15}N-spectrum of the ternary complex of TRIFP 1a/2a/HE 3b (1:1:1 stoichiometry, 600MHz, CD_2Cl_2, 180K).

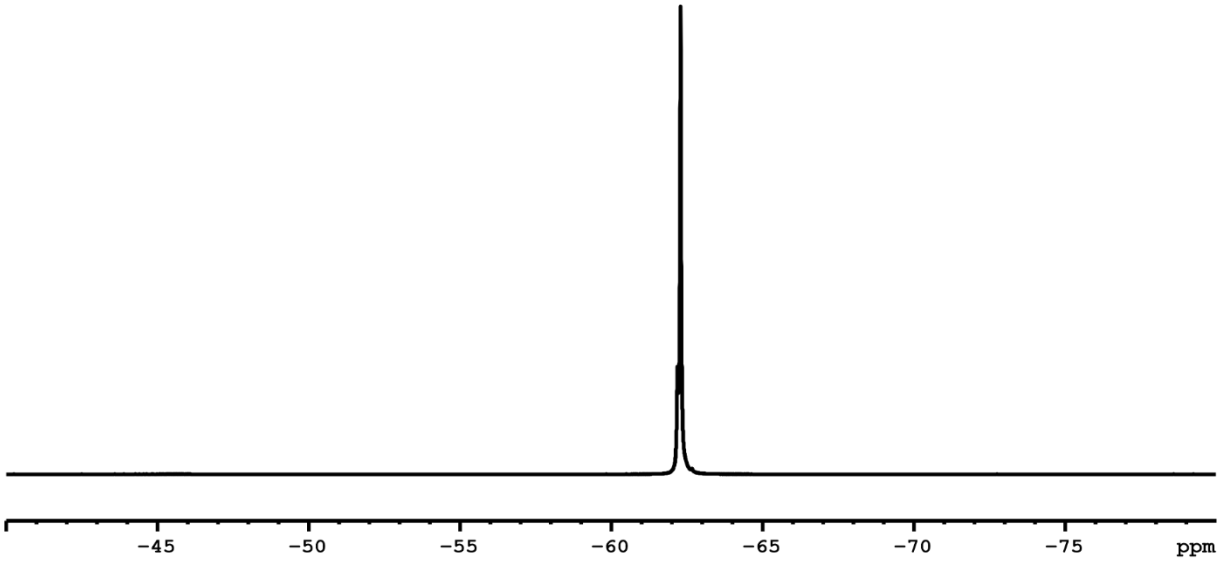

^{19}F-spectrum of the ternary complex of TRIFP 1a/2a/HE 3b (1:1:1 stoichiometry, 600MHz, CD_2Cl_2, 180K).

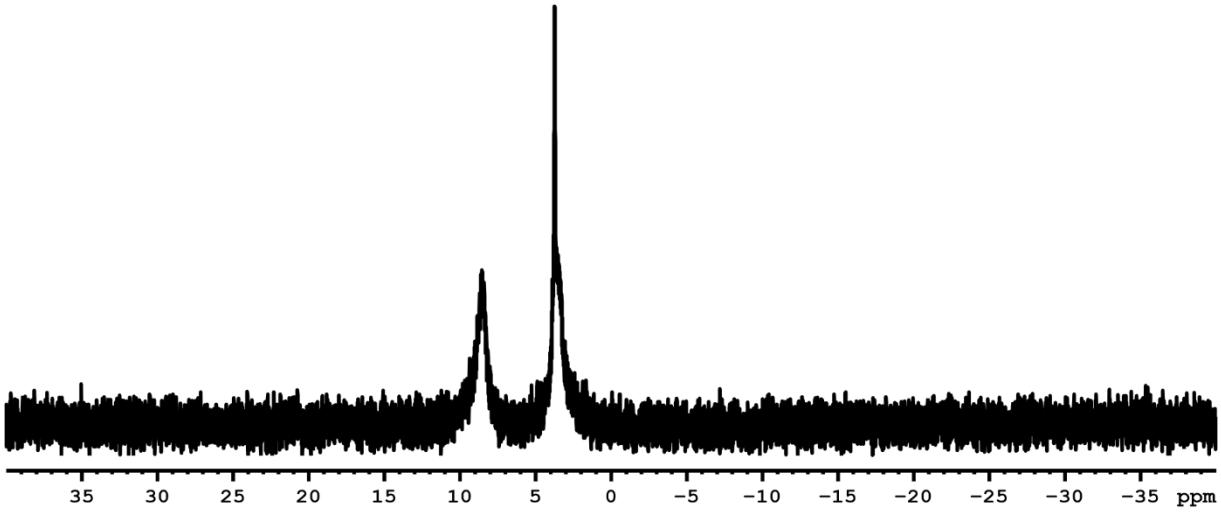

^{31}P-spectrum of the ternary complex of TRIFP 1a/2a/HE 3b (1:1:1 stoichiometry, 600MHz, CD_2Cl_2, 180K).

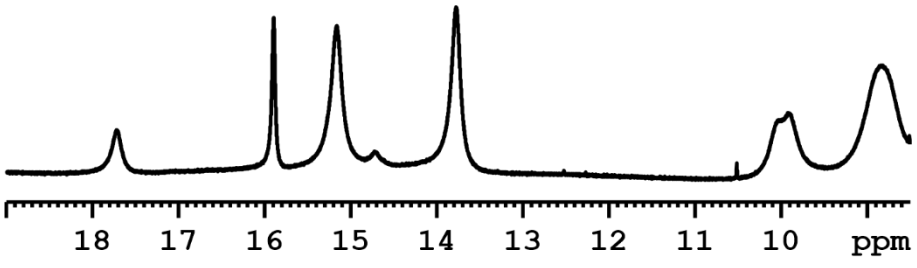

Hydrogen bond area of the ^{1}H-spectrum of the ternary complex of TRIFP 1a/2a/HE 3b (1:1:1 stoichiometry, 600MHz, CD_2Cl_2, 180K). Neither imine 2a nor HE 3b are ^{15}N-labeled. No doublets are observed anymore, confirming all species bond to either 2a or HE 3b.

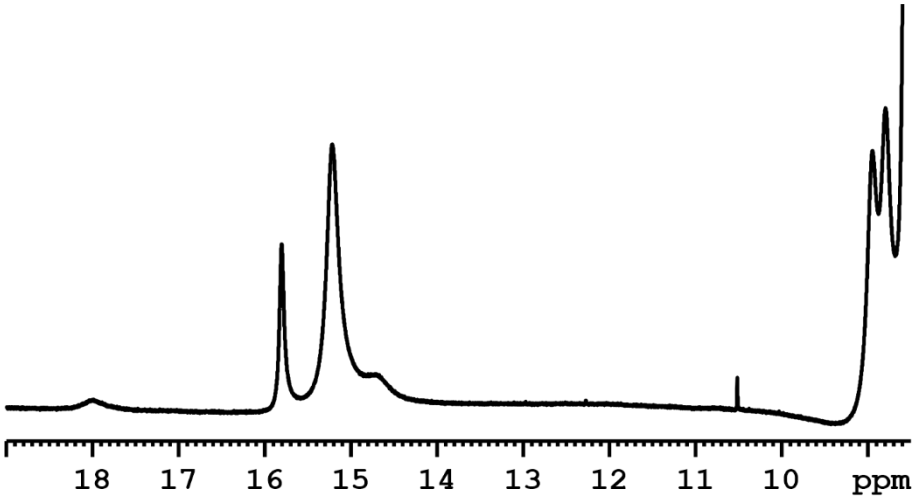

Hydrogen bond area of the ^{1}H-spectrum of the ternary complex of TRIFP 1a/2a/HE 3b (1:1:1 stoichiometry, 600MHz, CD_2Cl_2, 180K). Imine 2a is not ^{15}N-labeled while HE 3b is ^{15}N-labeled. No doublets are observed anymore for all imine 2a hydrogen-bonded species, while hydrogen-bonded HE 3b species still appear as a doublet.

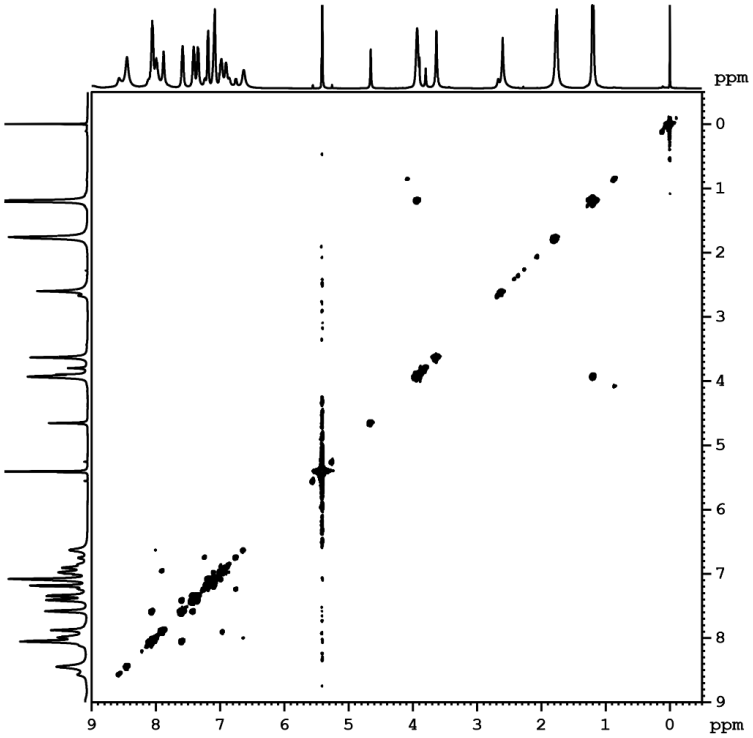

^{1}H,^{1}H-COSY of the ternary complex of TRIFP 1a/2a/HE 3b (1:1:1 stoichiometry, 600MHz, CD_2Cl_2, 180K).

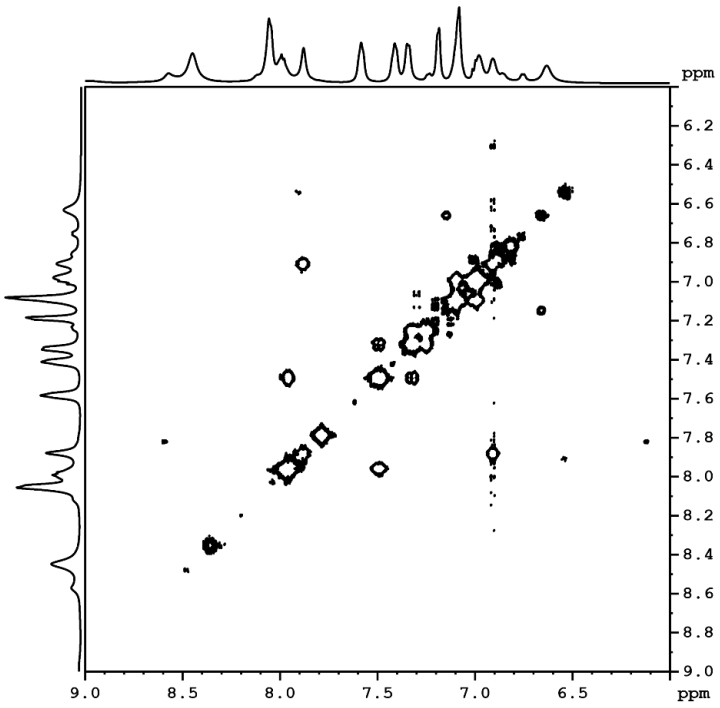

Aromatic region of $^{1}H,^{1}H$-COSY of the ternary complex of TRIFP 1a/2a/HE 3b (1:1:1 stoichiometry, 600MHz, CD_2Cl_2, 180K).

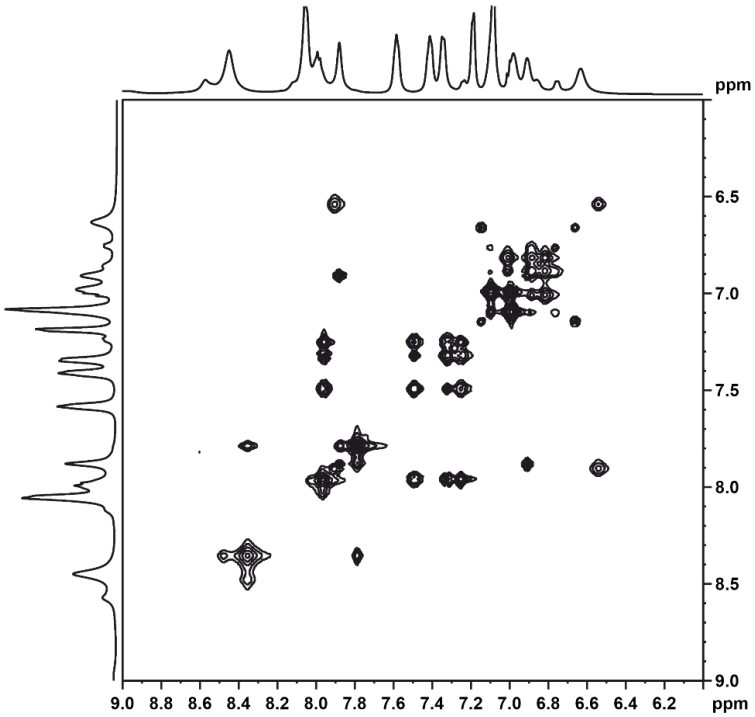

Aromatic region of $^{1}H,^{1}H$-TOCSY of the ternary complex of TRIFP 1a/2a/HE 3b (1:1:1 stoichiometry, 600MHz, CD_2Cl_2, 180K).

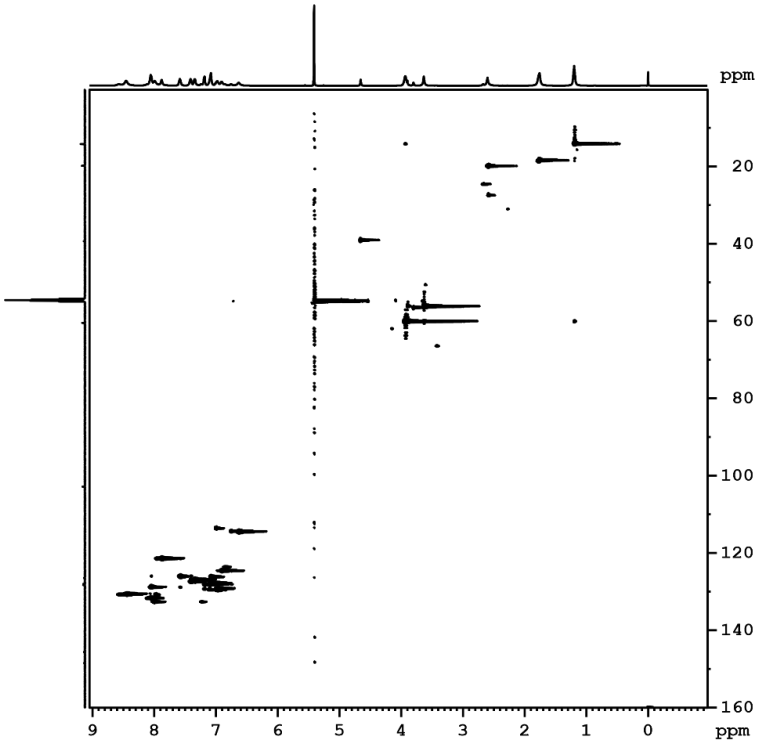

$^{1}H,^{13}C$-HSQC of the ternary complex of TRIFP 1a/2a/HE 3b (1:1:1 stoichiometry, 600MHz, CD_2Cl_2, 180K).

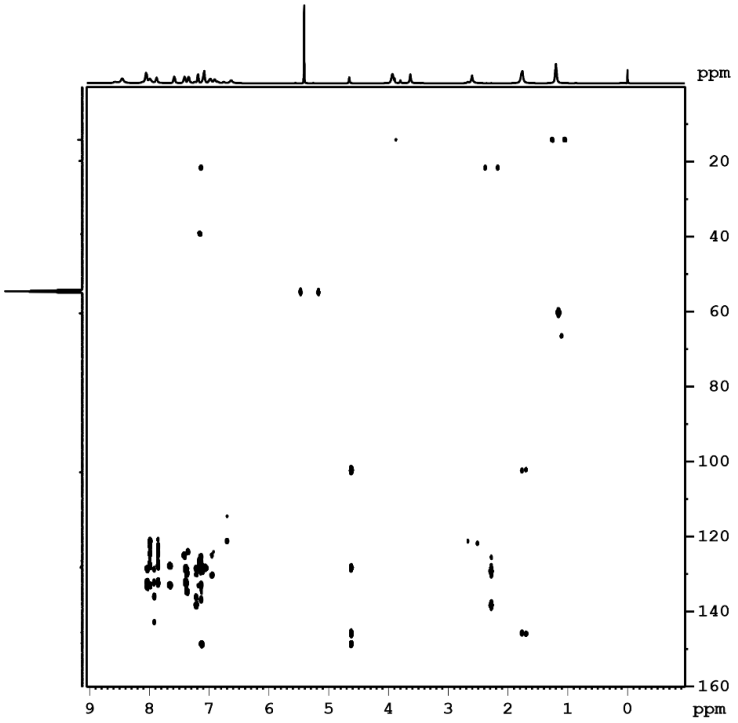

$^{1}H,^{13}C$-HMBC of the ternary complex of TRIFP 1a/2a/HE 3b (1:1:1 stoichiometry, 600MHz, CD_2Cl_2, 180K).

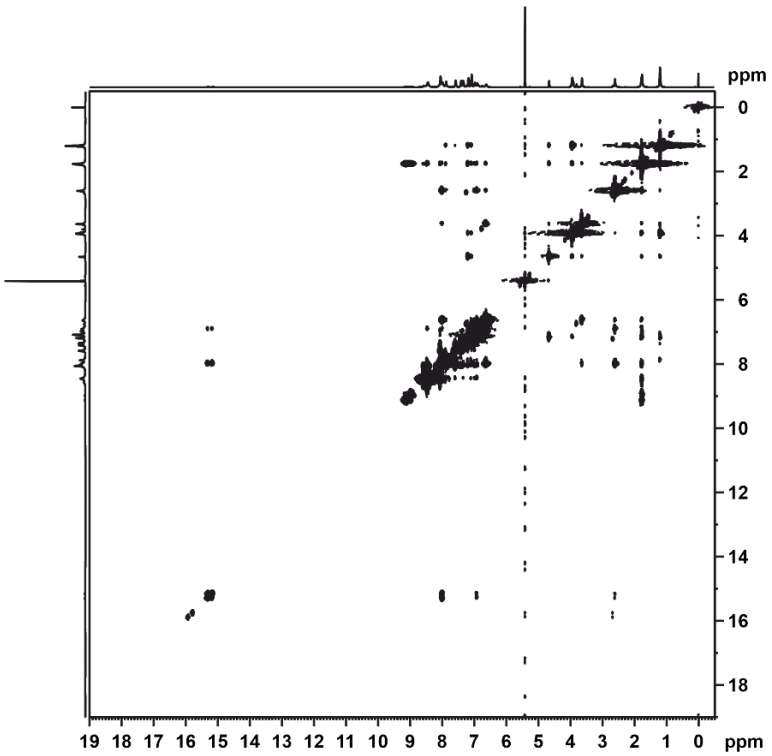

^{1}H,^{1}H-NOESY of the ternary complex of TRIFP 1a/2a/HE 3b (1:1:1 stoichiometry, 600MHz, CD_2Cl_2, 180K).

2.6.11.3. NMR Spectra of TRIFP 1a/*E*-2a/HE 3b

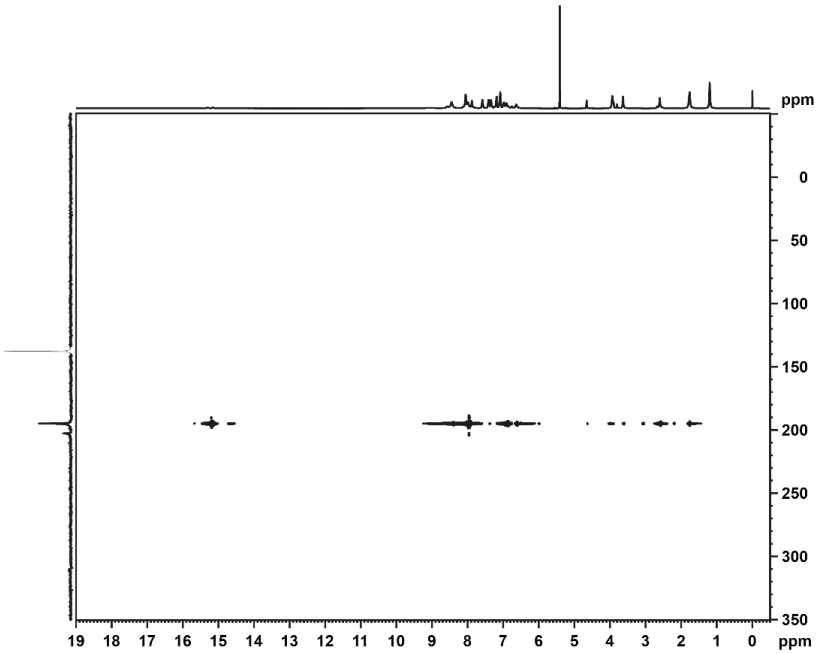

^{1}H,^{15}N-HSQC-NOESY of the ternary complex of TRIFP 1a/E-2a/HE 3b with a mixing time of 0.03 ms (1:1:1 stoichiometry, 600MHz, CD_2Cl_2, 180K).

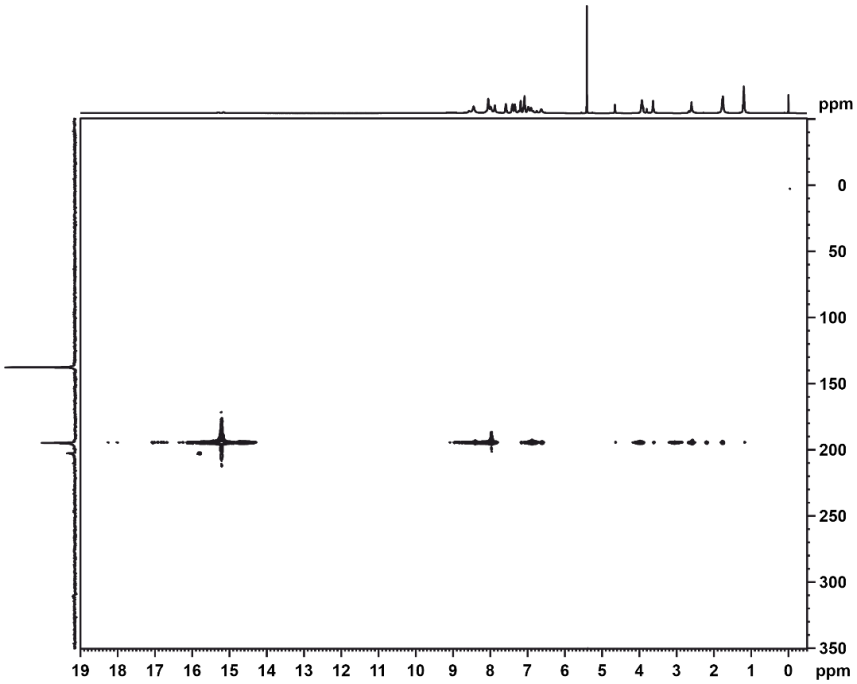

^{1}H,^{15}N-HSQC-NOESY of the ternary complex of TRIFP 1a/E-2a/HE 3b with a mixing time of 0.03 ms (1:1:1 stoichiometry, 600MHz, CD_2Cl_2, 180K).

2.6.11.4. NMR Spectra of OMe-CPA 1b/2a/HE 3b

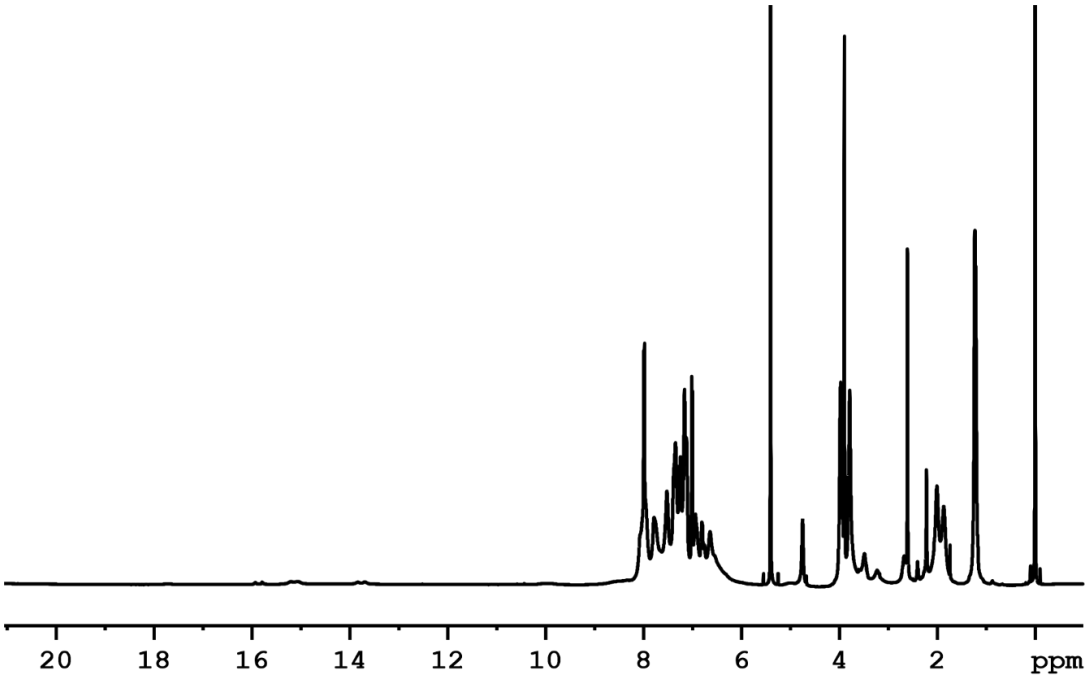

^{1}H-spectrum of the ternary complex of OMe-CPA 1b/2a/HE 3b (1:1:1 stoichiometry, 600MHz, CD_2Cl_2, 180K).

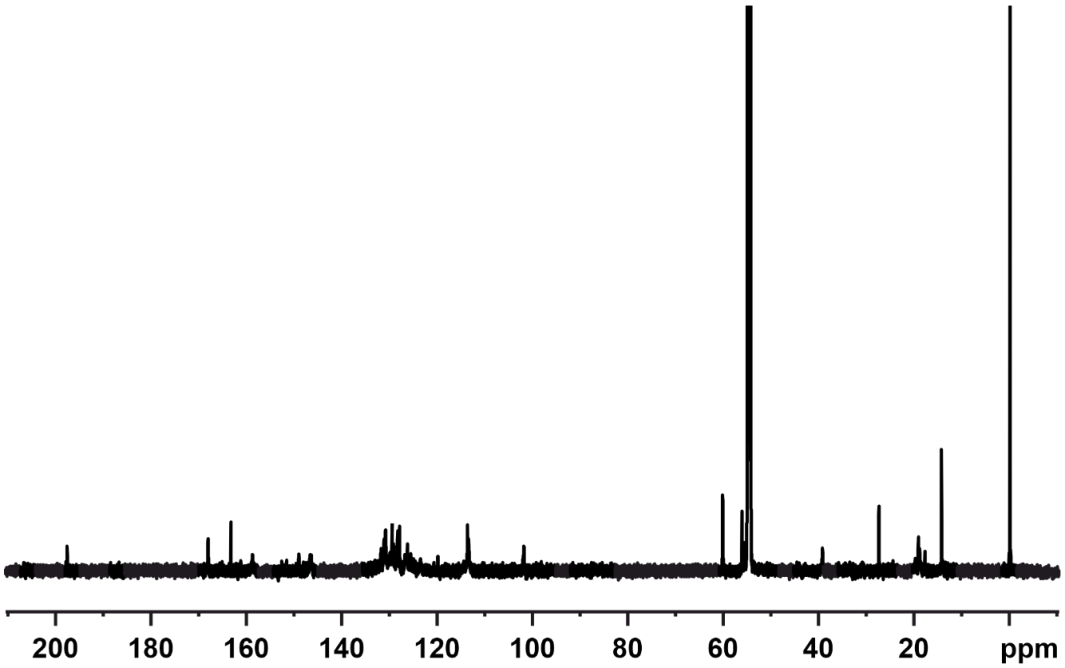

^{13}C-spectrum of the ternary complex of OMe-CPA 1b/2a/HE 3b (1:1:1 stoichiometry, 600MHz, CD_2Cl_2, 180K).

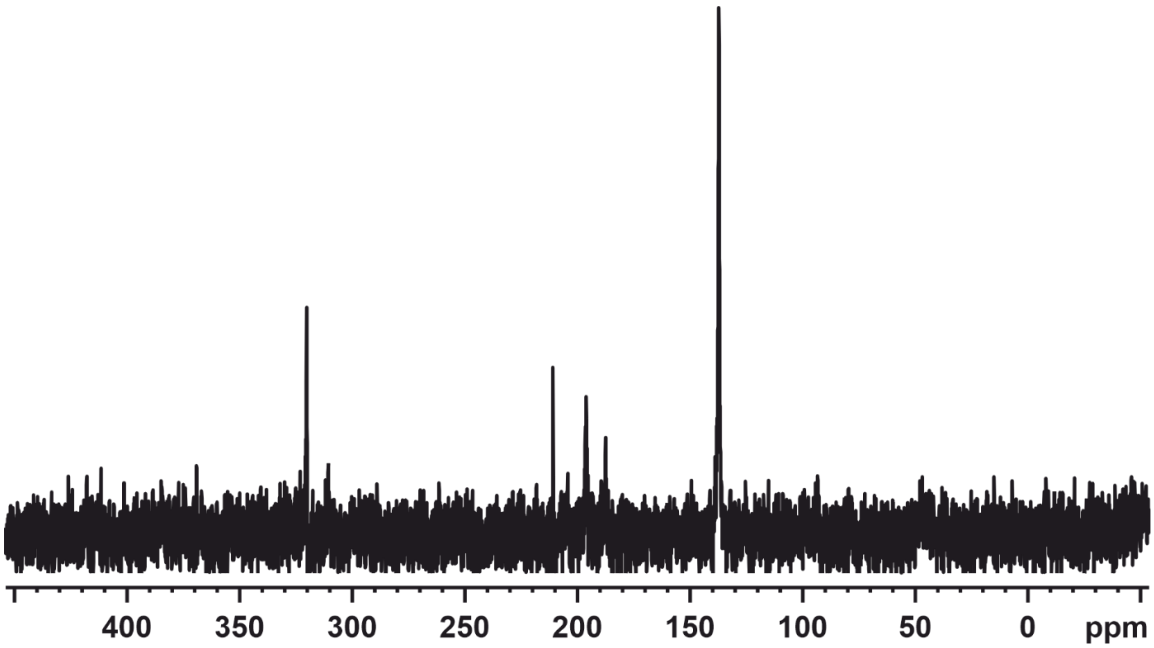

^{15}N-spectrum of the ternary complex of OMe-CPA 1b/2a/HE 3b (1:1:1 stoichiometry, 600MHz, CD_2Cl_2, 180K).

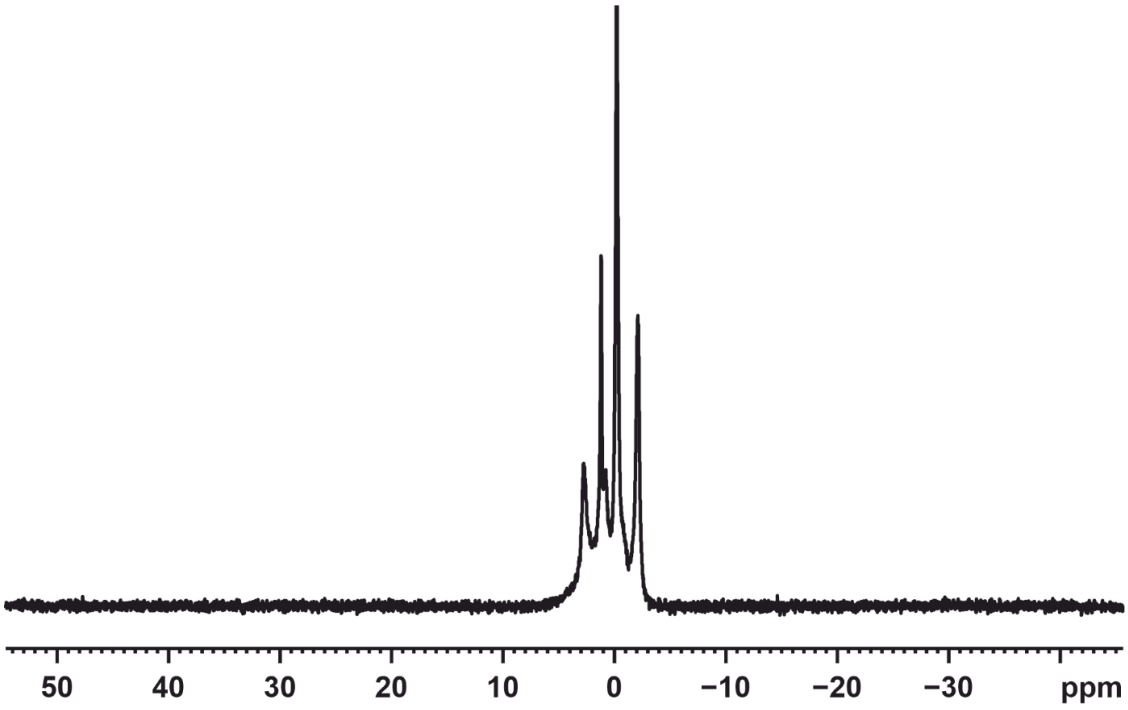

^{31}P-spectrum of the ternary complex of OMe-CPA 1b/2a/HE 3b (1:1:1 stoichiometry, 600MHz, CD_2Cl_2, 180K).

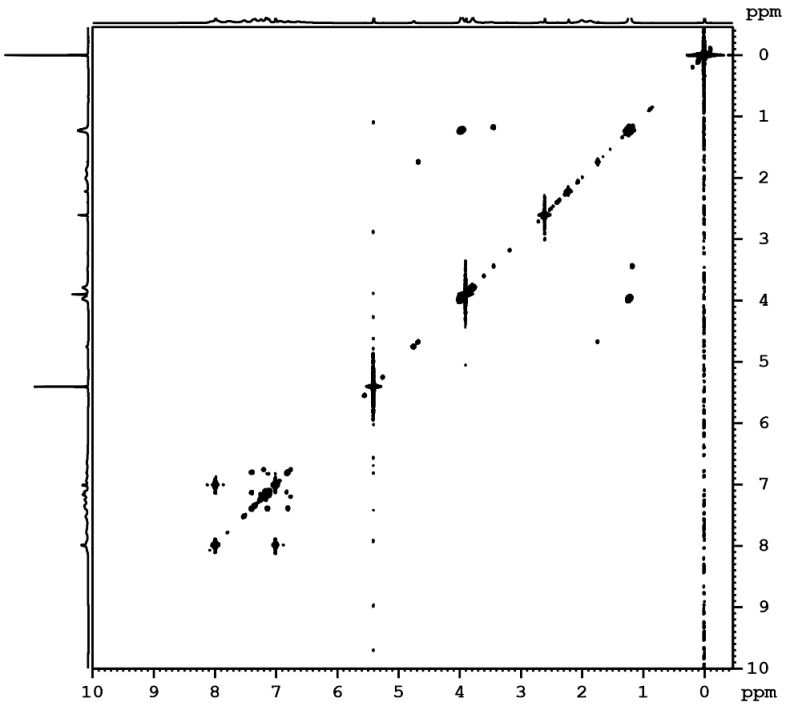

^{1}H,^{1}H-COSY-spectrum of the ternary complex of OMe-CPA 1b/2a/HE 3b (1:1:1 stoichiometry, 600MHz, CD_2Cl_2, 180K).

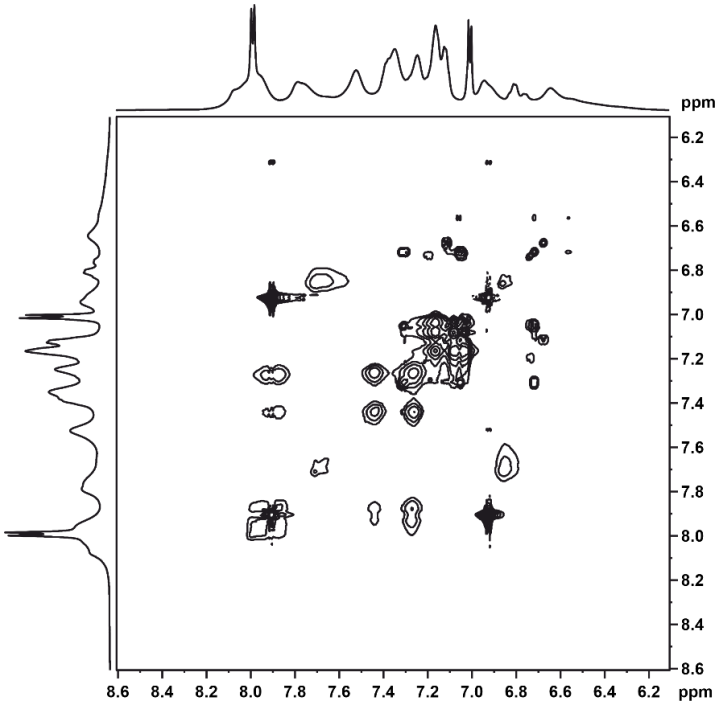

^{1}H,^{1}H-TOCSY-spectrum of the ternary complex of OMe-CPA 1b/2a/HE 3b (1:1:1 stoichiometry, 600MHz, CD_2Cl_2, 180K).

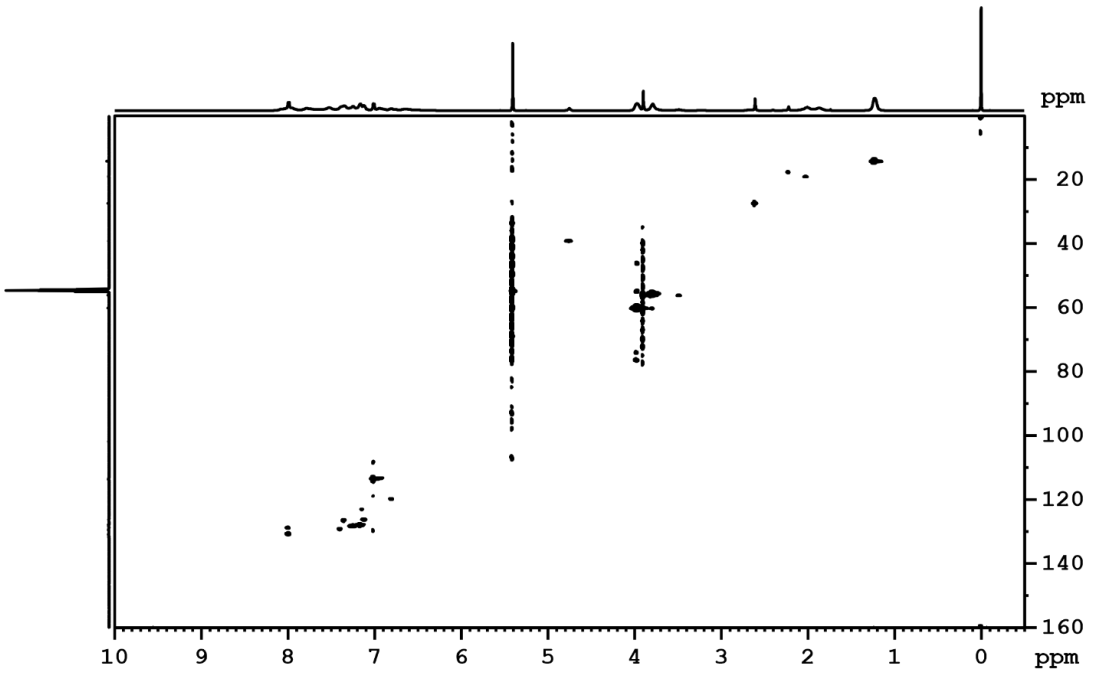

$^{1}H,^{13}C$-HSQC-spectrum of the ternary complex of OMe-CPA 1b/2a/HE 3b (1:1:1 stoichiometry, 600MHz, CD_2Cl_2, 180K).

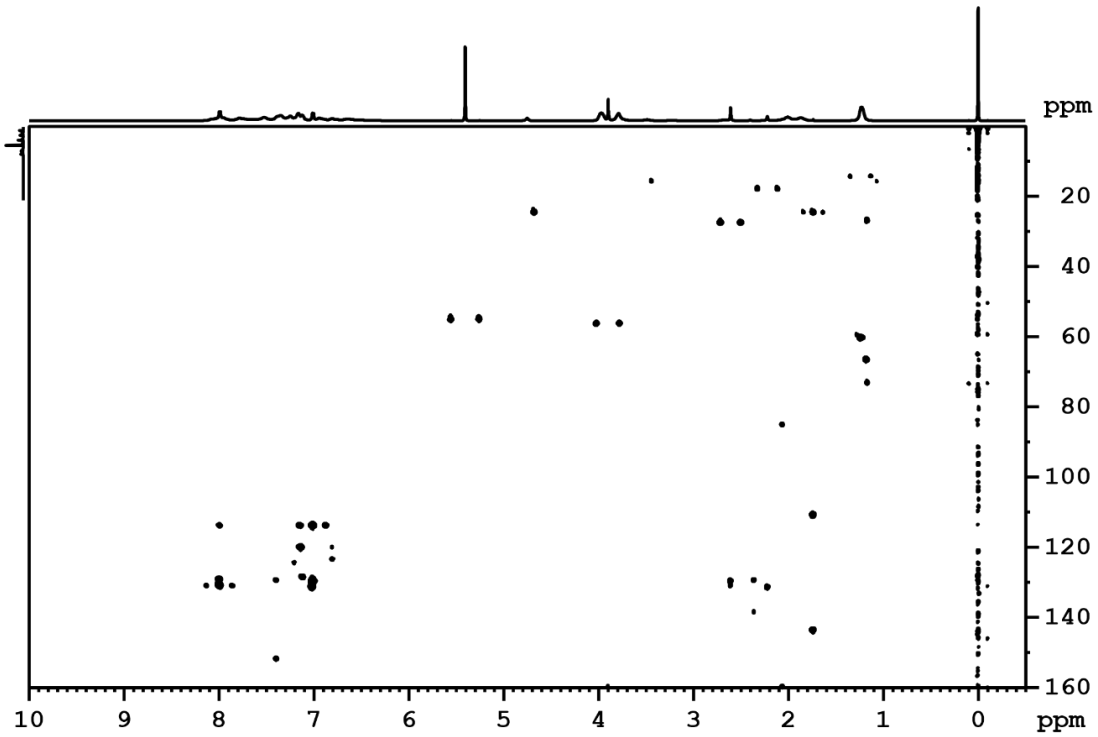

$^{1}H,^{13}C$-HMBC-spectrum of the ternary complex of OMe-CPA 1b/2a/HE 3b (1:1:1 stoichiometry, 600MHz, CD_2Cl_2, 180K).

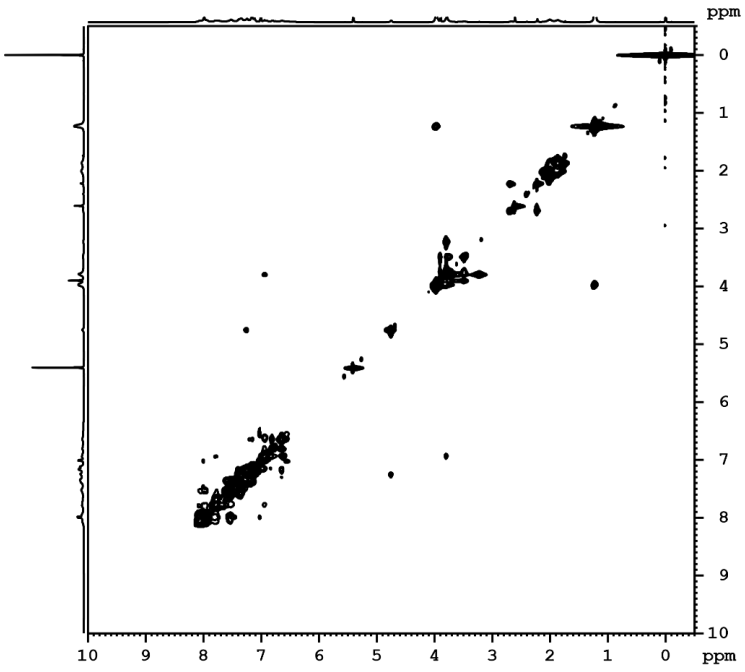

^{1}H,^{1}H-NOESY-spectrum of the ternary complex of OMe-CPA 1b/2a/HE 3b (1:1:1 stoichiometry, 600MHz, CD_2Cl_2, 180K).

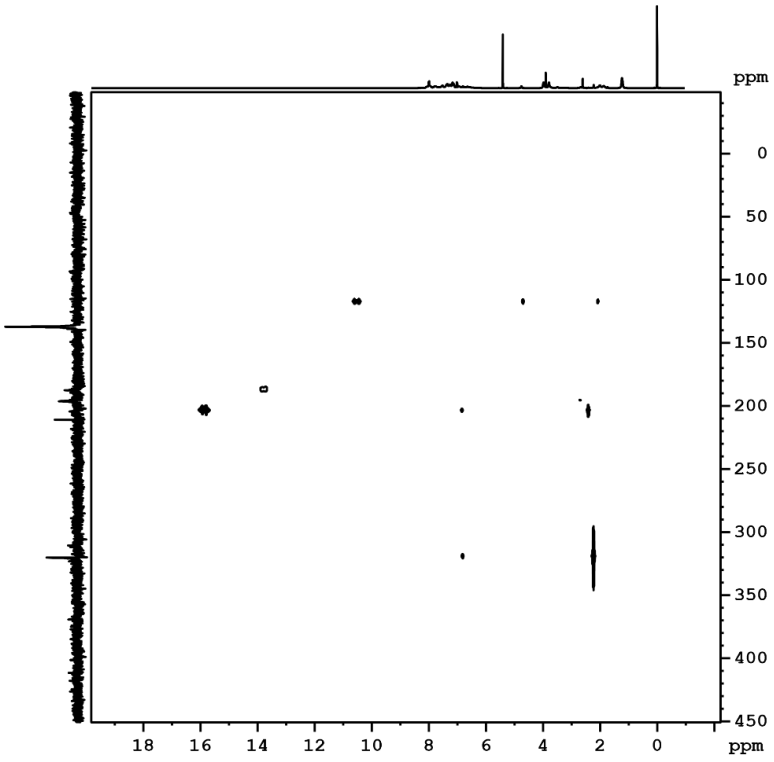

^{1}H,^{15}N-HMBC-spectrum of the ternary complex of OMe-CPA 1b/2a/HE 3b (1:1:1 stoichiometry, 600MHz, CD_2Cl_2, 180K).

2.6.12. Acknowledgements

This project was financed by the German Science Foundation (DFG; RTG 2620) project number 426795949.

2.6.13. References

[1] R. K. Harris, E. D. Becker, S. M. C. De Menezes, R. Goodfellow, P. Granger, *Solid State Nucl. Magn. Reson.* **2002**, *22*, 458–483.

[2] K. Taguchi, F. H. Westheimer, *J. Org. Chem.* **1971**, *36*, 1570–1572.

[3] P. Renzi, J. Hioe, R. M. Gschwind, *J. Am. Chem. Soc.* **2017**, *139*, 6752–6760.

[4] N. Sorgenfrei, J. Hioe, J. Greindl, K. Rothermel, F. Morana, N. Lokesh, R. M. Gschwind, *J. Am. Chem. Soc.* **2016**, *138*, 16345–16354.

[5] J. Gramüller, M. Franta, R. M. Gschwind, *J. Am. Chem. Soc.* **2022**, *144*, 19861–19871.

[6] Q. Li, Y. Li, J. Wang, Y. Lin, Z. Wei, H. Duan, Q. Yang, F. Bai, Y. Li, *New J. Chem.* **2018**, *42*, 827–831.

[7] M. Žabka, R. M. Gschwind, *Chem. Sci.* **2021**, *12*, 15263–15272.

[8] K. Rothermel, M. Melikian, J. Hioe, J. Greindl, J. Gramüller, M. Žabka, N. Sorgenfrei, T. Hausler, F. Morana, R. M. Gschwind, *Chem. Sci.* **2019**, *10*, 10025–10034.

[9] N. Lokesh, J. Hioe, J. Gramüller, R. M. Gschwind, *J. Am. Chem. Soc.* **2019**, *141*, 16398–16407.

[10] M. Melikian, J. Gramüller, J. Hioe, J. Greindl, R. M. Gschwind, *Chem. Sci.* **2019**, *10*, 5226–5234.

[11] D. Jansen, J. Gramüller, F. Niemeyer, T. Schaller, M. C. Letzel, S. Grimme, H. Zhu, R. M. Gschwind, J. Niemeyer, *Chem. Sci.* **2020**, *11*, 4381–4390.

[12] S. Zerbe, O. Jurt, Applied NMR Spectroscopy for Chemists and Life Scientists, Wiley, **2013**.

[13] T. D. W. Claridge, HighResolution NMR Techniques in Organic Chemistry, Elsevier, **2016**.

[14] P. Kuzmič, Anal. Biochem. **1996**, 237, 260–273.

[15] A. Jerschow, N. Müller, Macromolecules **1998**, 31, 6573–6578.

[16] E. O. Stejskal, J. E. Tanner, J. Chem. Phys. **1965**, 42, 288–292.

[17] A. Macchioni, G. Ciancaleoni, C. Zuccaccia, D. Zuccaccia, Chem. Soc. Rev. **2008**, 37, 479–489.

[18] D. Zuccaccia, A. Macchioni, Organometallics **2005**, 24, 3476–3486.

[19] H. C. Chen, S. H. Chen, J. Phys. Chem. **1984**, 88, 5118–5121.

[20] D. Ben-amotz, K. G. Willis, **1993**, I, 7736–7742.

3. Dimeric Pathway in Chiral Phosphoric Acid Catalysis — A General Feature?

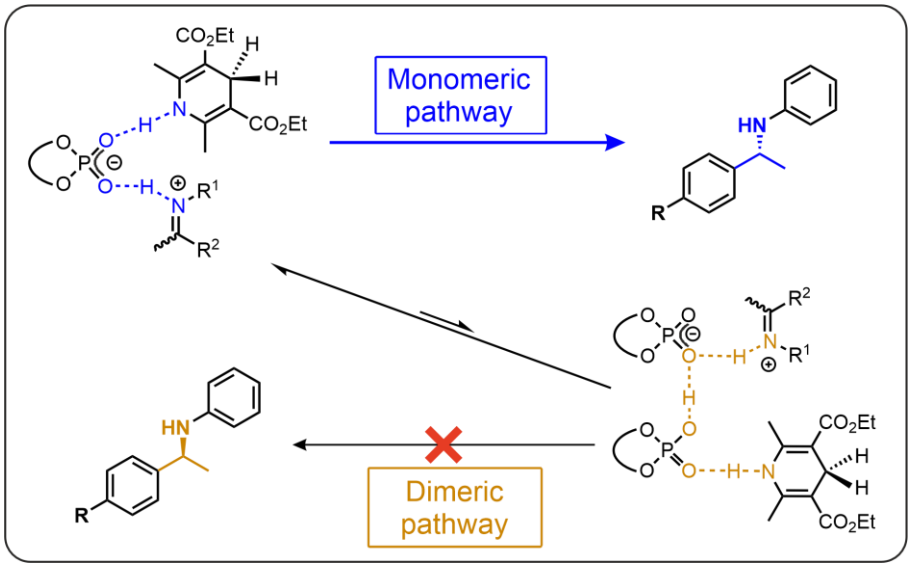

Maximilian Franta, Johannes Gramüller, Philipp Dullinger, Christian Scholtes, Simon Kaltenberger, Neal Deng, Prof. Dr. Donna Blackmond, Prof. Dr. Dominik Horinek, Prof. Dr. Ruth M. Gschwind

To be submitted

A) NMR measurements for steric and electronic trends were performed by Maximilian Franta. All HPLC measurements were performed by Maximilian Franta. The manuscript was mainly written by Maximilian Franta, assisted by Johannes Gramüller. B) NMR measurements regarding the dimeric pattern and system screening were performed by Johannes Gramüller and Maximilian Franta. C) All theoretical calculations were performed by Philipp Dullinger, in assistance of Prof. Dr. Dominik Horinek. D) All reactions were performed by Maximilian Franta and Christian Scholtes, assisted by Simon Kaltenberger. E) Non-Linear Effect studies were conducted by Neal Deng. Prof. Dr. Donna Blackmond contributed to interpretation of data. F) Prof. Dr. Ruth M. Gschwind contributed to conceptualization of the project, design of experiments, interpretation of data, writing and proof-reading of the manuscript and provided funding.

3.1. Abstract

Chiral phosphoric acids (CPA) have become a privileged catalyst type in organocatalysis, but the selection of the optimum catalyst is still challenging. Potentially hidden competing reaction pathways may limit the maximum stereoselectivities and the potential of prediction models. In studies of the CPA-catalyzed transfer hydrogenation of quinolines, two reaction pathways with inverse stereoselectivity were identified, which feature either one CPA or a hydrogen bond bridged dimer as active catalyst. In our effort to investigate whether this pathway is also active for classical imine CPA complexes, we conducted NMR measurements and DFT calculations which revealed the existence of dimeric intermediates. Additionally, several formation trends for the 2:1 dimeric species were elucidated by NMR spectroscopy. However, no influence on stereoselectivity was observed independent of temperature, concentration and catalyst loading. Thus, this study demonstrates that dimeric complexes seem to be a general structural feature in CPA catalysis at high catalyst concentrations and low temperatures. But the concentration of the 2:1 dimer under synthetic conditions is so low that only in the case of an extreme kinetic acceleration this dimeric pathway may affect the catalytic outcome at room temperature, which is not the case for the classical imines investigated here.

3.2. Introduction

Brønsted acid catalysis has become one of the central pillars in organocatalysis over the last decades due to its huge potential and versatility in organic asymmetric synthesis.[1–5] BINOL (1,1'-bi-2-naphthol) derived chiral phosphoric acids (CPAs) emerged as one of the most famous catalyst types in this field. After their initial report by Akiyama[6] and Terada,[7] various CPAs with different 3,3'-substituents were introduced by several groups[8–10] and adapted to a myriad of transformations.[11–18]

From these reactions, the transfer hydrogenation of imines with Hantzsch Ester (HE) was later established as model system for mechanistic investigations (see Figure 3.1). NMR measurements were key to investigate and assess the hydrogen bond assisted ion-pair CPA/imine intermediates. These experimental investigations allowed a better understanding of the reaction mechanisms by revealing transition states,[19] structures[20–22] and hydrogen bond strengths.[23,24] In our NMR studies we detected intermediates with one or two catalyst molecules.[24–26] Furthermore, Niemeyer et al. revealed that supramolecularly linked CPAs show cooperativity effects in the transformation of quinolines.[25] This raised the question, whether competing monomeric and dimeric reaction pathways may be a general feature in catalytic reactions with CPAs or even in Brønsted acid catalysis. In case monomeric and dimeric pathways provide different enantioselectivities, guidelines to switch on and off one of the pathways would allow to improve synthetic applications and mechanistic studies.

Besides experimental and spectroscopic investigations, computational studies have been key to a deeper understanding of the reactivity and stereoselectivity of CPA-catalyzed reactions.[27,28] Goodman et al. linked the stereoselectivity to two parameters reflecting the steric properties of the 3,3'-substituents and developed a model for predicting suitable CPAs based on reactant structures.[29,30] Independent studies of Sigman et al. established a data-driven prediction model to elucidate the influence of multiple parameters of the reagents on the stereoselectivity.[31–33] Nevertheless, despite the groundbreaking achievements of computations,[34] NMR measurements and other methods,[35] a simple and easy prediction of the optimal catalyst for each substrate/reagent combination remains still extremely challenging.

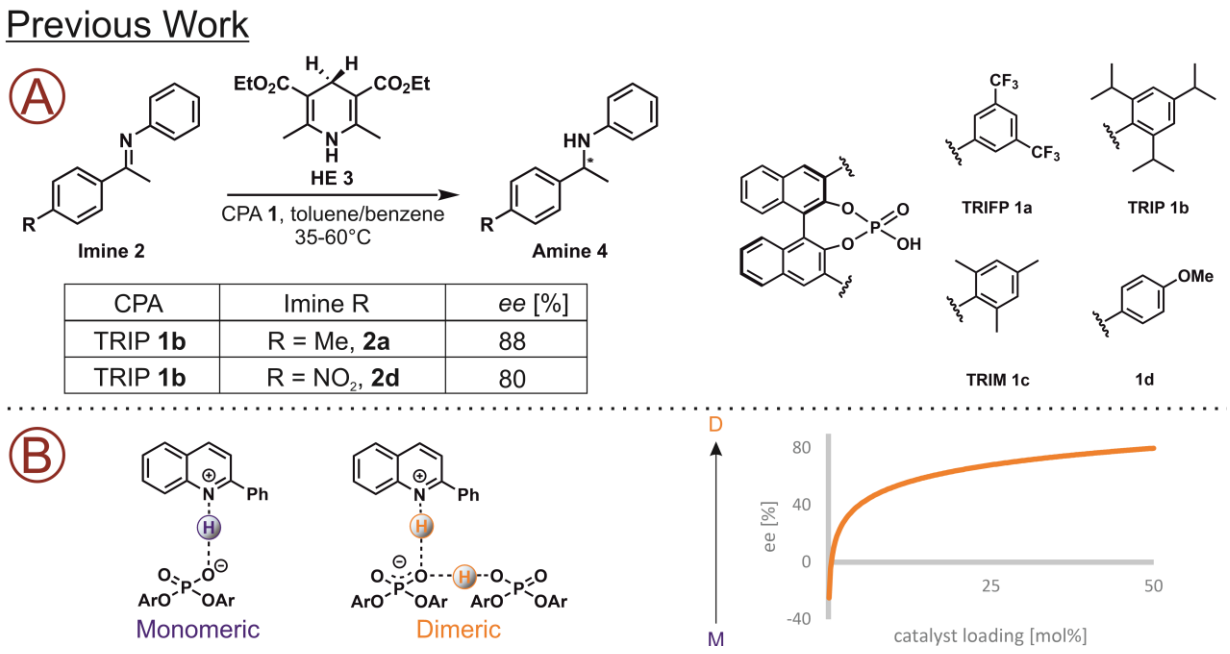

CPA	Imine R	*ee* [%]
TRIP **1b**	R = Me, **2a**	88
TRIP **1b**	R = NO_2, **2d**	80

Figure 3.1 Previously optimized CPA-catalyzed transfer hydrogenation of imines. At a temperature range of 35-60 °C, stereoselectivities of 80 to 93 % were achieved B) Monomeric CPA/substrate and dimeric CPA/CPA/substrate intermediates observed in our previous work with Niemeyer.[25] The competition of monomeric and dimeric reaction channel led to a strong dependence of stereoselectivity on the catalyst loading.

A potential explanation for the observed complexity of effects might be the overlooked competition of monomeric and dimeric pathways mentioned above. Here, two independent studies demonstrated that dimeric CPA complexes can significantly impact the stereoselectivity. On the one hand, Ishihara et al. discovered metal-ion bridged CPA dimers that lead to an inversed stereoselectivity for Mannich-type reactions.[36] On the other hand, Niemeyer et al. discovered a competing reaction pathway pathway for covalently interlocked CPA dimers as well as hydrogen bond bridged dimeric CPAs for the transfer hydrogenation of quinolines (see Figure 3.1B).[25,37] This observation was further corroborated by a recent study with a broader scope of covalently bonded CPA dimers that showcase the same influence on stereoselectivity as observed in prior studies.[38] In general a very low population of dimeric CPA/CPA/substrate intermediates is expected. However, the observed stereoselectivity/catalyst loading correlation revealed that the dimeric pathway leads to an inversion of the enantiomeric excess (ee) even at catalyst loadings <10 mol% typical for organocatalysis.[25] The minimal concentration of CPA/CPA/quinoline intermediates was additionally corroborated by our NMR investigations. The specific hydrogen bond pattern in the 1H-NMR spectra could be only detected at a CPA quinoline ratio of 2:1. To explain the strong effect of CPA/CPA/quinoline complex on the catalytic outcome, the tiny concentration must be

overcompensated by a strong kinetic preference of the dimeric pathway. Indeed, the respective DFT calculations of the twofold transfer hydrogenation of quinolines showed a kinetic dominance of the dimeric species in the stereoselective second reduction step.[25,39] Therefore, the dimeric pathway can take over the stereoselectivity of the reaction despite a very low population of the CPA/CPA/quinoline intermediate at <10 mol% catalyst loading. This observation raises the question, whether the dominance of the dimeric pathway is an exception for quinolines and metal-ion bridged catalysts or whether it is a general feature of CPA-catalyzed reactions.

Therefore, in this study, we investigated the competition between monomeric and dimeric pathway in the CPA-catalyzed transfer hydrogenation of imines. Therefore, a screening of 7 CPAs and 13 imines with NMR spectroscopy and studies of the enantiomeric excess by chiral HPLC were conducted. The NMR experiments revealed the existence of the 2:1 dimeric species at 180 K, however no influence on the *ee* was detected during various reaction conditions. Thus, the dimeric complexes seem to be a general structural feature of CPA-imine complexes at high catalyst concentrations and low temperatures but the extreme kinetic acceleration of the dimeric pathway necessary to affect the stereoselectivity in CPA catalyzed transfer hydrogenation seems to be valid only for special CPA/substrate combinations as observed with quinolines.

3.3. Results and Discussion

3.3.1. Model Systems

In order to check, whether 2:1 CPA/CPA/imine intermediates (further referred to as dimers) are a general feature in CPA catalysis we selected as model systems the most commonly used CPAs[1] TRIFP **1a** (3,3´-bis(3,5-bis-(trifluoromethyl)phenyl)-1,1´-binaphthyl-2,2´diyl hydrogen phosphate),[10,40] TRIP **1b** (3,3´-bis(2,4,6-triisopropylphenyl)-1,1´-binaphthyl-2,2´diyl hydrogen phosphate),[8] TRIM **1c** (3,3´-bis(2,4,6-trimethylphenyl)-1,1´-binaphthyl-2,2´diyl hydrogen phosphate) and TiPSY **1e** (3,3´-bis(triphenylsilyl)-1,1´-binaphthyl-2,2´diyl hydrogen phosphate)[41] as well as catalysts **1d,f,g** to probe the effects of varying steric and electronic properties (see Figure 3.2A). As substrates the imines **2a**-**2n** were chosen to test the influence of steric and electronic effects of the imine on the dimer formation (see Figure 3.2B).

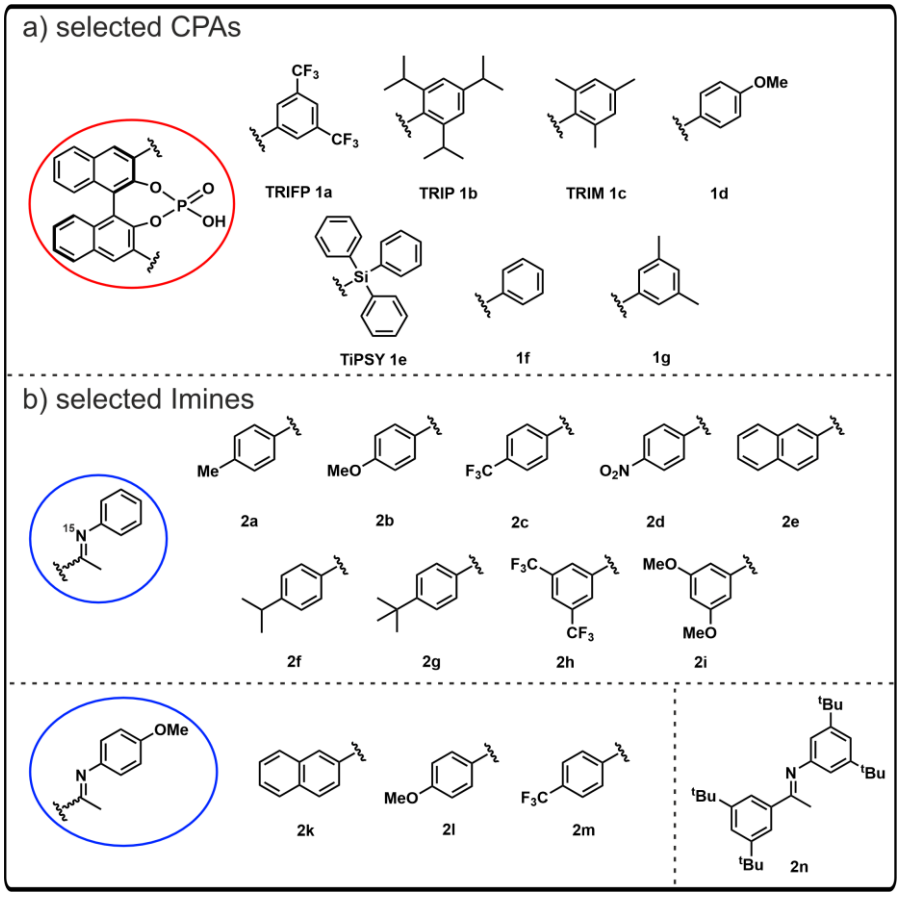

Figure 3.2 Structures of the investigated a) chiral phosphoric acids (CPAs) with different 3,3 – substituents and b) imines with different steric and electronic properties of the imine. A variety of combinations of these imines was investigated by NMR spectroscopy to elucidate trends of the dimer formation.

3.3.2. NMR Investigations on CPA/CPA/Imine Formation

To reveal the structure and mode of activation of the CPA/CPA/imine intermediates as well as factors favoring their formation, we performed a detailed NMR spectroscopic study. Already trace amounts of the dimer intermediates below the NMR detection limit could significantly affect the stereoselectivity with quinolines, while the best experimental conditions to investigate the dimeric species via NMR spectroscopy were found to be a 2:1 ratio of catalyst to quinoline.[25,39]

Therefore, also the NMR measurements for the CPA/imine combinations were conducted at a 2:1 ratio of catalyst and imine. Low temperature is the key to slow down exchange processes and to make the proton signals in the hydrogen bonds detectable, which are crucial for the differentiation of the monomeric and the dimeric intermediates.[21,25] Therefore, all NMR spectra were recorded in CD_2Cl_2 at -93 °C.

To our surprise we were able to clearly identify the 2:1 CPA/CPA/imine dimer for many CPA/imine combinations at these conditions (see SI 3.1 and 6.1). In addition, for some systems we even obtained well resolved spectra with reasonable line widths, which allowed for the first time ^{1}H, ^{1}H-NOESY, ^{1}H, ^{19}F-HOESY and relaxation dispersion measurements for CPA/CPA/imine dimers (see SI 3.6). In the following, the NMR spectroscopic identification and characterization of the dimeric intermediate is exemplarily discussed for **1a**/**1a**/**2b**.

In the hydrogen bond region[21] of the ^{1}H-spectrum the characteristic pattern of four complexes can be identified. Most prominent is the H-bond signal pattern for dimeric **1a**/**1a**/**2b** with an *E*-configured imine while the respective dimeric complex with a *Z*-imine is by far less populated (see Figure 3.3A, orange signals). Due to the ^{15}N labelling of the imine (I(^{15}N) = ½), the PO^{-}---H-N^{+} hydrogen bonds can be clearly identified via their doublet splitting, while the PO-H---OP hydrogen bonds of **1a**/**1a**/**2b** appear as singlets (both signals have a 1:1 integral ratio confirming the dimeric species). In addition, small amounts of the corresponding monomeric **1a**/**2b** species with both *E*- and *Z*-imine are observed (see Figure 3.3A, blue signals). The assignment of *E*- and *Z*-configurations in the dimeric complexes was based on ^{1}H, ^{1}H-NOESY spectra and characteristic exchange peaks with the previously investigated monomeric **1a**/**2b** complexes.[20]

Diffusion ordered spectroscopy (DOSY) measurements were performed and validated the assignment as dimeric species (for details see SI 3.6.5). ^{1}H, ^{1}H NOESY and ^{1}H, ^{19}F HOESY studies were conducted to shed light onto the potential structure of **1a**/**1a**/*E*-**2b** (see Figure 3.3B and SI 3.6.6). Furthermore, DFT calculations were performed on a TPSS/def2-SVP (def2/J) level of theory with implicit solvent (CPCM) as well as a D3BJ correction based on the previous DFT studies[25,39] and the observed NOE restraints (see SI 3.6 for details and references).

Similar to the monomeric **1a**/**2b** complexes showing one set of signals for two conformations in fast exchange on the NMR time scale, also for this dimeric species two conformations Type I, and Type II were found both matching the experimentally observed pattern of NOE/HOE contacts (see Figure 3.3B, red arrows). DFT pointed towards Type II as the more stable one (see SI 3.6). Relaxation dispersion $R_{1\rho}$ measurements corroborated the presence of a fast exchange process potentially between Type I and Type II (for details see SI 3.6).[42] In structure Type I both hydrogen bonds are directed to one oxygen atom of the central phosphoric acid while in Type II two oxygen atoms of the central CPA are involved. Furthermore, Type I offers a nucleophile binding site close to the imine which hypothetically would lead to the correct inverse product selectivity for the dimeric pathway. In Type II a reorganization would be necessary to enable the hydride transfer (see SI 3.6 for detailed discussion). The presented structures show that in the dimeric complexes both catalyst molecules together create the stereoinductive environment for the downstream transformation. Future theoretical calculations of these demanding systems with many degrees of freedom may be able to reveal which of the many potential transition state pathways is most probably active. These transition states may differ in the stacking of imine and Hantzsch ester (nucleophilic attack from top or bottom), *E*- or *Z*-imine configuration or hydrogen bonding motif (both H-bonds to one or two oxygen atoms, see Figure 3.3B).

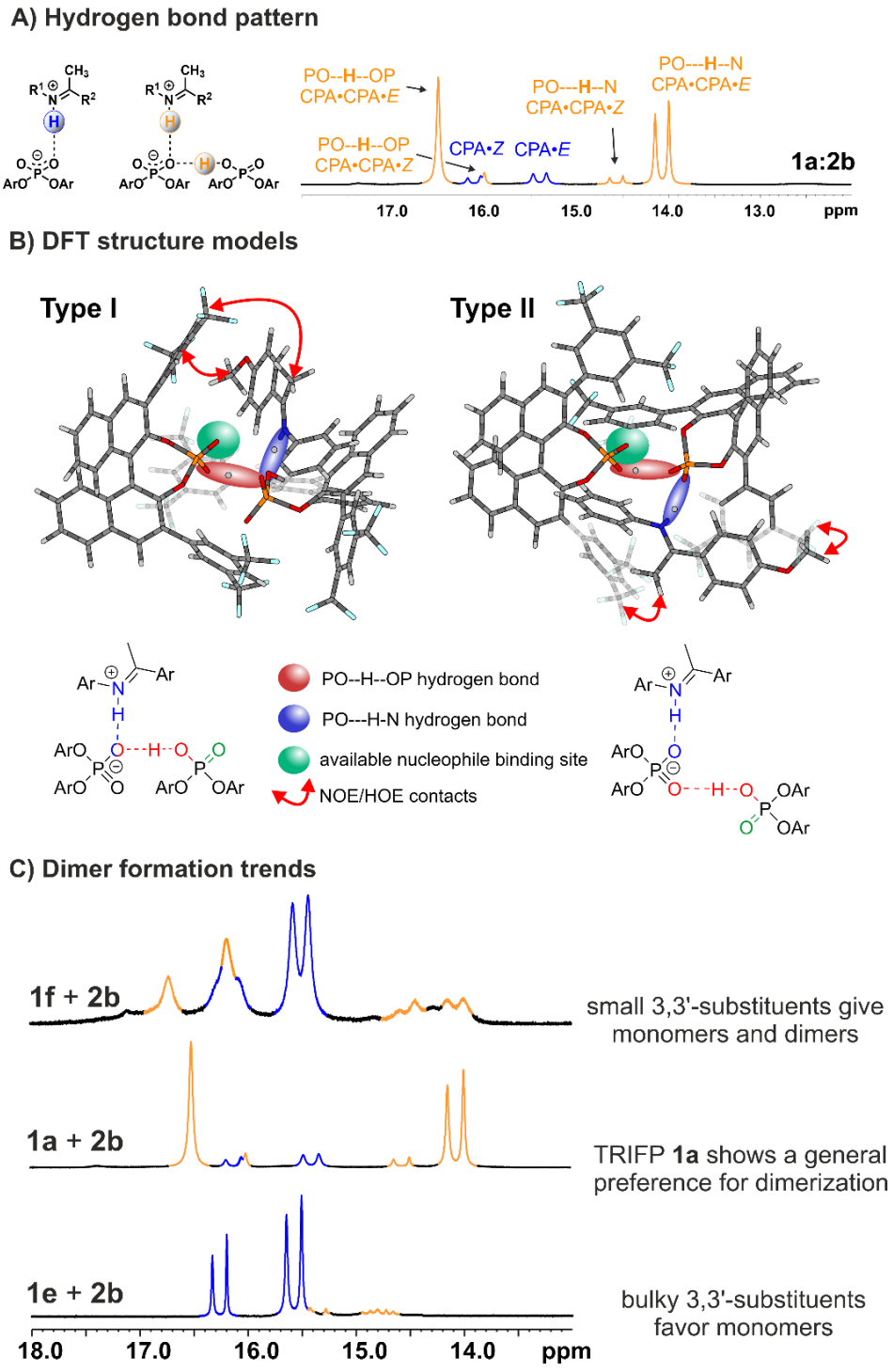

Figure 3.3 A) General hydrogen bond pattern observed for CPA/CPA/imine intermediates featuring PO⁻---H-N⁺ and PO-H---OP hydrogen bonds for the monomeric (blue) and dimeric (orange) complex. B) DFT structure models for the two different conformers of [1a/1a/E-2b] differing in the hydrogen bond situation and accessibility of the P=O hydrogen bond acceptor. DFT calculations were performed on a TPSS/def2-SVP (def2/J) level of theory with implicit solvent (CPCM) and the D3BJ correction based on the previous DFT studies[37] and the observed NOE restraints. C) ^{1}H-NMR spectra of the systems TiPSY 1e + 2b (bottom), TRIFP 1a + 2b (middle) and Phenyl-CPA 1f + 2b (2:1 stoichiometry, 50mM:25mM, CD_2Cl_2, 180K, 600MHz) show the steric influence of the 3,3'-substituents on dimer formation: Bulky substituents favour the formation of the monomers, small substituents give monomers and dimers, while for TRIFP 1a a general preference for dimer formation is observed.

Next the hydrogen bond properties of dimeric versus monomeric complexes were analyzed based on their NMR parameters. Both ^{1}H and ^{15}N chemical shifts of the dimeric species are clearly high field shifted and the $^{1}J_{NH}$ coupling constants are increased compared to the monomeric complexes with the same imine configuration (see SI 3.6.4). As demonstrated in previous H-Bond studies ,[24,25] this clearly reflects a stronger proton transfer onto the imine in the dimeric intermediate based on cooperativity effects introduced by the second PO-H---OP hydrogen bond.[41–43] As the proton transfer onto the substrate is directly linked to the substrate's electrophilicity/activation towards nucleophilic attacks, this might contribute to the dimeric reaction channel being kinetically dominant even at low catalyst loadings (<10 mol%). Overall the NMR investigations show that the CPA/CPA/imine dimer intermediates seem to be a self-assembled supramolecular version of List's IDPIs[44] or Gong's linked bisphosphoric acids[45] regarding the spatial confinement provided by two CPA units and the increased acidity. Additionally, the observed hydrogen bond cooperativity is a prime example of "Brønsted acid assisted Brønsted acid catalysis"[46,47] as also observed for other Brønsted acid or hydrogen bond catalysts[48–50] and is typical for enzyme catalysis.[51,52]

Next, the hydrogen bond properties of dimeric versus monomeric complexes were analyzed based on their NMR parameters. Both ^{1}H and ^{15}N chemical shifts of the dimeric species are clearly high field shifted and the $^{1}J_{NH}$ coupling constants are increased compared to the monomeric complexes with the same imine configuration (see SI 3.4). As demonstrated in previous H-Bond studies ,[23,24] this clearly reflects a stronger proton transfer onto the imine in the dimeric intermediate based on cooperativity effects introduced by the second PO-H---OP hydrogen bond.[43–45] As the proton transfer onto the substrate is directly linked to the substrate's electrophilicity/activation towards nucleophilic attacks, this might contribute to the dimeric reaction channel being kinetically dominant even at low catalyst loadings (<10 mol%). Overall the NMR investigations show that the CPA/CPA/imine dimer intermediates seem to be a self-assembled supramolecular version of List's IDPIs[46] or Gong's linked bisphosphoric acids[47] regarding the spatial confinement provided by two CPA units and the increased acidity. Additionally, the observed hydrogen bond cooperativity is a prime example of "Brønsted acid assisted Brønsted acid catalysis"[48,49] as also observed for other Brønsted acid or hydrogen bond catalysts[50–52] and is typical for enzyme catalysis.[53,54]

Next, we investigated, whether special structural features of the CPA and/or the imine favor the formation of the dimeric species. For this analysis, we used the characteristic signal pattern of the complexes in the hydrogen bond region. For TRIFP **1a** a general preference for dimer formation was observed for several imines (see SI 3.4), while for catalysts with bulkier 3,3'-substituents (TRIP **1b** and TiPSY **1e**) no preference for the respective dimeric species was detected (see Figure 3.3C and SI 3.6.4.1). For catalysts with smaller 3,3'-substituents (TRIM **1c**, **1d**, **1f**, **1g**) the CPA/CPA/imine dimers are populated but not the dominant species and additional hydrogen-bonded species were detected. In contrast, the steric properties of the imine had no significant influence on the dimer formation. Even for the extremely bulky imine **2n** featuring four *tert*-butyl groups, dimer formation was still observed with TRIFP **1a** (see SI 3.4.1). For imines with electron-withdrawing substituents such as **2c** and **2d,** a variety of hydrogen-bonded species was detected. For electron-donating substituents of the imine the dimeric species was generally preferred (see SI 3.4.2). Remarkably, by combining electron-donating with electron-withdrawing groups on the 3,3'-substituents and the imine or the other way around (e.g., **1d**/**2d** or **1a**/**2b**) a stronger preference for the dimeric species was observed (up to 95 % dimeric species; for specific ratios see SI 3.6.4.2 and 3.6.4.3).

Thus, we were able to identify CPA/CPA/imine species for many CPA imine combinations during our low temperature NMR investigations. Especially TRIFP **1a** and combinations with donating and withdrawing electronic properties on catalyst and imine favor dimer formation. The general hydrogen bond pattern reveals a cooperativity effect of the PO-H---OP and PO^----H-N^+ hydrogen bond resulting in a stronger proton transfer onto the substrate potentially contributing to the kinetic preference of the dimeric reaction pathway. For the first time NOESY/HOESY studies gave experimental insights into the dimer structure. Together with DFT calculations they indicate that both catalyst molecules may contribute to the stereoinduction. Overall, for many CPA/imine combinations the dimeric species was detected, but for all combinations the formation trend is small that 200 % catalyst concentration is needed to detect significant NMR signals of the 2:1 complex.

3.3.3. Dimeric Pathway in CPA Catalysis

Next, we explored if this dimeric species can lead to a second reactive pathway in the CPA-catalyzed transfer hydrogenation of imines that has a similar influence on the stereoselectivity as previously observed CPA dimers.[25,36] Therefore, we selected and studied our NMR model system consisting of TRIFP **1a** and imine **2b**, which showed the highest preference for the dimeric species, to investigate a potential impact on stereoselectivity. In general, high overall concentrations, high catalyst loadings and sterically less hindered CPAs should favor the dimeric pathway. Furthermore, in case the activation barrier of the dimeric pathway is significantly lower than the one of the monomeric pathways, decreased temperatures should also favor the dimeric pathway. Therefore, multiple reaction conditions were adjusted and evaluated to reveal if the dimeric pathway contributes significantly. Enantioselectivities with varying catalyst loadings with (*R*)-TRIFP **1a** and imine **2b** were determined by chiral HPLC. Catalyst loadings of 1 mol% and 20 mol% (as typical upper limit in synthesis) were chosen as standard reference points for the monomeric and the dimeric pathway, respectively.

First, a screening of the reaction was performed at 5 °C, -5 °C, -10 °C and -20 °C. Decreasing the temperature should favor dimerization and thus the dimeric pathway. In addition, six different catalyst loadings (1, 3, 5, 10, 15, 20 mol%) were tested for each temperature. Assuming analogous behavior to the CPA/CPA/quinoline system (inverse stereoselectivities for the monomeric and the dimeric pathway), with increasing catalyst concentration the *ee* should be decreasing in case of a dimeric pathway.[25] However, despite NMR investigations at 180 K indicated the presence of a dimeric species, no significant change in *ee* was observed under these conditions for any of the studied systems (see Table 1, see SI Table S7). Even at extreme conditions supporting the formation of catalyst dimers (-20 °C and 100 % catalyst loading see entry 7 in Table 1) no significant change in ee was detected. Additionally, exchanging DCM with toluene as solvent also resulted in no significant change in ee even with 40 mol% catalyst loading.

Table 3.1 Conditions screening for a potential dimeric pathway. The reaction was performed according to GP II (see SI 4.1) with TRIFP 1a, imine 2b (0.06 M, 1.0 eq.) and Hantzsch Ester 3 (0.084 M, 1.4 eq.). All listed reactions were run for 3 d. Variable conditions such as temperature and catalyst loading, which were investigated on their influence on the enantiomeric excess (ee), are listed.

Solvent	[2b] / M	Temperature / °C	Catalyst loading / mol%	Reaction time / d	*ee* / %
DCM	0.06	5	1	3	64
DCM	0.06	5	20	3	70
DCM	0.06	-10	1	3	73
DCM	0.06	-10	20	3	71
DCM	0.06	-20	1	3	73
DCM	0.06	-20	20	3	69
Toluene	0.06	-5	1	3	73
Toluene	0.06	-5	20	3	78
Toluene	0.06	-5	40	3	78

Overall, the results from NMR low temperature studies show that the thermodynamic preference of dimeric complex formation at 180 K is similar with quinolines as substrates and the imines investigated here. However, the strong kinetic preference for the dimeric pathway present for quinolines is not existent for the imines investigated in this study.

The presence of dimers was proven by NMR investigations at 180 K using an excess of 200 % catalyst relative to imine (see Figure 3.3). Similar to the quinoline system of the Niemeyer group at 100 % catalyst loading the signal of the dimer is below the NMR detection limit at 180 K.[25] In general, at room temperature the key signals of the hydrogen bonds cannot be detected using NMR spectroscopy and given the results from 180 K only traces are expected. To examine whether dimers are relevant at reaction conditions non-linear effect (NLE) experiments developed by Kagan[55] and Noyori[56] are the method of choice. The respective experiments checking for a NLE have been carried out using TRIFP 1a and TRIP 1b.[55] For this purpose, reactions with different (R)- to (S)-ratios of the corresponding CPA were performed. The corresponding ee of the product was plotted against the ee of the CPA. In case of a monomeric pathway, a linear correlation is expected, while any deviation from linearity suggests the relevance of dimers. Indeed, aligning with our HPLC results, a linear correlation was observed demonstrating that dimers are not contributing in any relevant amount and that the reaction follows exclusively the monomeric pathway (see Figure 3.4).

3.3.4. Ion Supported Dimer Formation

Besides the quinoline study of Niemeyer et al.,[25] prior studies of chiral phosphoric acids revealed a potential metal ion-bridged CPA dimer which can also lead to inverse stereoselectivity for some CPA catalyzed reactions.[36] Similar changes in stereoselectivity of chiral reagents with salt additives have been observed.[57] Considering the synthesis route of chiral phosphoric acids which often involves several metal ions, this species could regularly and unintentionally be involved in CPA catalyzed reactions.[3,13,58] Therefore, besides investigating the hydrogen bond-bridged dimeric species with imines, we also investigated a potential influence of metal ion-bridged CPA dimers.

Here, we selected 12 different metal salts based on the best accessible solubility in DCM and added them to the reaction to observe any influence (see Table 4, see SI Table S12-13). This approach allowed the investigation of both potential dimerization occurring during synthesis due to remaining metal ions and dimerization caused by contaminated laboratory equipment.

For this screening both excess of the respective metal salt as well as stoichiometric amounts were added to the reaction mixture at -10 °C. These temperatures were used to support a dimerization which should be favored with lower temperatures.

Table 3.2 Metal ion screening for a potential metal linked CPA dimer pathway. The reaction was conducted with TRIFP 1a, imine 2b and Hantzsch Ester 3 and a metal additive in DCM. The reaction was performed at -10 °C with an imine concentration of 0.06 M and 20 mol% catalyst loading, and the enantiomeric excess (ee) was determined by HPLC.

Additive	**1a:Additive stoichiometry**	***ee* / %**
$Ca(OH)_2$	1:0.25	58
$Mg(OH)_2$	1:0.25	61
Ba(OH)2	1:0.25	69
LiClO4	1:0.5	45
LiClO4	1:4	9
KOMe	1:0.5	64
CaH2	1:0.5	69
PdCl2	Excess	67
PtNa2Cl6	Excess	72
$Cu(OH)CO_3$	Excess	73
$NaVO_3$	Excess	74

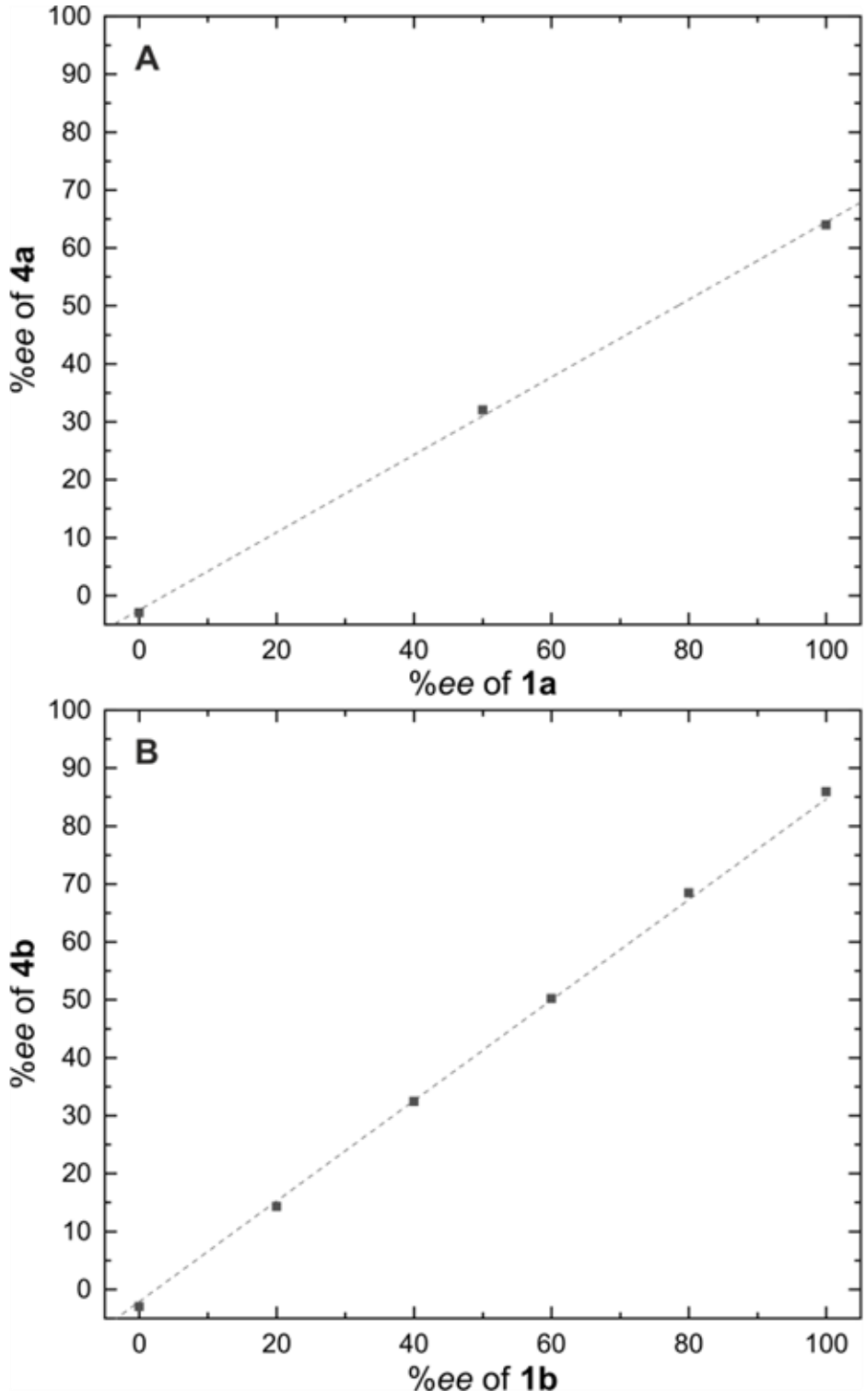

Figure 3.4 A) The %ee of the amine 4a plotted against the %ee of TRIFP 1a. The reaction has been conducted using 0.06 M of the imine 2a, 0.084 M of the Hantzsch Ester 3 and a catalyst loading of 25 mol% TRIFP 1a at room temperature. B) The %ee of the amine 4b plotted against the %ee of TRIP 1b. The reaction has been conducted using 0.2 M of the imine 2b, 0.22 M of the Hantzsch Ester 3 and a catalyst loading of 5 mol% TRIP 1b at 5 °C. In both cases, a linear effect is observed, confirming that no dimers are formed in a relevant amount to affect the outcome of the reaction. Linear Fits were added in both plots as a guideline.

First, we started using excess amount of the additives which led to poor or no product formation for most reactions (see SI Table S13). These low conversions were probably caused by a deprotonation of the CPA or oxidation of the Hantzsch ester **3**. Following, stoichiometric amounts relative to the CPA concentration were employed. Thereby, similar to our investigation of the dimeric pathway only small changes in *ee* are observed for most of the metal ions (see Table 4). For a few, such as $Ca(OH)_2$ and $LiClO_4$, a considerable decrease in *ee* can be observed. However, no deviations from linearity in a non-linear effect plot with $LiClO_4$, (see SI 4.2.2) suggest that other reasons than dimer formation cause this deviation. Nevertheless, we discovered that already small contaminations of metal ions can lead to reduced stereoselectivity. Hence, quality control of the catalyst is crucial to ensure the desired reaction outcomes.[59]

3.4. Conclusion

Despite the great success of chiral phosphoric acids as privileged Brønsted acid organocatalysts and detailed mechanistic studies, an easy and general prediction of the optimal catalyst still remains challenging. In prior studies on the CPA-catalyzed transfer hydrogenation of quinolines, Niemeyer[25] showed that in addition to the generally postulated monomeric pathway a dimeric pathway exists with opposite enantioselectivities. Therefore, we investigated if such a dimeric pathway is present for standard imines in CPA catalysis by NMR spectroscopy and HPLC.

Initial low-temperature NMR results indicated the presence of hydrogen bond-bridged CPA/CPA/imine dimer intermediates, with DFT calculations supporting this formation. Additionally, trends in the formation of such dimeric species were obtained. On the one hand, steric hinderance from the 3,3'-substituents of the CPA restricted dimer formation, with a defined limit based on the AREA(Θ) value. On the other hand, opposing electronic properties between the CPA and imine favored dimer formation, whereas similar electronic properties on both substrates did not. Despite these NMR findings, a dimeric pathway was not detected during the CPA-catalyzed transfer hydrogenation of imines. While an inversion similar to previously reported CPA dimers was expected, no change in stereoselectivity was observed under any screened reaction conditions. However, while investigating the influence of metal ions on CPA dimerization at -10 °C, we discovered a significant impact of metal ions on stereoselectivity, highlighting the importance of a thorough reaction workup for CPA synthesis.

In summary, we have shown that the 2:1 dimeric species is a common structural feature when investigating highly concentrated CPAs with low-temperature NMR spectroscopy. Similar to the complexes with quinolines, the dimeric complexes with classical imines are extremely low populated (NMR detectable only at a 2:1 ratio of catalyst to imine). Thus, only an extraordinary acceleration via a strong kinetic preference can produce significant effects of the dimeric pathway under synthetic conditions. This is not the case for the classical imines investigated here. Thus, the dimeric pathway seems to be a hidden channel in CPA catalysis, relying on an outstanding kinetic performance to overcome the low population. Hence, the relevance of dimers has to be investigated for each system individually.

3.5. References

[1] D. Parmar, E. Sugiono, S. Raja, M. Rueping, *Chem. Rev.* **2014**, 114, 9047–9153.

[2] M. Terada, *Synthesis (Stuttg).* **2010**, 1929–1982.

[3] T. Akiyama, *Chem. Rev.* **2007**, 107, 5744–5758.

[4] T. Akiyama, K. Mori, *Chem. Rev.* **2015**, 115, 9277–9306.

[5] M. Mahlau, B. List, *Angew. Chemie - Int. Ed.* **2012**, 52, 518–533.

[6] T. Akiyama, J. Itoh, K. Yokota, K. Fuchibe, *Angew. Chemie - Int. Ed*. **2004**, 43, 1566–1568.

[7] D. Uraguchi, M. Terada, *J. Am. Chem. Soc*. **2004**, 126, 5356–5357.

[8] S. Hoffmann, A. M. Seayad, B. List, *Angew. Chemie - Int. Ed*. **2005**, 44, 7424–7427.

[9] R. I. Storer, D. E. Carrera, Y. Ni, D. W. C. MacMillan, *J. Am. Chem. Soc*. **2006**, 128, 84–86.

[10] M. Rueping, E. Sugiono, C. Azap, T. Theissmann, M. Bolte, *Org. Lett.* **2005**, 7, 3781–3783.

[11] M. Sickert, F. Abels, M. Lang, J. Sieler, C. Birkemeyer, C. Schneider, *Chem. - A Eur. J.* **2010**, 16, 2806–2818.

[12] Q. X. Guo, H. Liu, C. Guo, S. W. Luo, Y. Gu, L. Z. Gong, *J. Am. Chem. Soc.* **2007**, 129, 3790–3791.

[13] D. Uraguchi, K. Sorimachi, M. Terada, *J. Am. Chem. Soc.* **2004**, 126, 11804–11805.

[14] G. B. Rowland, E. B. Rowland, Y. Liang, J. A. Perman, J. C. Antilla, *Org. Lett.* **2007**, 9, 2609–2611.

[15] M. Rueping, A. P. Antonchick, T. Theissmann, *Angew. Chemie - Int. Ed.* **2006**, 45, 6751–6755.

[16] P. Jiao, D. Nakashima, H. Yamamoto, Angew. Chemie **2008**, 120, 2445–2447.

[17] Q. Yin, S. G. Wang, S. L. You, *Org. Lett.* **2013**, 15, 2688–2691.

[18] M. Rueping, T. Theissmann, M. Stoeckel, A. P. Antonchick, *Org. Biomol. Chem.* **2011**, 9, 6844–6850.

[19] P. Renzi, J. Hioe, R. M. Gschwind, *J. Am. Chem. Soc*. **2017**, 139, 6752–6760.

[20] M. Melikian, J. Gramüller, J. Hioe, J. Greindl, R. M. Gschwind, *Chem. Sci.* **2019**, 10, 5226–5234.

[21] J. Greindl, J. Hioe, N. Sorgenfrei, F. Morana, R. M. Gschwind, *J. Am. Chem. Soc.* **2016**, 138, 15965–15971.

[22] M. Žabka, R. M. Gschwind, *Chem. Sci*. **2021**, 12, 15263–15272.

[23] N. Sorgenfrei, J. Hioe, J. Greindl, K. Rothermel, F. Morana, N. Lokesh, R. M. Gschwind, *J. Am. Chem. Soc*. **2016**, 138, 16345–16354.

[24] K. Rothermel, M. Melikian, J. Hioe, J. Greindl, J. Gramüller, M. Žabka, N. Sorgenfrei, T. Hausler, F. Morana, R. M. Gschwind, *Chem. Sci.* **2019**, 10, 10025–10034.

[25] D. Jansen, J. Gramüller, F. Niemeyer, T. Schaller, M. C. Letzel, S. Grimme, H. Zhu, R. M. Gschwind, J. Niemeyer, *Chem. Sci*. **2020**, 11, 4381–4390.

[26] J. Gramüller, M. Franta, R. M. Gschwind, *J. Am. Chem. Soc*. **2022**, 144, 19861–19871.

[27] L. Simón, J. M. Goodman, *J. Am. Chem. Soc*. **2008**, 130, 8741–8747.

[28] T. Marcelli, P. Hammar, F. Himo, *Chem. - A Eur. J.* **2008**, 14, 8562–8571.

[29] J. P. Reid, J. M. Goodman, *J. Am. Chem. Soc.* **2016**, 138, 7910–7917.

[30] J. P. Reid, J. M. Goodman, *Chem. - A Eur. J*. **2017**, 23, 14248–14260.

[31] J. P. Reid, M. S. Sigman, *Nature* **2019**, 571, 343–348.

[32] A. J. Neel, A. Milo, M. S. Sigman, F. D. Toste, *J. Am. Chem. Soc*. **2016**, 138, 3863–3875.

[33] M. Orlandi, J. A. S. Coelho, M. J. Hilton, F. D. Toste, M. S. Sigman, *J. Am. Chem. Soc*. **2017**, 139, 6803–6806.

[34] R. Maji, S. C. Mallojjala, S. E. Wheeler, *Chem. Soc. Rev.* **2018**, 47, 1142–1158.

[35] K. Kaupmees, N. Tolstoluzhsky, S. Raja, M. Rueping, I. Leito, *Angew. Chemie - Int. Ed.* **2013**, 52, 11569–11572.

[36] M. Hatano, K. Moriyama, T. Maki, K. Ishihara, *Angew. Chemie - Int. Ed*. **2010**, 49, 3823–3826.

[37] R. Mitra, M. Thiele, F. Octa-Smolin, M. C. Letzel, J. Niemeyer, *Chem. Commun.* **2016**, 52, 5977–5980.

[38] M. Thiele, T. Rose, M. Lõkov, S. Stadtfeld, S. Tshepelevitsh, E. Parman, K. Opara, C. Wölper, I. Leito, S. Grimme, J. Niemeyer, *Chem. – A Eur. J.* **2023**, 29, DOI 10.1002/chem.202202953.

[39] R. Mitra, H. Zhu, S. Grimme, J. Niemeyer, *Angew. Chemie - Int. Ed.* **2017**, 56, 11456–11459.

[40] M. Rueping, C. Azap, E. Sugiono, T. Theissmann, *Synlett* **2005**, 2367–2369.

[41] S. G. Ouellet, A. M. Walji, D. W. C. Macmillan, *Acc. Chem. Res*. **2007**, 40, 1327–1339.

[42] N. Lokesh, J. Hioe, J. Gramüller, R. M. Gschwind, *J. Am. Chem. Soc.* **2019**, 141, 16398–16407.

[43] S. Sharif, G. S. Denisov, M. D. Toney, H. H. Limbach, *J. Am. Chem. Soc.* **2007**, 129, 6313–6327.

[44] P. Schah-Mohammedi, I. G. Shenderovich, C. Detering, H. H. Limbach, P. M. Tolstoy, S. N. Smirnov, G. S. Denisov, N. S. Golubev, *J. Am. Chem. Soc.* **2000**, 122, 12878–12879.

[45] C. Detering, P. M. Tolstoj, N. S. Golubev, G. S. Denisov, H. H. Lumbach, *Dokl. Akad. Nauk* **2001**, 379, 353–357.

[46] L. Schreyer, R. Properzi, B. List, *Angew. Chemie - Int. Ed.* **2019**, 58, 12761–12777.

[47] X. H. Chen, W. Q. Zhang, L. Z. Gong, *J. Am. Chem. Soc.* **2008**, 130, 5652–5653.

[48] H. Yamamoto, K. Futatsugi, Angew. *Chemie - Int. Ed.* **2005**, 44, 1924–1942.

[49] R. Zhao, L. Shi, ChemCatChem **2014**, 6, 3309–3311.

[50] V. H. Rawal, A. N. Thadani, A. K. Unni, Y. Huang, *Nature* **2003**, 424, 146.

[51] N. T. Mcdougal, S. E. Schaus, **2003**, 12094–12095.

[52] T. Hashimoto, K. Maruoka, *J. Am. Chem. Soc.* **2007**, 129, 10054–10055.

[53] R. Davydov, S. Chemerisov, D. E. Werst, T. Rajh, T. Matsui, M. Ikeda-Saito, B. M. Hoffman, *J. Am. Chem. Soc.* **2004**, 126, 15960–15961.

[54] G. Dodson, A. Wlodawer, *Trends Biochem. Sci.* **1998**, 23, 347–352.

[55] D. Guillaneux, S.-H. Zhao, O. Samuel, D. Rainford, H. B. Kagan, *J. Am. Chem. Soc.* **1994**, 116, 9430–9439.

[56] M. Kitamura, S. Suga, H. Oka, R. Noyori, *J. Am. Chem. Soc.* **1998**, 120, 9800–9809.

[57] S. Arseniyadis, P. V. Subhash, A. Valleix, S. P. Mathew, D. G. Blackmond, A. Wagner, C. Mioskowski, *J. Am. Chem. Soc.* **2005**, 127, 6138–6139.

[58] M. Rueping, E. Sugiono, A. Steck, T. Theissmann, *Adv. Synth. Catal.* **2010**, 352, 281–287.

[59] M. Klussmann, L. Ratjen, S. Hoffmann, V. Wakchaure, R. Goddard, B. List, *Synlett*, **2010**, 2189–2192.

3.6. Supporting Information

3.6.1. Analytical Methods

3.6.1.1. NMR Spectrometer Data

For all NMR spectroscopic measurements on model systems a Bruker Avance III HD 600 MHz spectrometer with equipped with a 5 mm triple resonance broadband inverse probe TBI F (1H/19F, BB, 2H) with z-gradient (56 G·cm-1) and BVT unit was used. The temperature of the spectrometer was regulated by a BVT 3900 unit and liquid nitrogen. Furthermore, samples for the characterization of in this work synthesized imines were measured on a Bruker III 400 MHz spectrometer equipped with a 5 mm broadband observe probe BBFO (BB/19F, 1H, 2H) with z-gradient. For all NMR measurements, 5 mm NMR tubes were used. Spectrometer control and spectra processing was performed by Bruker Software TopSpin 3.2 PL7. For data processing, preparation, and presentation Microsoft Excel, ChemBioDraw 19.0 and CorelDraw 2019 were utilized.

Chemical shifts of ^{1}H and ^{13}C were referenced to TMS or the solvent. The heteronuclei ^{15}N and ^{31}P were referenced, employing $\nu(X) = \nu(TMS) \cdot \Xi reference / 100\ \%$ according to Harris et al.[1] The following frequency ratios and reference compounds were used: $\Xi(^{15}N) = 10.132912$ (lq. NH_3) and $\Xi(^{31}P) = 40.480742$ (H_3PO_4).

3.6.1.2. Pulse Sequence and Parameters

Standard pulse sequences from the Bruker pulse sequence catalogue (zg, zg30, etc.) have been used. For all ^{1}H-NMR spectra a sweep width of 22 ppm with an offset at 10 ppm were used. For ^{31}P spectra the sweep width was 40 ppm with the offset at 5 ppm and for ^{15}N a sweep width of 508 ppm with the offset at 200 ppm was used. Furthermore, the following acquisition parameter have been used:

^{1}H-NMR: Pulse program zg30, Relaxation delay = 2.00 s, Acquisition time = 2.48 s, SW = 22 ppm, TD = 66 K, ns = 1 – 64;

^{13}C NMR: Pulse program: zgpg30, Relaxation delay = 2.00 s, Acquisition time = 0.80 s, SW = 270.0 ppm, TD = 66k, NS = 1k – 4k;

^{15}N NMR: Pulse program: zg30; Relaxation delay = 3.00 s, Acquisition time = 1.06 s; SW = 508 ppm, TD = 66 K; NS = 1K – 4K;

^{31}P-NMR: Pulse program: zgpg30; Relaxation delay = 3.00 s, Acquisition time = 4.5 s, SW = 40.0 ppm, TD = 66k, NS = 256 - 512;

2D-^{1}H,^{1}H NOESY: Pulse program: noesygpph; Relaxation delay = 5.00 s, mixing time (D8) = 300.00 ms; NS = 8-14, TD = 4096;, increments = 1024;

2D-^{1}H,^{1}H COSY: Pulse program: cosygpqf; Relaxation delay = 5.00 s, NS = 4-16, TD = 4096; increments = 512;

2D-^{1}H,^{13}C HSQC: Pulse program: hsqcedetgpsisp2.3; Relaxation delay = 3.75 s, $^{1}J_{XH}$ = 145 Hz; NS = 8-10, TD = 4096; increments = 512;

2D-^{1}H,^{13}C HMBC: Pulse program: hmbcgplpndqf; Relaxation delay = 3.90 s, $^{1}J_{XH}$ = 145 Hz, J_{XH}(long range) = 10 Hz; NS = 14-22, TD = 4096; increments = 512 - 1k;

2D-^{1}H,^{31}P HMBC: Pulse program: inv4gplrndqf; Relaxation delay = 6.00 s, NS = 16, TD = 4096; increments = 256 - 512;

2D-^{1}H,^{15}N HMBC: Pulse program: inv4gplrndqf; Relaxation delay = 4.00 s, delay for evolution of long range couplings (D6) = 20.00 ms; NS = 8-10, TD = 4096; increments = 256;

^{1}H DOSY: Pulse program: see Appendix, Relaxation delay = 2.00 s, NS = 16-128, TD = 66 K, increments = 20, Diffusion time delay = 45.0 ms, gradient strength 5-95% linear, gradient pulse: 2.9 – 7.5 ms.

3.6.1.3. Chiral HPLC

Enantiomeric excess values (*ee*) of products were determined by HPLC on a chiral stationary phase employing an Agilent 1290 Infinity LC system equipped with a binary pump, autosampler and a photodiode array detector and using a CHIRALCEL OD-H column (see SI Chapter 3.6.7).

3.6.2. Materials and Chemicals

3.6.2.1. Solvents

Deuterated solvents were purchased from Deutero or Sigma Aldrich. Deuterated and non-deuterated dichloromethane (DCM) were refluxed over CaH_2 under Argon atmosphere and distilled and stored over activated molecular sieves (3Å). Toluene and Benzene were refluxed over Na under Argon atmosphere and distilled and stored over activated molecular sieves (4Å).

3.6.2.2. Chemicals

(*R*)-TRIFP **1a**, (*R*)-TRIM **1c**, (*R*)-OMe-CPA **1d**, (*R*)-TiPSY **1e**, (*R*)-Phenyl-CPA **1f**, (*R*)-3,5-Dimethylphenyl-CPA **1g** were purchased at abcr and (*R*)-TRIP **1b** at Sigma Aldrich. All synthesized imines were stored in a desiccator over anhydrous $CaCl_2$ or inside a glove box. Hantzsch Ester **3** was purchased at Sigma Aldrich and stored in the glovebox. The ^{15}N-enriched aniline for the presented synthesis below was purchased from Sigma Aldrich. The respective ketone-parts of the imines were purchased by Sigma Aldrich or abcr.

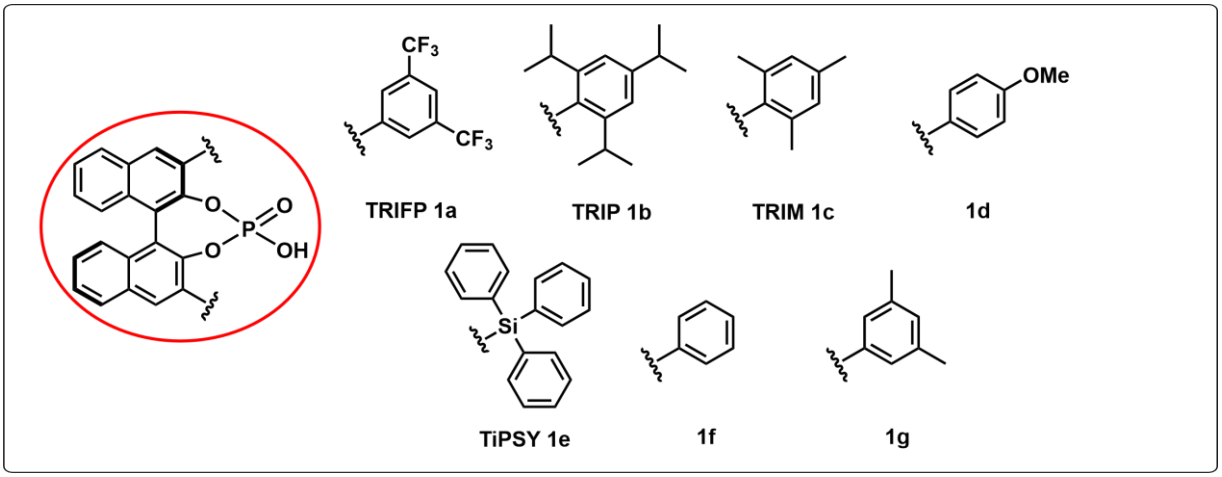

Figure S 3.1 Chiral Phosphoric Acids (CPAs) 1 used in NMR investigations and enantiomeric excess (ee) evaluation in this study.

3.6.2.3. Synthesis of Imines

The imines were prepared as described in literature.[2] The characterization of the in this work synthesized imines was performed on Bruker Avance 400 MHz-Spectrometer with a 5mm BBO BB-1H/D probe head with Z-Gradients.

General Procedure for the synthesis of imines GP I [2,3]

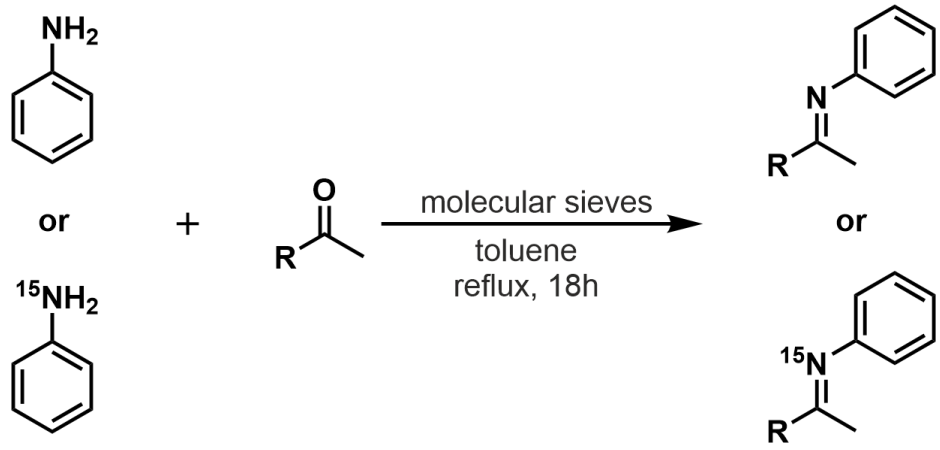

Molecular sieve (4 Å pore size, 3-5 g) was placed into a 50 mL Schlenk flask and dried with a heat gun at 400°C for 30 min under reduced pressure. Aniline or ^{15}N-Aniline (98% ^{15}N) (15.0 mmol, 1.40 g, 1.40 mL, 1.0 eq), the respective ketone (19.5 mmol, 1.3 eq.) and 25 mL anhydrous toluene were added under Argon flow. To this setup a reflux condenser was added under Argon flow and further flushed with Argon for 3 min. A drying tube, which was filled with $CaCl_2$, was attached to the reflux condenser and the solution was subsequently refluxed for 18 h. Afterwards, the heating bath was removed and the reaction mixture was allowed to cool down before being filtrated. Thereupon, the solvent was removed under reduced pressure to give a yellow solid, which was recrystallized in methanol 3-5 times to give the pure respective imine.

^{15}N-labelled Aniline was used for the synthesis to enable further investigations by NMR spectroscopy. For investigations on the enantioselectivity non-labelled Aniline was used (see Figure S3.2).

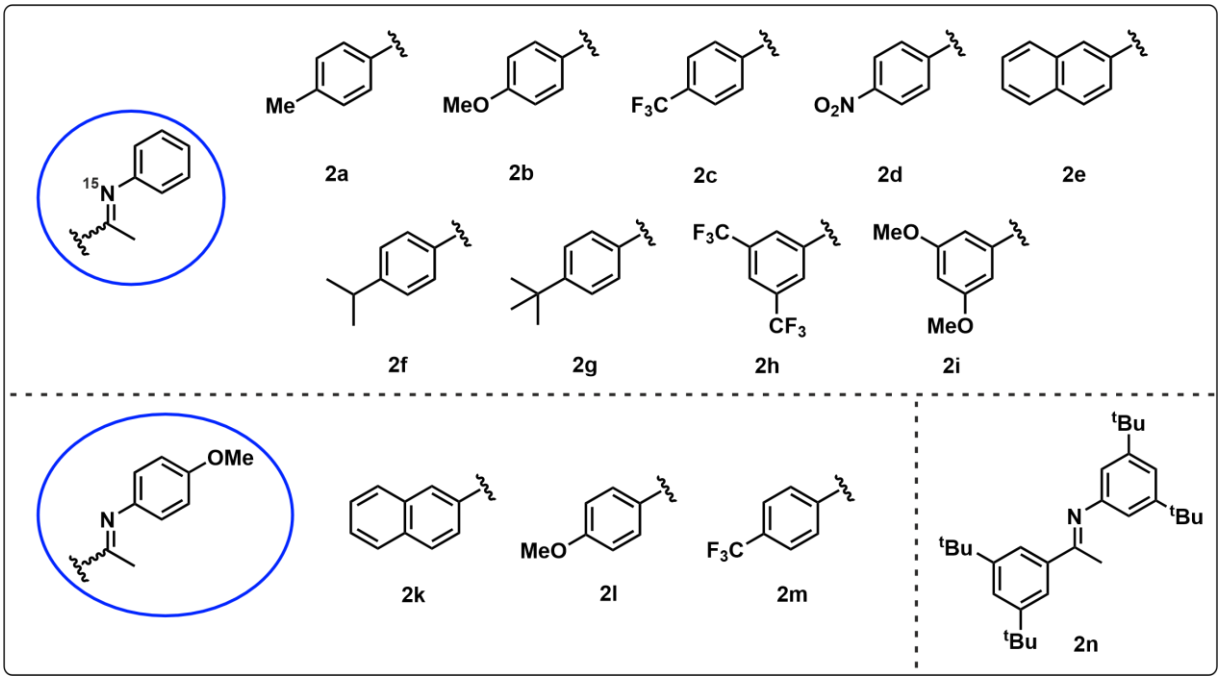

Figure S 3.2 Imines 2 used in NMR investigations and enantiomeric excess (ee) evaluation in this study.

All substrates (**2a** – **2n**) were prepared according to literature following GP I. All NMR spectra match with the literature reports.[3–6] ^{15}N labelled imines were synthesized analogously and the NMR spectra matched with the literature reports.[4]

3.6.3. NMR Investigations

3.6.3.1. Substrate Scope

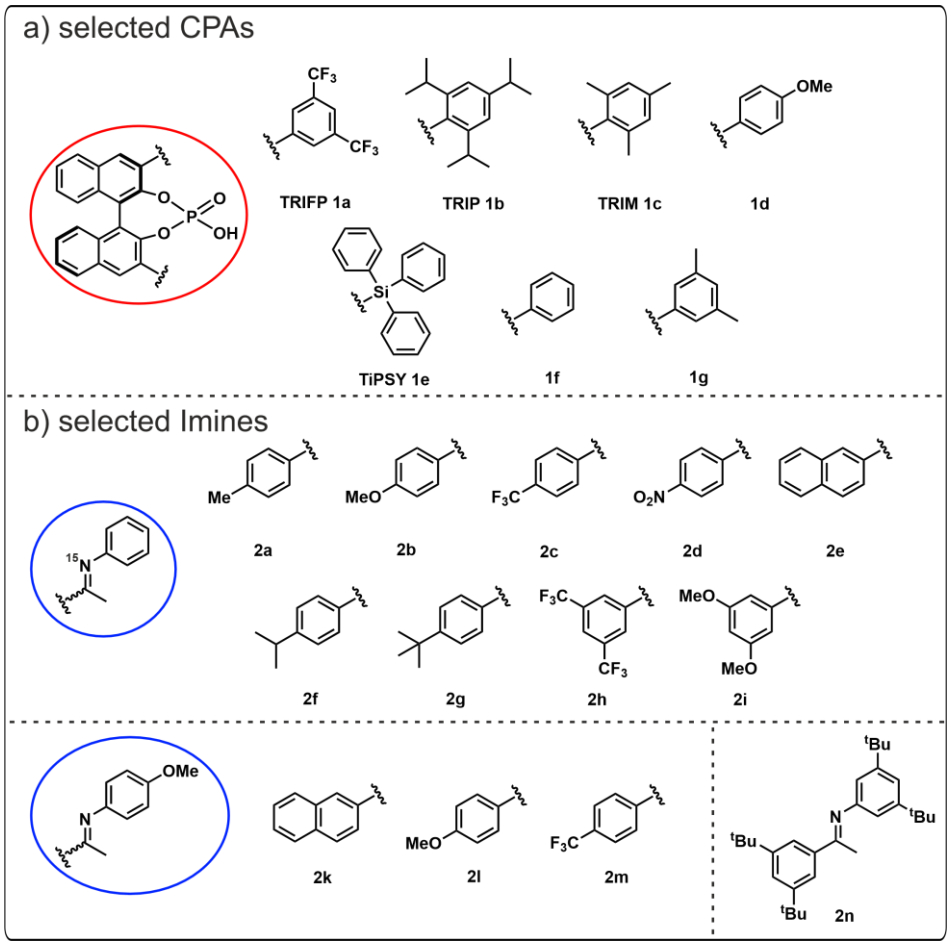

Figure S 3.3 Chiral Phosphoric Acids (CPAs) 1 and imines 2 used for NMR investigations in this study.

3.6.3.2. General Procedure for Sample Preparation (GPSP)

The CPA **1** (15-30 µmol, 1eq.) was directly weighed in a 5 mm NMR tube, which was subsequently dried with a heat gun at 140 °C for 30 min under reduced pressure. After the tube cooled down to room temperature, ^{15}N labelled imine **2** (15 µmol, 0.5-1 eq.) was weighed directly into the NMR tube. The tube was evacuated and flushed with Argon three times. Dry CD_2Cl_2 (*d*-DCM) (0.6 mL) was added under Argon flow as well as TMS atmosphere (0.5 mL). Thereupon, the tube was closed and sealed with parafilm and stored in the fridge at -80 °C or used immediately.

All samples used in this work were prepared following this procedure and are listed in Table S3.1 and S3.2.

E-only Samples

A stock solution with the ^{15}N-labelled imine **2** (48 µmol) in dry CD_2Cl_2 (*d*-DCM) was prepared and cooled down to -80°C. The CPA **1** (24 µmol) was directly weighed in a 5 mm NMR tube, which was subsequently dried with a heat gun at 140 °C for 30 min under reduced pressure. The tube was evacuated and flushed with Argon three times and also cooled down to -80°C. From the stock solution 0.6 mL were added to the NMR tube. TMS atmosphere (0.5 mL) was added to the NMR tube. Thereupon, the tube was closed and sealed with parafilm under continuous cooling and immediately investigated by NMR spectroscopy.

3.6.3.3. Investigated Systems

All samples used in this work were prepared following the GPSP (Chapter 3.2, see Table S3.1-3.2)

Table S 3.1 Investigated CPA/imine systems by NMR measurements in a 2:1 stoichiometry to investigate the dimeric species.

Sample Nr.	System	CPA•Imine	Concentration CPA **1** [mM]	Concentration imine **2** [mM]
1	**1a•2a**	2:1	50	25
2	**1a•2b**	2:1	50	25
3	**1a•2c**	2:1	50	25
4	**1a•2d**	2:1	50	25
5	**1a•2e**	2:1	50	25
6	**1a•2f**	2:1	50	25
7	**1a•2h**	2:1	50	25
8	**1a•2h**	2:1	50	25
9	**1a•2i**	2:1	50	25
10	**1a•2k**	2:1	50	25
11	**1a•2l**	2:1	50	25
12	**1a•2m**	2:1	50	25
13	**1a•2n**	2:1	50	25
14	**1b•2a**	2:1	50	25
15	**1b•2b**	2:1	50	25
16	**1b•2c**	2:1	50	25
17	**1c•2a**	2:1	50	25
18	**1c•2b**	2:1	50	25
19	**1c•2d**	2:1	50	25
20	**1c•2g**	2:1	50	25
21	**1c•2h**	2:1	50	25
22	**1d•2a**	2:1	50	25

23	**1d•2b**	2:1	50	25
24	**1d•2c**	2:1	50	25
25	**1d•2d**	2:1	50	25
26	**1e•2b**	2:1	50	25
27	**1f•2b**	2:1	50	25
28	**1f•2d**	2:1	50	25
29	**1g•2b**	2:1	50	25
30	**1g•2d**	2:1	50	25
31	**1a•2a** *E*-only	2:1	50	25
32	**1a•2b** *E*-only	2:1	50	25

Table S 3.2 Investigated CPA/imine systems by NMR measurements in a 1:1 stoichiometry for comparisons with the 2:1 samples by DOSY NMR measurements and/or hydrogen bond patterns.

Sample Nr.	System	CPA•Imine	Concentration [mM]
30	**1a•2e**	1:1	25
31	**1a•2f**	1:1	25
32	**1a•2h**	1:1	25
33	**1a•2h**	1:1	25
34	**1c•2d**	1:1	25
35	**1c•2h**	1:1	25
36	**1f•2b**	1:1	25

3.6.4. Dimeric Species NMR Investigations

To elucidate the dimeric pattern and trends for the formation of the 2:1 dimer of CPA/Imine systems with NMR spectroscopy, a variety of different CPAs and imines were investigated by NMR spectroscopy. Due to their different steric and electronic properties obtained by their respective substituents, a vast amount of systems is available to investigate trends of the formation of dimeric species. TRIP **1b**, TRIM **1c,** TiPSY **1e**, **1f** and **1g** were investigated on their steric impact on dimer formation. Furthermore, to investigate the impact of electronic effects of the CPAs on dimer formation, the electron-withdrawing TRIFP **1a**, the strongly electron-donating **1d** as well as the weakly electron-donating methyl substituents **1g** were used.

Similarly, the steric and electronic influence of the ketone-part of the imine on dimer formation was also investigated. For the investigation of the electronic influence on the formation of the dimeric species the weak electron-donating **2a**, the strong electron-donating **2b** and **2i**, the electron-withdrawing **2c** and the strong electron-withdrawing **2d** and **2h** were examined. Furthermore, to examine the influence of steric hinderance of the ketone-part substituent of the imines on dimer formation **2e**, **2g** and **2n** were used. Only the ketone-part of the imines was investigated to enable ^{15}N-labelling as it is not possible while changing substituents on the aniline-part. Nevertheless, unlabeled **2k**, **2l** and **2m** were investigated as well as PMP groups are also commonly used in synthesis. All samples were prepared according to GPSP.

3.6.4.1. Steric Influence

For investigations on the steric influence of the 3,3´-substituent of the CPA on the dimer formation, several CPAs were compared in combination with Imine **2b** (see Figure S3.4). Comparing the investigated systems led to the observation of a clear trend in dimer formation related to the size of the 3,3´-substituent. On the one hand, TiPSY 1e with an AREA (Θ) of 29 and TRIP **1b** with an AREA (θ) of 51 did not lead to any observable dimeric 2:1 species.[7] Due to the fact that TRIFP 1a and TRIM 1c have given good results for 2:1 dimers, both having an AREA (θ) of 62 respectively 61,[7] a correlation between AREA (θ) and dimer formation can be assumed based on the system investigated in this work. Hence, the border for dimer formation considering the AREA (θ) values would be in between 61 and 51. Therefore, systems with AREA (θ) values which are smaller than 51 could not form 2:1 dimeric species in an observable amount. Furthermore, in most

systems with AREA (θ) values above 61 the dimeric species is populated. However, with smaller substituents (higher AREA (θ)) a broad variance of other hydrogen bond species can be observed which diminish the role of the dimeric species in NMR spectroscopy.

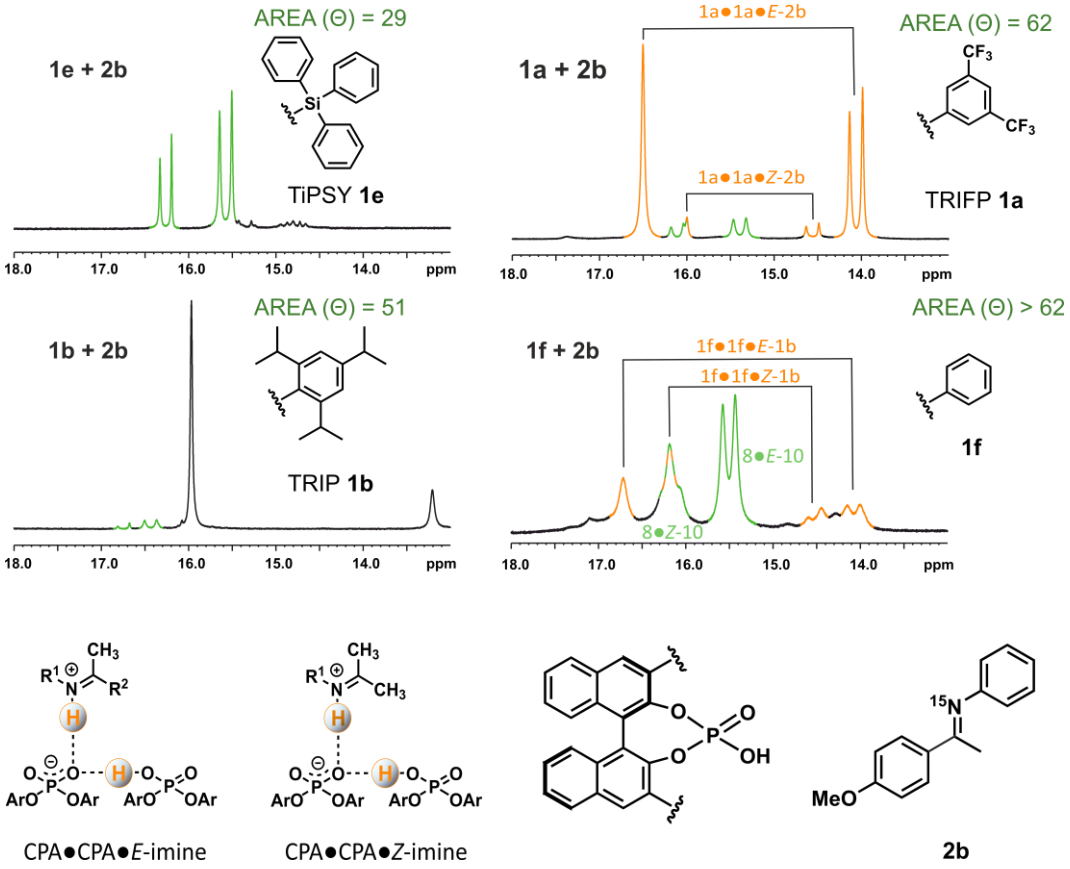

Figure S 3.4 ^{1}H-NMR spectra of systems with different CPAs in combination with 2b with an extended hydrogen bond area (2:1 stoichiometry, 50mM:25mM, CD_2Cl_2, 180K, 600MHz). The dimeric CPA/CPA/imine species is marked in orange while the monomeric CPA/imine species is marked in green. CPAs with different sterically demanding 3,3´-substituents are compared in combination with the same Imine 2b. The steric hinderance is expressed by the AREA (θ) which was introduced by Goodman et al. for 1a, 1b and 1e (1f´s 3,3´-substituent is smaller than the other ones displayed and therefore, is assumed to have a bigger AREA (θ) value than the other CPAs used here).[7] A clear steric hinderance can be observed as no observable dimeric species is formed for samples with AREA (θ) of 51 or lower. With all investigated CPAs with an AREA (θ) of 62 or higher a big variety of hydrogen bond species can be observed, in which the dimer can be detected as long as the signals are not overlapping and make any evaluation impossible.

For investigations on the steric influence of the imine on the dimer formation, several imines were compared in combination with CPA **1a** (see Figure S3.5). Imines **2a**, **2f** and **2g** clearly show the dimeric species as the major populated hydrogen bond species. The unlabeled imine **2e** also showed the dimer as major populated species. For the unlabeled Imine **2n** only the *Z*-isomer is observed, which is according to previous studies of the monomeric complex.[5] Therefore, with all investigated imines the dimeric species was

identified as long as line broadening and signal overlapping allowed it. Even for such sterically hindering substituents **2n** and aromatic systems as in **2e**.

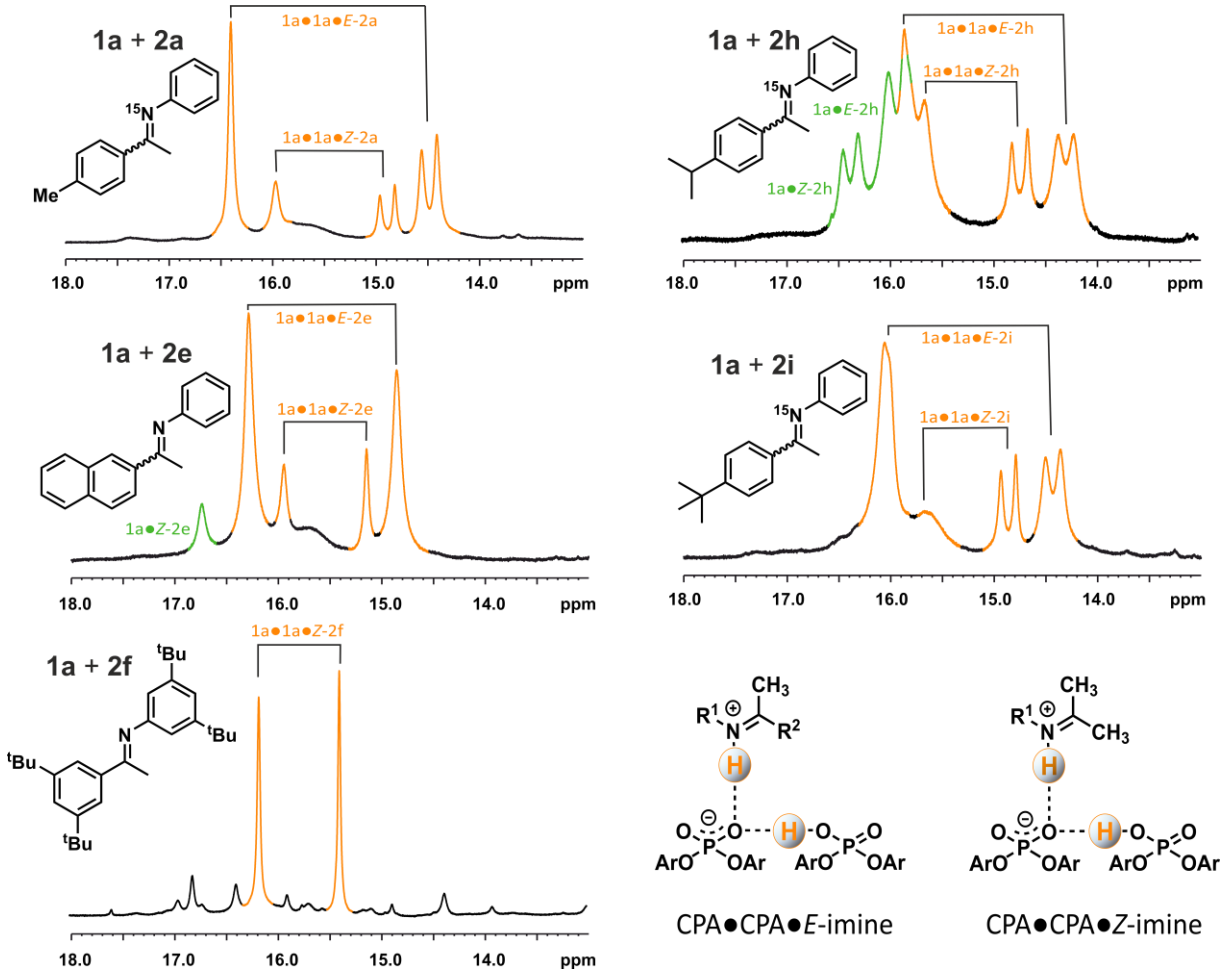

Figure S 3.5 ^{1}H-NMR spectra of systems with 1a in combination with different imines (2a, 2e-g, 2n) with an extended hydrogen bond area (2:1 stoichiometry, 50mM:25mM, CD_2Cl_2, 180K, 600MHz). The dimeric CPA/CPA/imine species is marked in orange while the monomeric CPA/imine species is marked in green. Imines with different sterically demanding substituents at the ketone-part are compared in combination with the same CPA 1a. For all systems the dimeric pattern can be clearly observed. Therefore, steric hinderance on the imine side is not expected for any combination.

3.6.4.2. Electronic Influence

To investigate the electronic influence on dimer formation, several electron-donating and electron-withdrawing imines/ CPAs were compared with each other. The effect of the electronic properties of the substrates was analyzed to determine their impact on the formation of dimeric species (see Figure S3.6). Based on the investigated systems it can be assumed that **1d**, except in combination with **2d**, leads to the formation of a variety of different hydrogen-bonded species that cannot be identified (e.g.**1d**/**2b**). Even if the 2:1 dimer does exist in these systems, it would not be favored. This is in contrast to TRIFP

1a systems in which the 2:1 dimer is observed as the major populated species in most systems. The only exception for TRIFP **1a** being the combination with electron-withdrawing substituents at the ketone-part of the imine such as **2c** and **2d**. Based on these results, dimer formation seems to be favored by electron-withdrawing 3,3´-substituents such as TRIFP **1a**. For electron-donating CPAs like **1d**, the dimer is favored only in combination with highly electron-withdrawing ketone-part substituents on the imine (e.g. **1d**/**2d**). Therefore, the assumption can be made that best resolutions, marginal overlapping and the preference of the 2:1 dimeric species can be observed with systems in which the 3,3´ - substituent of the CPA has the opposite electronic properties as the substituent at the ketone-part of the imine. However, combining the same properties on both substrates´ substituents leads to a huge variety of hydrogen-bonded species. Hence, the influence of the imine on the dimer formation is far more significant than in the previously investigated monomeric species.[4]

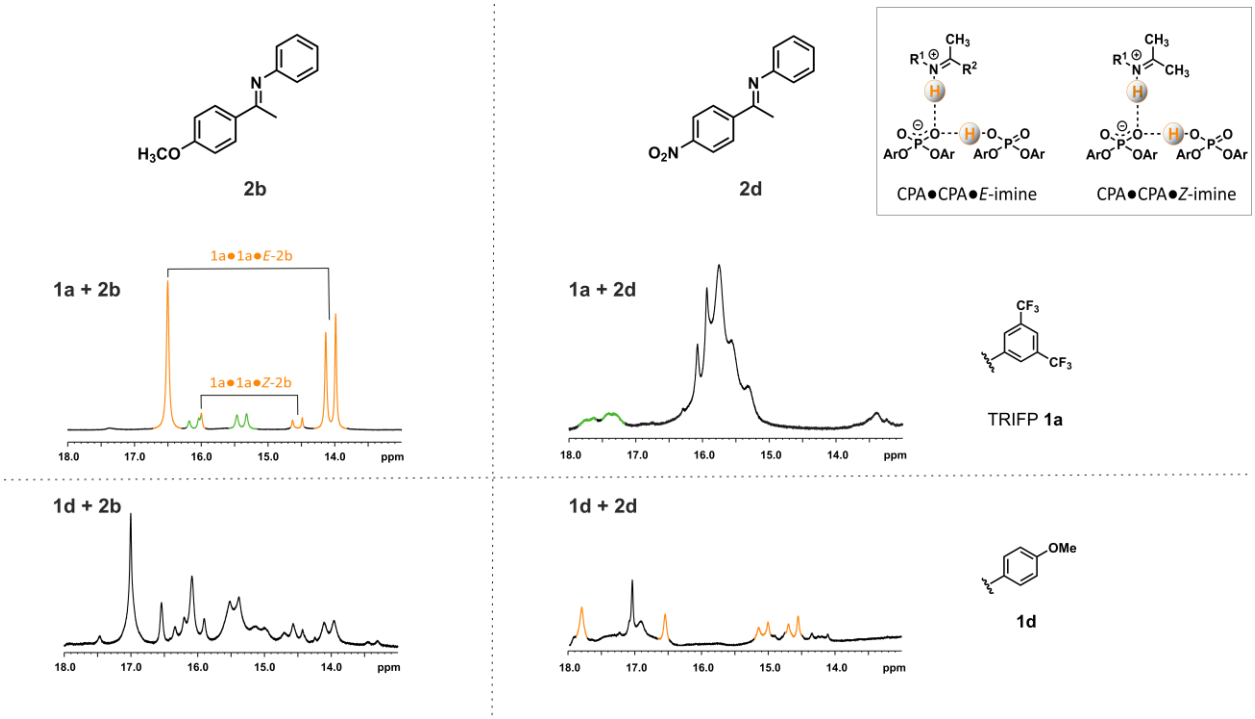

Figure S 3.6 ^{1}H-NMR spectra of systems with CPAs 1a, 1d and Imines 2b, 2d in various combinations with an extended hydrogen bond area (2:1 stoichiometry, 50mM:25mM, CD_2Cl_2, 180K, 600MHz). The dimeric CPA/CPA/imine species is marked in orange while the monomeric CPA/imine species is marked in green. Combinations of the same electronic properties on the ketone-part of the imine and the 3,3´-substituent of the CPA leads to a huge amount of hydrogen bond species and therefore, no preference for the dimeric species (1a/2d, top right; 1d/2b, bottom left). In contrast, by combining the same electronic properties on both substituents a better preference of the dimeric species can be observed (1a/2b, top left; 1d/2d bottom right).

3.6.4.3. Ratio between Monomeric and Dimeric Species

The impact of electronic and steric influences on dimer formation can be further elucidated by analyzing the ratio between the monomeric and dimeric species. This ratio can be determined by integrating the ^{1}H-NMR signal of the PO-H-N hydrogen bond of both species. To compare the populations of both species, the hydrogen bond signals for both isomers (*E*- and *Z*-imine) for the PO-H-N hydrogen bond were added up for each species. For imines **2a** and **2b**, an *E*-only sample was utilized to obtain the ratios, as there was less/no signal overlapping. These ratios are given for all systems in which the hydrogen bond signals were clearly assigned to each species and at least a rough estimation based on known patterns was possible (see Chapter 6.1.2).

In Chapter 3.4.2., we postulated that the combination of opposing electronic properties at the 3,3´ - substituent of the CPA and at the ketone-part of the imine favors dimer formation. This assumption is demonstrated by the ratios presented in Table S3.3. TRIFP **1a** shows an approximately 50/50 ratio for imines without electron-donating substituents on the ketone-part, such as **2a**, **2e**, and **2f**. The combination of opposing electronic properties on both substrates leads to a significant increase in dimer population. For TRIFP **1a** with imine **2b**, the dimeric species is populated to 82 % in relation to the monomeric species. For the combination of TRIFP **1a** with imine **2i**, with its two methoxy groups, even more dimeric species can be observed (95 %). The same trend is observed for CPA **1d**. While for the combination of **1d** and **2b**, no dimeric species can be clearly observed at all and is likely to be low populated in comparison to other hydrogen bond species, the combination of **1d** and **2d** leads to a ratio of approximately 58:42 in favor of the dimeric species. Moreover, the *p*-methoxyphenyl (PMP) group at the aniline part of the imine (**2k**, **2l**, **2m**) also leads to a similar preference for the dimeric species. For all three investigated substrates, an approximate 80/20 ratio can be observed. In the case of imine **2l** with an electron-donating substituent on both parts, there is a slightly better preference for the dimeric species in comparison to **2k** and **2m**. These results confirm the initial assumption that a combination of electron-withdrawing and electron-donating properties on both substrates leads to a preference for the dimeric species.

Table S 3.3 Investigated CPA/imine systems by NMR measurements in a 2:1 stoichiometry. The PO---H-N hydrogen bond of both the monomeric as well as the dimeric species were integrated and the sum of the integrals was set to 100 to give the percentage of each species.

Entry	System	Monomeric species	Dimeric species
1	**1a** + **2a** *E*-only	52	48
2	**1a** + **2b** *E*-only	18	82
3	**1a** + **2e ***	33	67
4	**1a** + **2f ***	55	45
5	**1a** + **2i**	5	95
6	**1a** + **2k**	21	79
7	**1a** + **2l**	16	84
8	**1a** + **2m**	22	78
9	**1d** + **2d ***	42	58

**Values are estimated based on their PO---H-N hydrogen bond due to overlapping with others signals. The knowledge of the standard pattern for the dimeric species is also used to recalculate the presumed integral of the monomeric species if necessary.*

3.6.5. DOSY Results

All DOSY measurements were performed with the convection suppressing DSTE (double stimulated echo) pulse sequence developed by Jerschow and Müller in a pseudo 2D mode.[8] Therefore, TMS was added to the sample and used as reference for the ^{1}H chemical shifts as well as the viscosity of the solvent. For the measurement a set of 0 dummy scans and 32 scans or 120 dummy scans and 64 scans were used with a relaxation delay of 2 s. The diffusion time delay was set to 45 ms and the gradient pulse lengths (p16, SMSQ10.100 pulse shape) were optimized for each species to give a sigmoidal signal decay for varying gradient strengths between 5 and 95%. Optimal pulse length of 0.8 ms was found at 300 K for TMS, and an optimal pulse length of 1.1 - 1.3 ms and 1.35 - 1.4 ms was found for CPA•imine and CPA•CPA•imine complexes respectively (at 180 K: 3 ms for TMS, 5.5 - 6.25 and 6.5 – 7.0 for CPA/imine and CPA/CPA/imine). For each species, twenty spectra with linear varying gradient strength from 5 to 95% were measured. Either characteristic substituent signals or the methyl-groups of the Imines were integrated and used for DOSY evaluation. Thereby, no line broadening occurred for increased gradient strengths.

The signal intensities of these groups were analyzed as a function of the gradient strength by the in Bruker TopSpin 3.2 included software T1/T2 relaxation package by employing the Stejskal-Tanner equation.[9] Based on the obtained translational diffusion coefficients, the hydrodynamic radii of the analytes r_H were estimated following the Stokes-Einstein

equation (1), with D_i = self-diffusion coefficient k = Boltzmann constant, T = temperature, η = viscosity of the sample, c = correcting factor, F = shape factor:[10]

$$(1)\ D_i = \frac{k_B T}{F c \pi \eta r_H}$$

The shape factor F was set to 1 for a spherical shape. The semi-empirical modification by Chen (2) was used to calculate the correction factor c. Therefore, a from literature known value for the radius of the corresponding solvent was used ($r_{CD_2Cl_2}$ = 2.46 Å[11]).[12]

$$(2)\quad c_{Chen} = \frac{6F}{1 + 0.695\ (\frac{r_{solv}}{r_{ref}})^{2.234}}$$

Viscosity calibration of the derived D_i values was performed with literature known values for the radii of TMS (r_{ref} = 2.96 Å, calculated from hard-sphere increments[13]) and the experimentally determined diffusion coefficient D_{ref} of TMS, which is determined individually for each sample.

$$(3)\quad \eta\ [kg/ms] = \frac{kT\ (1 + 0.695\ \left(\frac{r_{solv}}{r_{ref}}\right)^{2.234})}{6\pi D_{ref}\ r_{ref}}$$

After including all correction and calibration equations in the Stokes equation (1), the equation was rearranged for the hydrodynamic radii r_H (4). For easier imagination, the corresponding volumes V_A were calculated with the assumption of a spherical shape.

$$(4)\qquad 0 = D6\pi\eta r_A - kT\ 0.695\ {r_{solv}}^{2.234}\ {r_A}^{-2.234} - kT$$

The resulting self-diffusion coefficients D_i, the corresponding hydrodynamic radii r_H and the average D_i values of each species as well as of TMS as reference are depicted in Table S3.4-3.6. The average D_i values were derived by using all baseline separated signals that were referring to the same species.

For **1a**/**1a**/*E*-**2b** and **1a**/*E*-**2b** the hydrodynamic volumes at 180 K were determined to confirm the assignment as dimeric species. For both **1a**/**1a**/*E*-**2b** and **1a**/*E*-**2b**, the *para*-methoxy group of the imine was selected as probe signal. The DOSY measurements for **1a**/*E*-**2b** were performed at a 1:1 stoichiometry to receive better signal intensities for the CPA/imine monomer and to suppress significant exchange contributions from the dimer

on the diffusion coefficient. To estimate an error, the measurements were performed at three different pulse field gradient lengths which all gave an appropriate fit curve.

Additionally, comparing the diffusion coefficients D_i of samples with a 2:1 stoichiometry (see Table S3.5) with the diffusion coefficients D_i of samples with 1:1 stoichiometry (see Table S3.6) enables investigations on the formation of higher aggregates for other systems. By calculating the hydrodynamic radii r_H for the *E*- and *Z*- configurations of both imines an unambiguous difference between both stoichiometries can be seen. Samples with a 2:1 stoichiometry have increased r_H in comparison to the 1:1 stoichiometry. This clearly indicates the formation of higher aggregates than the monomeric species (1:1 stoichiometry) also for these systems. Therefore, it stands to reason that the increase in r_H is here also corresponding to the detected 2:1 dimeric species (2:1 stoichiometry). The measurements were performed at different stoichiometries at 300 K, as no clear assignment based on separated signals at low temperature was possible at a 2:1 ratio, as it was the case for **1a**/**2b**.

Table S 3.4 Measured self-diffusion coefficients and derived molecular radii of 1a/1a/E-2b and 1a/E-2b at 180 K. Entry 1-8: SW = 22 Hz, O1P = 10.00 ppm, gradient strength 5-95% linear.

Entry	P16 [ms]	δ [ppm]	D_i [m²/s]	r_H [Å]
1	3.0	0.00 (TMS)	2.16E-11	---
2	6.5	3.44	4.58E-12	9.68
3	6.75	3.44	4.69E-12	9.66
4	7.0	3.44	4.68E-12	9.62
5	3.0	0.00 (TMS)	2.25E-11	---
6	5.5	3.74	6.04E-12	7.94
7	6.0	3.74	6.05E-12	7.92
8	6.25	3.74	5.97E-12	8.03

Based on the hydrodynamic radii, the sphere volume was determined. For the dimeric species, thus a hydrodynamic volume of 3770 ± 27 Å^3 and for the monomeric one a volume of 2110 ± 36 Å^3 was determined. The almost doubled hydrodynamic volume clearly identifies this species as a dimer.

Table S 3.5 Measured self-diffusion coefficients and derived molecular radii of samples with 2:1 stoichiometry of CPA to imine at 300 K. Entry 1-4: SW = 22 Hz, O1P = 10.00 ppm, gradient strength 5-95% linear. For entry 4 the E and Z values of the radius were averaged as no differentiation was possible.

Entry	Species	p16 [ms]	D_i of TMS [m^2/s]	Averaged D_i of CPA•imine aggregate[m^2/s]	r_H *E*-Imine [A]	r_H *Z*-Imine [A]
1	TMS	0.8			-	-
2	**1a** + *E*/*Z*-**2f**	1.35	2.89E-09	8.04E-10	7.696	8.338
3	**1a** + *E*/*Z*-**2g**	1.4	6.89E-10	1.83E-10	6.933	8.008
4	**1a** + *E*/*Z*-**2k**	1.4	3.06E-09	7.09E-10	8.59	

Table S 3.6 Measured self-diffusion coefficients and derived molecular radii of samples with 1:1 stoichiometry of CPA to imine at 300 K. Entry 1-4: SW = 22 Hz, O1P = 10.00 ppm, gradient strength 5-95% linear. For entry 4 the E- and Z- values of the radius were averaged as no differentiation was possible.

Entry	Species	p16 [ms]	D_i of TMS [m^2/s]	Averaged D_i of CPA•imine aggregate[m^2/s]	r_H *E*-isomer [A]	r_H *Z*-isomer [A]
1	TMS	0.8			-	-
2	**1a** + *E*/*Z*-**2f**	1.1	2.60E-09	8.62E-10	6.59	6.76
3	**1a** + *E*/*Z*-**2g**	1.3	2.70E-09	8.36E-10	6.05	6.99
4	**1a** + *E*/*Z*-**2k**	1.1	2.63E-09	2.06E-09	5.82	

3.6.6. CPA-Catalyzed Transfer Hydrogenation of Imines

3.6.6.1. General Procedure for CPA-Catalyzed Transfer Hydrogenation of Imines with Hantzsch-Ester 3 (GP II)

A Schlenk tube was dried with a heat gun at 400°C under reduced pressure for 10 min. Imine **2b** (0.06 M, 1.0 eq.), TRIFP **1a** (0.01-0.2 eq.) and Hantzsch ester **3** (0.084 M, 1.4 eq.) were added into the tube. The tube was then evacuated und flushed with Argon three times. Afterwards, anhydrous toluene/DCM (1.0 mL) was added under Argon flow. The reaction was stirred for 1-7 d. 0.1 - 0.2 mL of the crude reaction mixture were taken out of the Schlenk tube under Argon flow and quenched by the addition to a vial that was filled with hexane (1.5 mL) and NEt_3 (10 µL, 7.3 µg, 0.072 M, 7.2 – 144 eq. based on the catalyst). Then the mixture was filtered and analyzed by chiral HPLC. [14-16]

No yields were determined. However, based on the intensities of the product signals in the HPLC chromatograms relative to others (e.g. imine **2**) it is assumed that in general, most of the educt is converted to the product under the used conditions.

Table S 3.7 Results for the experiments done with TRIFP 1a, imine 2b (0.06 M, 1.0 eq.) and Hantzsch ester 3 (0.084 M, 1.4 eq.) according to GP II. All reaction were run for 3 d. Variable conditions such as concentration, temperature and catalyst loading are listed, which were investigated on their influence on the enantiomeric excess (ee). Values marked in red are based on a poor baseline or low conversion and therefore cannot be interpreted.

Solvent	c [M]	Temperature [°C]	Catalyst loading [%]	Reaction time [d]	Minor [Area%]	Major [Area%]	*ee* [%]
DCM	0.06	5	1	3	18,2	81,8	64
DCM	0.06	5	3	3	16,2	83,8	68
DCM	0.06	5	5	3	16,4	83,6	67
DCM	0.06	5	10	3	15,4	84,6	69
DCM	0.06	5	15	3	15,5	84,5	69
DCM	0.06	5	20	3	15,0	85.0	70
Toluene	0.06	-5	1	3	13,6	86,4	73
Toluene	0.06	-5	10	3	11,3	88,7	77
Toluene	0.06	-5	20	3	11,2	88,8	78
Toluene	0.06	-5	40	3	11,2	88,8	78
DCM	0.06	-10	1	3	13,6	86,4	73
DCM	0.06	-10	3	3	13,7	86,3	73
DCM	0.06	-10	5	3	14.0	86,0	72
DCM	0.06	-10	10	3	13,8	86,2	72
DCM	0.06	-10	15	3	15,1	84,9	70
DCM	0.06	-10	20	3	14,6	85,4	71
DCM	0.06	-20	1	3	13.6	86.4	73
DCM	0.06	-20	3	3	13.3	86.7	73
DCM	0.06	-20	5	3	14.0	86.0	72
DCM	0.06	-20	10	3	13.0	87.0	74
DCM	0.06	-20	15	3	27.1	72.9	46
DCM	0.06	-20	20	3	15.5	84.5	69

Table S 3.8 Results for the experiments done with TRIFP 1a/TRIP 1b (100 mol%), imine 2b (0.06 M, 1.0 eq.) and 3 different Hantzsch ester derivates (0.084 M, 1.4 eq.) according to GP II. The reaction was performed over 4 d at -40 °C with a catalyst loading of 100 mol% as a limit test for a potential dimeric pathway and its influence on enantioselectivity (ee). However, at -40 °C the reaction did not proceed. Values marked in red are based on a poor baseline or low conversion and therefore cannot be interpreted.

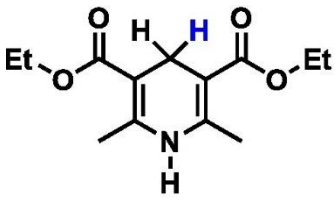

reference

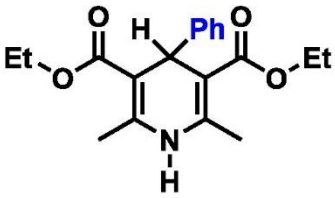

unreactive

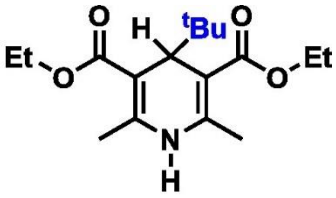

decrease in *ee*

Solvent	c [M]	Catalyst	HE derivate	Reaction time [d]	Minor [Area%]	Major [Area%]	*ee* [%]
DCM	0.06	TRIP 1b	H	4	6.8	93.2	86
DCM	0.06	TRIP 1b	Ph	4	-	-	-
DCM	0.06	TRIP 1b	^{t}Bu	4	15.9	84.1	68
Toluene	0.06	TRIP 1b	H	4	3.1	97.0	94
Toluene	0.06	TRIP 1b	Ph	4	-	-	-
Toluene	0.06	TRIP 1b	^{t}Bu	4	24.8	75.2	50
DCM	0.06	TRIFP 1a	H	4	10.2	89.8	80
DCM	0.06	TRIFP 1a	Ph	4	-	-	-
DCM	0.06	TRIFP 1a	^{t}Bu	4	35.1	64.9	30

Table S 3.9 Results for the experiments done with TRIFP 1a/TRIP 1b, imine 2b (0.06 M, 1.0 eq.) and 3 different Hantzsch ester derivates (0.084 M, 1.4 eq.) according to GP II. The reaction was performed over 4 d at -20°C with a catalyst loading of 100 mol% as a limit test for a potential dimeric pathway and its influence on enantioselectivity (ee).

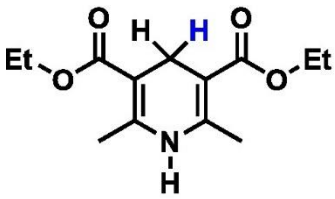

reference

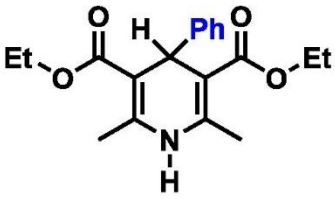

unreactive

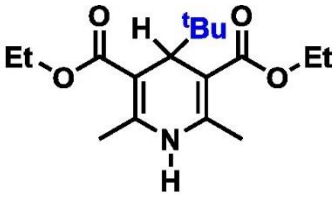

decrease in *ee*

Solvent	c [M]	Catalyst	HE derivate	Reaction time [d]	Minor [Area%]	Major [Area%]	*ee* [%]
DCM	0.06	TRIP 1b	H	4	11.7	88.3	77
DCM	0.06	TRIP 1b	Ph	4	-	-	-
DCM	0.06	TRIP 1b	^{t}Bu	4	34.6	65.4	31
Toluene	0.06	TRIP 1b	H	4	4.8	95.2	90
Toluene	0.06	TRIP 1b	Ph	4	-	-	-
Toluene	0.06	TRIP 1b	^{t}Bu	4	24.4	75.6	51
DCM	0.06	TRIFP 1a	H	4	11.8	88.2	76
DCM	0.06	TRIFP 1a	Ph	4	-	-	-
DCM	0.06	TRIFP 1a	^{t}Bu	4	15.1	84.9	70

Table S 3.10 Results for the experiments done with TRIFP 1a, imine 2b (1.0 eq.) and Hantzsch ester 3 (0.042 – 0.126 M, 1.4 eq.) according to GP II. The reaction was performed over 3 d at -20 °C with imine 2b concentrations ranging from 0.03 M to 0.09 M, to investigate the influence of the total concentration on the enantiomeric excess (ee). Values marked in red are based on a poor baseline or low conversion and therefore cannot be interpreted.

Solvent	c [M]	Temperature [°C]	Catalyst loading [%]	Reaction time [d]	Minor [Area%]	Major [Area%]	*ee* [%]
DCM	0.03	-20	1	3	16.3	83.7	67
DCM	0.06	-20	1	3	15.7	84.6	69
DCM	0.09	-20	1	3	12.3	88.0	76
DCM	0.03	-20	20	3	22.2	77.8	56
DCM	0.06	-20	20	3	22.1	77.9	56
DCM	0.09	-20	20	3	27.4	72.6	45
Toluene	0.03	-20	20	3	11.8	88.2	76
Toluene	0.06	-20	20	3	11.2	88.8	78
Toluene	0.09	-20	20	3	12.6	87.4	75

Table S 3.11 Results for the experiments done with TRIFP 1a (20 mol%), imine 2b (0.06 M, 1.0 eq.) Hantzsch ester 3 (0.084 M, 1.4 eq.) according to GP II. The reaction was performed over 5 d at -10 °C in DCM. The varied water concentration is listed. Water was added from a stock solution to reveal a potential water influence on the dimer formation.

Solvent	c [M]	Temperature [°C]	Catalyst loading [%]	H_2O [M]	Minor [Area%]	Major [Area%]	*ee* [%]
DCM	0.06	-10	20	0	15.3	84.7	69
DCM	0.06	-10	20	0.003	15.5	84.5	69
DCM	0.06	-10	20	0.006	13.8	86.2	72
DCM	0.06	-10	20	0.009	14.2	85.8	72
DCM	0.06	-10	20	0.012	14.4	85.6	71
DCM	0.06	-10	20	0.024	14.5	85.5	71
DCM	0.06	-10	20	0	24.6	75.4	51
DCM	0.06	-10	20	0.003	19.2	80.8	62
DCM	0.06	-10	20	0.006	26.1	73.9	48
DCM	0.06	-10	20	0.009	14.3	85.7	71
DCM	0.06	-10	20	0.012	22.8	77.2	54
DCM	0.06	-10	20	0.024	16.6	83.4	67

Table S 3.12 Results for the experiments done with TRIFP 1a, Imine 2b Hantzsch Ester 3 according to GP II with the addition of metal ions via additives. The reaction was performed at -10°C with 20 mol% catalyst loading. Additive was added stoichiometric relative to the CPA to hinder a CPA deprotonation.

Solvent	Additive	c [M]	CPA:Additive stoichiometry	Minor [Area%]	Major [Area%]	*ee* [%]
DCM	$Ca(OH)_2$	0.06	1:0.25	20.8	79.2	58
DCM	$Mg(OH)_2$	0.06	1:0.25	19.4	80.6	61
DCM	$Ba(OH)_2$	0.06	1:0.25	15.6	84.4	69
DCM	$LiClO_4$	0.06	1:0.5	27.7	72.3	45
DCM	$LiClO_4$	0.06	1:4	45.6	54.4	9
DCM	KOMe	0.06	1:0.5	18.2	81.8	64
DCM	CaH_2	0.06	1:0.5	15.3	84.7	69

Table S 3.13 Results for the experiments done with TRIFP 1a (20 mol%), imine 2b (0.06 M, 1.0 eq.) and Hantzsch ester 3 (0.084 M, 1.4 eq.) according to GP II with the addition of metal ions via additives. The reaction was performed at -10 °C in DCM for 3 d. Additives were added in excess which resulted in poor/no conversion, most likely due to CPA deprotonation for most additives. Values marked in red are based on a poor baseline or low conversion and therefore cannot be interpreted.

Solvent	Additive	c [M]	CPA:Additive stoichiometry	Minor [Area%]	Major [Area%]	*ee* [%]
DCM	KOMe	0.06	Excess	-	-	-
DCM	Cs_2CO_3	0.06	Excess	-	-	-
DCM	$LiClO_4$	0.06	Excess	-	-	-
DCM	NaOH	0.06	Excess	81.1	18.9	74
DCM	$Mg(OH)_2$	0.06	Excess	13.2	86.8	66
DCM	$Ca(OH)_2$	0.06	Excess	16.8	83.2	72
DCM	$Ba(OH)_2$	0.06	Excess	14.2	85.8	62
DCM	$PdCl_2$	0.06	Excess	18.9	81.1	67
DCM	$PtNa_2Cl_6$	0.06	Excess	16.6	83.4	72
DCM	$FeCl_3$ * 6 H_2O	0.06	Excess	14.2	85.8	-1
DCM	$Cu(OH)CO_3$	0.06	Excess	50.3	49.7	73
DCM	$NaVO_3$	0.06	Excess	13.6	86.4	74

Table S 3.14 Results for the experiments done with TRIFP 1a (20 mol%), imine 2b (0.06 M, 1.0 eq.) and Hantzsch ester 3 (0.084 M, 1.4 eq.) according to GP II adding a different co-solvent. The reaction was performed in DCM at -10 °C for 3 d.

Solvent	Additive	c [M]	C (Additive) [M]	Minor [Area%]	Major [Area%]	*ee* [%]
DCM	THF	0.06	0.012	15.652	84.348	69
DCM	MeOH	0.06	0.012	21.556	78.444	57

3.6.7. HPLC Investigations

General Procedure for Sample Preparation

0.1 - 0.2 mL of the crude reaction mixture were taken out of the Schlenk tube under Argon flow and quenched by the addition to a vial that was filled with hexane (1.5 mL) and NEt_3 (10 µL, 7.3 µg, 0.072 M, 7.2 – 144 eq. based on the catalyst). Then the mixture was filtered and analyzed by chiral HPLC.

HPLC Conditions for Amines (GP V)

2 **4**

Imine **2** (0.6 M, 1 eq.) and $NaBH_4$ (226.9 mg, 6 M, 10 eq.) were added in a round-bottomed flask. A septum was put on top of the round-bottomed flask and 6 mL of a mixture of DCM/MeOH (5:1) were added through the septum. The reaction was stirred at room temperature for 24 h. The reaction was quenched with a saturated aqueous $NaHCO_3$ solution and the aqueous phase was extracted with diethyl ether. The combined organic phases were dried with Na_2SO_4, filtered and the solvent was evaporated under reduced pressure. The resulting amine **4** was used to determine the HPLC conditions.

Characterization of Amines

All NMR spectra match with the literature reports (see citation).

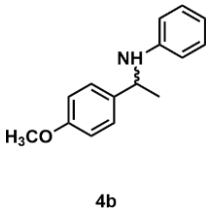

4b

4b: The *ee* was determined by CSP-HPLC, CHIRALCEL OD-H column, eluant *n*-hexane/*i*-propanol 98/2, flow 0.6 mL/min, retention times: τ1= 23.24 min, τ2= 25.64 min, column compartment temperature 20°C, λ= 280 nm.[3]

3.6.8. Appendix

3.6.8.1. NMR Spectroscopy

Investigations on Dimeric Species – ^{1}H-NMR of Investigated Systems

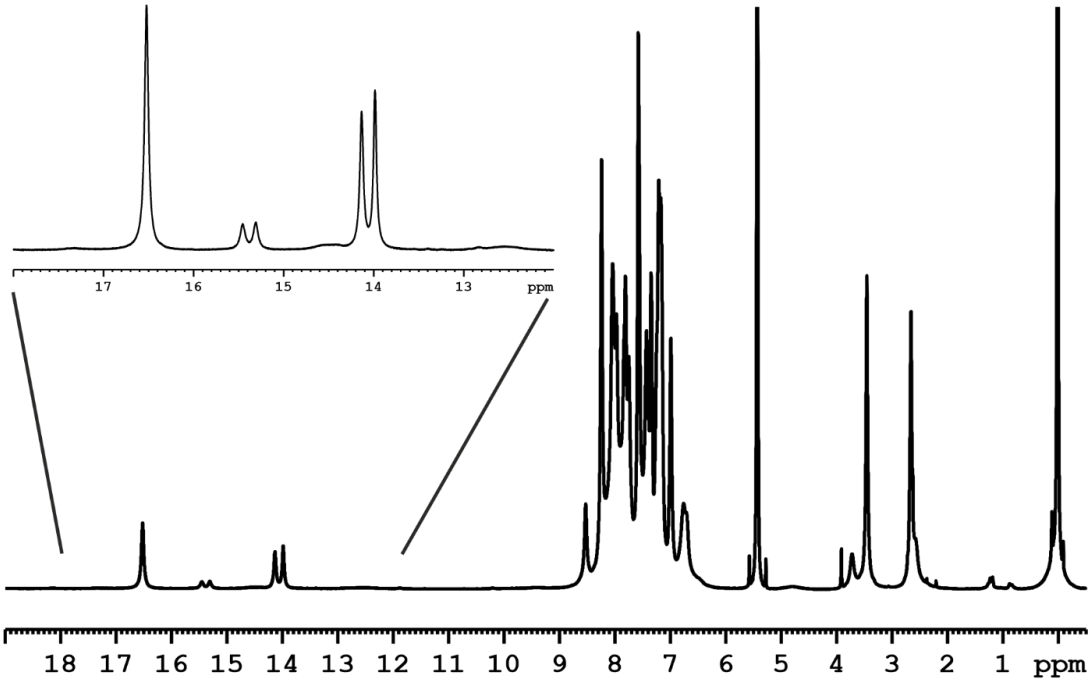

^{1}H-NMR spectra of an E-only sample of 1a•2b with an extended hydrogen bond area (2:1 stoichiometry, 50mM:25mM, CD2Cl2, 180K, 600MHz). Before adding the imine to a solution of the CPA in CD_2Cl_2, the solution is cooled down to -60°C which is preventing isomerization. Hence, only the E-isomer of the imine can be observed.

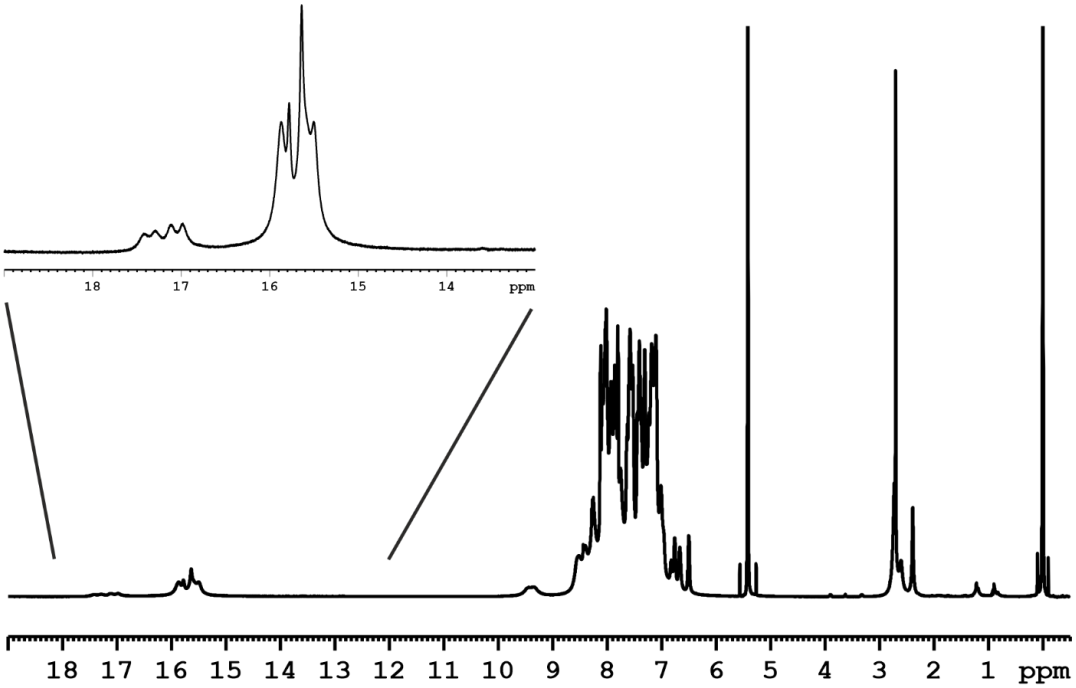

^{1}H-NMR spectra of 1a•2c with an extended hydrogen bond area (2:1 stoichiometry, 50mM:25mM, CD_2Cl_2, 180K, 600MHz).

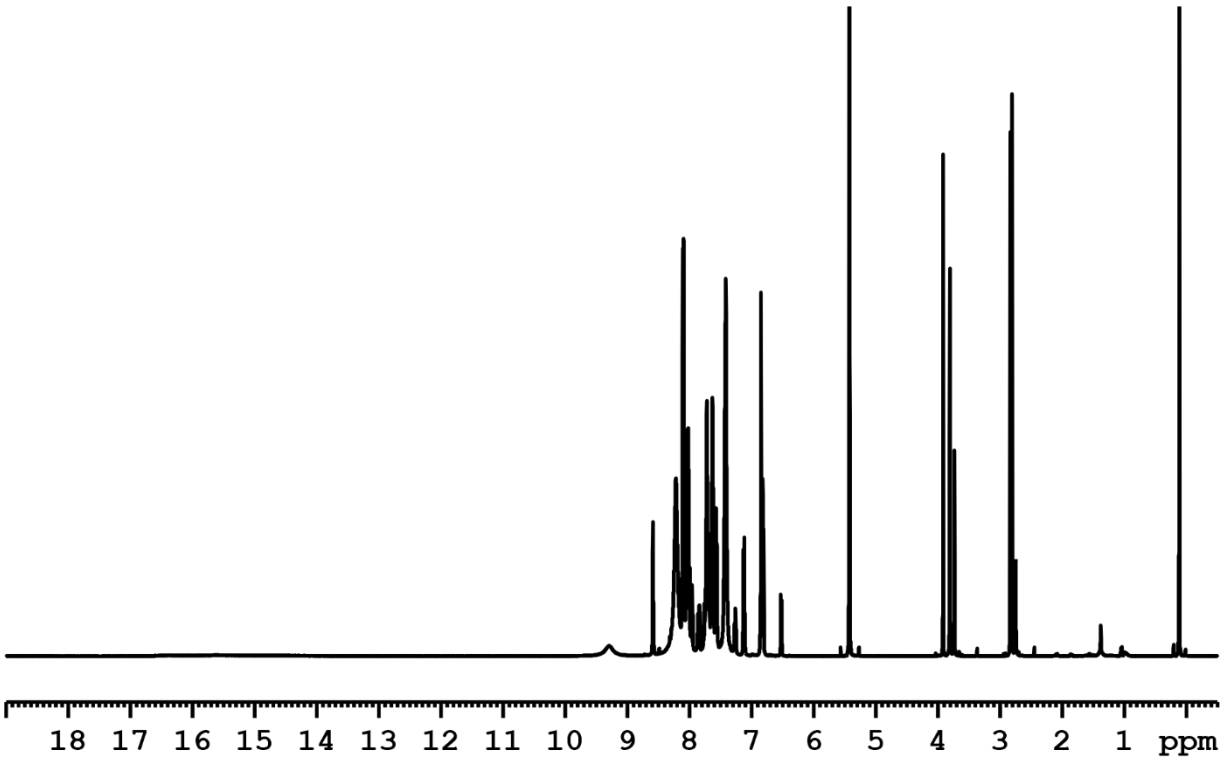

^{1}H-NMR spectra of 1a•2k (2:1 stoichiometry, 50mM:25mM, CD_2Cl_2, 180K, 600MHz).

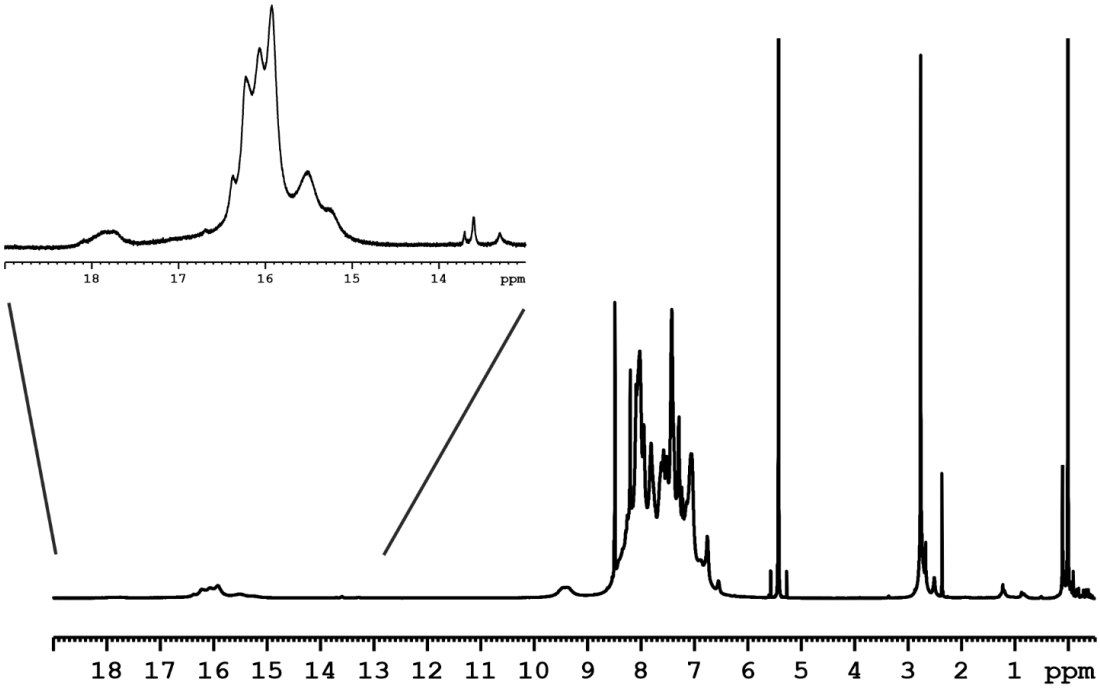

^{1}H-NMR spectra of 1a•2h with an extended hydrogen bond area (2:1 stoichiometry, 50mM:25mM, CD_2Cl_2, 180K, 600MHz).

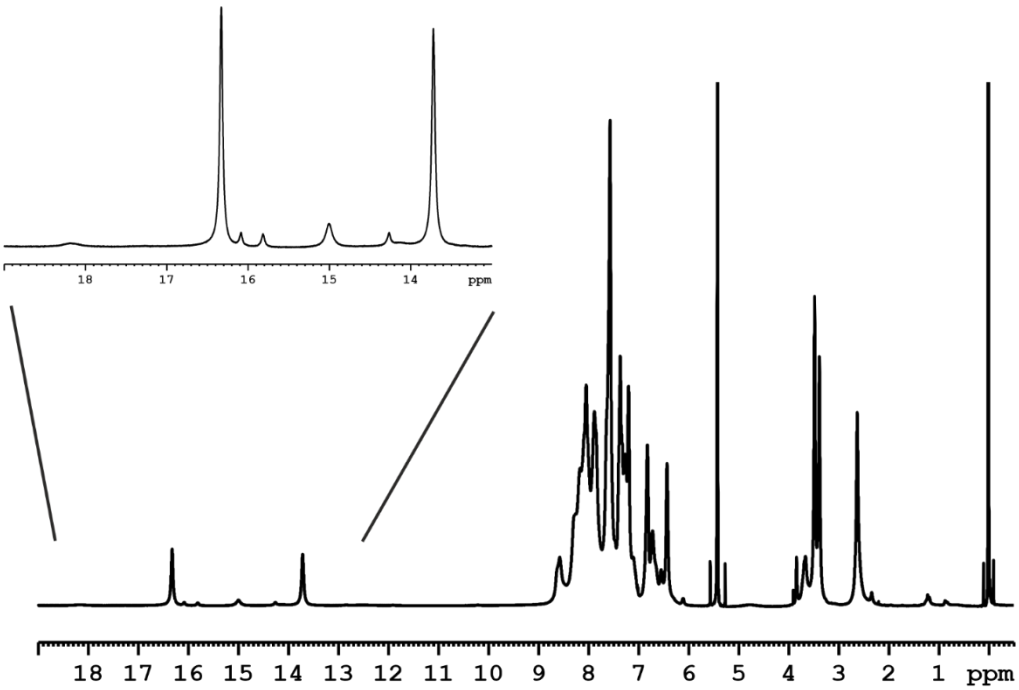

^{1}H-NMR spectra of 1a•2l with an extended hydrogen bond area (2:1 stoichiometry, 50mM:25mM, CD_2Cl_2, 180K, 600MHz).

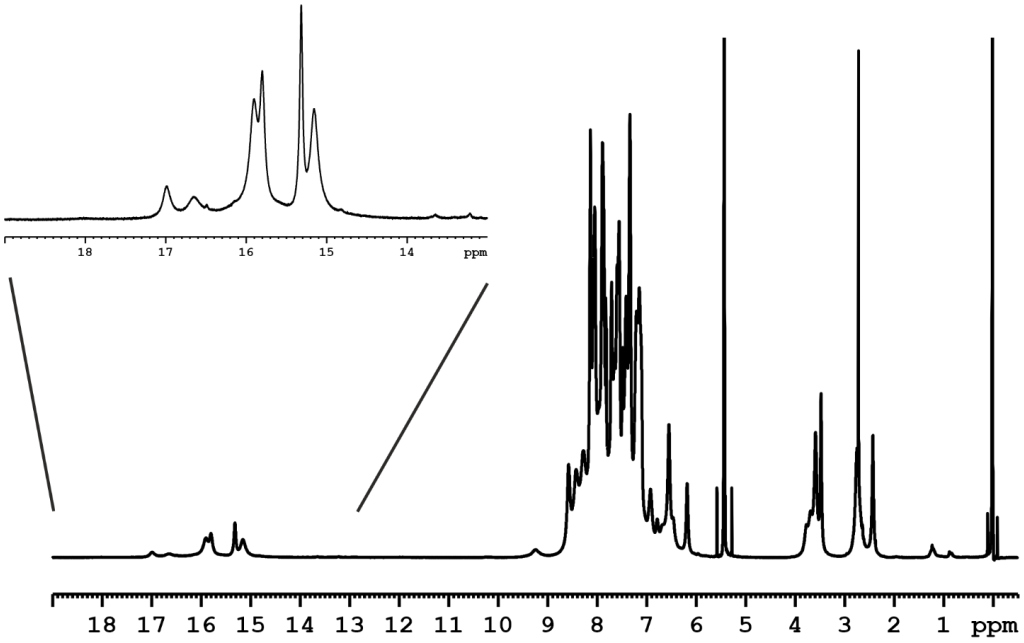

^{1}H-NMR spectra of 1a•2m with an extended hydrogen bond area (2:1 stoichiometry, 50mM:25mM, CD_2Cl_2, 180K, 600MHz).

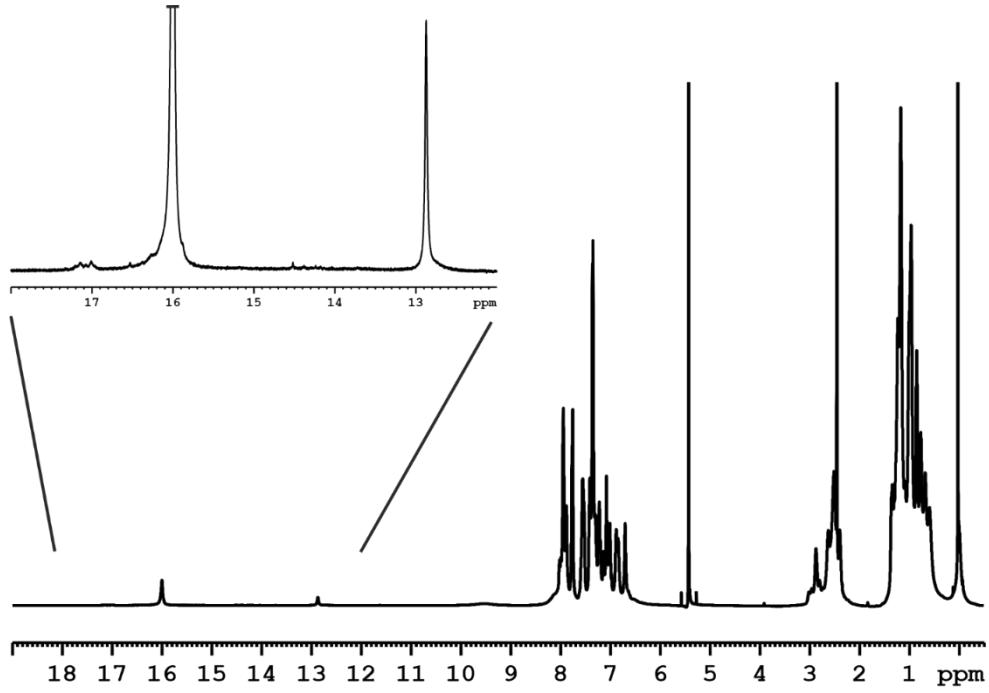

^{1}H-NMR spectra of 1b•2a with an extended hydrogen bond area (2:1 stoichiometry, 50mM:25mM, CD_2Cl_2, 180K, 600MHz).

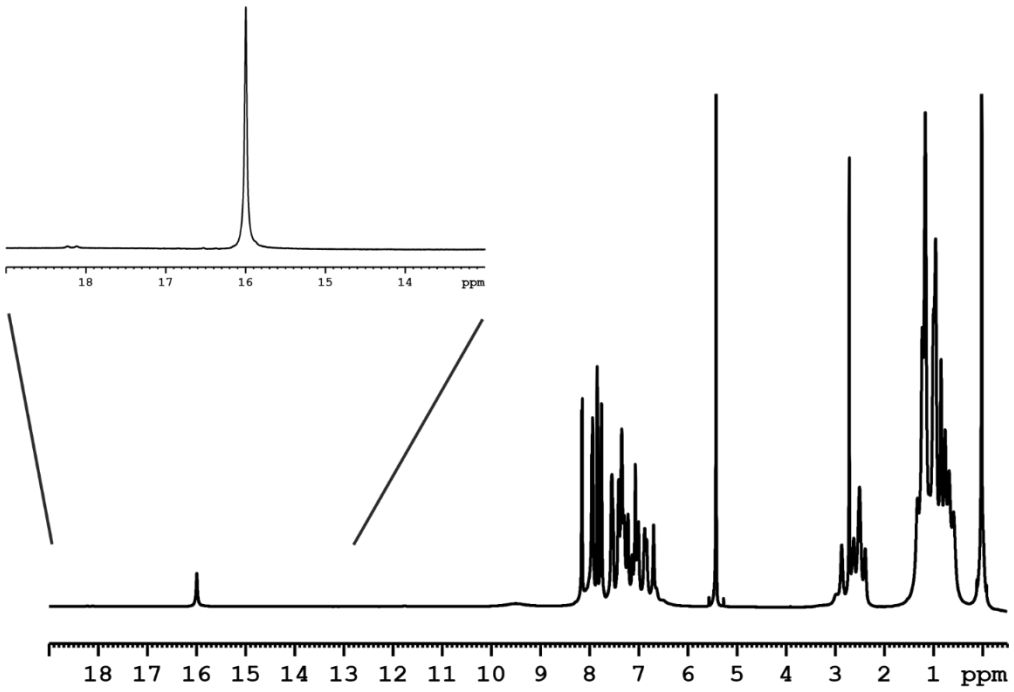

^{1}H-NMR spectra of 1b•2c with an extended hydrogen bond area (2:1 stoichiometry, 50mM:25mM, CD_2Cl_2, 180K, 600MHz).

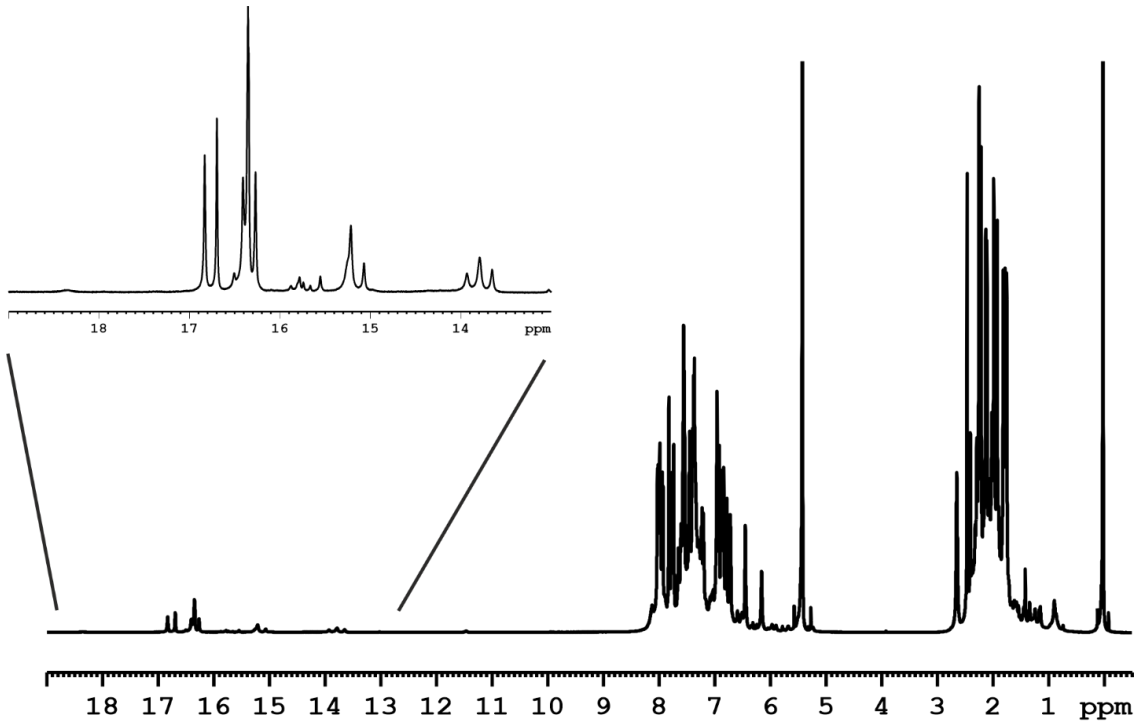

^{1}H-NMR spectra of 1c•2a with an extended hydrogen bond area (2:1 stoichiometry, 50mM:25mM, CD_2Cl_2, 180K, 600MHz).

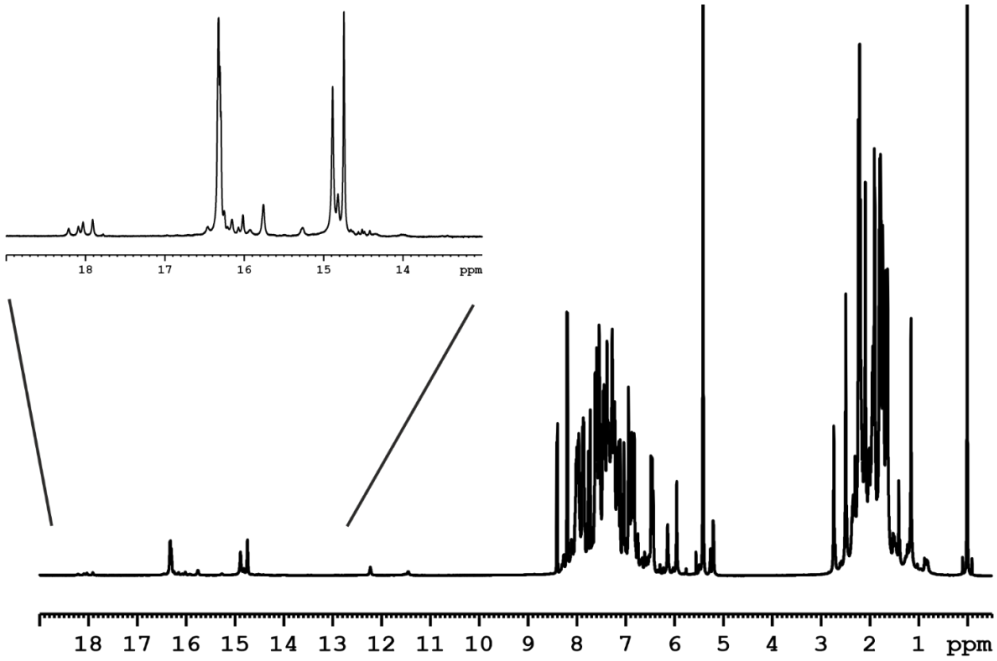

^{1}H-NMR spectra of 1c•2d with an extended hydrogen bond area (2:1 stoichiometry, 50mM:25mM, CD_2Cl_2, 180K, 600MHz).

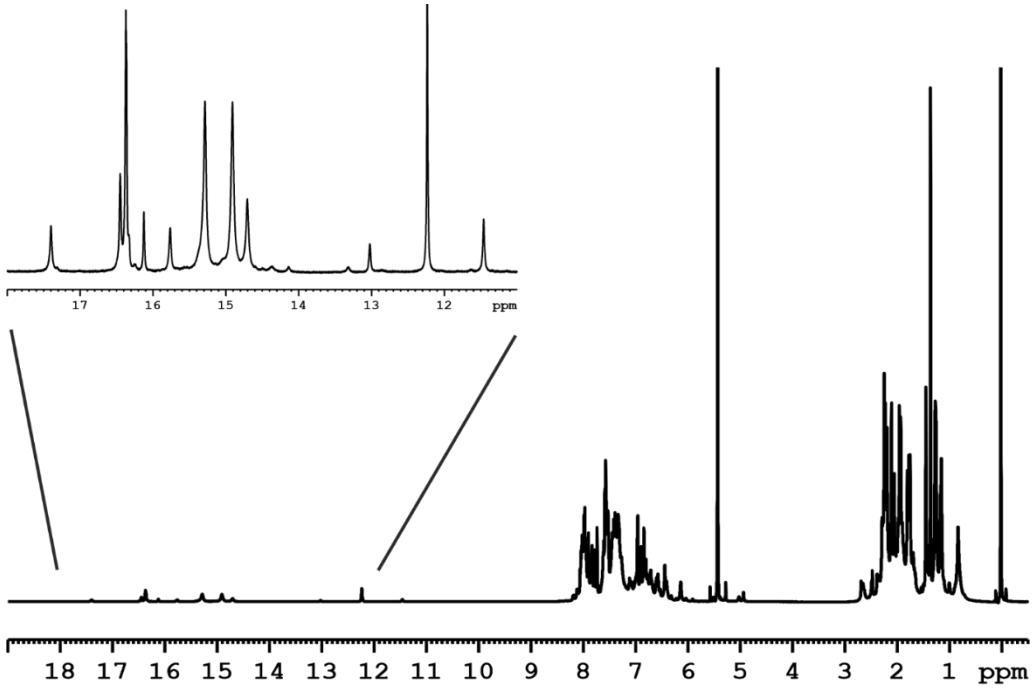

^{1}H-NMR spectra of 1c•2g with an extended hydrogen bond area (2:1 stoichiometry, 50mM:25mM, CD_2Cl_2, 180K, 600MHz).

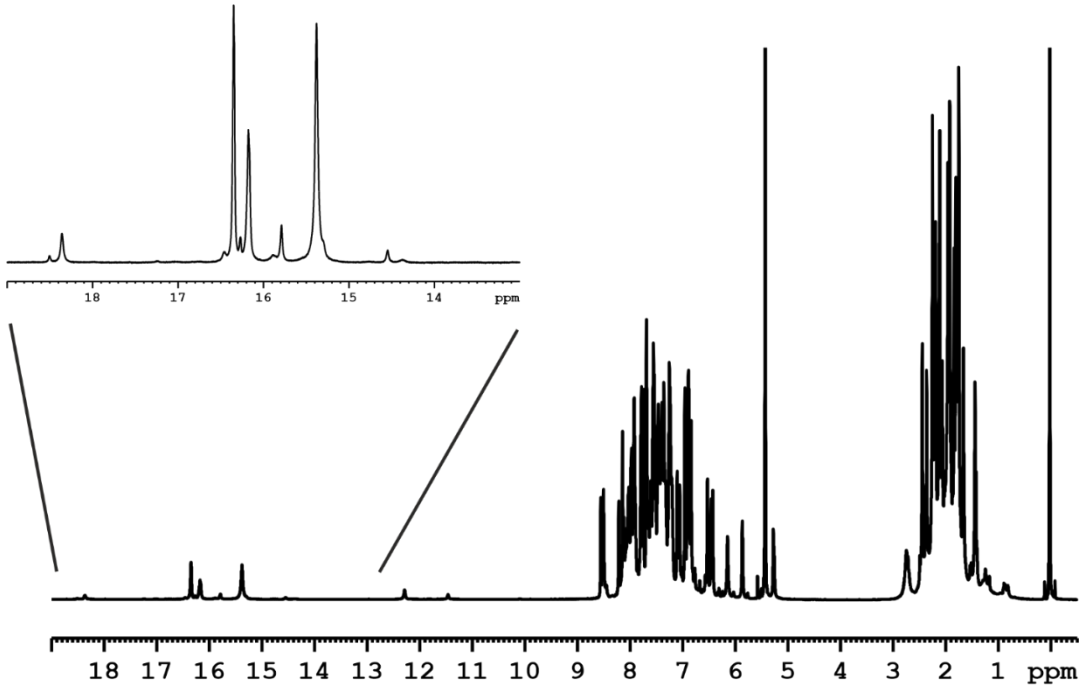

^{1}H-NMR spectra of 1c•2h with an extended hydrogen bond area (2:1 stoichiometry, 50mM:25mM, CD_2Cl_2, 180K, 600MHz).

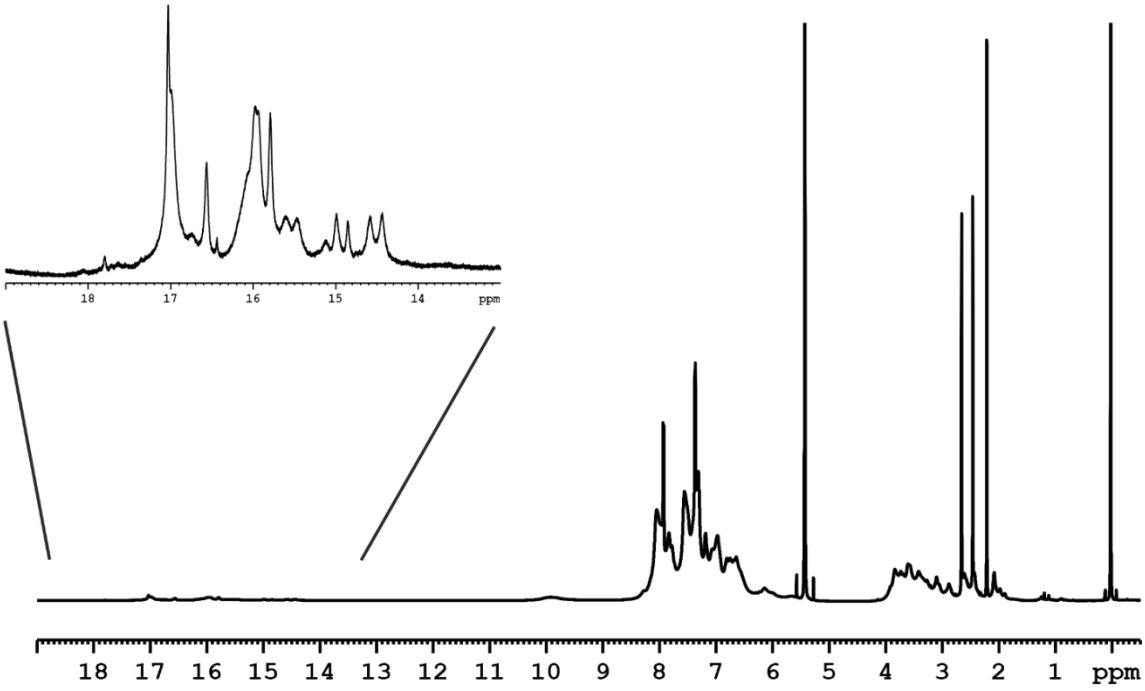

^{1}H-NMR spectra of 1d•2a with an extended hydrogen bond area (2:1 stoichiometry, 50mM:25mM, CD_2Cl_2, 180K, 600MHz).

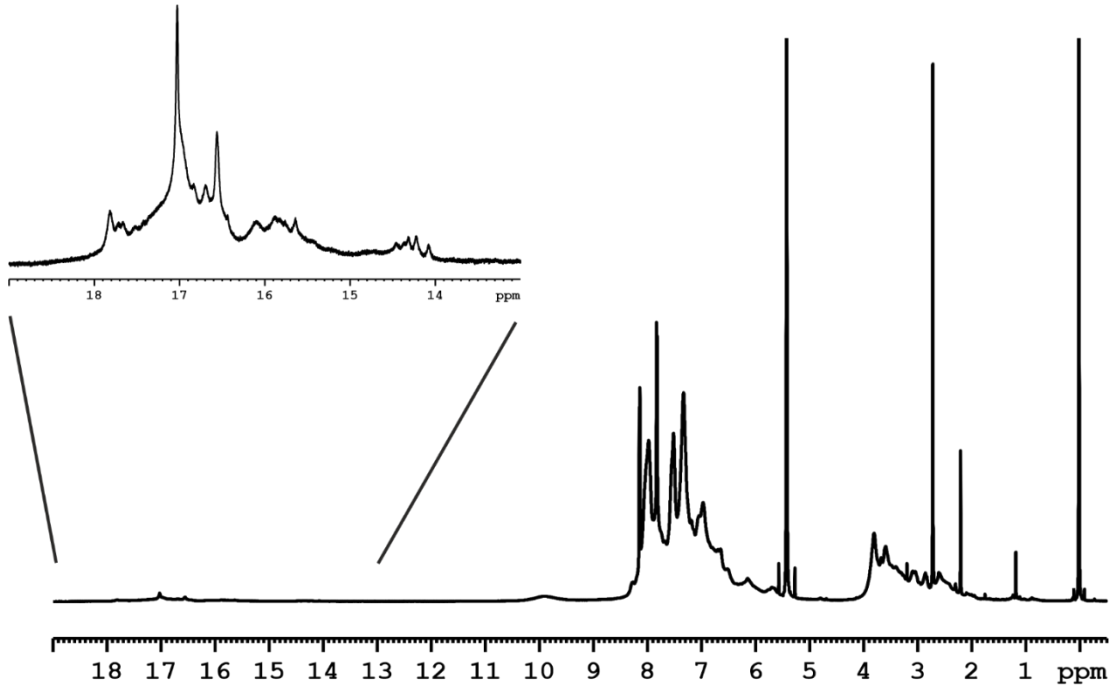

^{1}H-NMR spectra of 1d•2c with an extended hydrogen bond area (2:1 stoichiometry, 50mM:25mM, CD_2Cl_2, 180K, 600MHz).

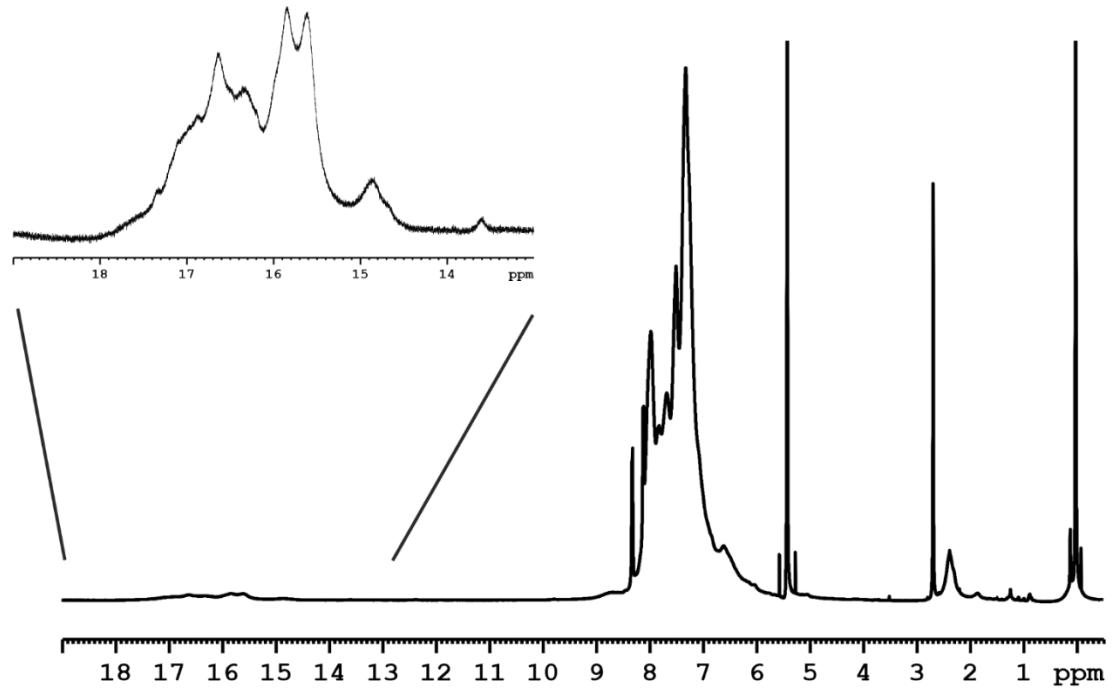

^{1}H-NMR spectra of 1f•2d with an extended hydrogen bond area (2:1 stoichiometry, 50mM:25mM, CD_2Cl_2, 180K, 600MHz).

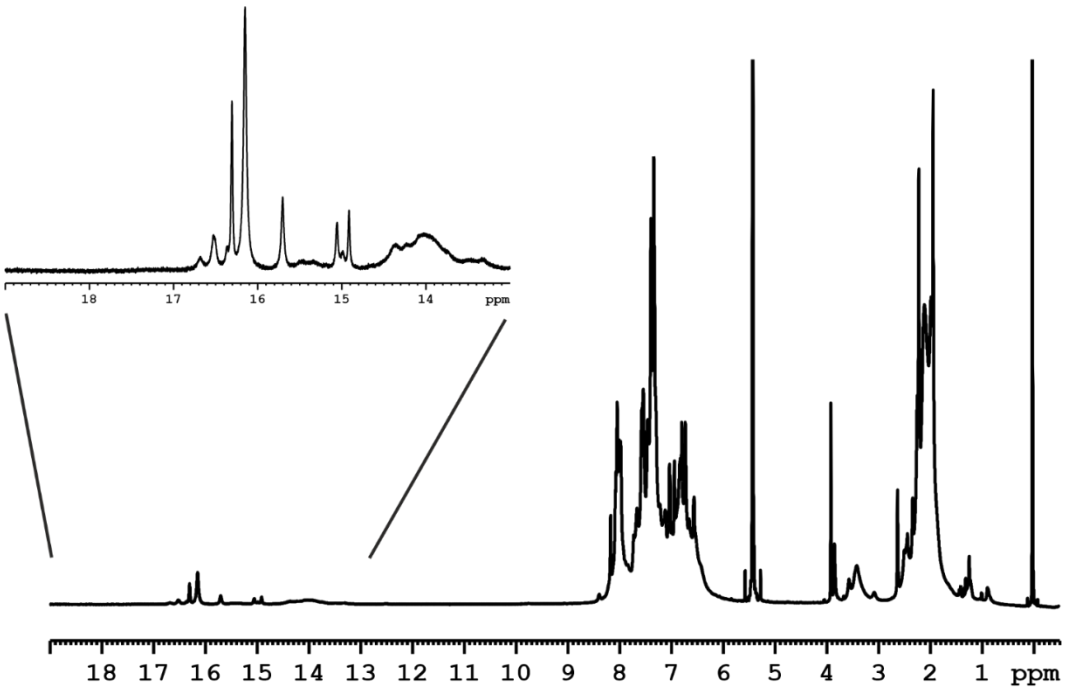

^{1}H-NMR spectra of 1g•2b with an extended hydrogen bond area (2:1 stoichiometry, 50mM:25mM, CD_2Cl_2, 180K, 600MHz).

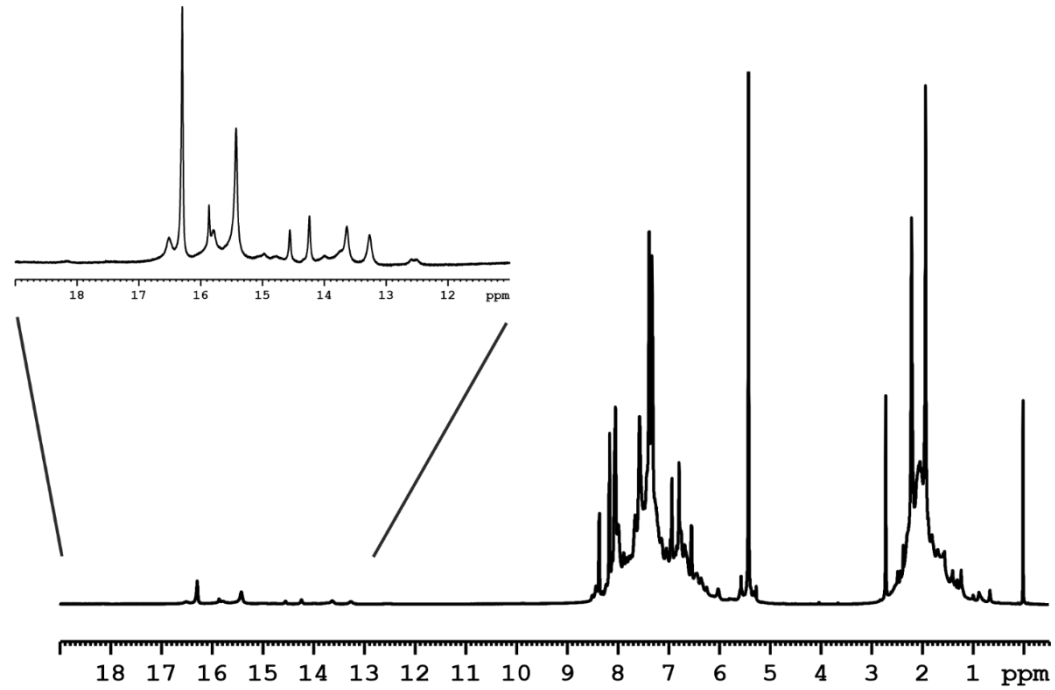

^{1}H-NMR spectra of 1g•2d with an extended hydrogen bond area (2:1 stoichiometry, 50mM:25mM, CD_2Cl_2, 180K, 600MHz).

Ratio of Monomeric to Dimeric Species

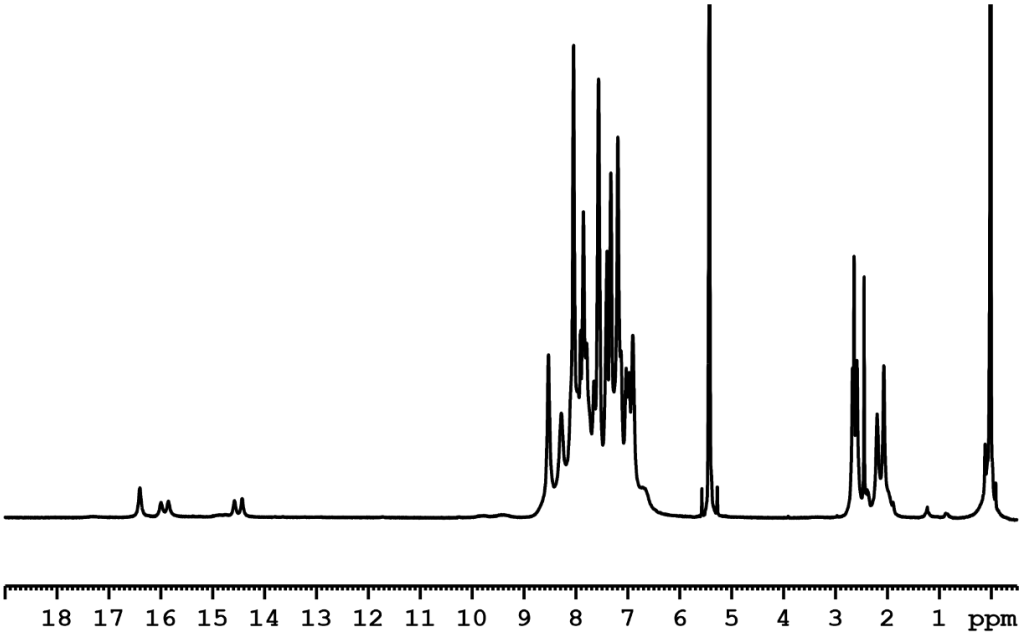

^{1}H-NMR spectra of 1a•2a E-only sample with an extended hydrogen bond area (2:1 stoichiometry, 50mM:25mM, CD_2Cl_2, 180K, 600MHz).

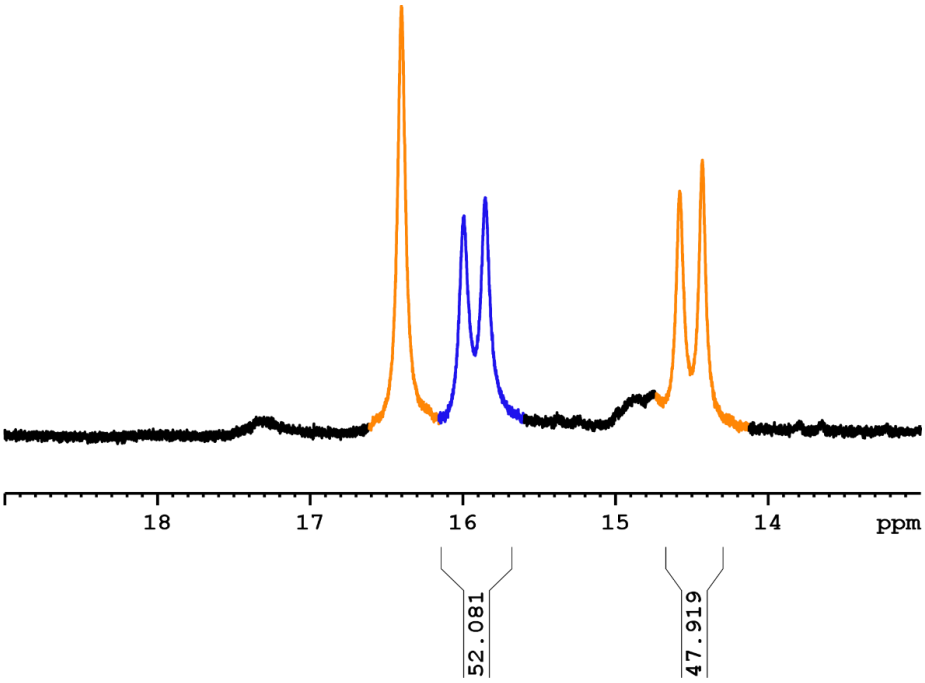

Section of the ^{1}H-NMR spectra of 1a•2a E-only sample zoomed in on the hydrogen bond are (2:1 stoichiometry, 50mM:25mM, CD_2Cl_2, 180K, 600MHz). The dimeric CPA/CPA/E-imine species is marked in orange while the monomeric CPA/E-imine species is marked in blue (for pattern see Chapter 3.4).

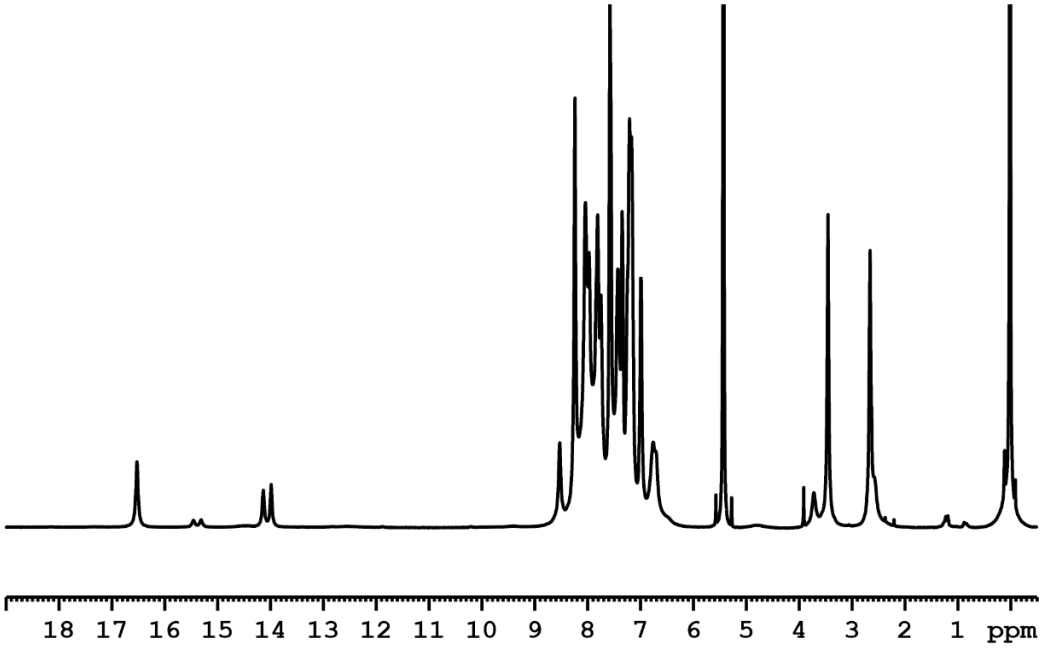

^{1}H-NMR spectra of 1a•2b E-only sample with an extended hydrogen bond area (2:1 stoichiometry, 50mM:25mM, CD_2Cl_2, 180K, 600MHz).

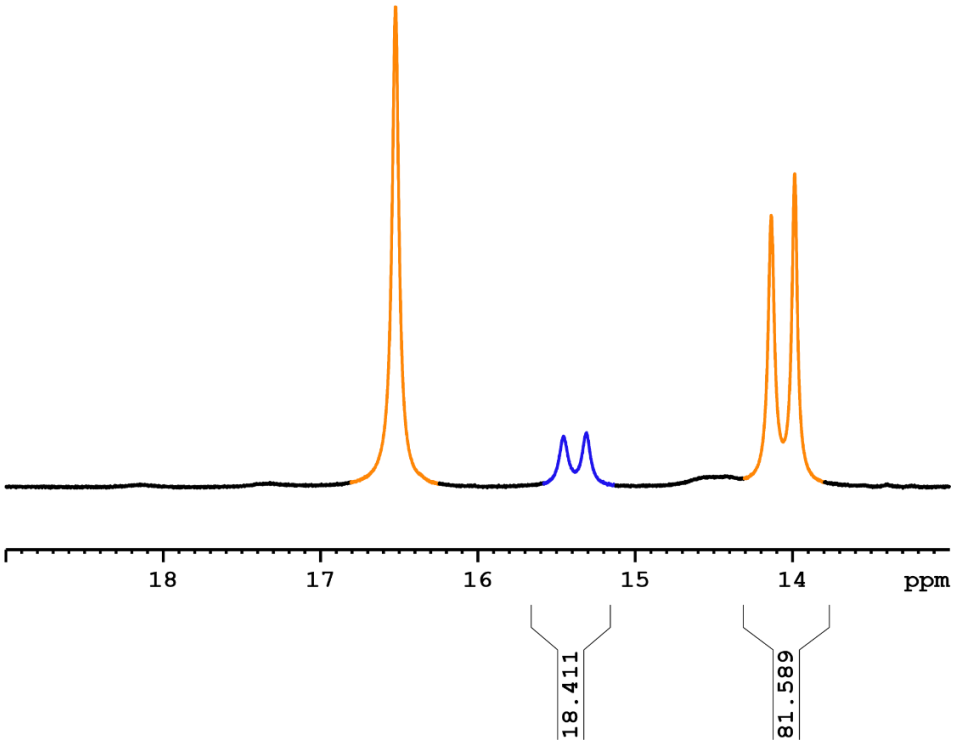

Section of the ^{1}H-NMR spectra of 1a•2b E-only sample zoomed in on the hydrogen bond are (2:1 stoichiometry, 50mM:25mM, CD_2Cl_2, 180K, 600MHz). The dimeric CPA/CPA/E-imine species is marked in orange while the monomeric CPA/E-imine species is marked in blue (for pattern see Chapter 3.4).

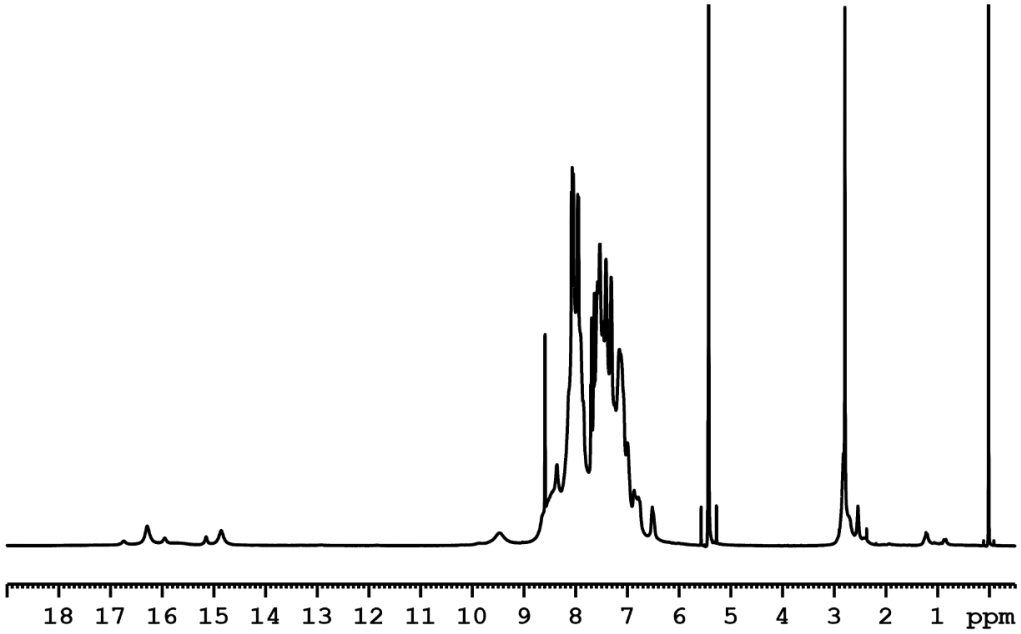

^{1}H-NMR spectra of 1a•2e sample with an extended hydrogen bond area (2:1 stoichiometry, 50mM:25mM, CD_2Cl_2, 180K, 600MHz).

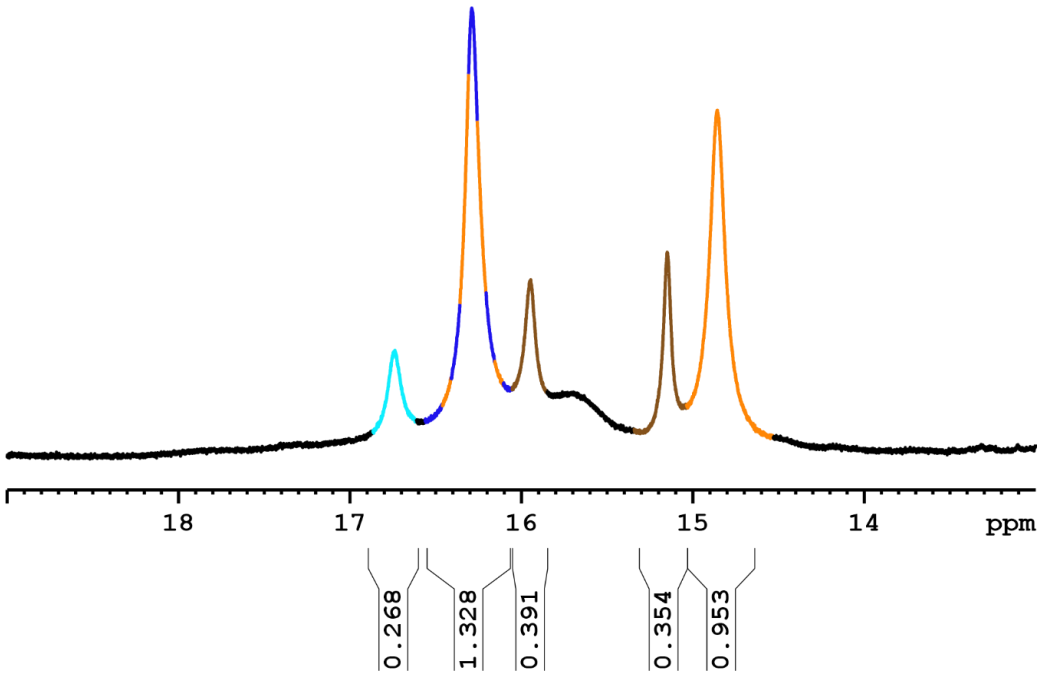

Section of the ^{1}H-NMR spectra of 1a•2e sample zoomed in on the hydrogen bond are (2:1 stoichiometry, 50mM:25mM, CD_2Cl_2, 180K, 600MHz). The dimeric CPA/CPA/E-imine species is marked in orange and the dimeric CPA/CPA/Z-imine species is marked in brown. The monomeric CPA/E-imine species is marked in blue and the monomeric CPA/Z-imine species is marked in light blue (for pattern see Chapter 3.4).

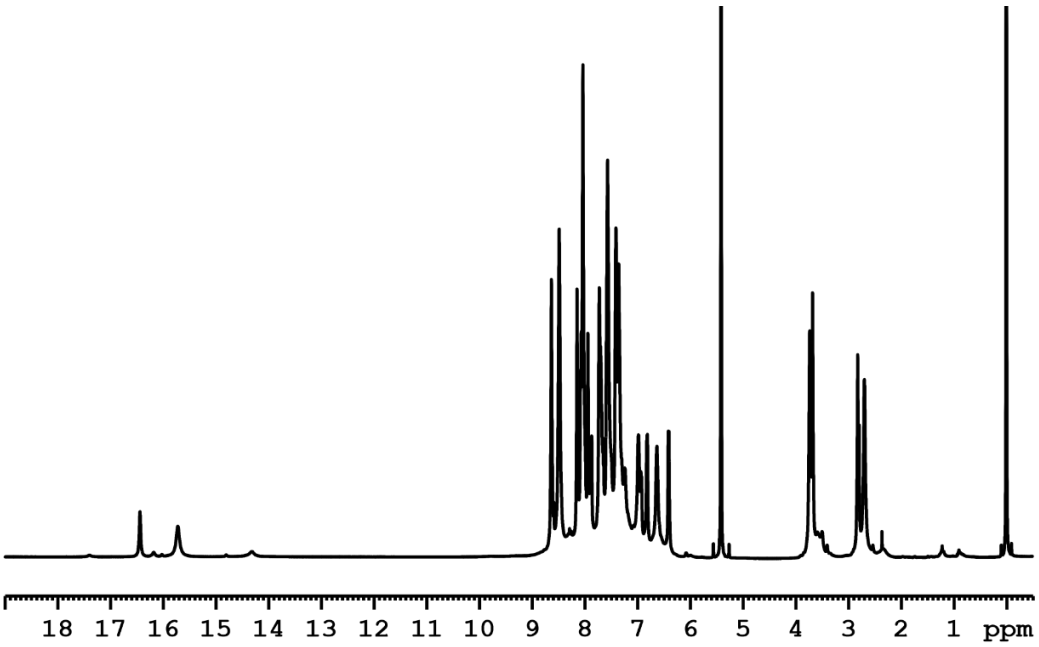

^{1}H-NMR spectra of 1a•2k sample with an extended hydrogen bond area (2:1 stoichiometry, 50mM:25mM, CD_2Cl_2, 180K, 600MHz).

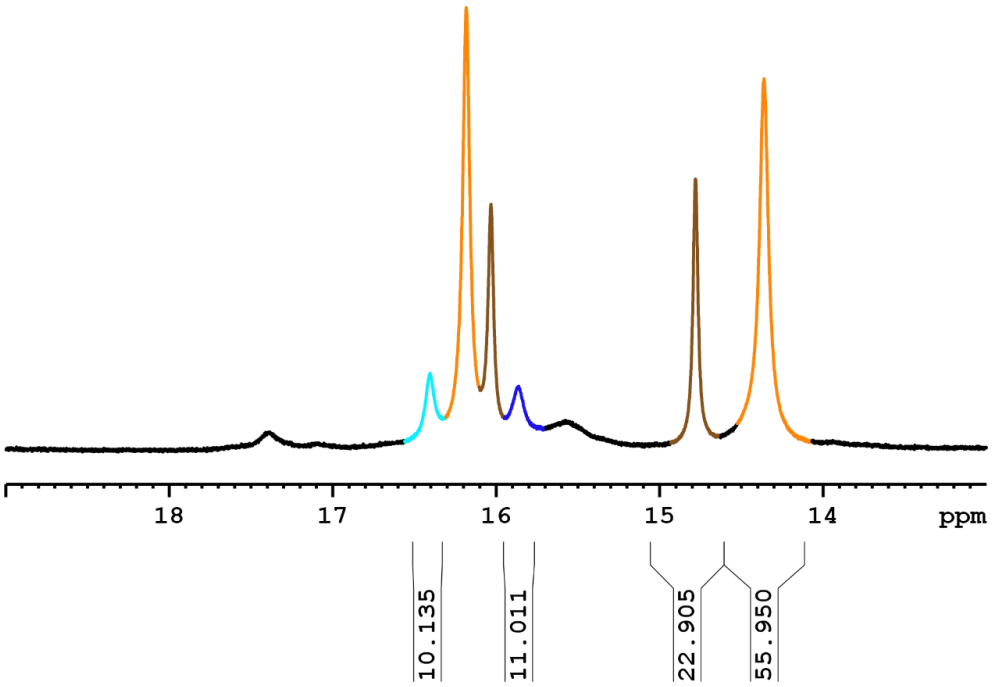

Section of the ^{1}H-NMR spectra of 1a•2k sample zoomed in on the hydrogen bond are (2:1 stoichiometry, 50mM:25mM, CD_2Cl_2, 180K, 600MHz). The dimeric CPA/CPA/E-imine species is marked in orange and the dimeric CPA/CPA/Z-imine species is marked in brown. The monomeric CPA/E-imine species is marked in blue and the monomeric CPA/Z-imine species is marked in light blue (for pattern see Chapter 3.4).

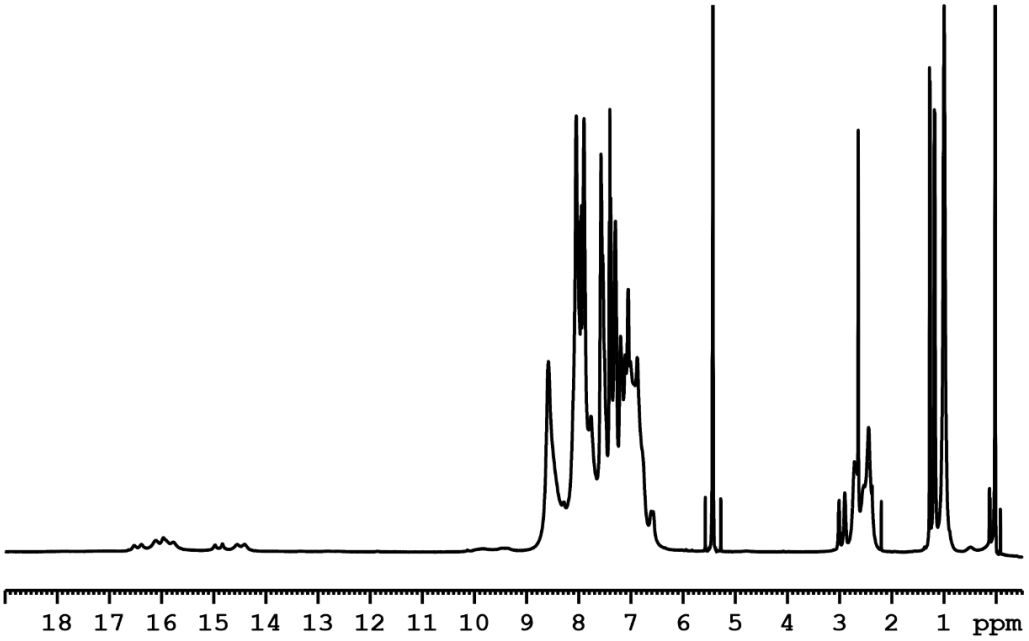

^{1}H-NMR spectra of 1a•2f sample with an extended hydrogen bond area (2:1 stoichiometry, 50mM:25mM, CD_2Cl_2, 180K, 600MHz).

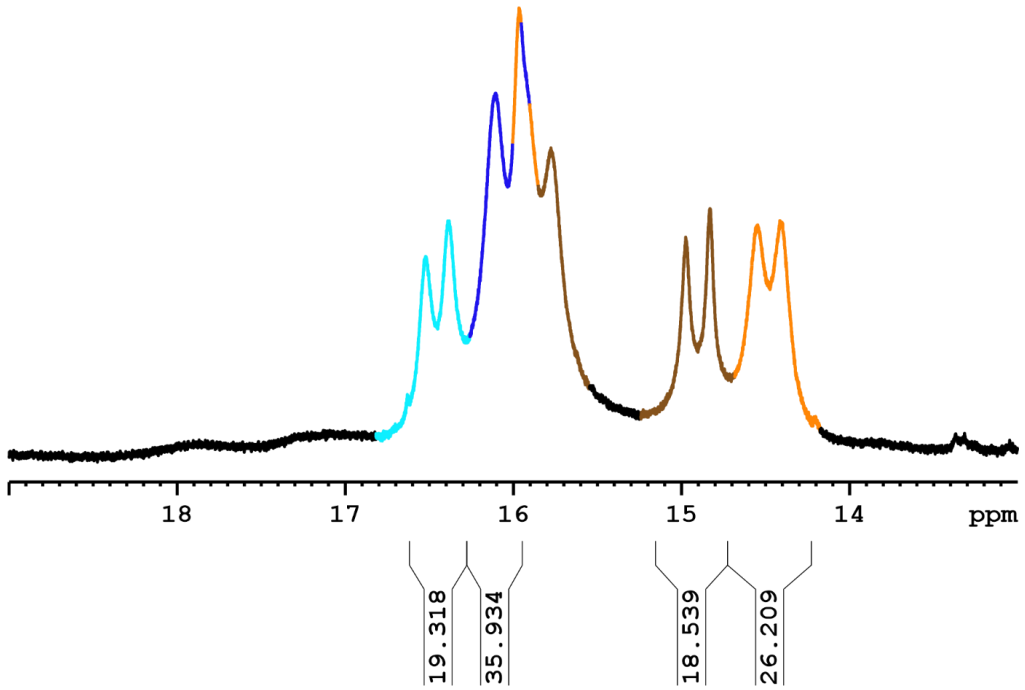

Section of the ^{1}H-NMR spectra of 1a•2f sample zoomed in on the hydrogen bond are (2:1 stoichiometry, 50mM:25mM, CD_2Cl_2, 180K, 600MHz). The dimeric CPA/CPA/E-imine species is marked in orange and the dimeric CPA/CPA/Z-imine species is marked in brown. The monomeric CPA/E-imine species is marked in blue and the monomeric CPA/Z-imine species is marked in light blue (for pattern see Chapter 3.4).

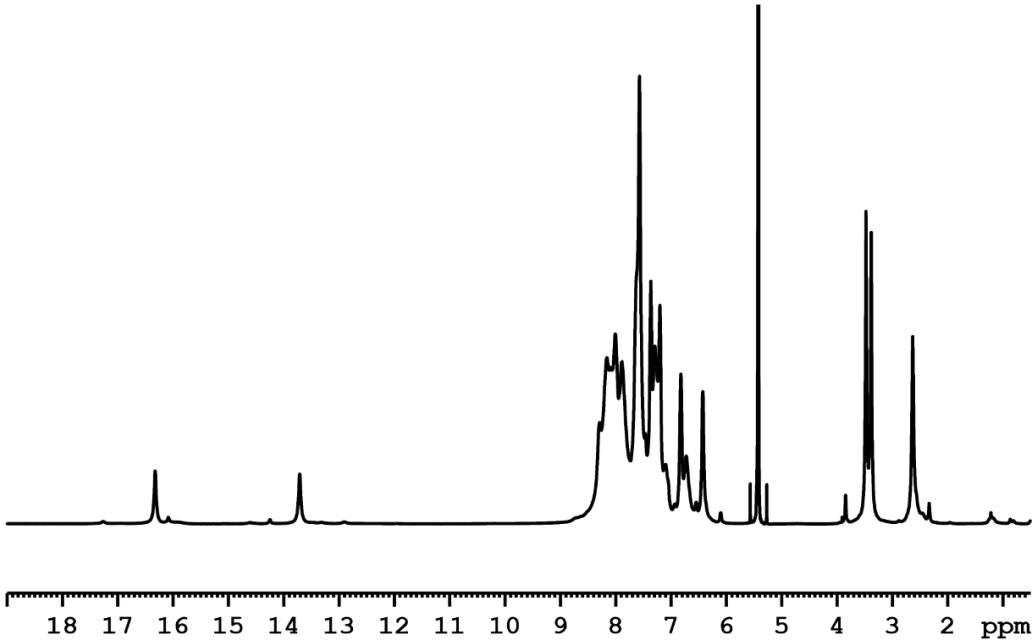

^{1}H-NMR spectra of 1a•2i sample with an extended hydrogen bond area (2:1 stoichiometry, 50mM:25mM, CD_2Cl_2, 180K, 600MHz).

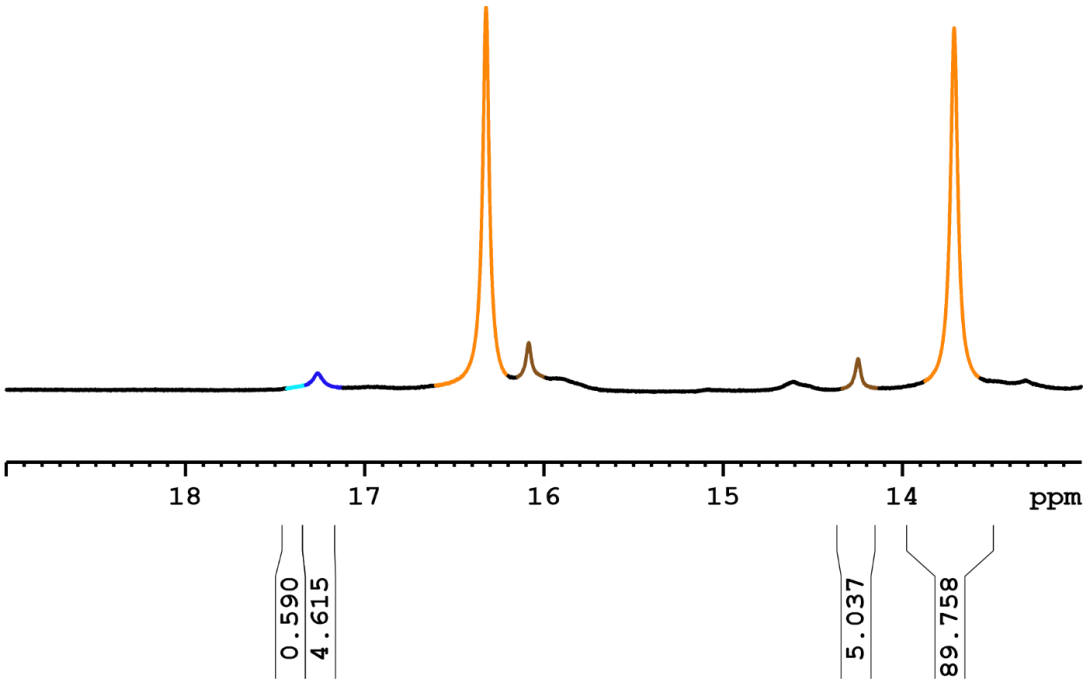

Section of the ^{1}H-NMR spectra of 1a•2i sample zoomed in on the hydrogen bond are (2:1 stoichiometry, 50mM:25mM, CD_2Cl_2, 180K, 600MHz). The dimeric CPA/CPA/E-imine species is marked in orange and the dimeric CPA/CPA/Z-imine species is marked in brown. The monomeric CPA/E-imine species is marked in blue and the monomeric CPA/Z-imine species is marked in light blue (for pattern see Chapter 3.4).

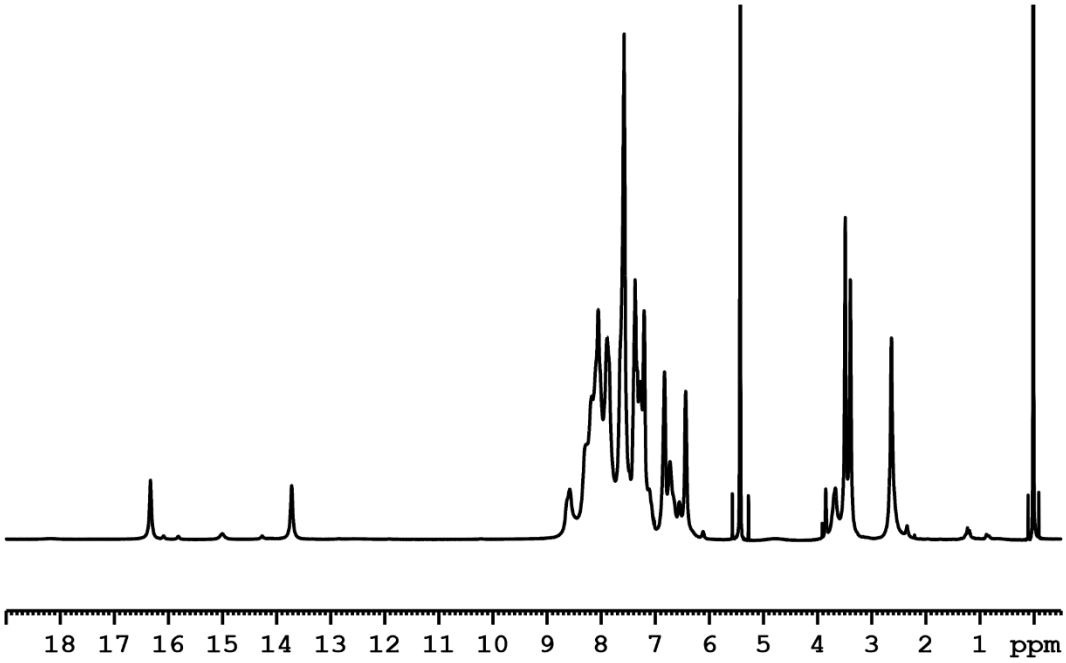

^{1}H-NMR spectra of 1a•2l sample with an extended hydrogen bond area (2:1 stoichiometry, 50mM:25mM, CD_2Cl_2, 180K, 600MHz).

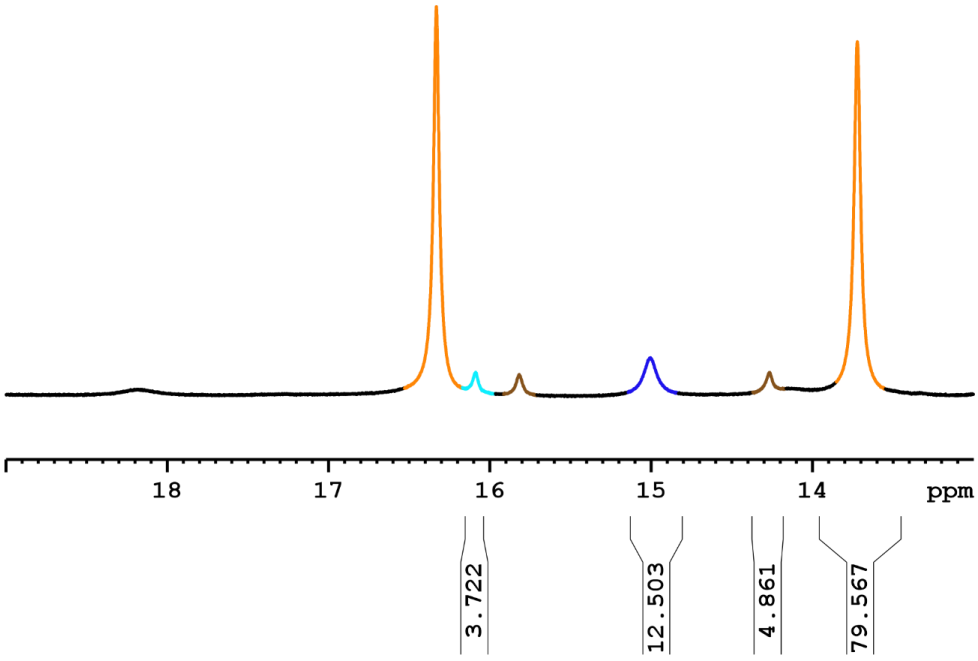

Section of the ^{1}H-NMR spectra of 1a•2l sample zoomed in on the hydrogen bond are (2:1 stoichiometry, 50mM:25mM, CD_2Cl_2, 180K, 600MHz). The dimeric CPA/CPA/E-imine species is marked in orange and the dimeric CPA/CPA/Z-imine species is marked in brown. The monomeric CPA/E-imine species is marked in blue and the monomeric CPA/Z-imine species is marked in light blue (for pattern see Chapter 3.4).

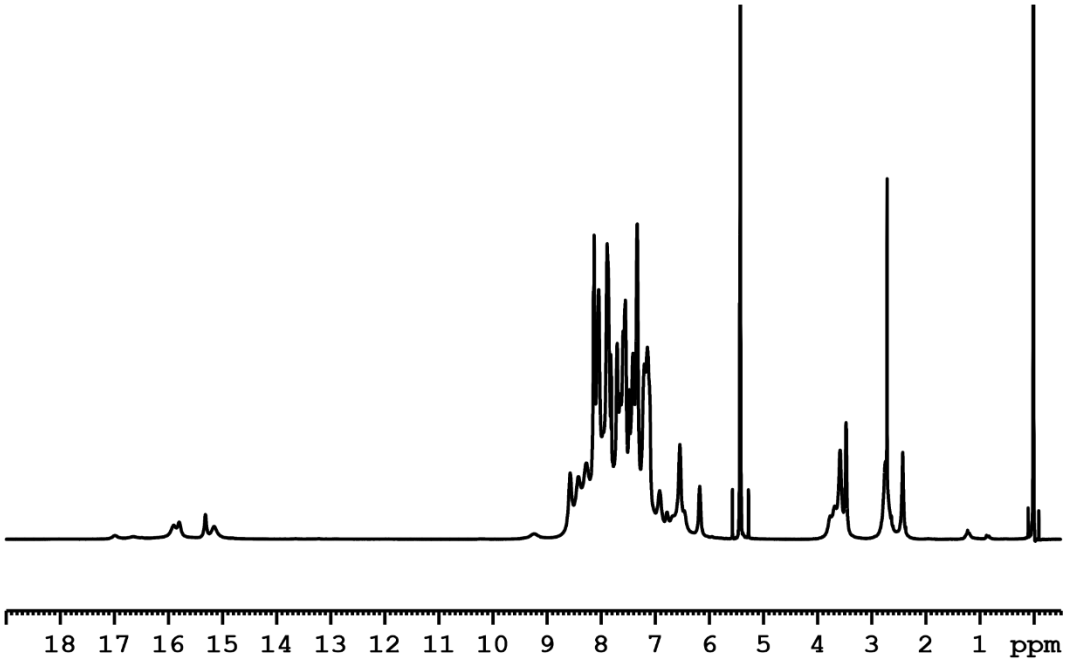

^{1}H-NMR spectra of 1a•2m sample with an extended hydrogen bond area (2:1 stoichiometry, 50mM:25mM, CD_2Cl_2, 180K, 600MHz).

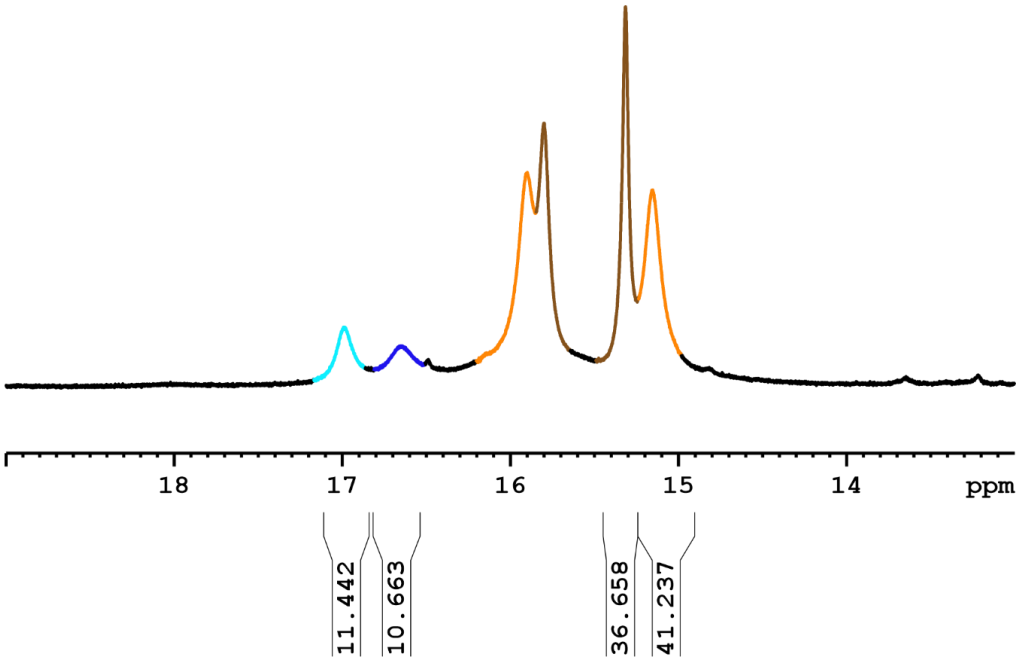

Section of the ^{1}H-NMR spectra of 1a•2m sample zoomed in on the hydrogen bond are (2:1 stoichiometry, 50mM:25mM, CD_2Cl_2, 180K, 600MHz). The dimeric CPA/CPA/E-imine species is marked in orange and the dimeric CPA/CPA/Z-imine species is marked in brown. The monomeric CPA/E-imine species is marked in blue and the monomeric CPA/Z-imine species is marked in light blue (for pattern see Chapter 3.4).

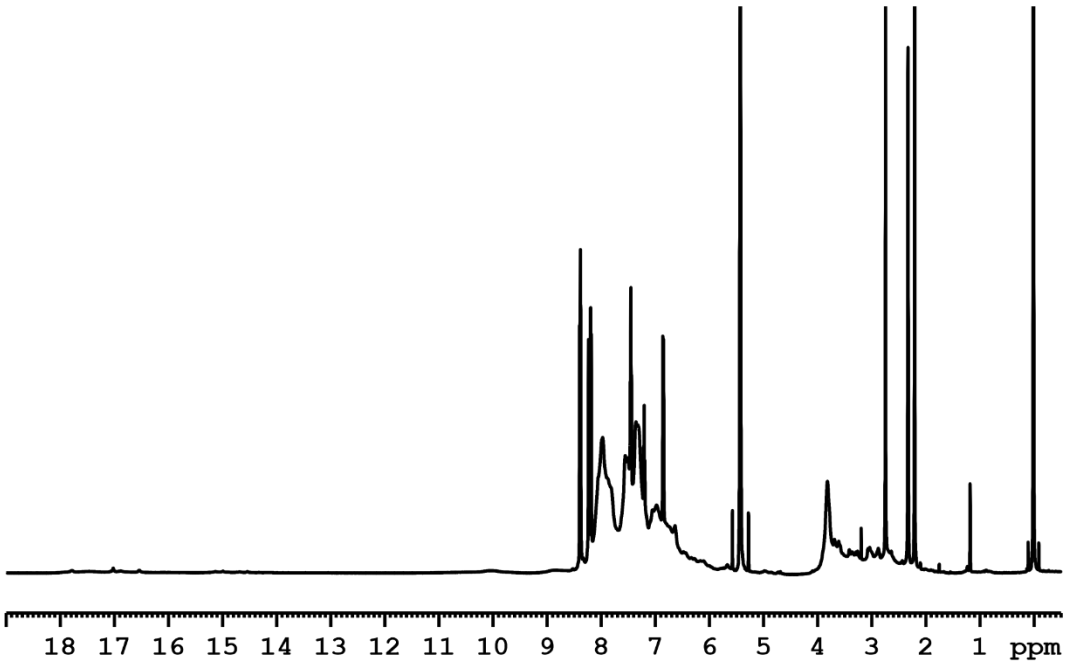

^{1}H-NMR spectra of 1d•2d sample with an extended hydrogen bond area (2:1 stoichiometry, 50mM:25mM, CD_2Cl_2, 180K, 600MHz).

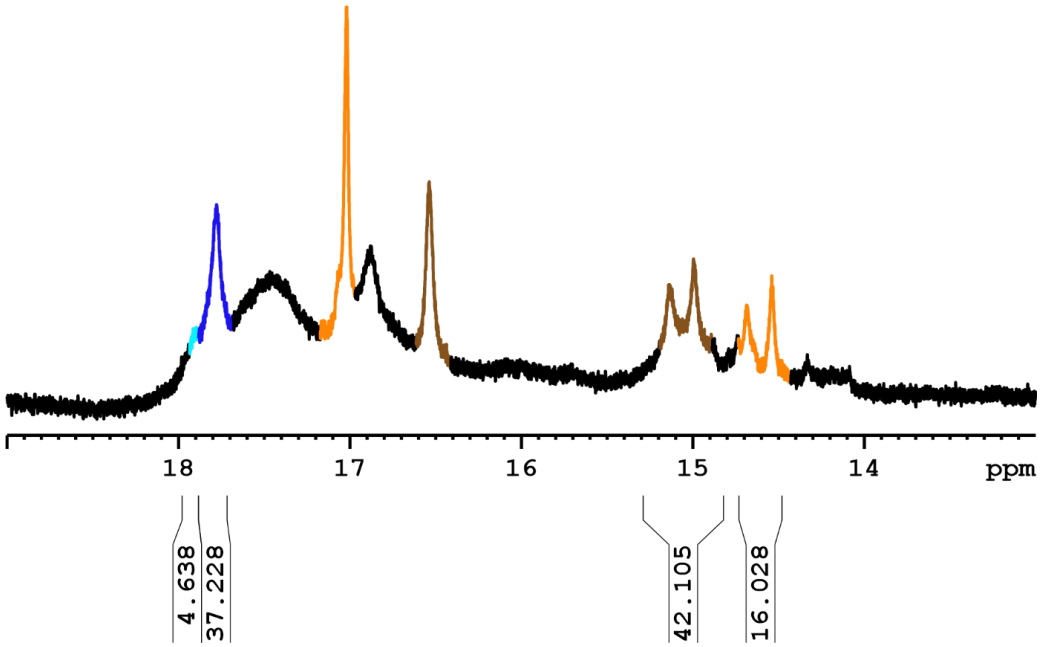

Section of the ^{1}H-NMR spectra of 1d•2d sample zoomed in on the hydrogen bond are (2:1 stoichiometry, 50mM:25mM, CD_2Cl_2, 180K, 600MHz). The dimeric CPA/CPA/E-imine species is marked in orange and the dimeric CPA/CPA/Z-imine species is marked in brown. The monomeric CPA/E-imine species is marked in blue and the monomeric CPA/Z-imine species is marked in light blue (for pattern see Chapter 3.4).

3.6.8.2. HPLC Chromatograms

The conditions for separating major and minor enantiomer were previously established in our group.[3] In this work, major and minor enantiomer were assigned based on the analogous retention times. Chromatograms are displayed including the UV spectra of the respective peaks (top right corner) and a zoomed in version of the chromatogram (bottom).

Amine **4b**; racemic

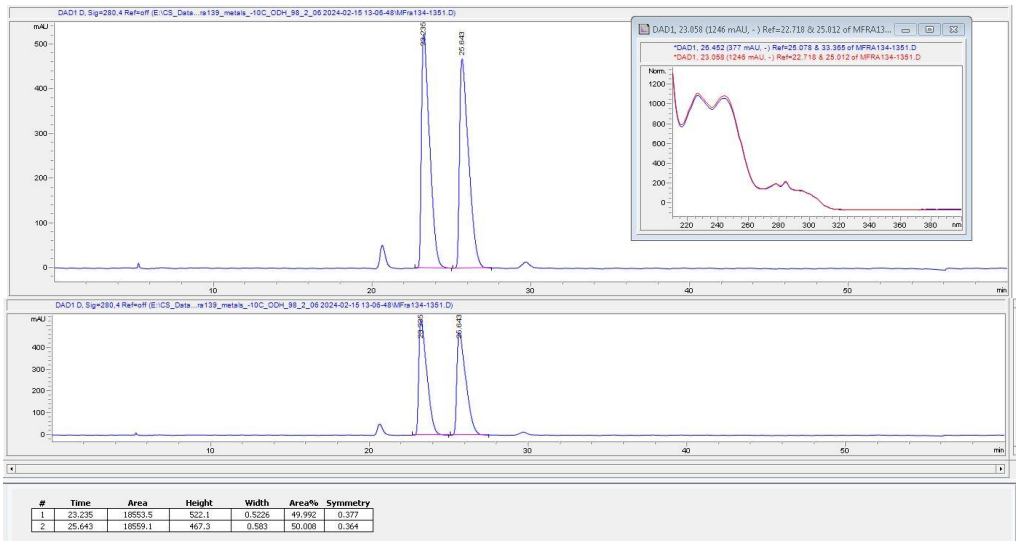

#	Time	Area	Height	Width	Area%	Symmetry
1	23.235	18553.5	522.1	0.5226	49.992	0.377
2	25.643	18559.1	467.3	0.583	50.008	0.364

Amine **4b**; GP II (5°C); 1 mol% TRIFP **1a**

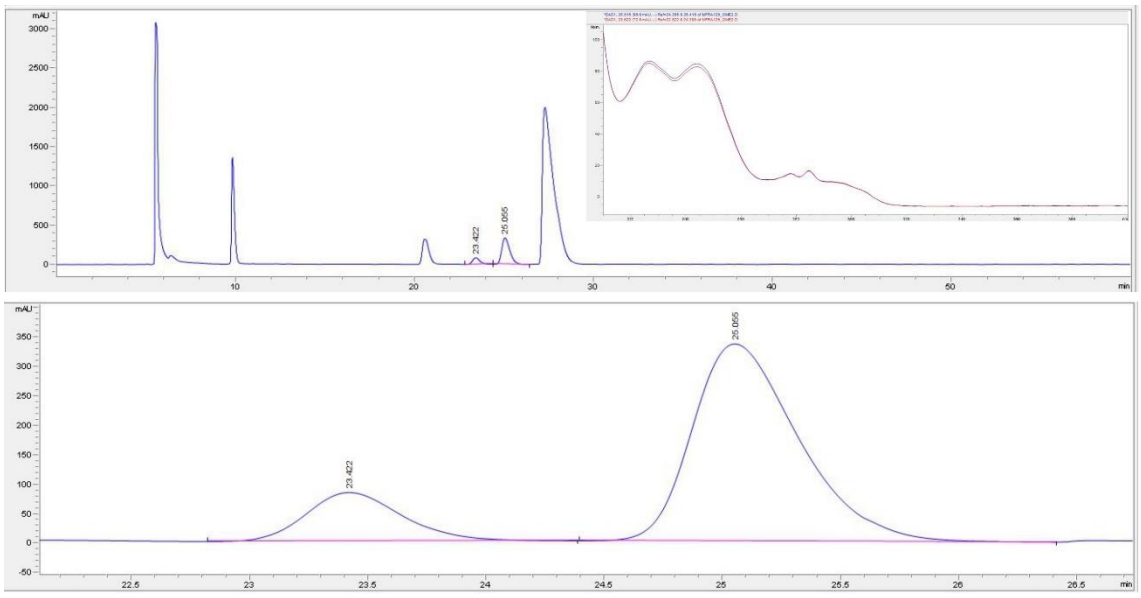

#	Time	Area	Height	Width	Area%	Symmetry
1	23.422	2342.7	82.8	0.4341	18.246	0.778
2	25.055	10496.8	335.8	0.4787	81.754	0.64

Amine **4b**; GP II (5°C); 3 mol% TRIFP **1a**

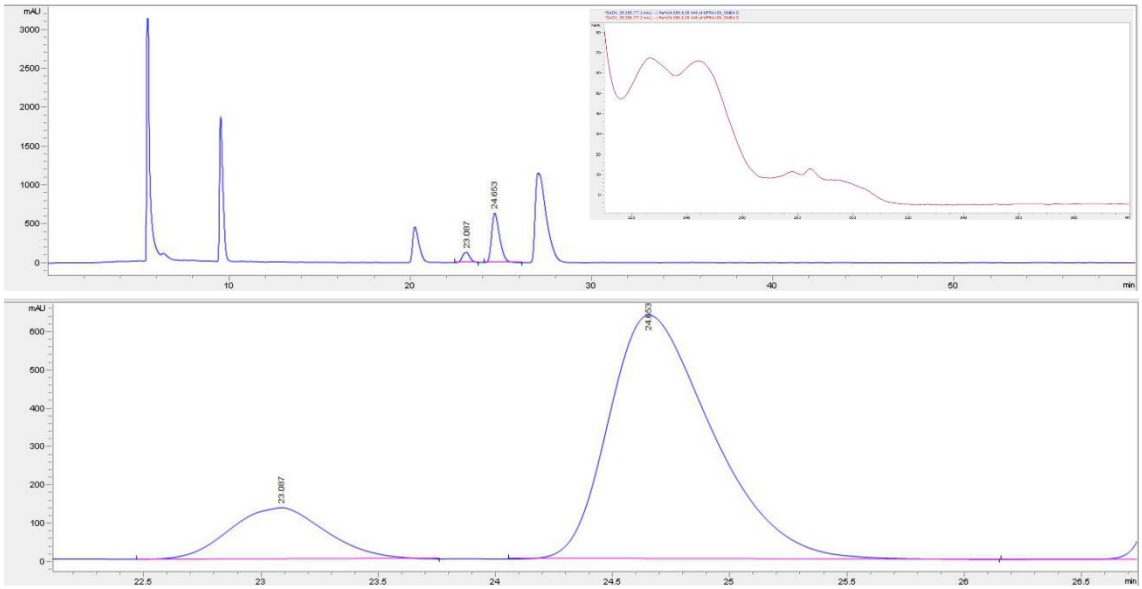

#	Time	Area	Height	Width	Area%	Symmetry
1	23.087	3762.3	133.6	0.3827	16.205	1.102
2	24.653	19453.8	634.1	0.4719	83.795	0.607

Amine **4b**; GP II (5°C); 5 mol% TRIFP **1a**

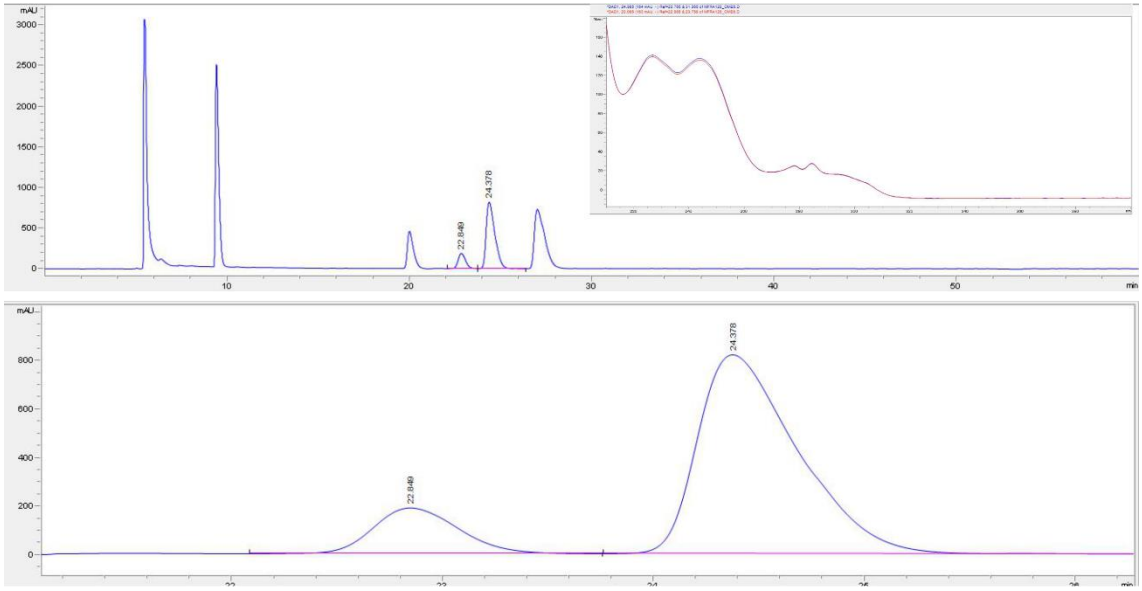

#	Time	Area	Height	Width	Area%	Symmetry
1	22.849	5303.3	188.4	0.4444	16.425	0.762
2	24.378	26984.2	820.1	0.4952	83.575	0.513

Amine **4b**; GP II (10°C); 1 mol% TRIFP **1a**

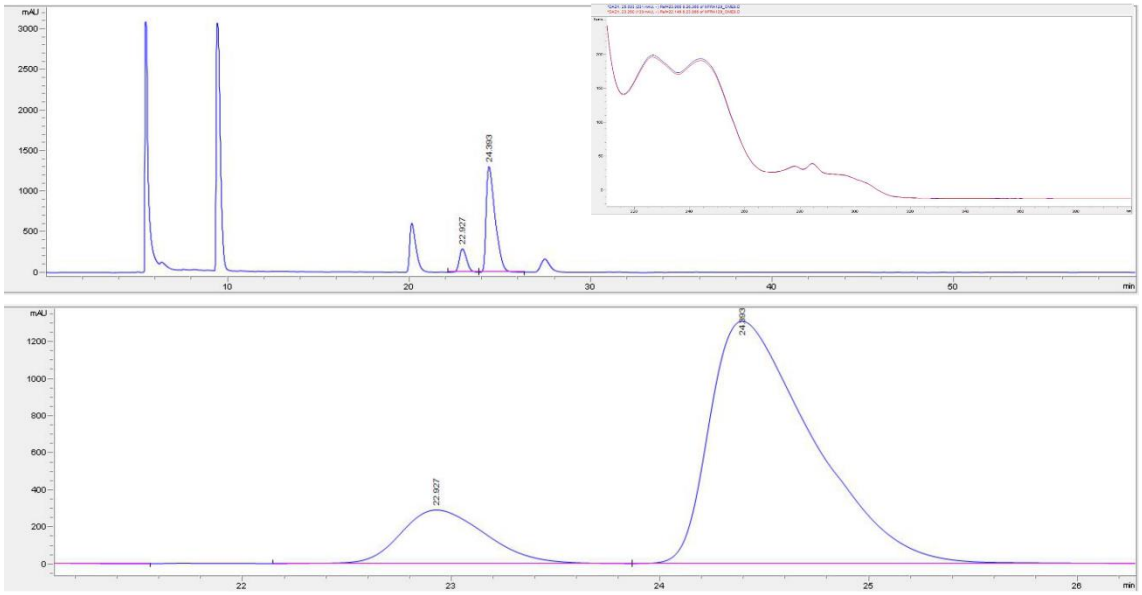

#	Time	Area	Height	Width	Area%	Symmetry
1	22.927	8144.6	289.4	0.4484	15.374	0.706
2	24.393	44830.6	1308.2	0.5178	84.626	0.431

Amine **4b**; GP II (5°C); 15 mol% TRIFP **1a**

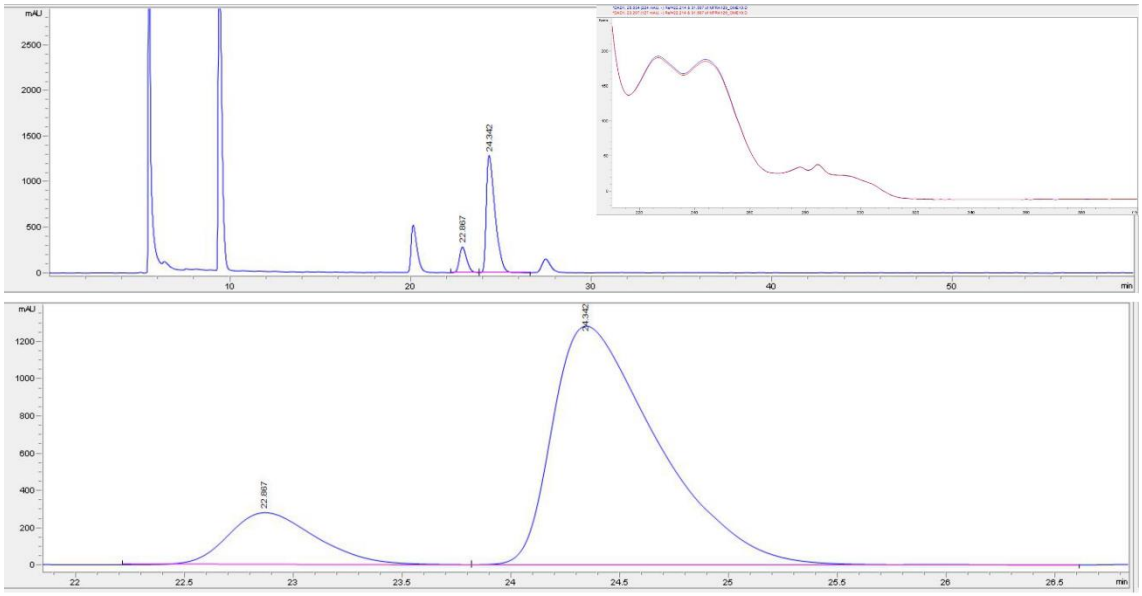

#	Time	Area	Height	Width	Area%	Symmetry
1	22.867	7899.8	280.7	0.4343	15.462	0.693
2	24.342	43192.8	1286.4	0.4972	84.538	0.442

Amine **4b**; GP II (5°C); 20 mol% TRIFP **1a**

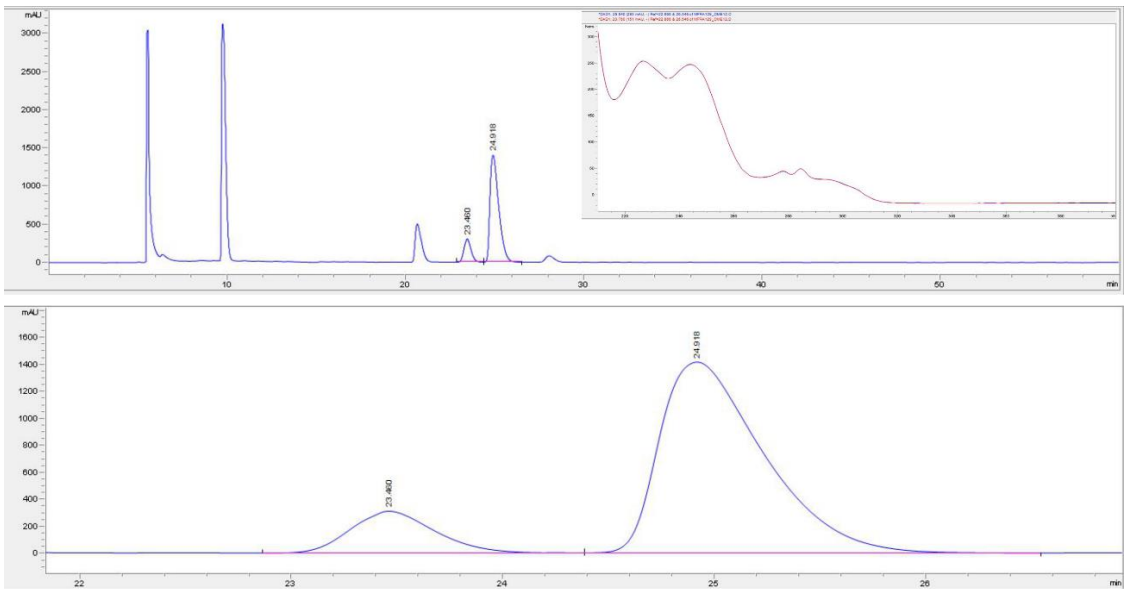

#	Time	Area	Height	Width	Area%	Symmetry
1	23.46	8505.8	309	0.3885	15.008	0.799
2	24.918	48169.2	1410.7	0.5204	84.992	0.524

Amine **4b**; GP II (-10°C); 1 mol% TRIFP **1a**

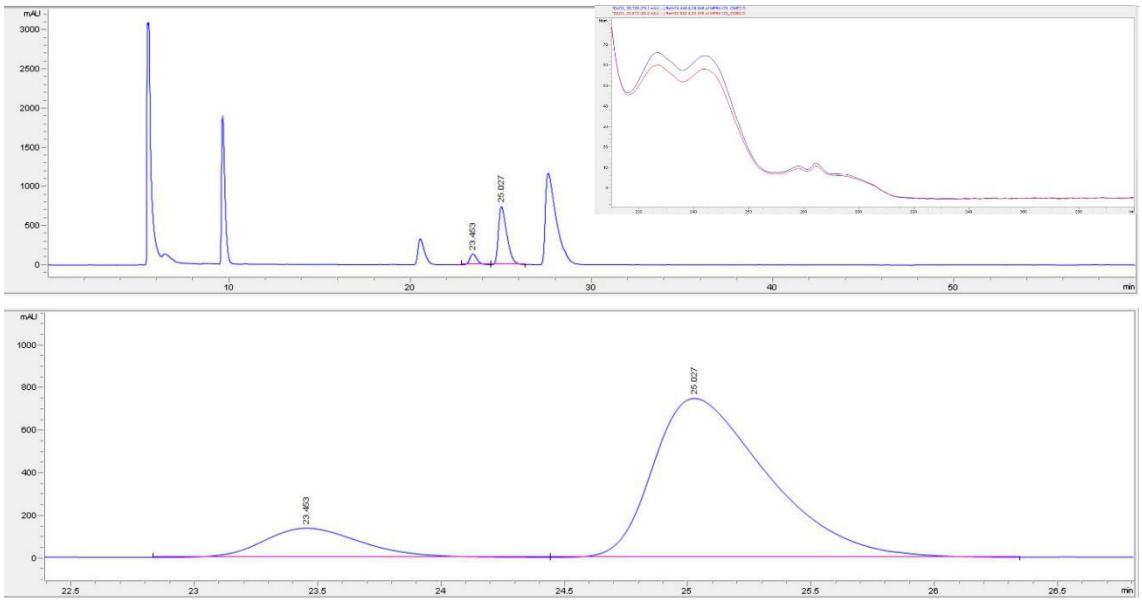

#	Time	Area	Height	Width	Area%	Symmetry
1	23.453	3774	136.8	0.4278	13.597	0.752
2	25.027	23982.4	745.5	0.4893	86.403	0.534

Amine **4b**; GP II (-10°C); 3 mol% TRIFP **1a**

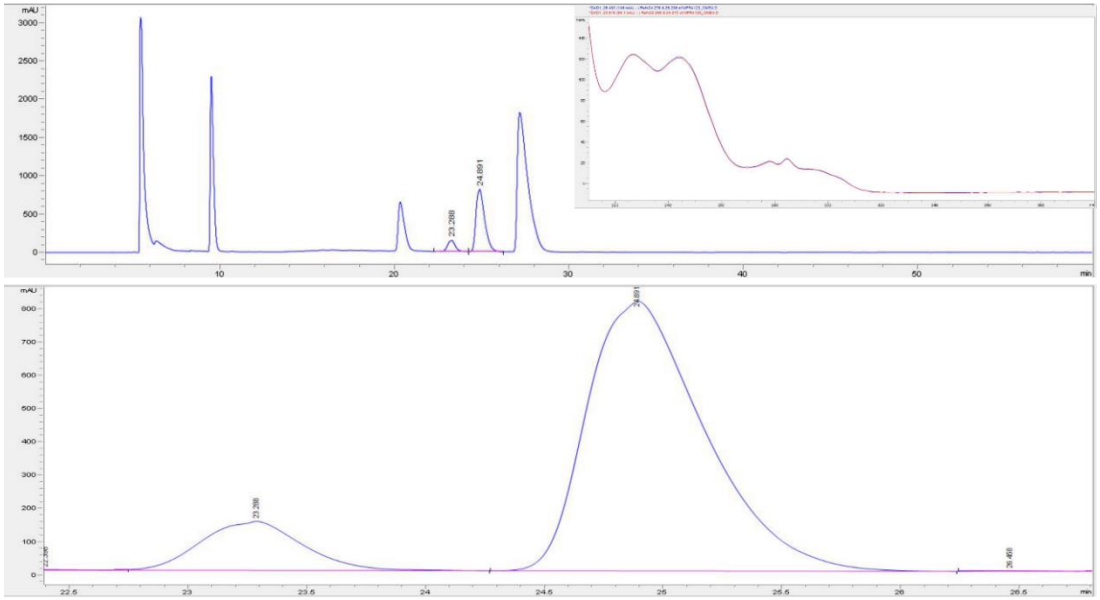

#	Time	Area	Height	Width	Area%	Symmetry
1	23.288	4434	148.1	0.399	13.702	1.177
2	24.891	27925.2	812.3	0.4691	86.298	0.716

Amine **4b**; GP II (-10°C); 5 mol% TRIFP **1a**

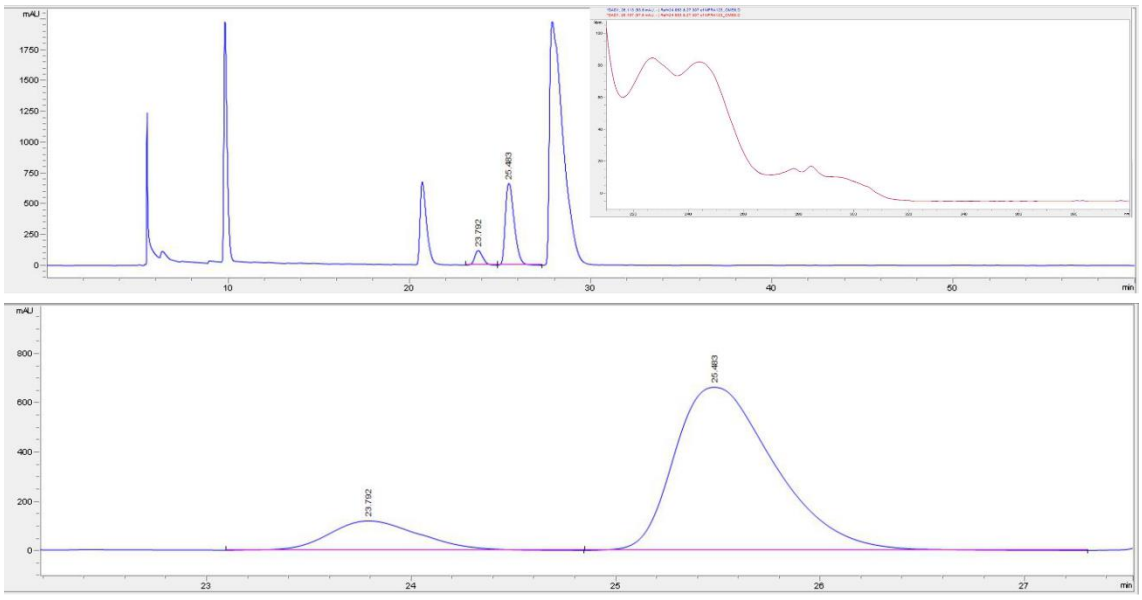

#	Time	Area	Height	Width	Area%	Symmetry
1	23.792	3668.6	119.3	0.4688	13.958	0.747
2	25.483	22614.9	663.7	0.5235	86.042	0.617

Amine **4b**; GP II (-10°C); 10 mol% TRIFP **1a**

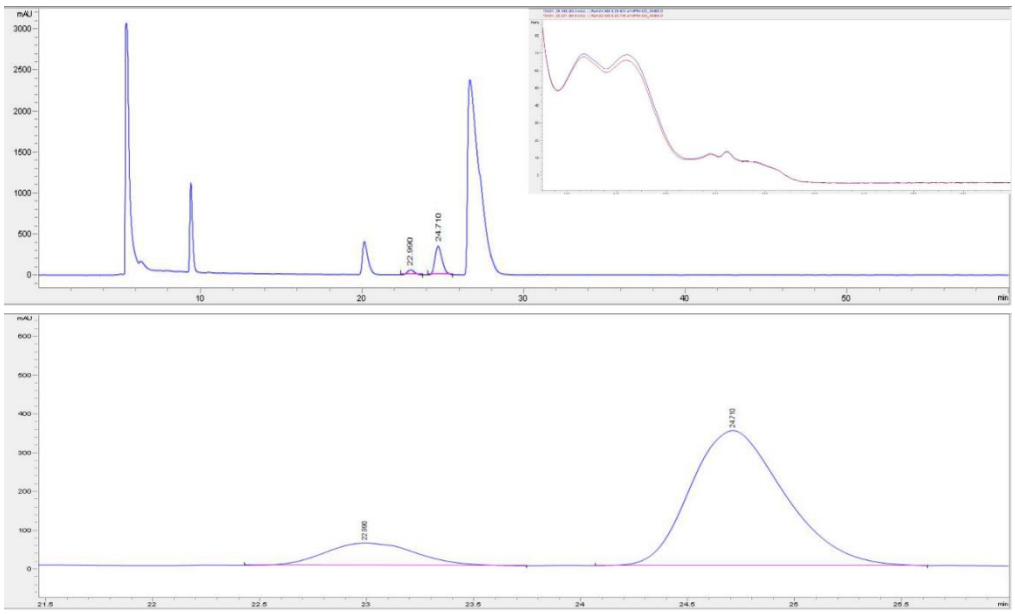

#	Time	Area	Height	Width	Area%	Symmetry
1	22.99	1704	57.8	0.4202	13.774	0.783
2	24.71	10667.8	348.8	0.4748	86.226	0.779

Amine **4b**; GP II (-10°C); 15 mol% TRIFP **1a**

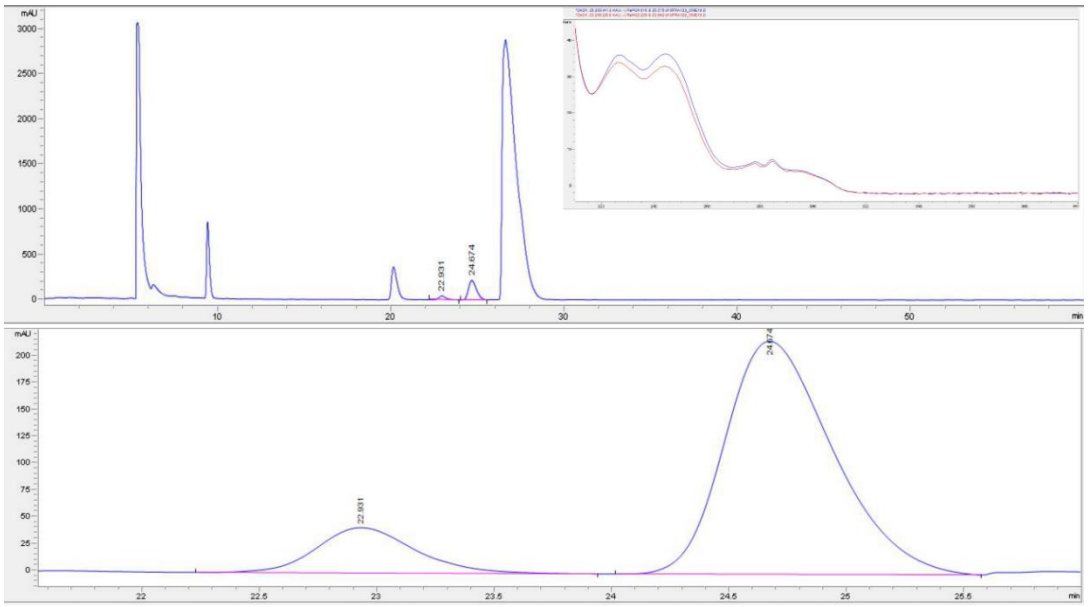

#	Time	Area	Height	Width	Area%	Symmetry
1	22.931	1240.9	42.2	0.4447	15.133	0.798
2	24.674	6958.6	217.2	0.4897	84.867	0.687

Amine **4b**; GP II (-10°C); 20 mol% TRIFP **1a**

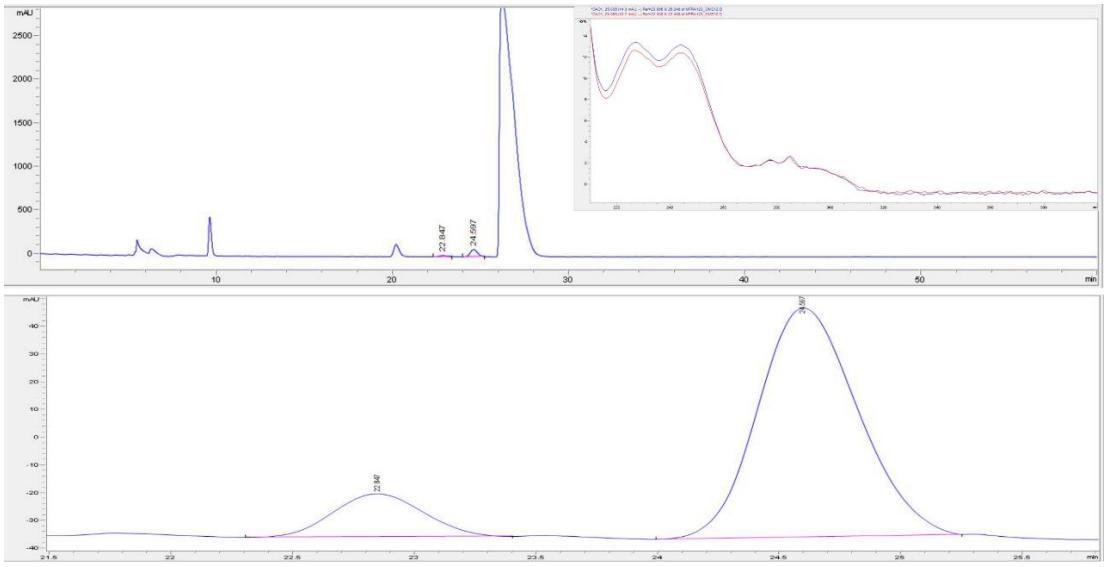

#	Time	Area	Height	Width	Area%	Symmetry
1	22.847	402.2	15.5	0.4005	14.600	0.943
2	24.597	2352.8	82.4	0.4449	85.400	0.818

Amine **4b**; GP II (-20°C); 1 mol% TRIFP **1a**

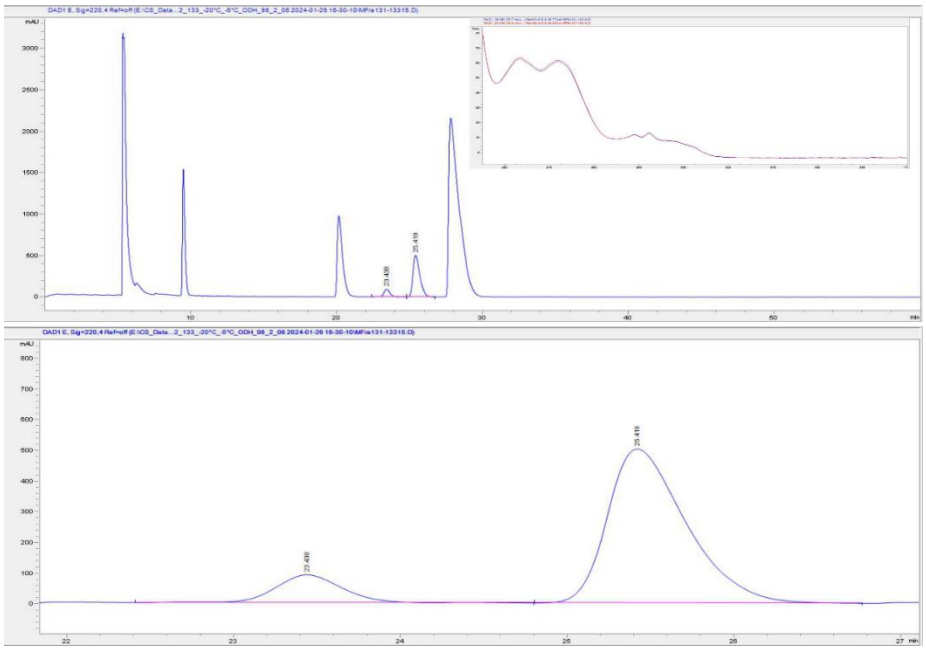

#	Time	Area	Height	Width	Area%	Symmetry
1	23.438	2586.9	91	0.4294	13.599	0.893
2	25.419	16436.6	502.6	0.4976	86.401	0.586

Amine **4b**; GP II (-20°C); 3 mol% TRIFP **1a**

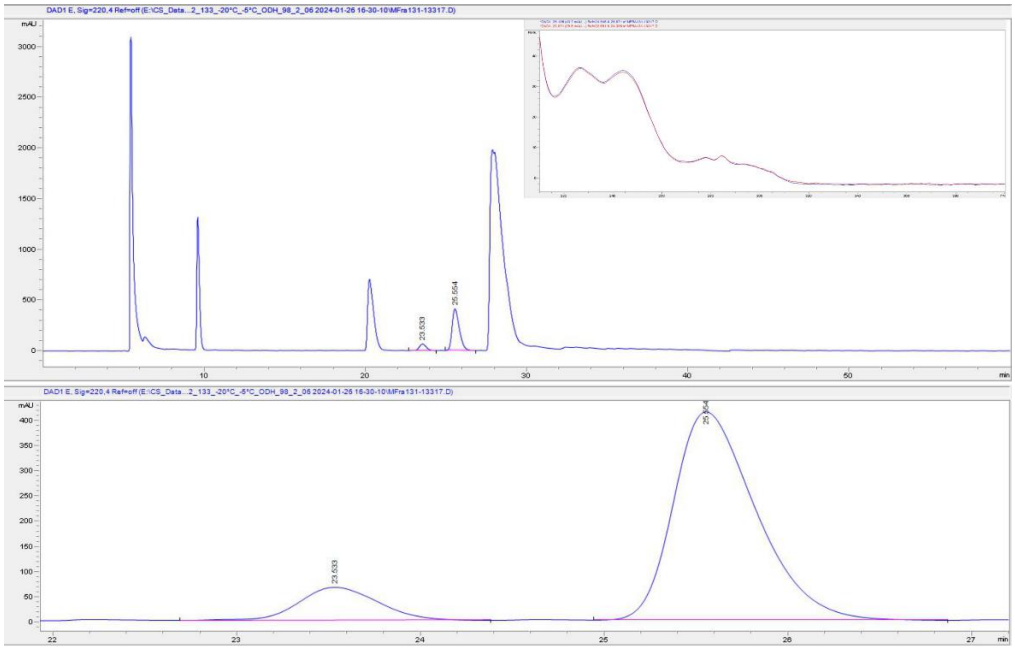

#	Time	Area	Height	Width	Area%	Symmetry
1	23.533	1980.9	65.6	0.4782	13.331	0.82
2	25.554	12878.6	412.7	0.4801	86.669	0.621

Amine **4b**; GP II (-20°C); 5 mol% TRIFP **1a**

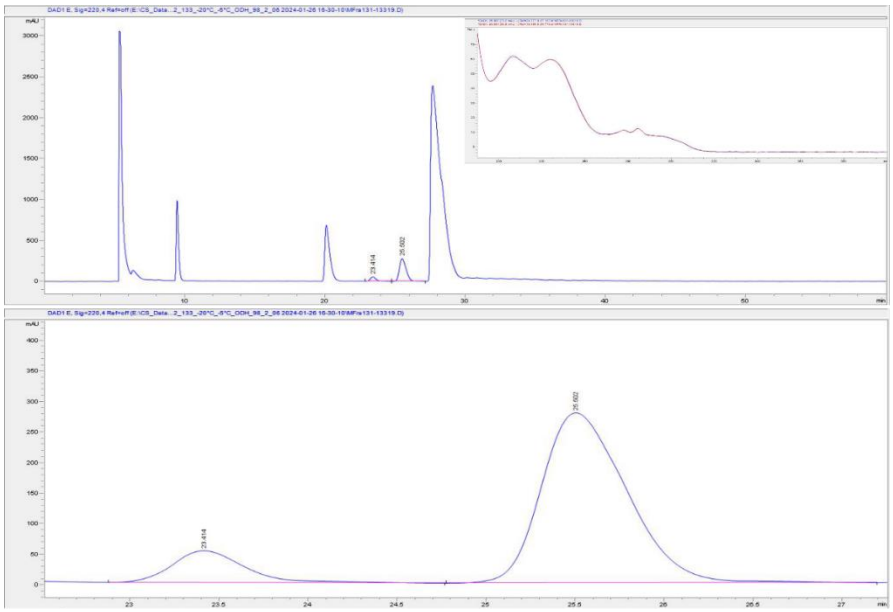

#	Time	Area	Height	Width	Area%	Symmetry
1	23.414	1501.5	52	0.4389	13.963	0.716
2	25.502	9251.4	277.7	0.4986	86.037	0.655

Amine **4b**; GP II (-20°C); 10 mol% TRIFP **1a**

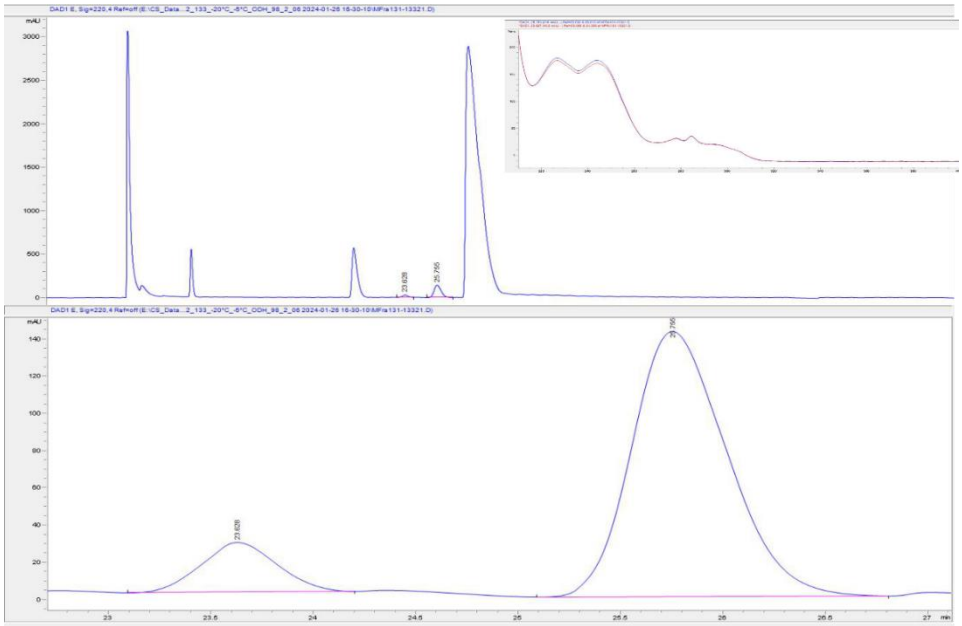

#	Time	Area	Height	Width	Area%	Symmetry
1	23.628	688	26.7	0.3825	12.999	0.896
2	25.755	4604.9	142.4	0.4912	87.001	0.728

Amine **4b**; GP II (-20°C); 15 mol% TRIFP **1a**

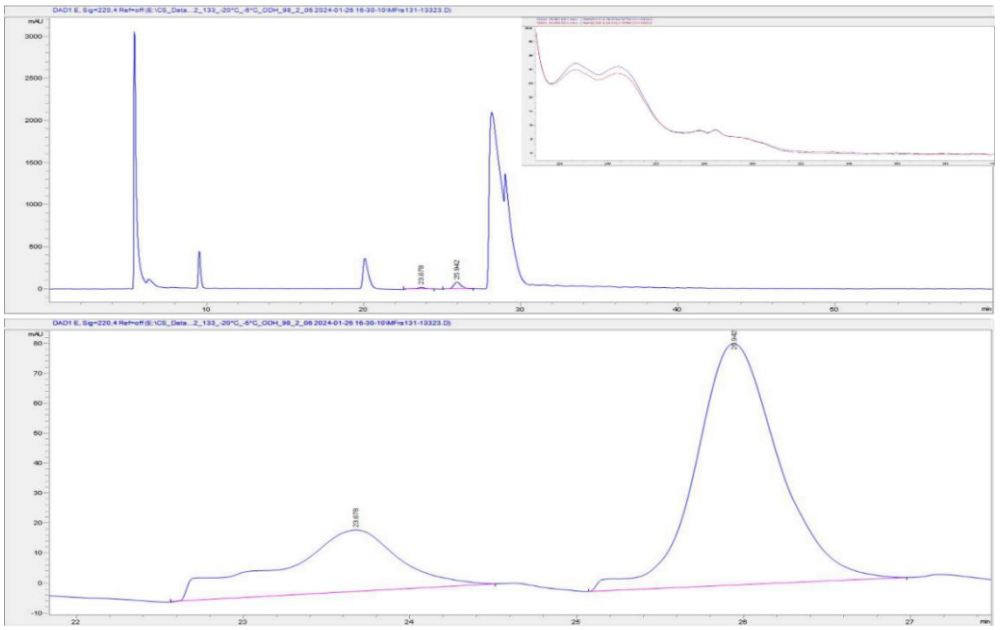

#	Time	Area	Height	Width	Area%	Symmetry
1	23.678	1035.9	20.5	0.6928	27.123	1.867
2	25.942	2783.3	80.5	0.5254	72.877	0.837

Amine **4b**; GP II (-20°C); 20 mol% TRIFP **1a**

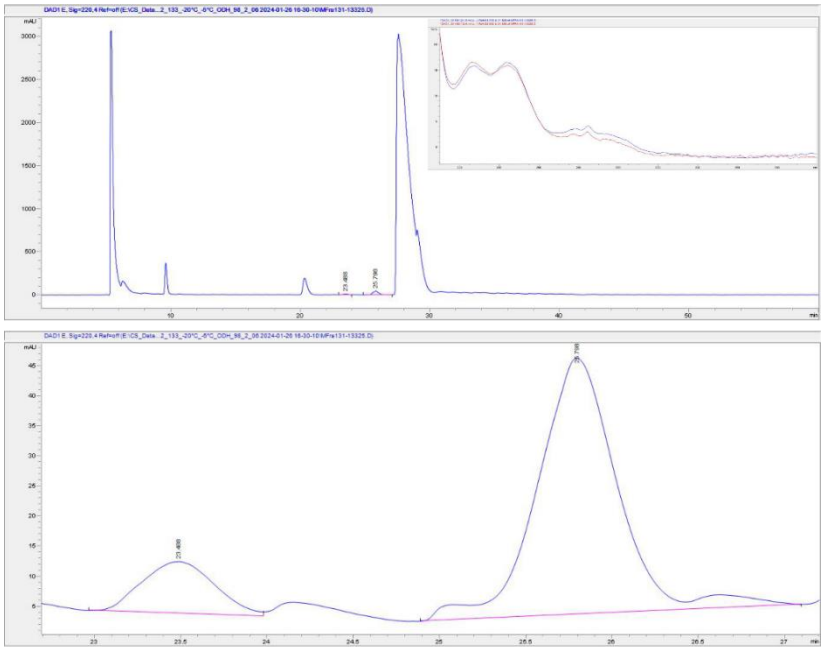

#	Time	Area	Height	Width	Area%	Symmetry
1	23.488	254	8.6	0.4187	15.483	0.956
2	25.798	1386.7	42.8	0.4435	84.517	1.012

Amine **4b**; GP II (-20°C); 1 mol% TRIFP **1a**, 0.03 M

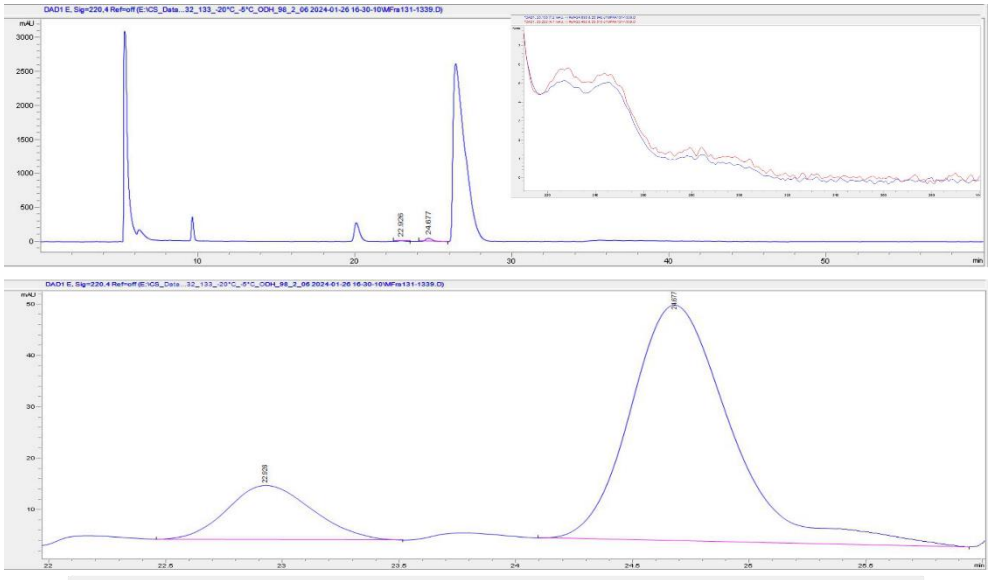

#	Time	Area	Height	Width	Area%	Symmetry
1	22.926	267.9	10.6	0.3936	16.255	0.813
2	24.677	1380	46	0.4597	83.745	0.724

Amine **4b**; GP II (-20°C); 20 mol% TRIFP **1a**, 0.03 M

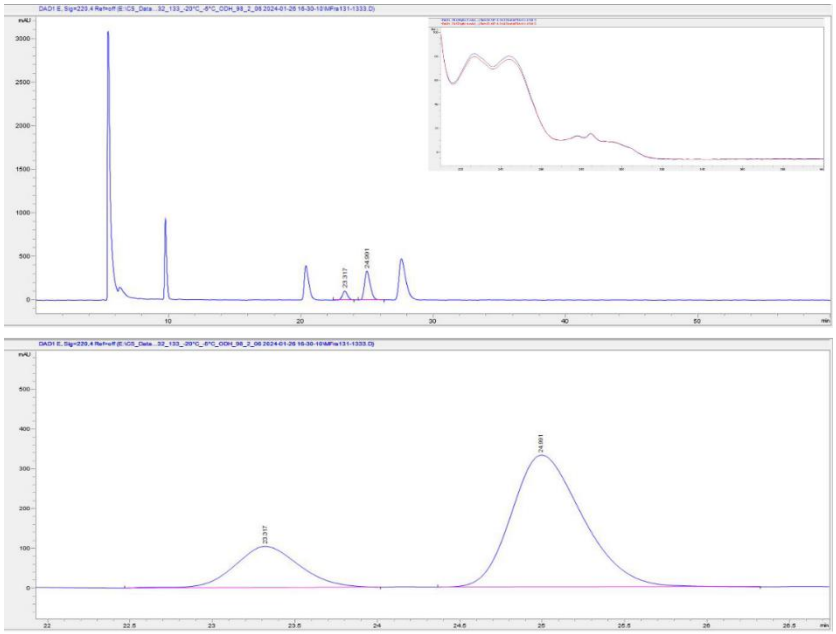

#	Time	Area	Height	Width	Area%	Symmetry
1	23.317	2814.8	103.3	0.4178	22.124	0.898
2	24.991	9908.3	331.3	0.461	77.876	0.703

Amine **4b**; GP II (-20°C); 1 mol% TRIFP **1a**, 0.09 M

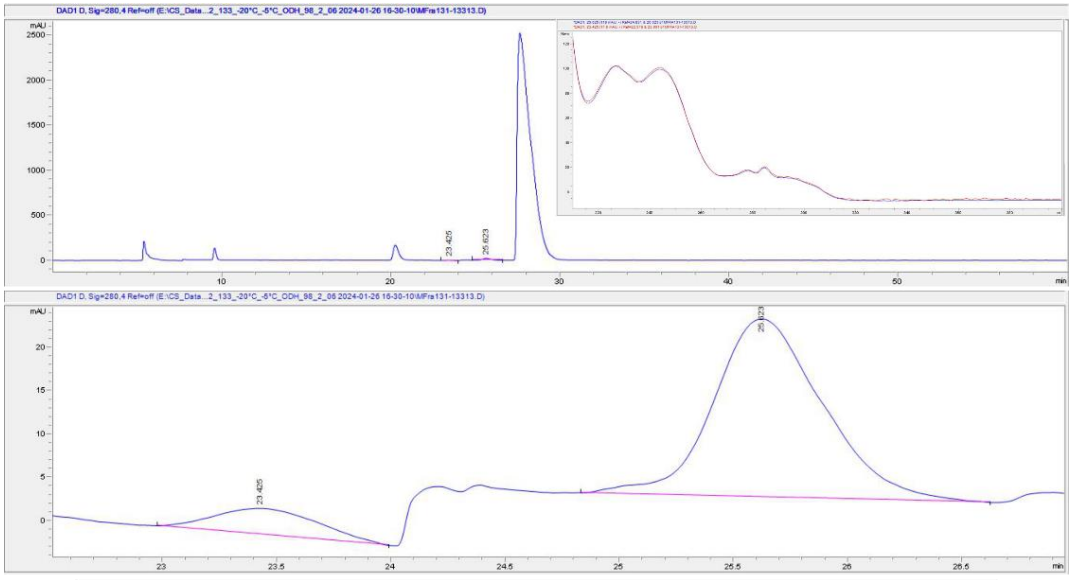

#	Time	Area	Height	Width	Area%	Symmetry
1	23.425	96.6	3	0.389	12.318	0.725
2	25.623	687.3	20.6	0.4715	87.682	0.787

Amine **4b**; GP II (-20°C); 20 mol% TRIFP **1a**, 0.09 M

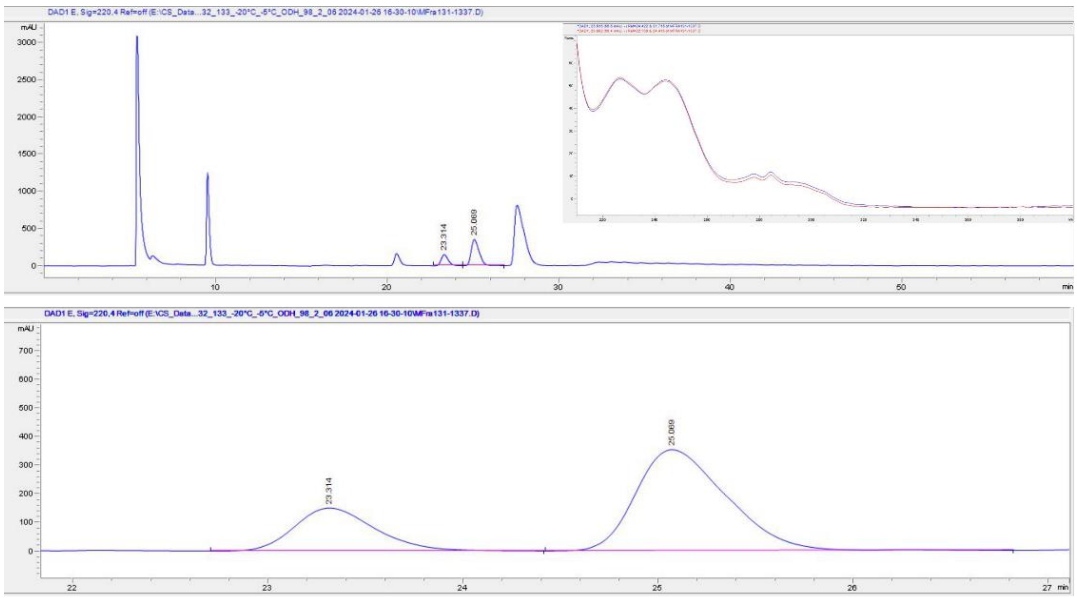

#	Time	Area	Height	Width	Area%	Symmetry
1	23.314	4319.3	150.3	0.4434	27.376	0.738
2	25.069	11458.3	353.9	0.4899	72.624	0.641

Amine **4b**; GP II (-20°C); 1 mol% TRIFP **1a**, 0.06 M, toluene

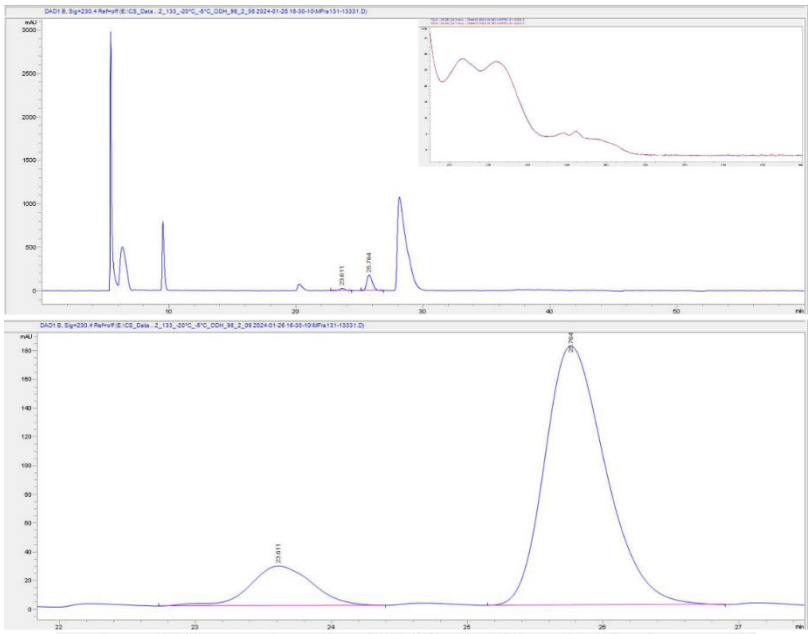

#	Time	Area	Height	Width	Area%	Symmetry
1	23.611	884.4	27.6	0.456	13.639	0.869
2	25.764	5599.5	180	0.4769	86.361	0.717

Amine **4b**; GP II (-20°C); 10 mol% TRIFP **1a**, 0.06 M, toluene

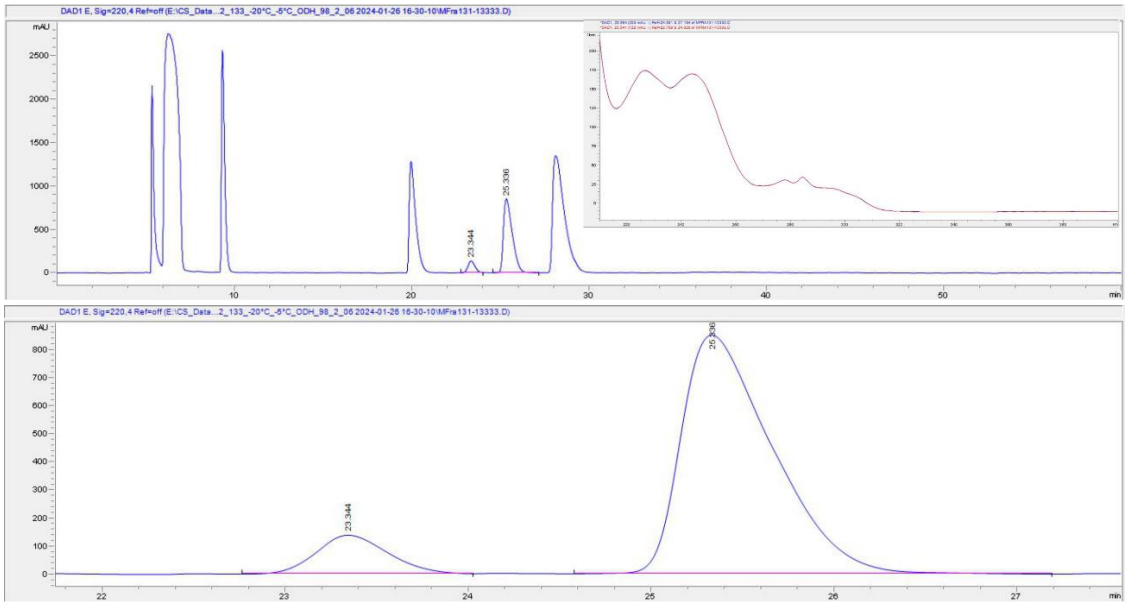

#	Time	Area	Height	Width	Area%	Symmetry
1	23.344	3754.4	137.4	0.4148	11.318	0.787
2	25.336	29417.6	848.8	0.5184	88.682	0.478

Amine **4b**; GP II (-20°C); 20 mol% TRIFP **1a**, 0.06 M, toluene

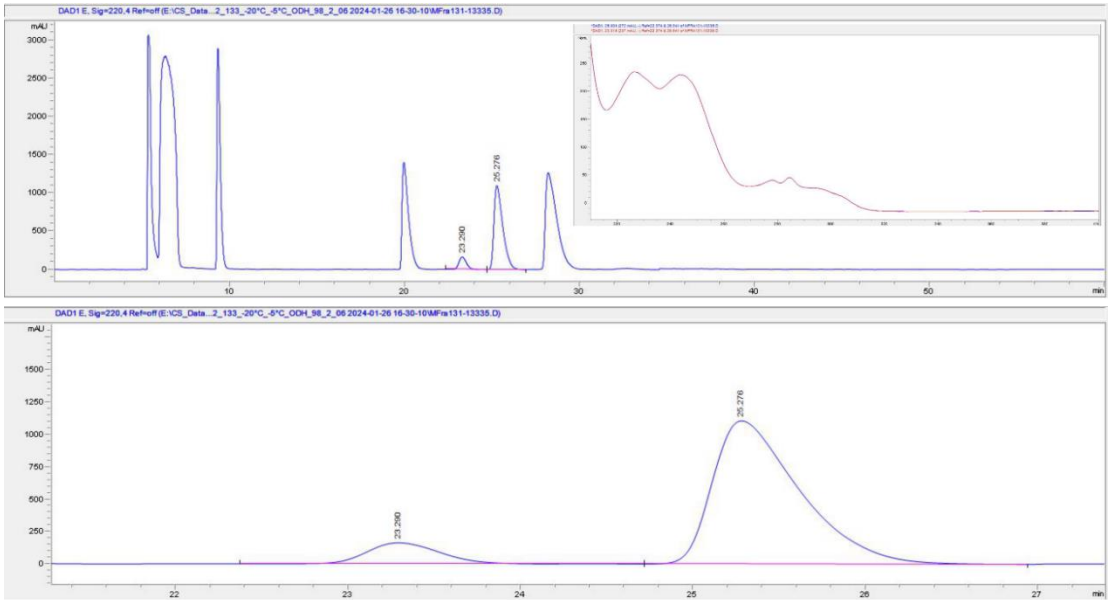

#	Time	Area	Height	Width	Area%	Symmetry
1	23.29	4836.7	162.2	0.4662	11.158	0.755
2	25.276	38509.1	1101.9	0.5277	88.842	0.473

Amine **4b**; GP II (-20°C); 40 mol% TRIFP **1a**, 0.06 M, toluene

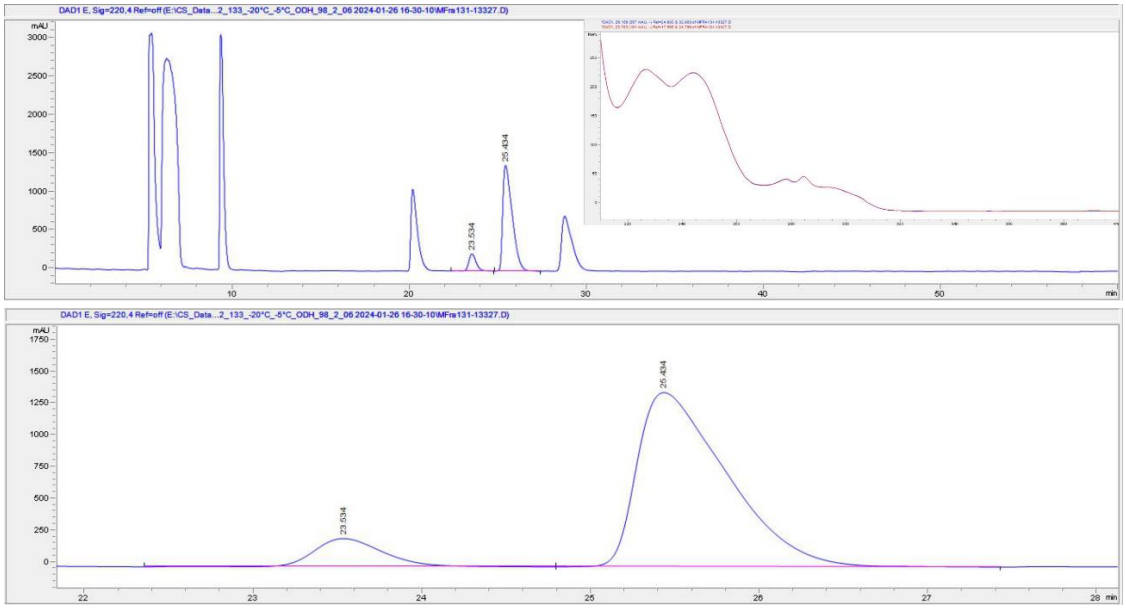

#	Time	Area	Height	Width	Area%	Symmetry
1	23.534	6395.2	222.8	0.439	11.218	0.744
2	25.434	50614	1374	0.5372	88.782	0.403

Amine **4b**; GP II (-20°C); 20 mol% TRIFP **1a**, 0.03 M, toluene

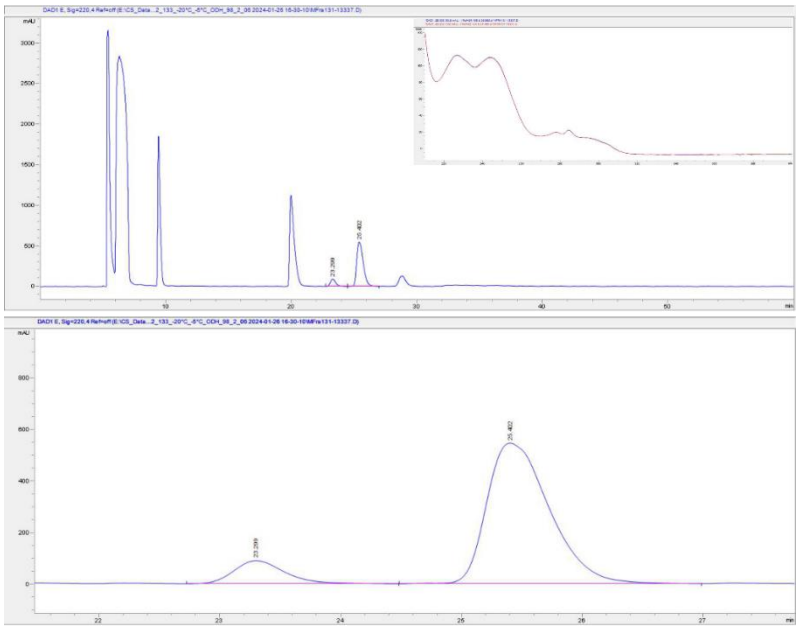

#	Time	Area	Height	Width	Area%	Symmetry
1	23.299	2625.8	89.5	0.4462	11.797	0.74
2	25.402	19631.6	545.4	0.5559	88.203	0.571

Amine **4b**; GP II (-20°C); 20 mol% TRIFP **1a**, 0.09 M, toluene

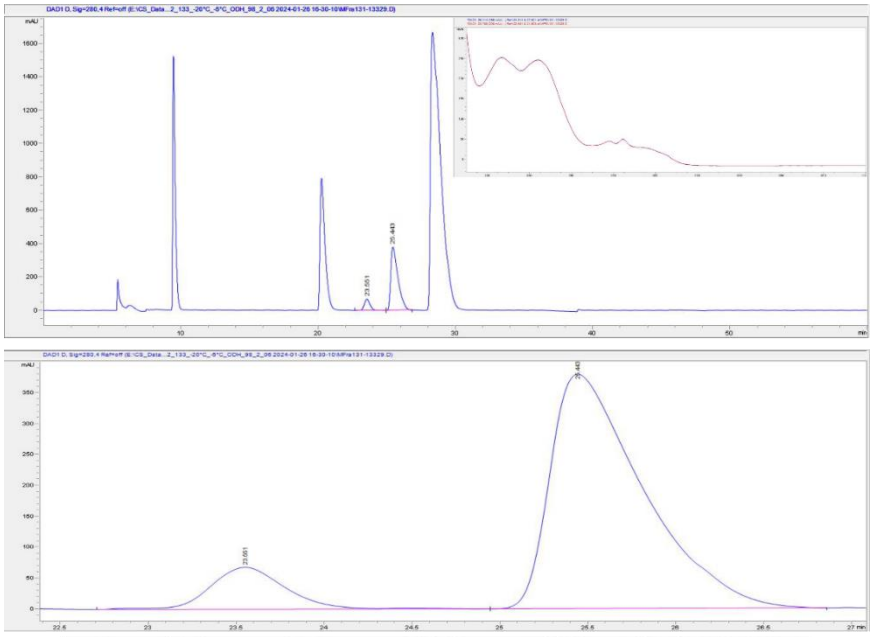

#	Time	Area	Height	Width	Area%	Symmetry
1	23.551	2012.7	68	0.4525	12.631	0.844
2	25.443	13921.1	380.2	0.5432	87.369	0.398

Amine **4b**; GP II (-40°C); 100 mol% TRIP **1b**, DCM, HE

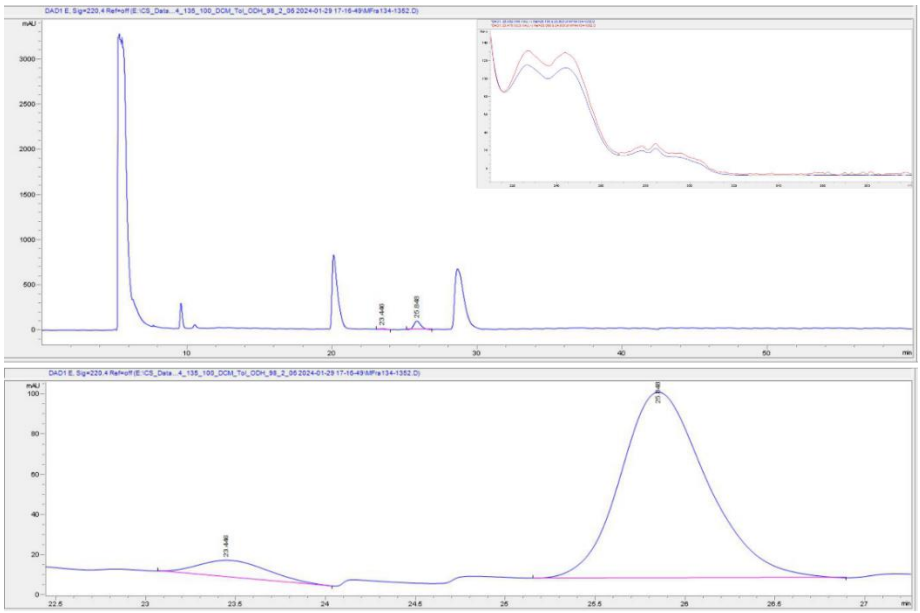

#	Time	Area	Height	Width	Area%	Symmetry
1	23.446	226.1	8.2	0.4179	6.822	0.651
2	25.848	3088.4	92.5	0.5054	93.178	0.755

Amine **4b**; GP II (-40°C); 100 mol% TRIP **1b**, DCM, Ph-HE

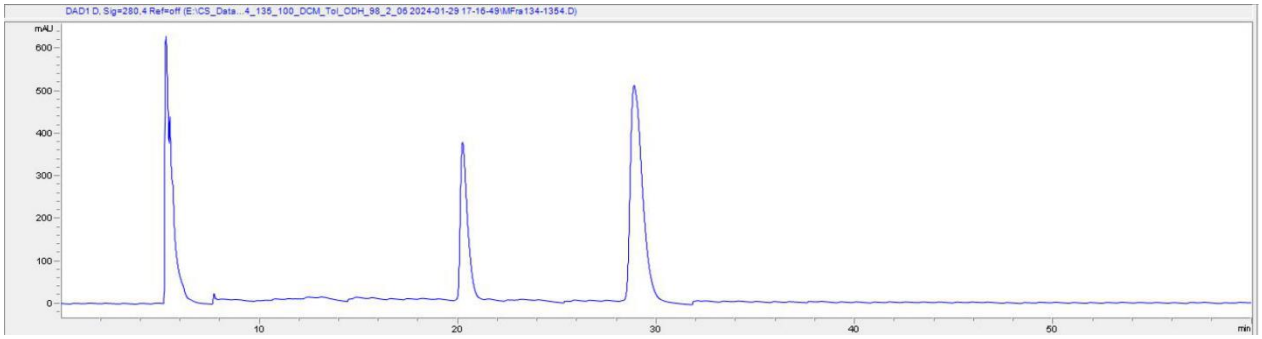

Amine **4b**; GP II (-40°C); 100 mol% TRIP **1b**, DCM, *t*Bu-HE

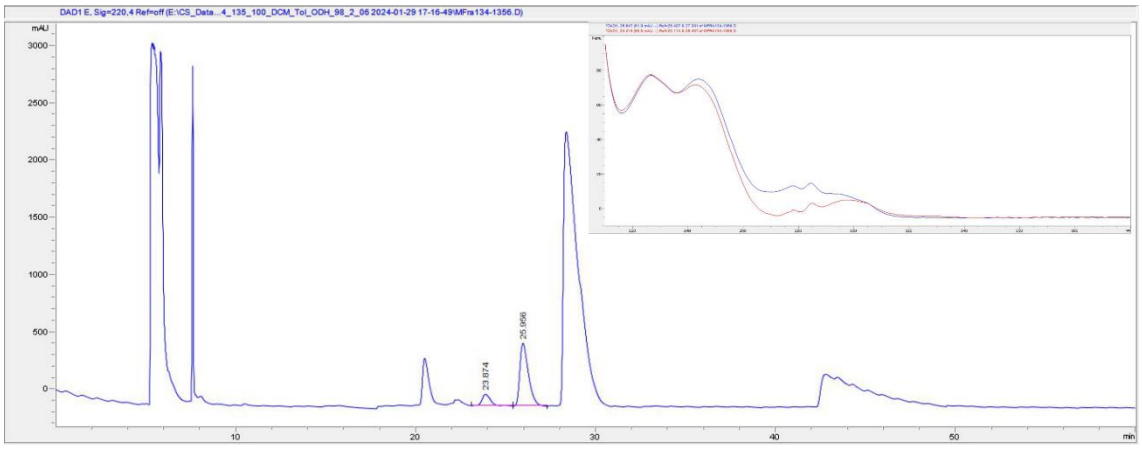

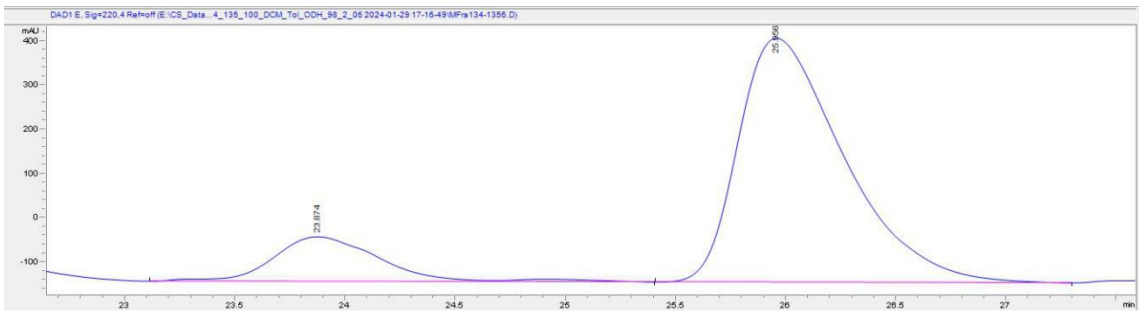

#	Time	Area	Height	Width	Area%	Symmetry
1	23.874	3452.4	100.9	0.473	15.865	0.734
2	25.956	18309.3	550.7	0.5079	84.135	0.535

Amine **4b**; GP II (-40°C); 100 mol% TRIP **1b**, toluene, HE

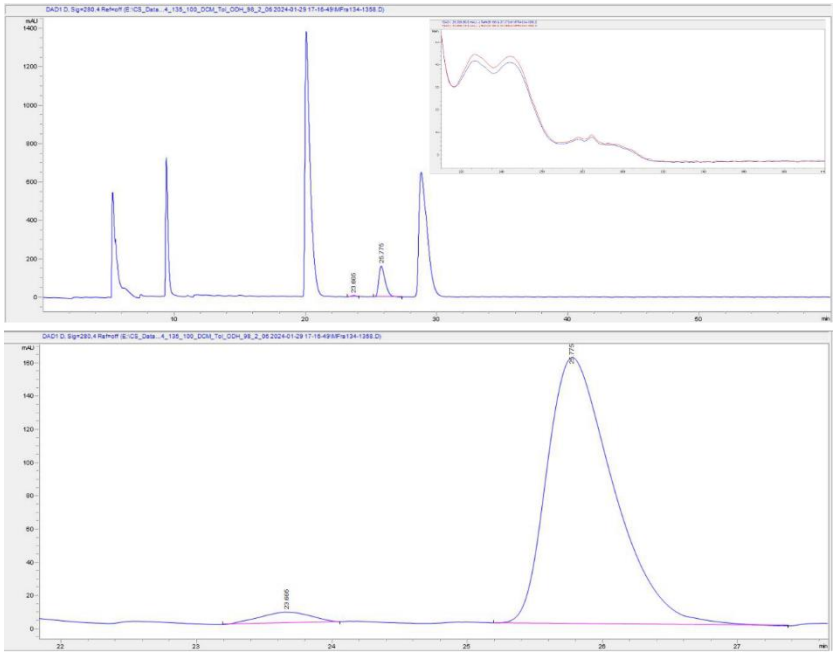

#	Time	Area	Height	Width	Area%	Symmetry
1	23.665	171.2	6.5	0.3228	3.050	1.209
2	25.775	5441.3	159.9	0.5151	96.950	0.581

Amine **4b**; GP II (-40°C); 100 mol% TRIP **1b**, toluene, Ph-HE

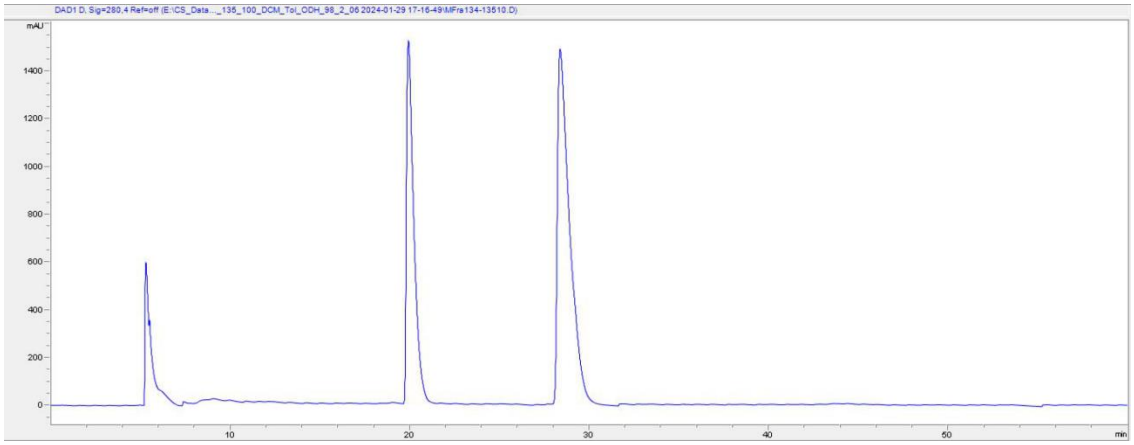

Amine **4b**; GP II (-40°C); 100 mol% TRIP **1b**, toluene, *t*Bu-HE

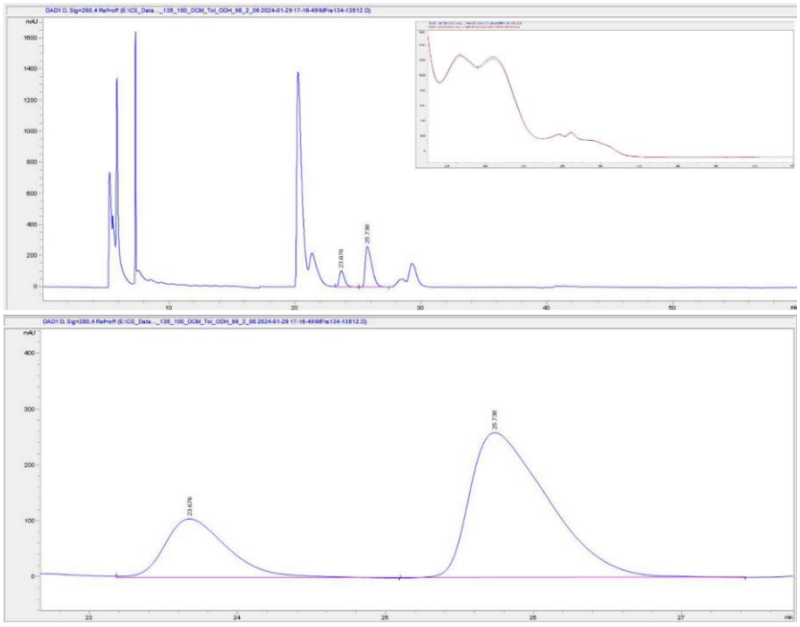

#	Time	Area	Height	Width	Area%	Symmetry
1	23.676	3173.8	106.1	0.4549	24.834	0.609
2	25.738	9606.3	260.7	0.5438	75.166	0.44

Amine **4b**; GP II (-40°C); 100 mol% TRIFP **1a**, DCM, HE

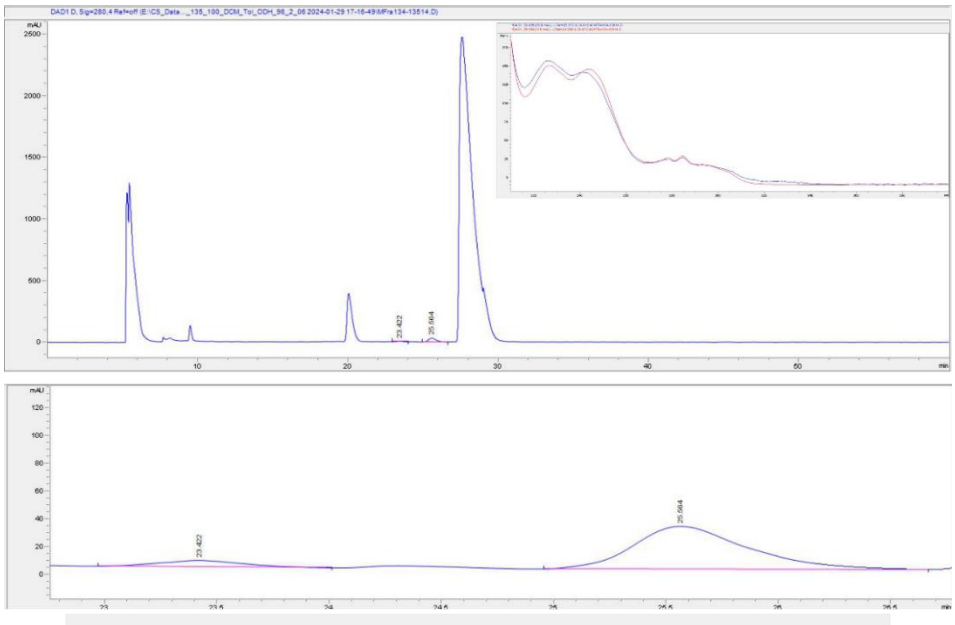

#	Time	Area	Height	Width	Area%	Symmetry
1	23.422	123.8	4.7	0.3433	10.208	0.873
2	25.564	1089.4	30.8	0.5287	89.792	0.683

Amine **4b**; GP II (-40°C); 100 mol% TRIFP **1a**, DCM, Ph-HE

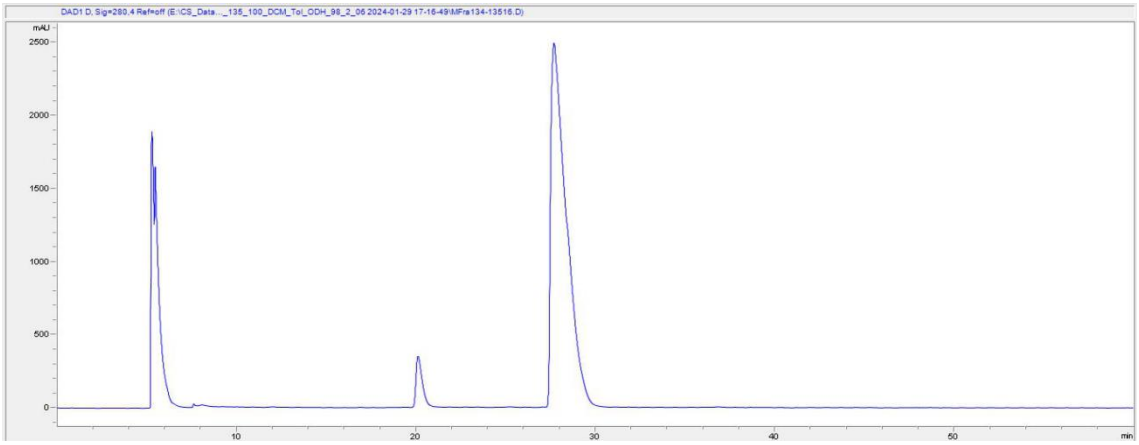

Amine **4b**; GP II (-40°C); 100 mol% TRIFP **1a**, DCM, *t*Bu-HE

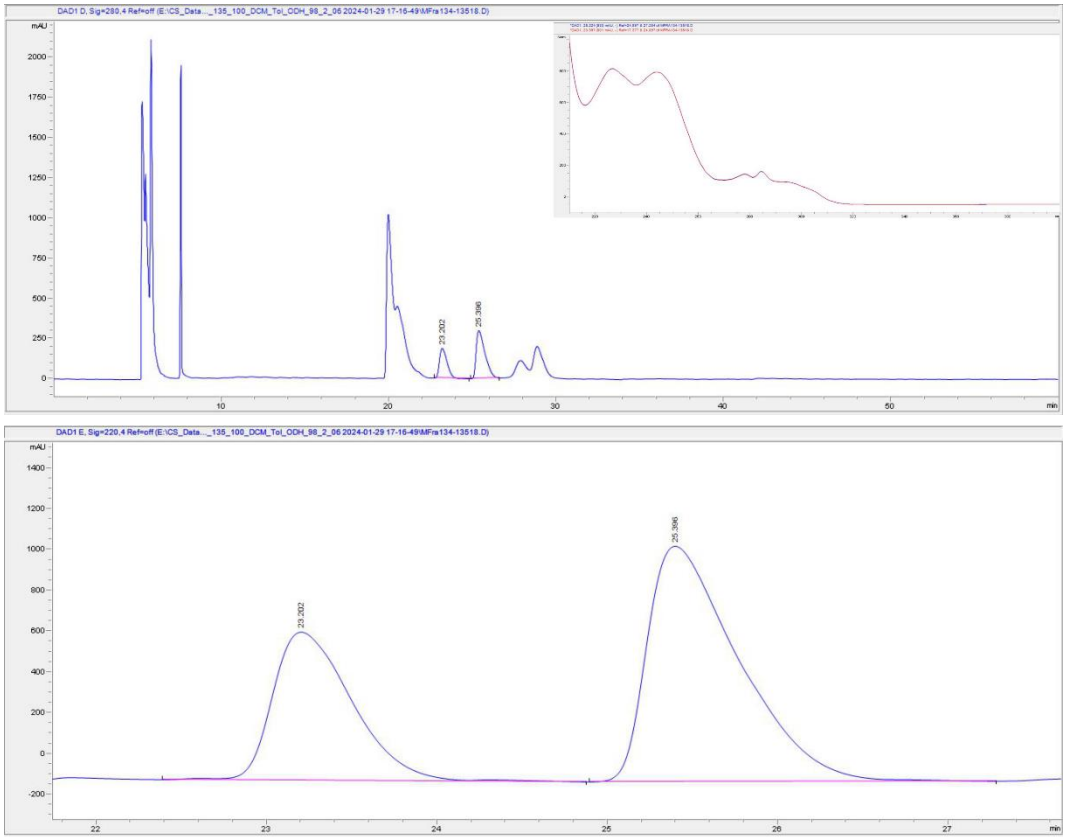

#	Time	Area	Height	Width	Area%	Symmetry
1	23.202	5919.4	187.3	0.4934	35.123	0.537
2	25.396	10934.1	299.6	0.5478	64.877	0.421

Amine **4b**; GP II (-20°C); 100 mol% TRIP **1b**, DCM, HE

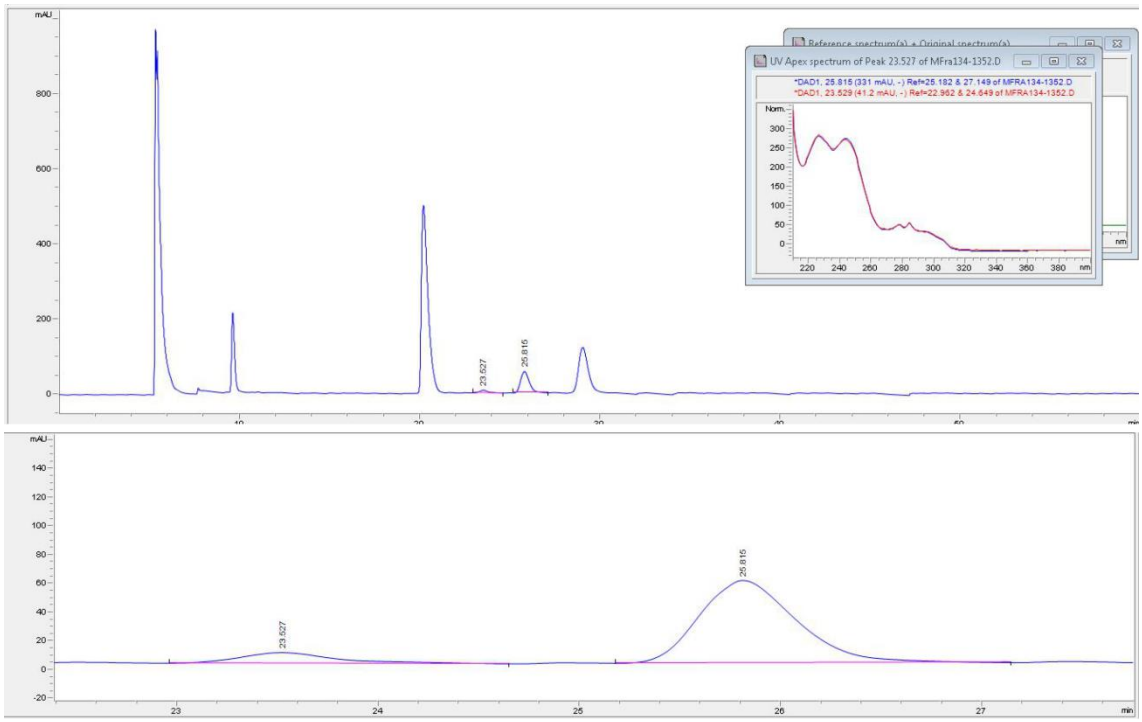

#	Time	Area	Height	Width	Area%	Symmetry
1	23.527	255.8	7.5	0.4581	11.736	0.729
2	25.815	1924.2	57.4	0.5228	88.264	0.763

Amine **4b**; GP II (-20°C); 100 mol% TRIP **1b**, DCM, Ph-HE

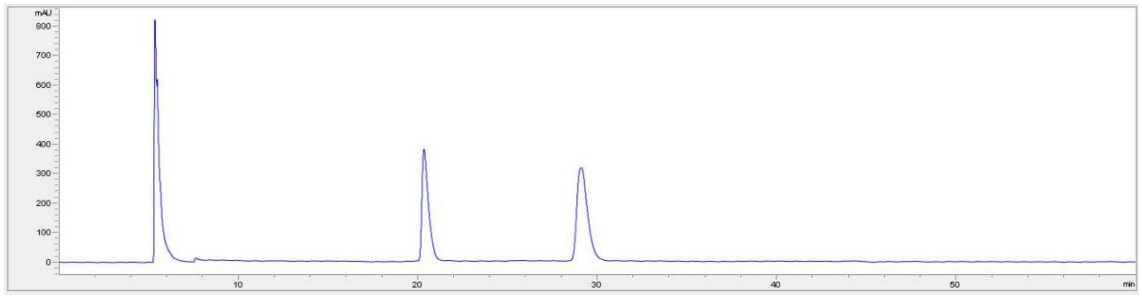

Amine **4b**; GP II (-20°C); 100 mol% TRIP **1b**, DCM, *t*Bu-HE

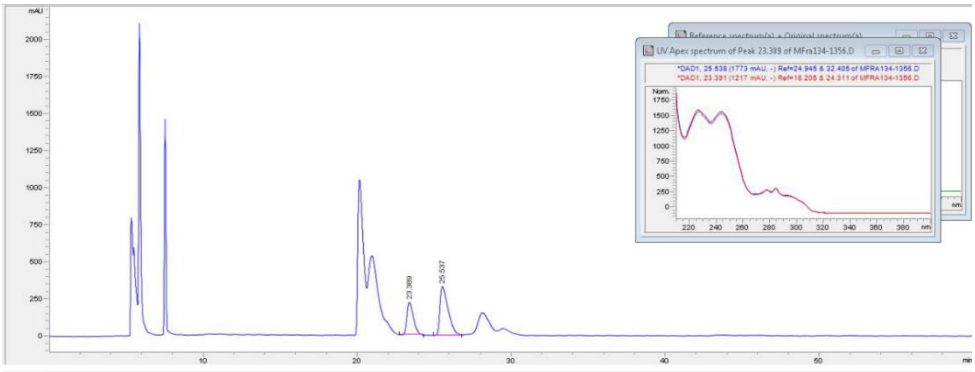

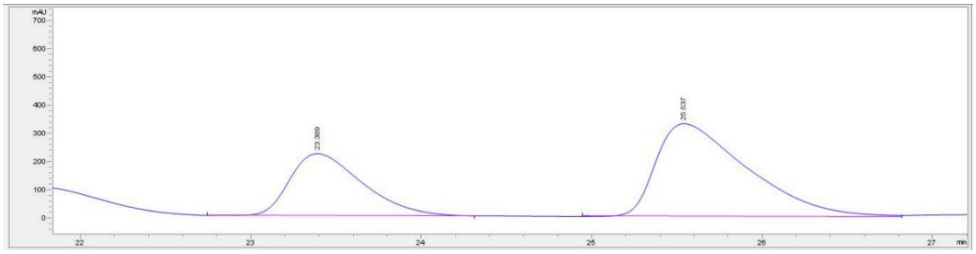

#	Time	Area	Height	Width	Area%	Symmetry
1	23.389	6475	219.6	0.4539	34.635	0.585
2	25.537	12219.7	328.4	0.5581	65.365	0.414

Amine **4b**; GP II (-20°C); 100 mol% TRIP **1b**, toluene, HE

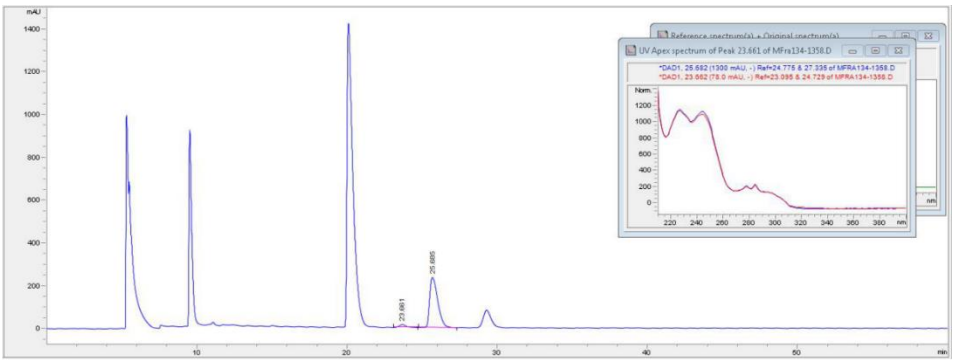

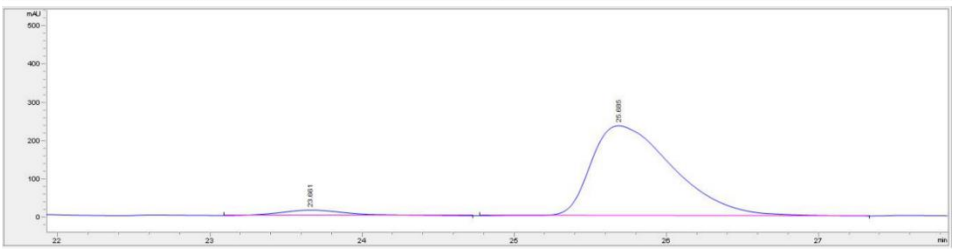

#	Time	Area	Height	Width	Area%	Symmetry
1	23.661	443	13.9	0.4536	4.793	0.741
2	25.685	8799.2	234.8	0.5753	95.207	0.484

Amine **4b**; GP II (-20°C); 100 mol% TRIP **1b**, toluene, Ph-HE

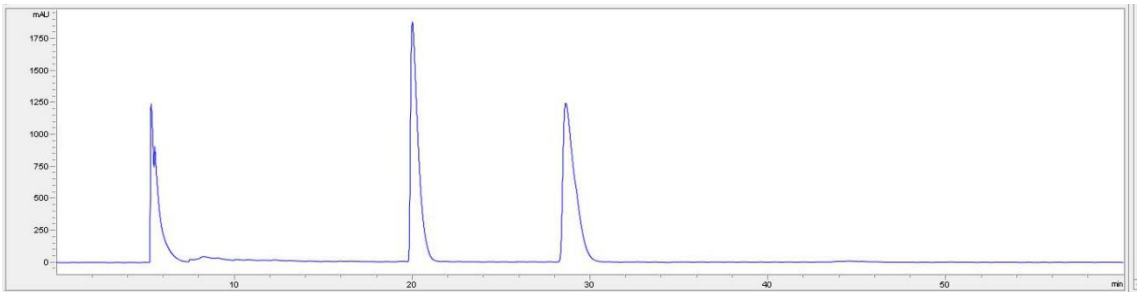

Amine **4b**; GP II (-20°C); 100 mol% TRIP **1b**, toluene, *t*Bu-HE

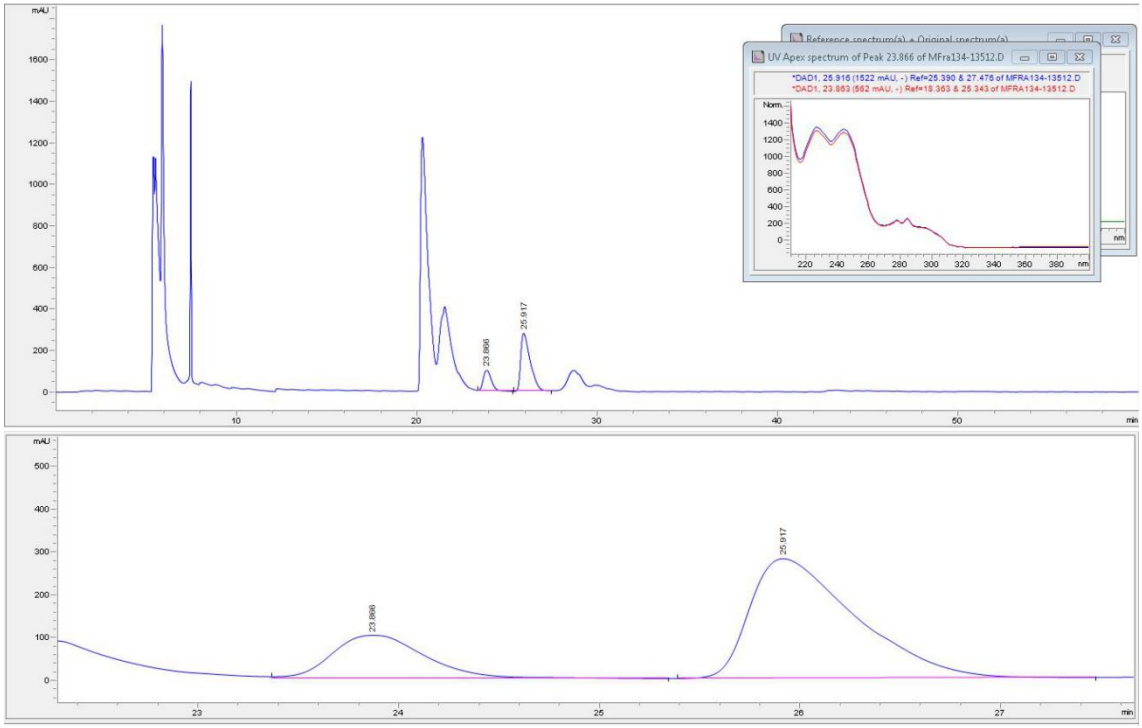

#	Time	Area	Height	Width	Area%	Symmetry
1	23.866	3274	100.4	0.5004	24.367	0.719
2	25.917	10162.4	278.6	0.5515	75.633	0.432

Amine **4b**; GP II (-20°C); 100 mol% TRIFP **1a**, DCM, HE

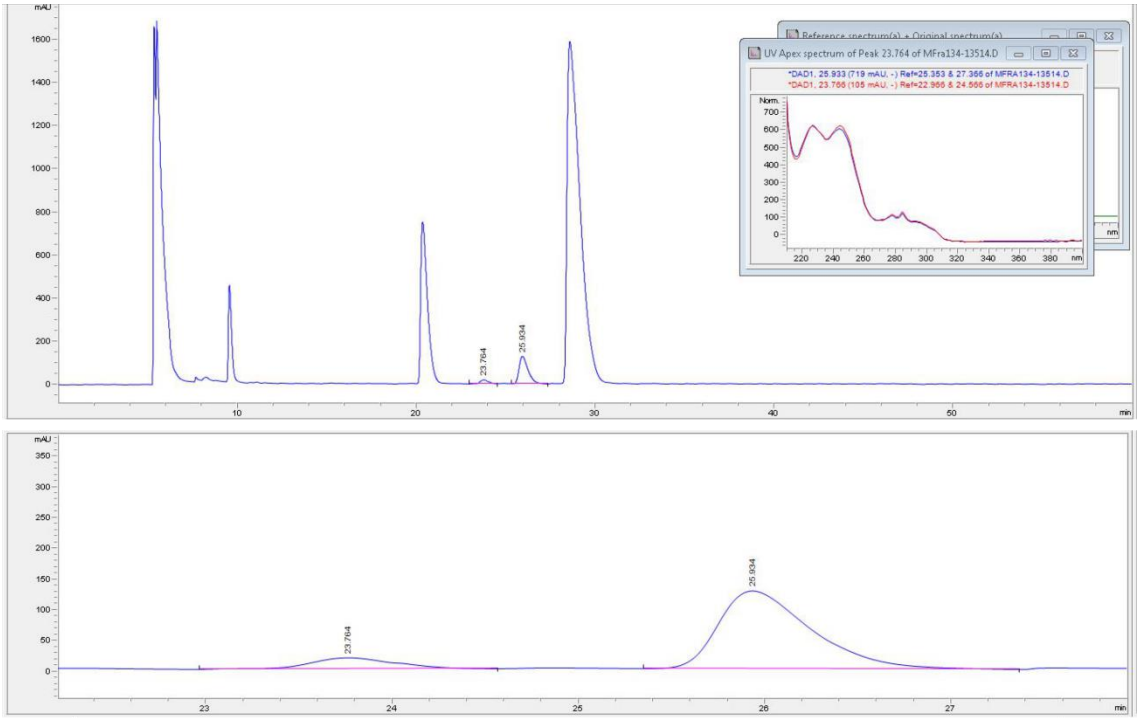

#	Time	Area	Height	Width	Area%	Symmetry
1	23.764	589.4	18.3	0.4697	11.821	0.795
2	25.934	4396.5	127.1	0.5156	88.179	0.545

Amine **4b**; GP II (-20°C); 100 mol% TRIFP **1a**, DCM, Ph-HE

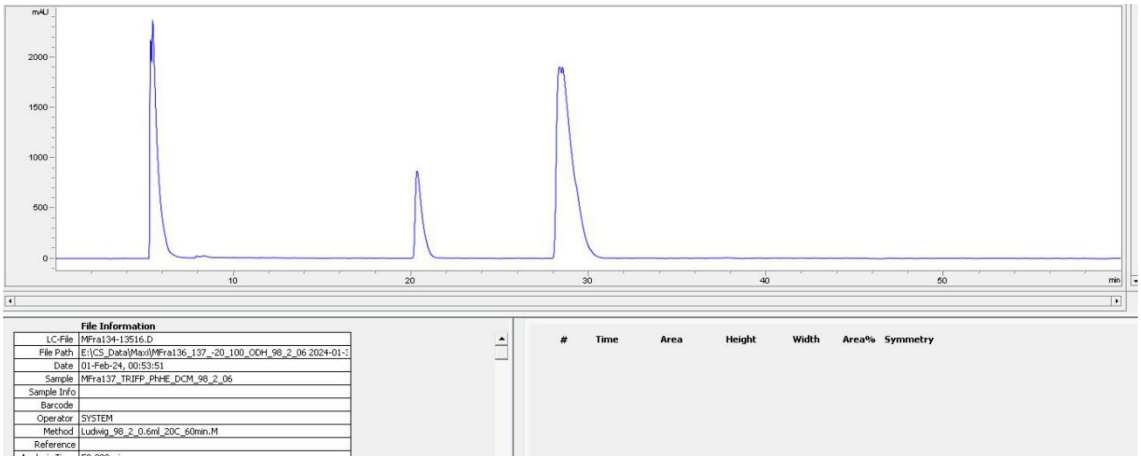

Amine **4b**; GP II (-20°C); 100 mol% TRIFP **1a**, DCM, *t*Bu-HE

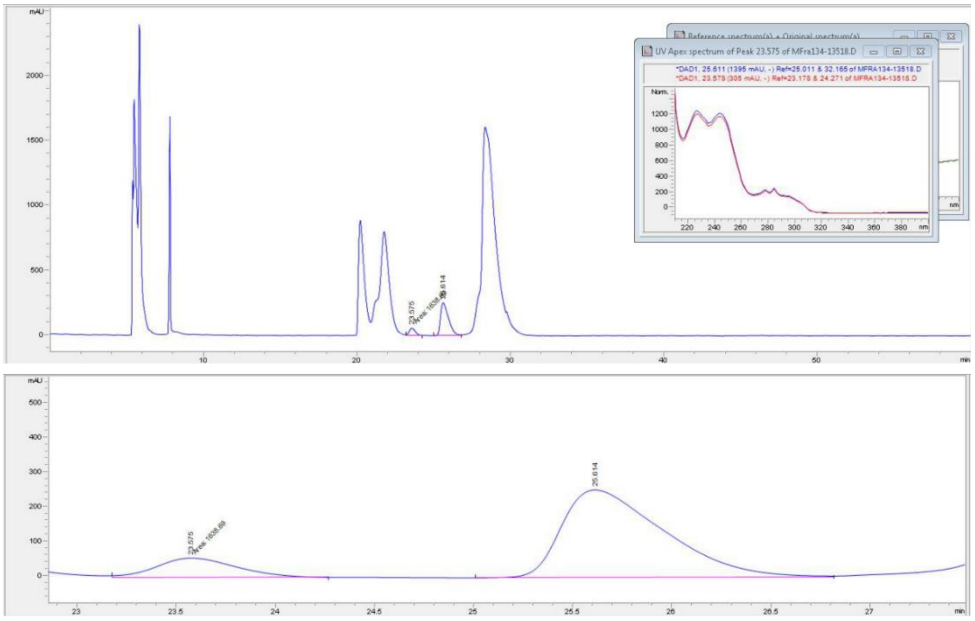

#	Time	Area	Height	Width	Area%	Symmetry
1	23.575	1638.7	57.5	0.4749	15.140	0.789
2	25.614	9185.2	254.5	0.535	84.860	0.455

Amine **4b**; GP II (-10°C); 20 mol% TRIFP **1a**, $Ba(OH)_2$ (Excess)

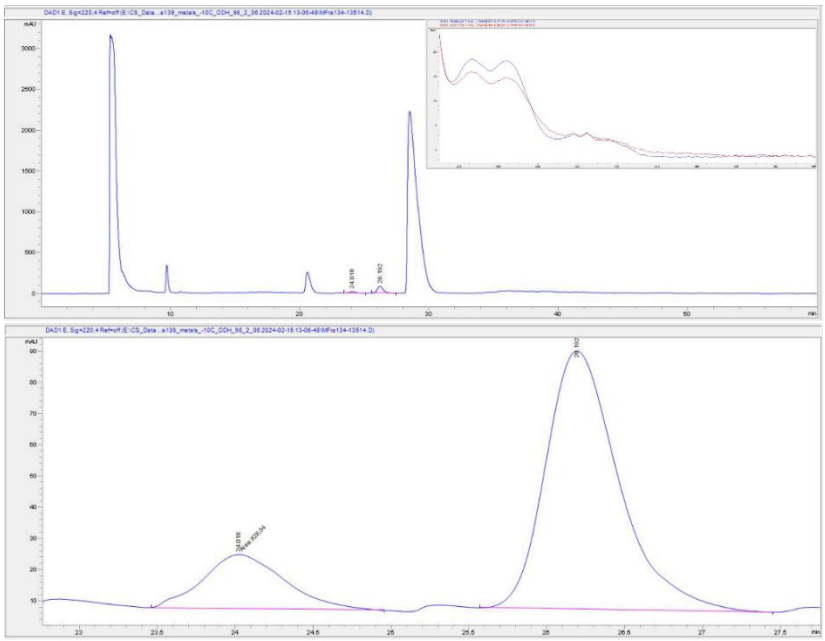

#	Time	Area	Height	Width	Area%	Symmetry
1	24.018	626.5	17.3	0.605	18.874	0.781
2	26.192	2693.1	82.5	0.4967	81.126	0.704

Amine **4b**; GP II (-10°C); 20 mol% TRIFP **1a**, $Ca(OH)_2$ (Excess)

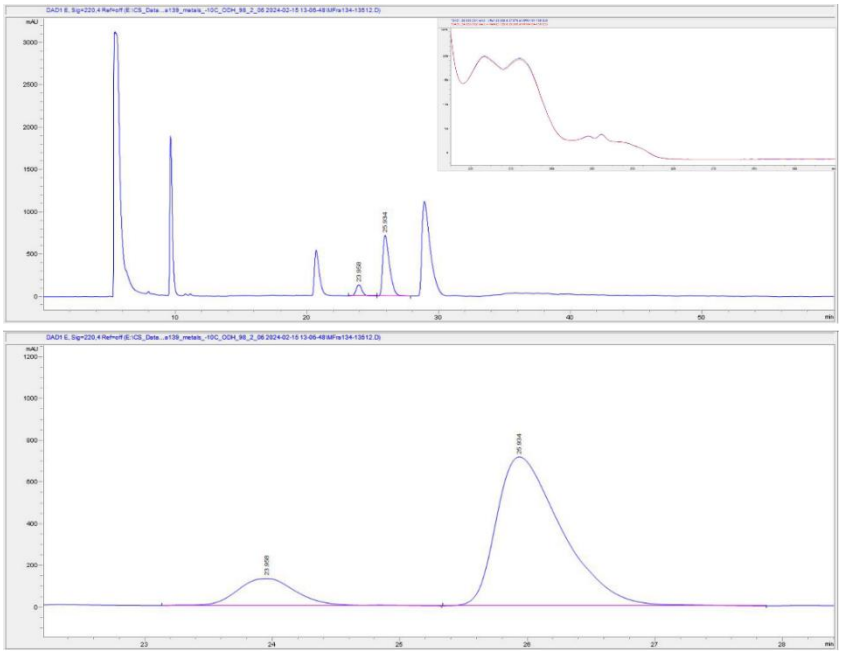

#	Time	Area	Height	Width	Area%	Symmetry
1	23.958	4195.4	129.8	0.4949	14.199	0.988
2	25.934	25350.8	714.2	0.5361	85.801	0.509

Amine **4b**; GP II (-10°C); 20 mol% TRIFP **1a**, $Mg(OH)_2$ (Excess)

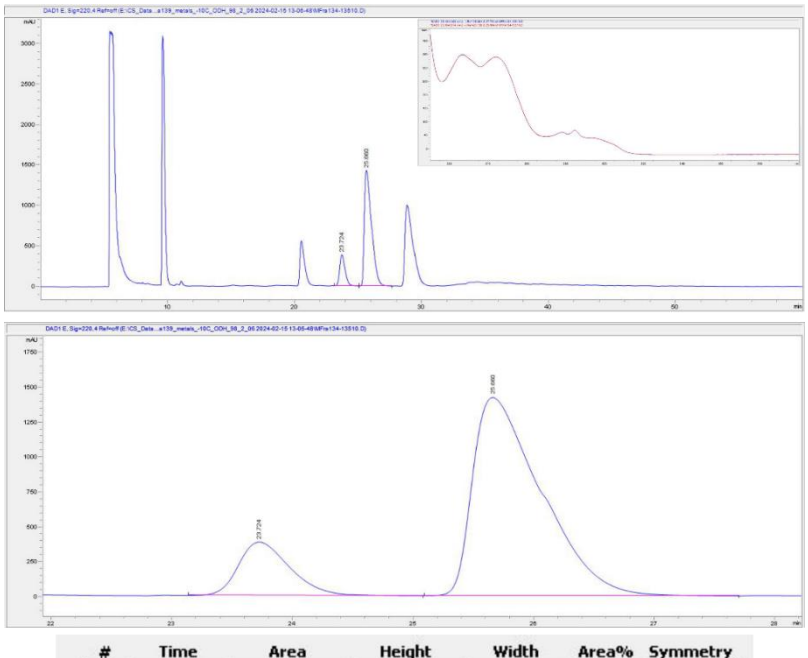

#	Time	Area	Height	Width	Area%	Symmetry
1	23.724	11315.9	382.8	0.4549	16.776	0.649
2	25.66	56135.4	1423.4	0.5861	83.224	0.389

Amine **4b**; GP II (-10°C); 20 mol% TRIFP **1a**, NaOH (Excess)

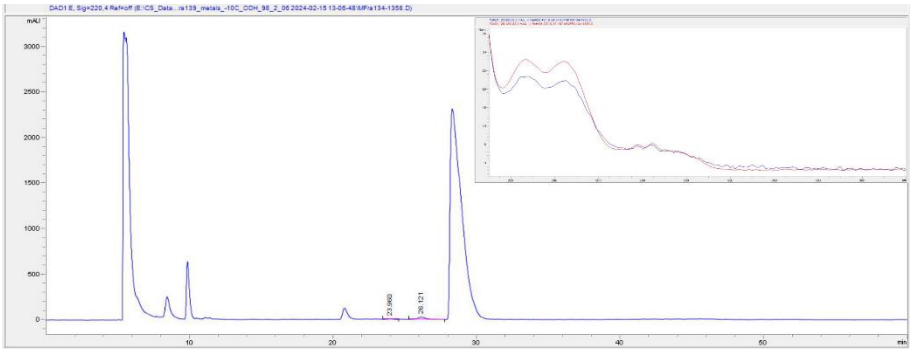

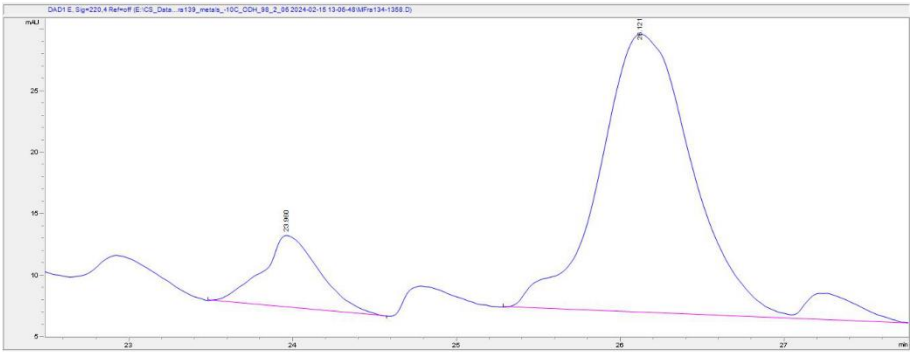

#	Time	Area	Height	Width	Area%	Symmetry
1	23.96	143.1	5.9	0.343	13.201	0.765
2	26.121	941.1	22.7	0.5372	86.799	0.798

Amine **4b**; GP II (-10°C); 20 mol% TRIFP **1a**, Cs_2CO_3 (Excess)

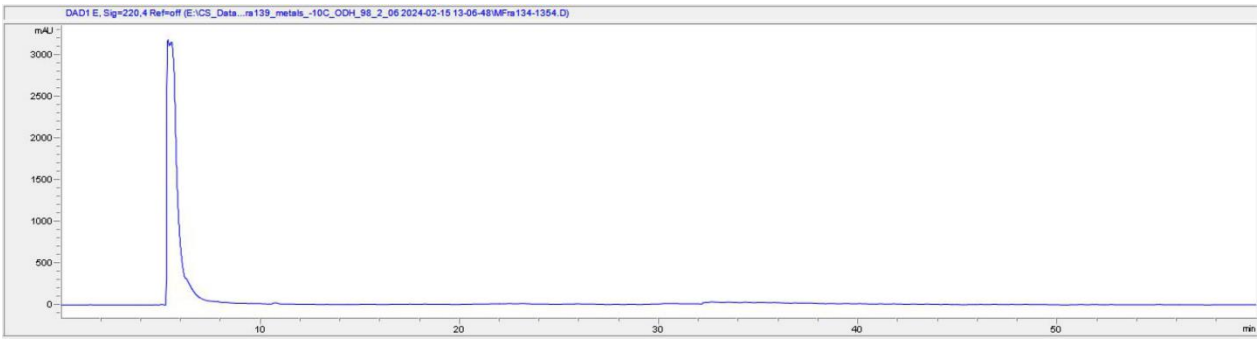

Amine **4b**; GP II (-10°C); 20 mol% TRIFP **1a**, $CuOHCO_3$ (Excess)

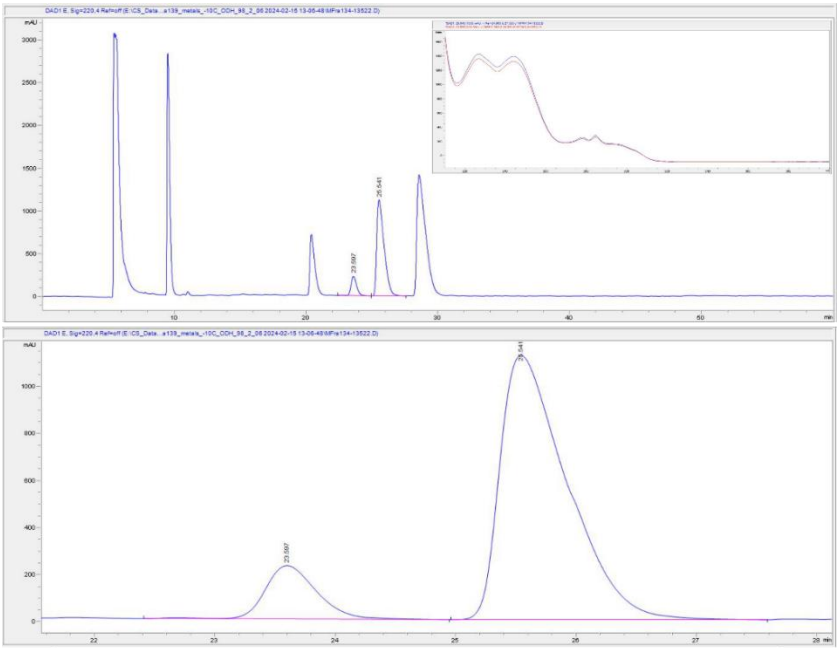

#	Time	Area	Height	Width	Area%	Symmetry
1	23.597	6819.3	227.5	0.455	13.577	0.737
2	25.541	43407.6	1124.3	0.5764	86.423	0.428

Amine **4b**; GP II (-10°C); 20 mol% TRIFP **1a**, $FeCl_3$ 6*H_2O (Excess)

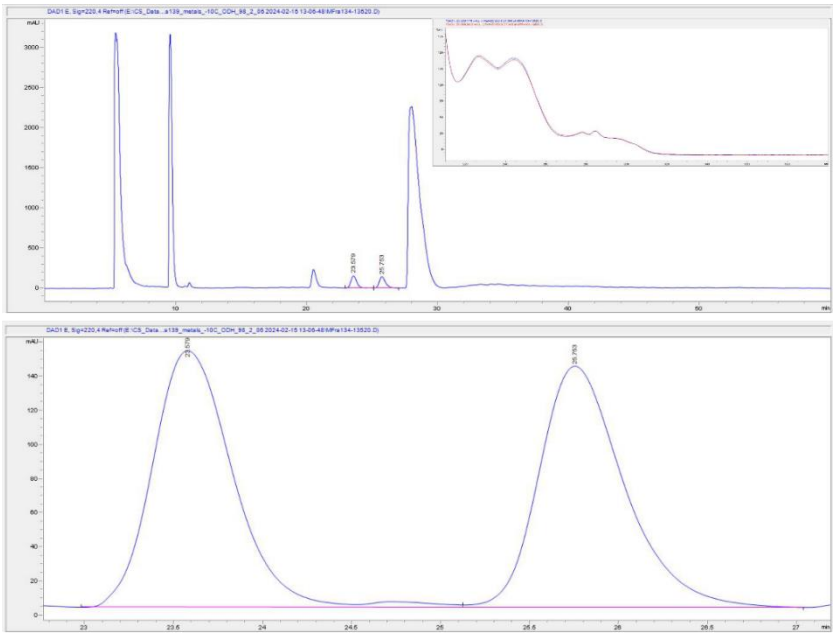

#	Time	Area	Height	Width	Area%	Symmetry
1	23.579	4739.1	150.2	0.4843	50.269	0.752
2	25.753	4688.3	141.2	0.5054	49.731	0.695

Amine **4b**; GP II (-10°C); 20 mol% TRIFP **1a**, KOMe (Excess)

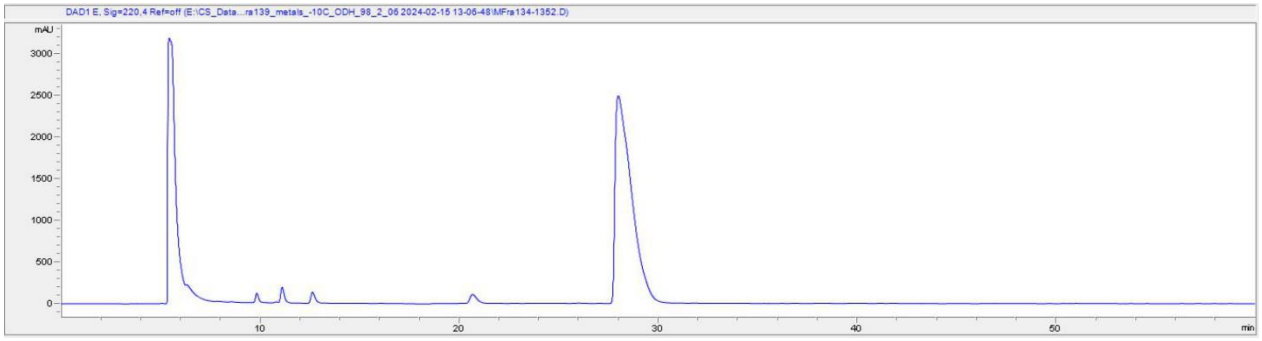

Amine **4b**; GP II (-10°C); 20 mol% TRIFP **1a**, $LiClO_4$ (Excess)

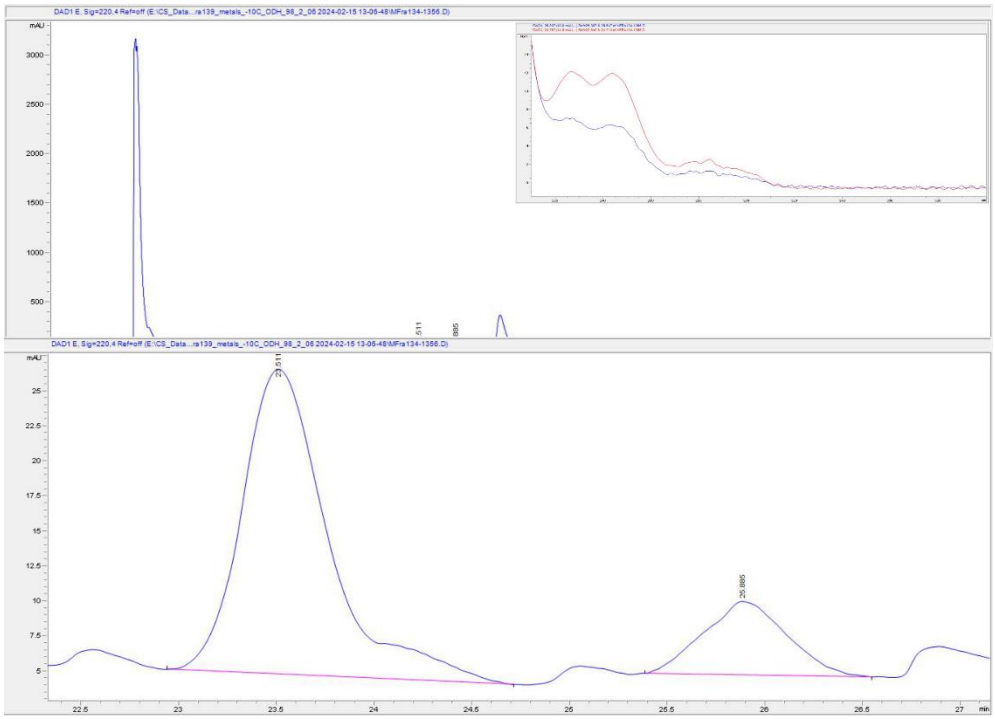

#	Time	Area	Height	Width	Area%	Symmetry
1	23.511	667.5	21.7	0.4662	81.121	0.683
2	25.885	155.4	5.2	0.3755	18.879	0.87

Amine **4b**; GP II (-10°C); 20 mol% TRIFP **1a**, $NaVO_3$ (Excess)

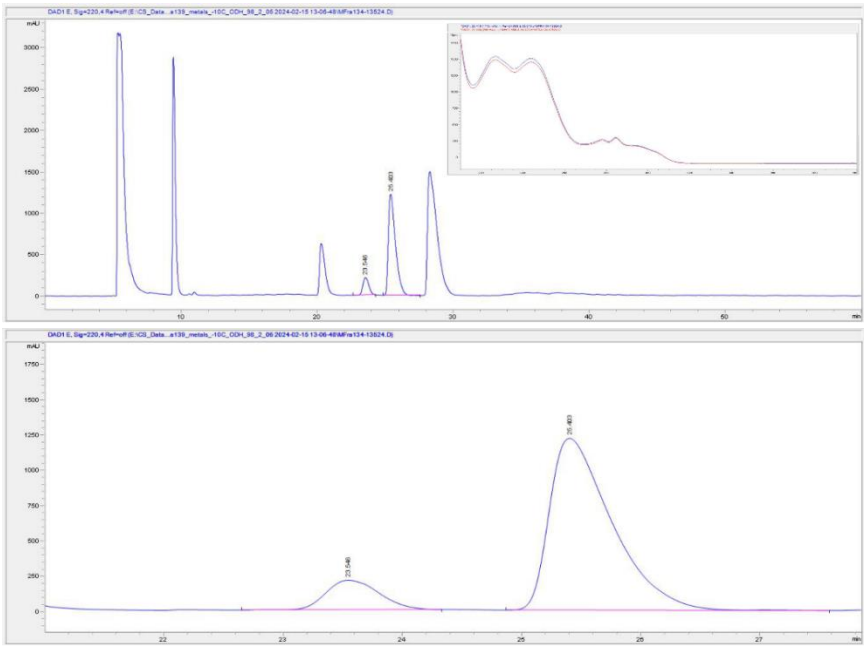

#	Time	Area	Height	Width	Area%	Symmetry
1	23.546	6522.7	210	0.4463	12.819	0.732
2	25.403	44361.9	1219.9	0.5436	87.181	0.444

Amine **4b**; GP II (-10°C); 20 mol% TRIFP **1a**, $PdCl_2$ (Excess)

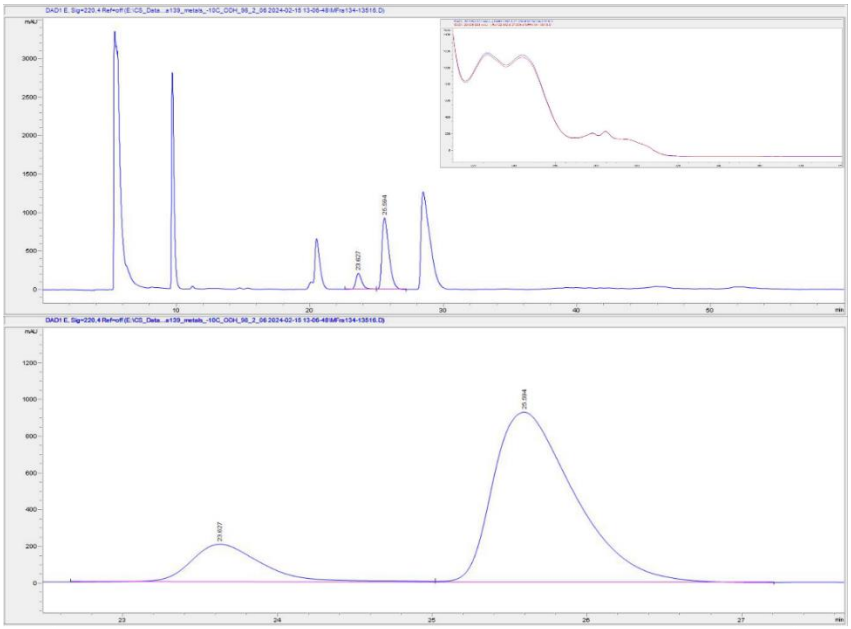

#	Time	Area	Height	Width	Area%	Symmetry
1	23.627	6735.4	206.4	0.4888	16.580	0.642
2	25.594	33888.1	928.1	0.562	83.420	0.568

Amine **4b**; GP II (-10°C); 20 mol% TRIFP **1a**, $PtNa_2Cl_6$ (Excess)

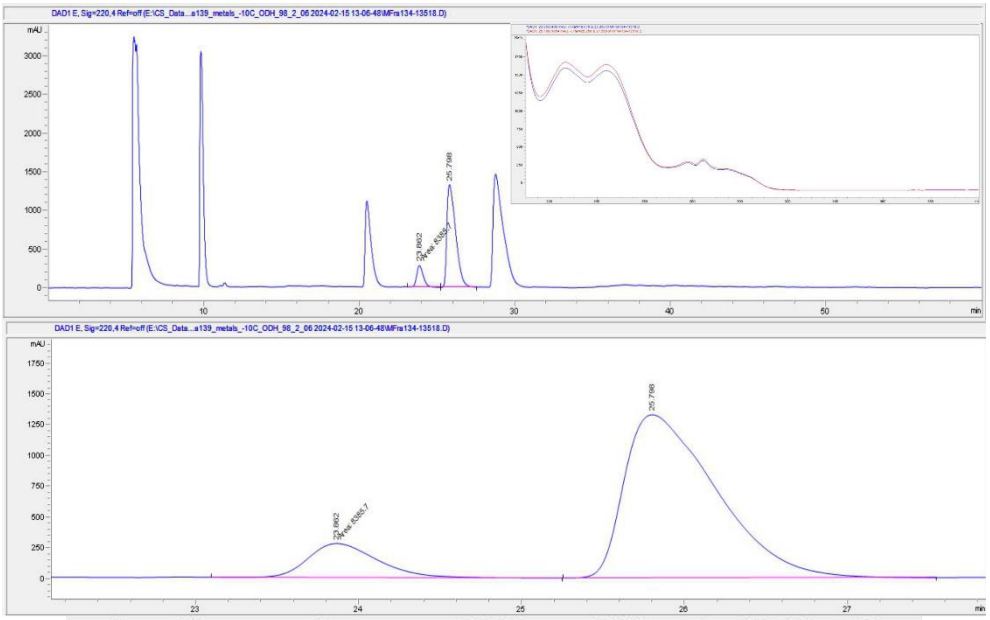

#	Time	Area	Height	Width	Area%	Symmetry
1	23.862	8575.4	278.1	0.4577	14.217	0.782
2	25.798	51743.3	1323.8	0.562	85.783	0.414

Amine **4b**; GP II (-10°C); 20 mol% TRIFP **1a**, $Ba(OH)_2$ (3 mM)

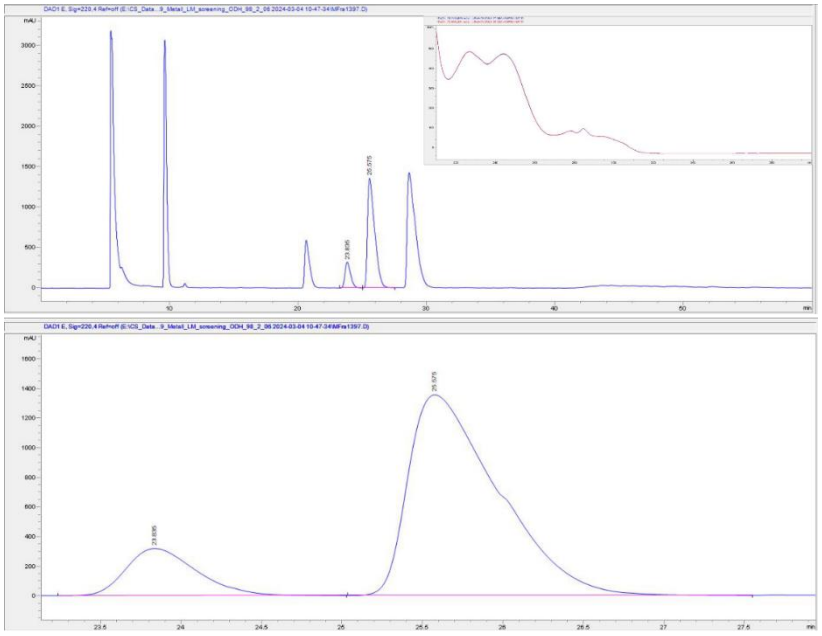

#	Time	Area	Height	Width	Area%	Symmetry
1	23.835	9727.3	318.8	0.4739	15.612	0.656
2	25.575	52580.7	1356.5	0.5742	84.388	0.395

Amine **4b**; GP II (-10°C); 20 mol% TRIFP **1a**, $Ca(OH)_2$ (3 mM)

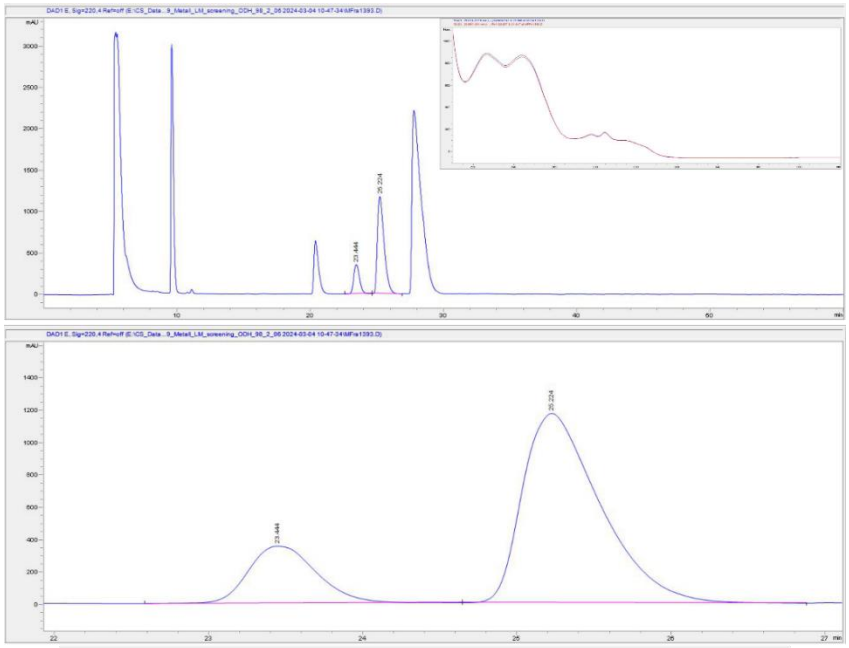

#	Time	Area	Height	Width	Area%	Symmetry
1	23.444	10819	352.6	0.4753	20.841	0.734
2	25.224	41094.5	1171.4	0.5353	79.159	0.556

Amine **4b**; GP II (-10°C); 20 mol% TRIFP **1a**, $Mg(OH)_2$ (3 mM)

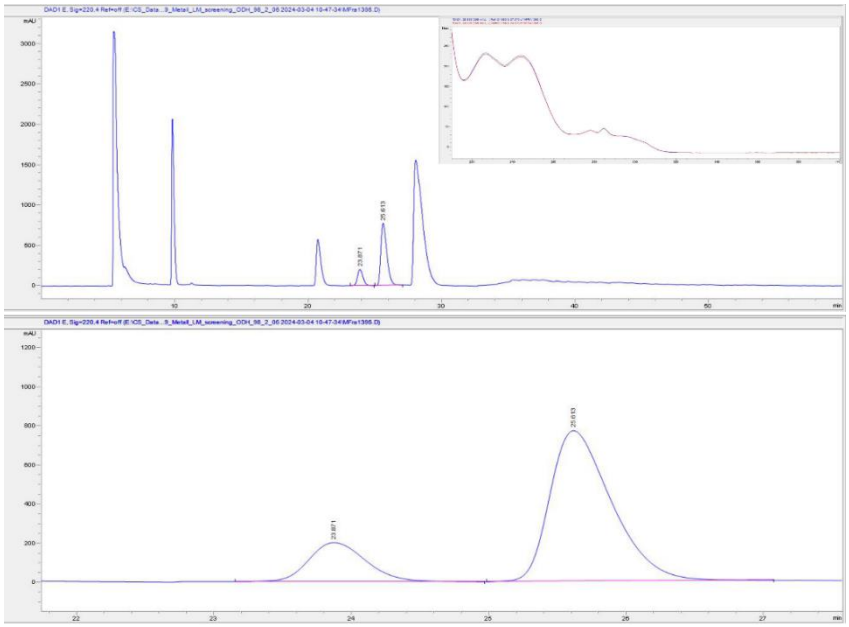

#	Time	Area	Height	Width	Area%	Symmetry
1	23.871	5774.7	199.9	0.447	19.365	0.769
2	25.613	24046.2	771.5	0.4816	80.635	0.585

Amine **4b**; GP II (-10°C); 20 mol% TRIFP **1a**, CaH_2 (6 mM)

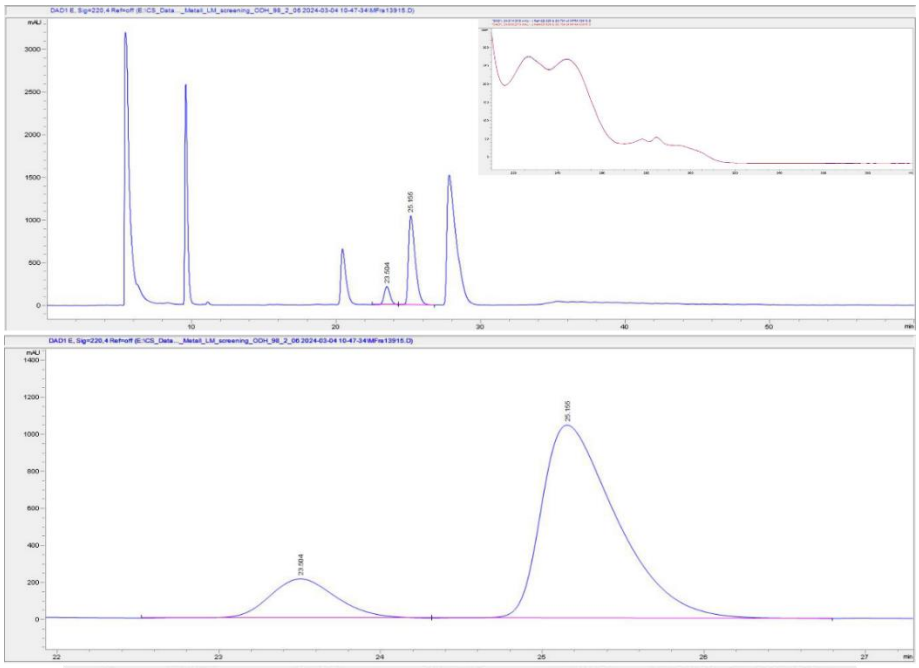

#	Time	Area	Height	Width	Area%	Symmetry
1	23.504	6097.9	212.4	0.447	15.261	0.832
2	25.155	33859.8	1046.4	0.4915	84.739	0.485

Amine **4b**; GP II (-10°C); 20 mol% TRIFP **1a**, KOMe (6 mM)

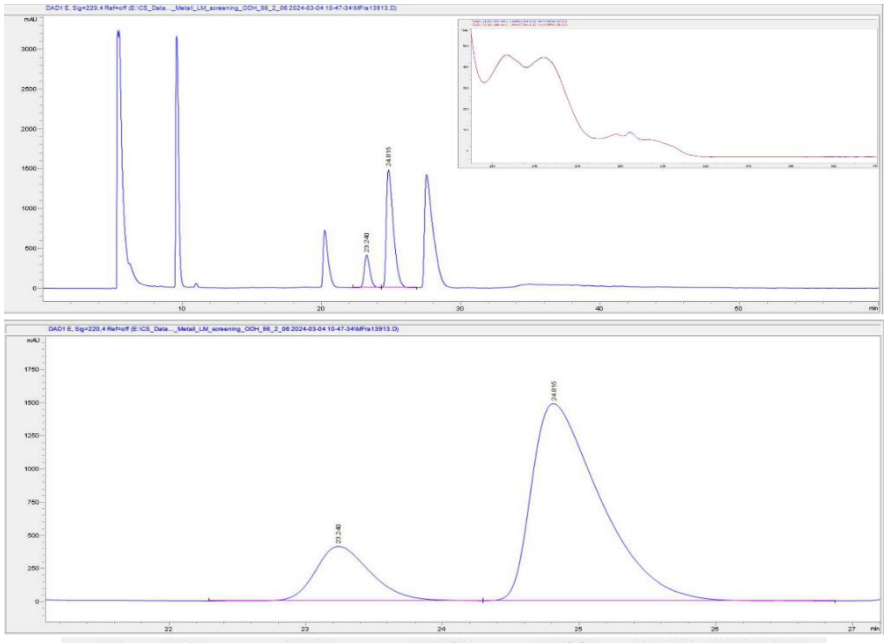

#	Time	Area	Height	Width	Area%	Symmetry
1	23.24	11545.4	410.8	0.4259	18.161	0.69
2	24.815	52028.3	1483.9	0.5269	81.839	0.433

Amine **4b**; GP II (-10°C); 20 mol% TRIFP **1a**, $LiClO_4$ (6 mM)

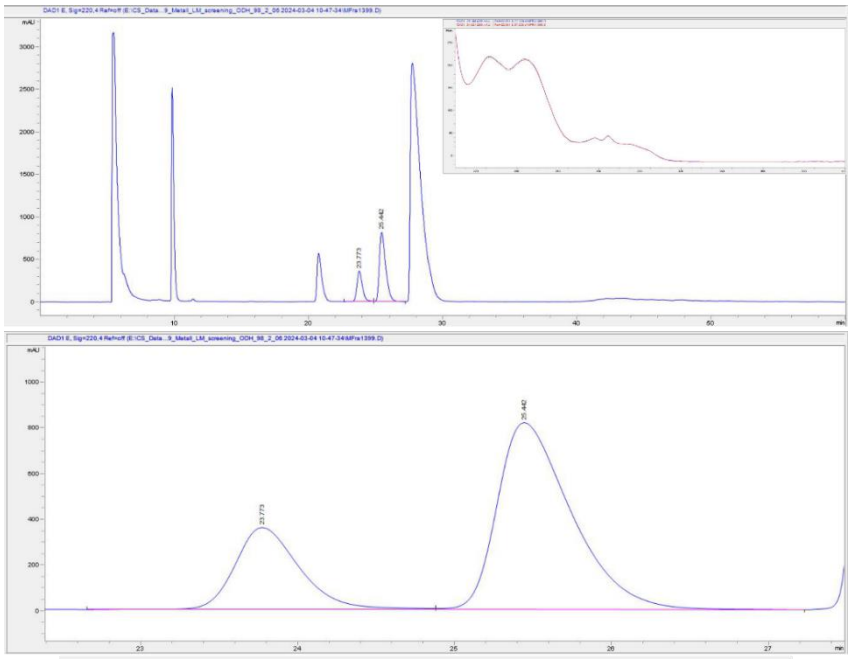

#	Time	Area	Height	Width	Area%	Symmetry
1	23.773	10249.6	358	0.432	27.666	0.693
2	25.442	26797.7	816.2	0.495	72.334	0.541

Amine **4b**; GP II (-10°C); 20 mol% TRIFP **1a**, $LiClO_4$ (42 mM)

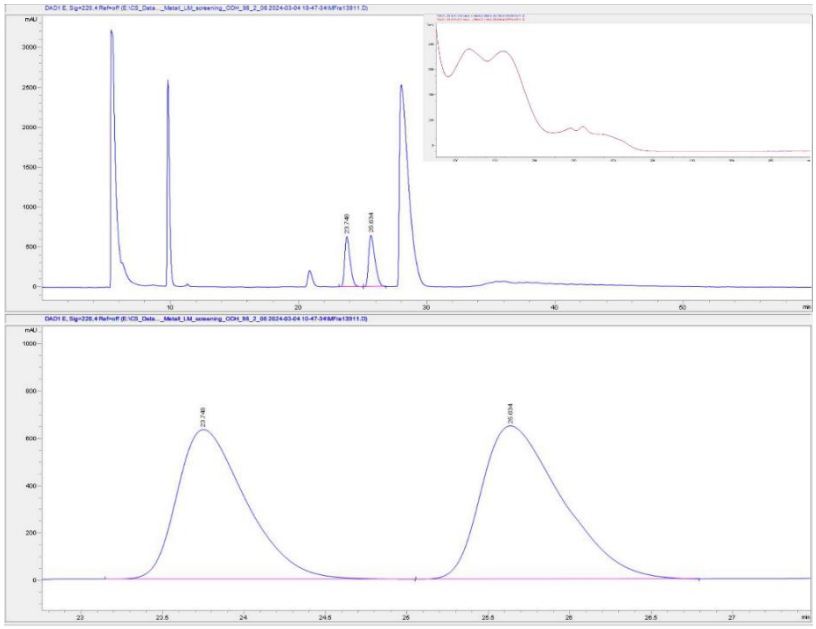

#	Time	Area	Height	Width	Area%	Symmetry
1	23.748	18531.7	630.6	0.4509	45.563	0.582
2	25.634	22140.9	645.6	0.5201	54.437	0.539

Amine **4b**; GP II (-10°C); 20 mol% TRIFP **1a**, DCM with MeOH (12 mM)

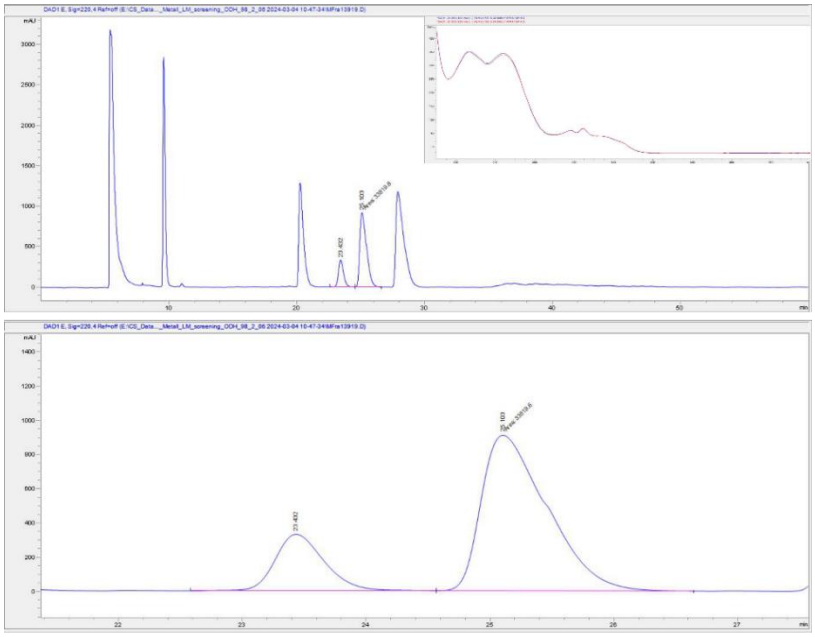

#	Time	Area	Height	Width	Area%	Symmetry
1	23.432	9293.3	332.8	0.4277	21.556	0.709
2	25.103	33819.6	914.2	0.6166	78.444	0.48

Amine **4b**; GP II (-10°C); 20 mol% TRIFP **1a**, DCM with THF (12 mM)

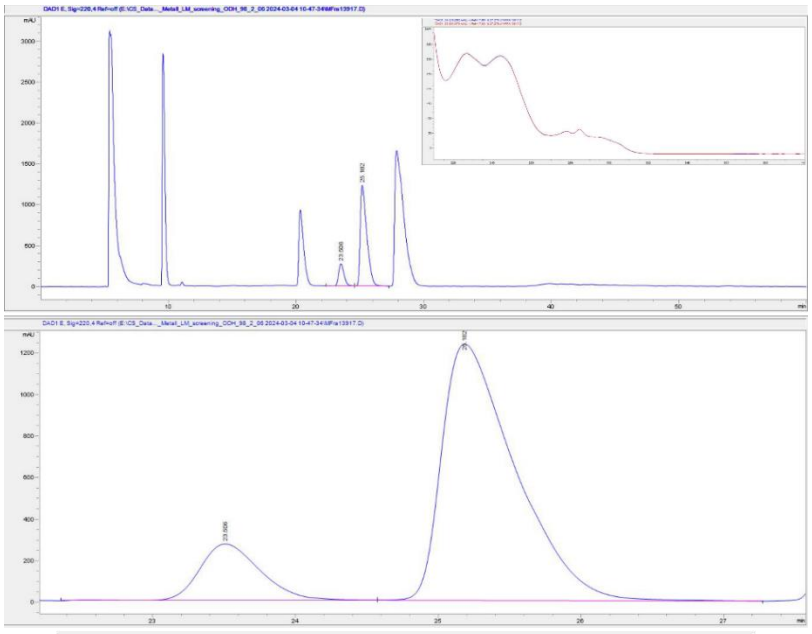

#	Time	Area	Height	Width	Area%	Symmetry
1	23.506	8212.6	273	0.4555	15.652	0.717
2	25.182	44255.9	1235.2	0.532	84.348	0.427

Amine **4b**; GP II (-10°C); 20 mol% TRIFP **1a**, DCM with H_2O (0 mM)

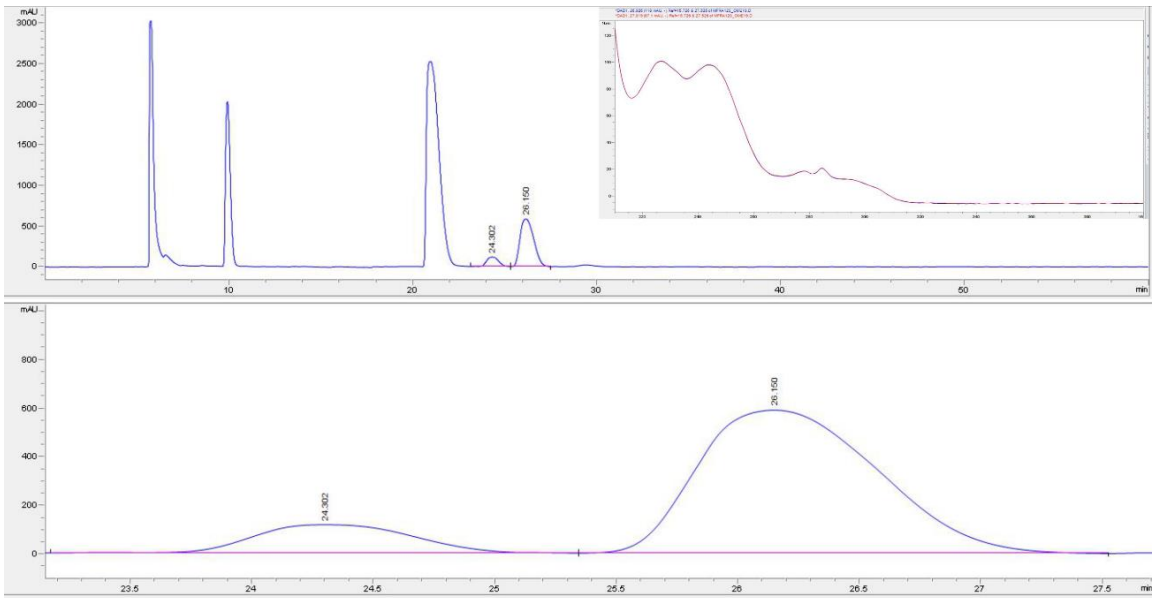

#	Time	Area	Height	Width	Area%	Symmetry
1	24.302	5489.5	118.1	0.7445	15.296	0.825
2	26.15	30399	590.4	0.8347	84.704	0.696

Amine **4b**; GP II (-10°C); 20 mol% TRIFP **1a**, DCM with H_2O (3 mM)

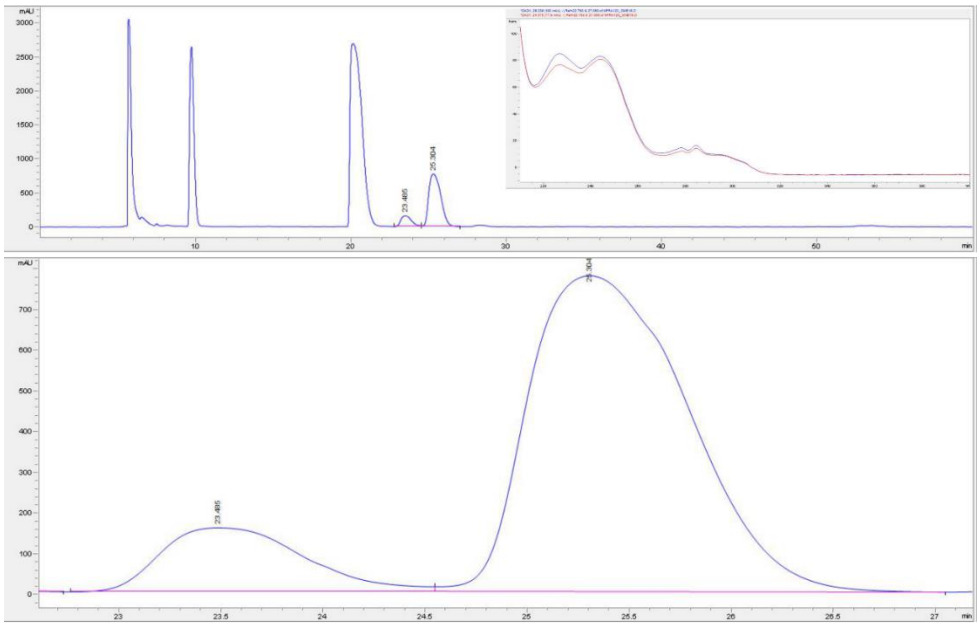

#	Time	Area	Height	Width	Area%	Symmetry
1	23.485	7709.9	157.4	0.7774	15.527	0.631
2	25.304	41946.2	778.1	0.7989	84.473	0.61

Amine **4b**; GP II (-10°C); 20 mol% TRIFP **1a**, DCM with H_2O (6 mM)

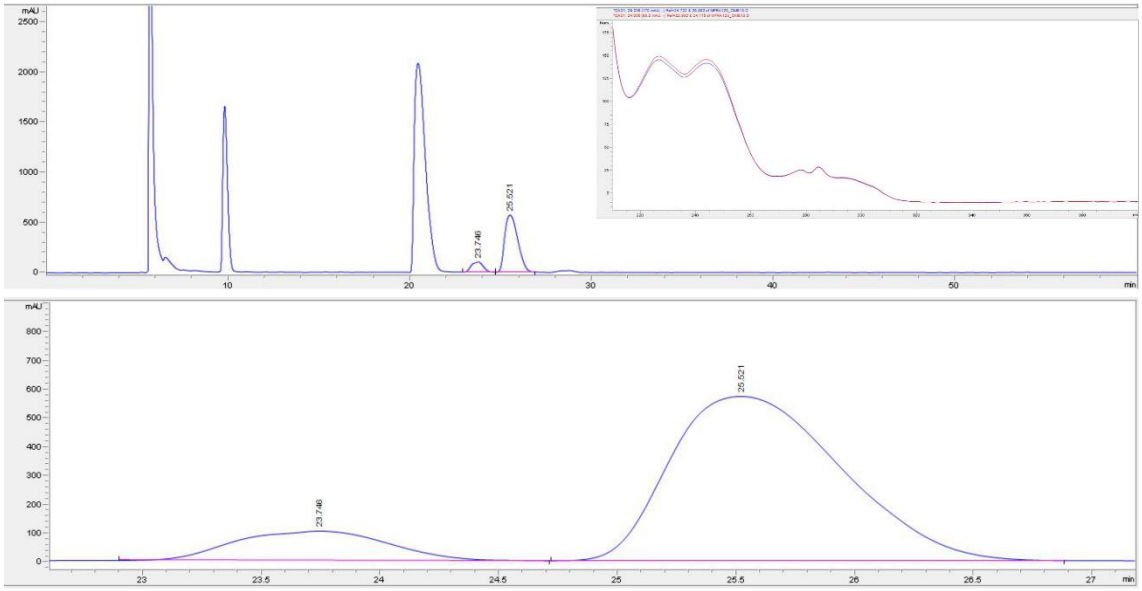

#	Time	Area	Height	Width	Area%	Symmetry
1	23.746	4591	102.2	0.6359	13.827	1.192
2	25.521	28613.4	571	0.7966	86.173	0.678

Amine **4b**; GP II (-10°C); 20 mol% TRIFP **1a**, DCM with H_2O (9 mM)

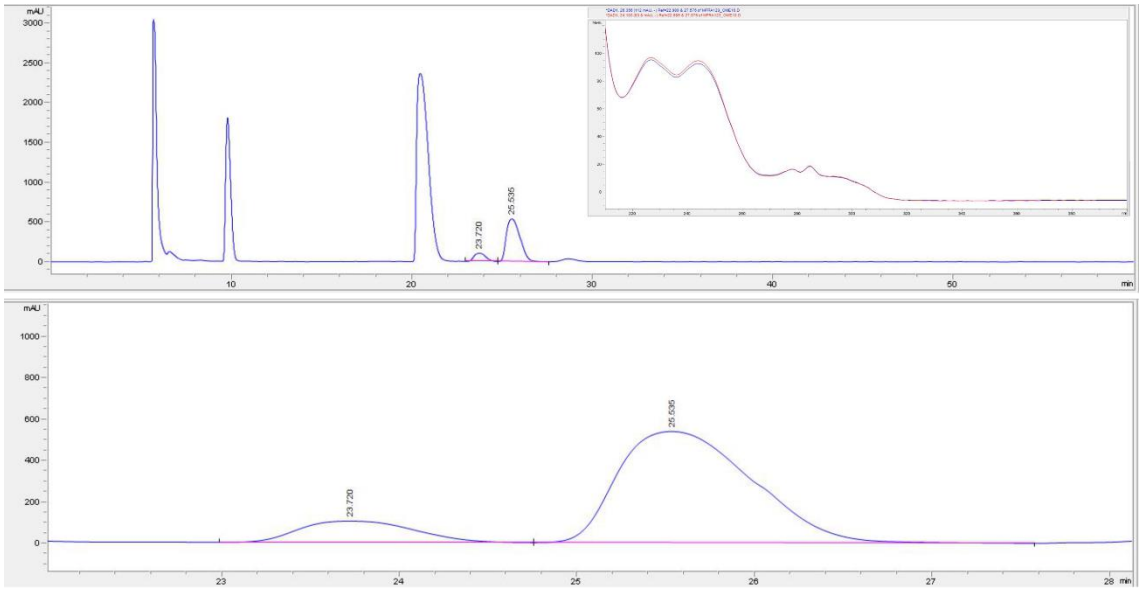

#	Time	Area	Height	Width	Area%	Symmetry
1	23.72	4663.2	102.9	0.7325	14.179	0.76
2	25.535	28224.4	537.2	0.833	85.821	0.635

Amine **4b**; GP II (-10°C); 20 mol% TRIFP **1a**, DCM with H_2O (12 mM)

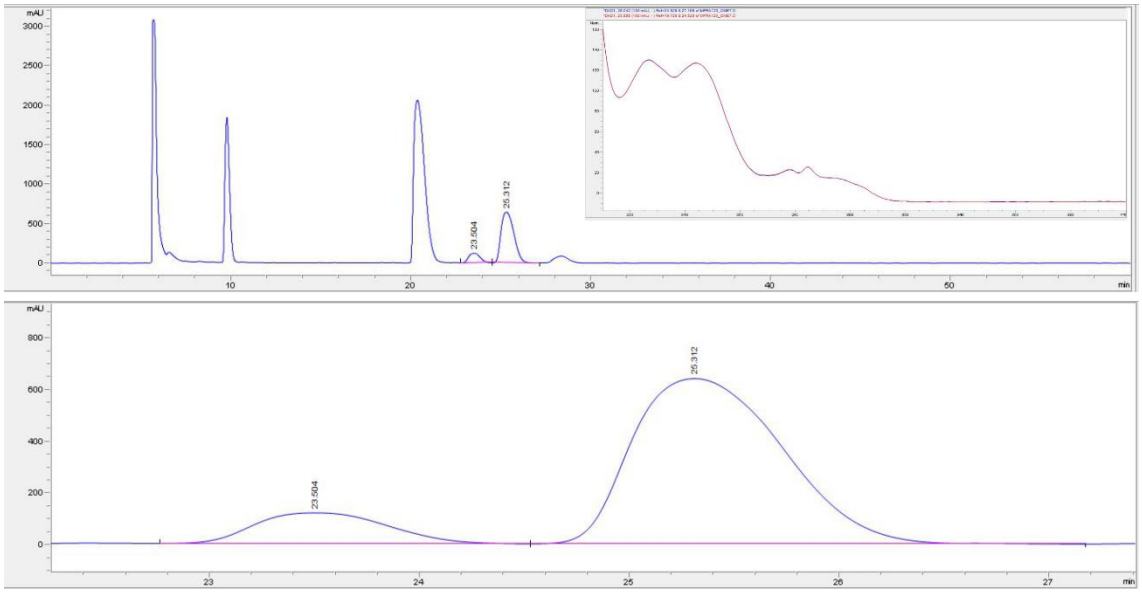

#	Time	Area	Height	Width	Area%	Symmetry
1	23.504	5369.7	120.6	0.7152	14.394	0.824
2	25.312	31935.1	641.4	0.8142	85.606	0.681

Amine **4b**; GP II (-10°C); 20 mol% TRIFP **1a**, DCM with H_2O (24 mM)

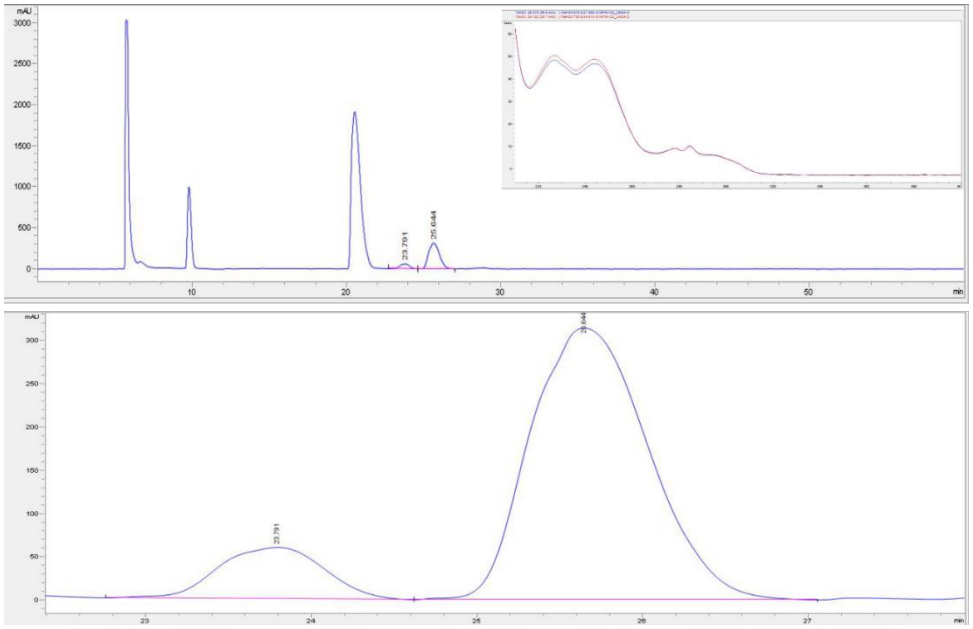

#	Time	Area	Height	Width	Area%	Symmetry
1	23.791	2650.5	59.8	0.6352	14.542	1.199
2	25.644	15576.8	315.1	0.7248	85.458	0.815

3.6.9. Acknowledgments

This project was financed by the German Science Foundation (DFG; RTG 2620) project number 426795949. P.D. thanks the German Academic Scholarship Foundation for funding.

3.6.10. References

[1] R. K. Harris, E. D. Becker, S. M. C. De Menezes, R. Goodfellow, P. Granger, Solid State Nucl. Magn. Reson. **2002**, 22, 458–483.

[2] K. Taguchi, F. H. Westheimer, J. Org. Chem. **1971**, 36, 1570–1572.

[3] P. Renzi, J. Hioe, R. M. Gschwind, J. Am. Chem. Soc. **2017**, 139, 6752–6760.

[4] N. Sorgenfrei, J. Hioe, J. Greindl, K. Rothermel, F. Morana, N. Lokesh, R. M. Gschwind, J. Am. Chem. Soc. **2016**, 138, 16345–16354.

[5] J. Gramüller, M. Franta, R. M. Gschwind, J. Am. Chem. Soc. **2022**, 144, 19861–19871.

[6] Q. Li, Y. Li, J. Wang, Y. Lin, Z. Wei, H. Duan, Q. Yang, F. Bai, Y. Li, New J. Chem. **2018**, 42, 827–831.

[7] J. P. Reid, J. M. Goodman, J. Am. Chem. Soc. **2016**, 138, 7910–7917.

[8] A. Jerschow, N. Müller, Macromolecules **1998**, 31, 6573–6578.

[9] E. O. Stejskal, J. E. Tanner, J. Chem. Phys. **1965**, 42, 288–292.

[10] A. Macchioni, G. Ciancaleoni, C. Zuccaccia, D. Zuccaccia, Chem. Soc. Rev. **2008**, 37, 479–489.

[11] D. Zuccaccia, A. Macchioni, Organometallics **2005**, 24, 3476–3486.

[12] H. C. Chen, S. H. Chen, J. Phys. Chem. **1984**, 88, 5118–5121.

[13] D. Ben-Amotz, K. G. Willis, J. Phys. Chem. **1993**, 97, 7736–7742.

[14] S. Hoffmann, A. M. Seayad, B. List, Angew. Chem. Int. Ed. **2005**, 44, 7424–7427.

[15] M. Rueping, E. Sugiono, C. Azap, T. Theissmann, M. Bolte, Org. Lett. **2005**, 7, 3781–3783.

4. Highly Nucleophilic Pyridinamide Anions in Apolar Organic Solvents due to Asymmetric Ion Pair Association

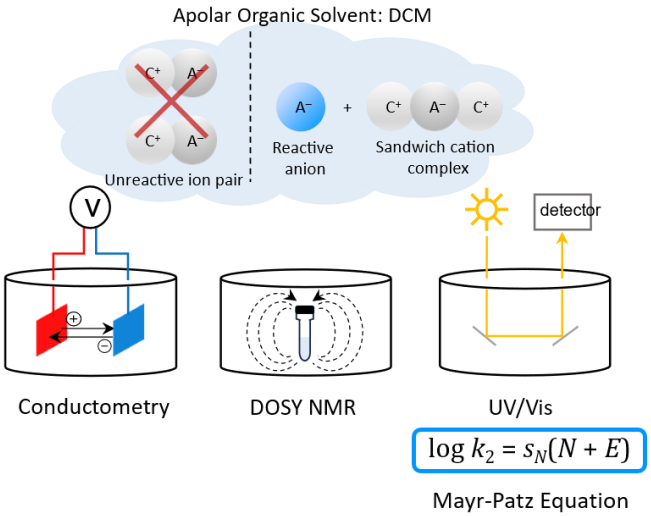

Veronika Burger, **Maximilian Franta**, Dr. Armin Ofial, Prof. Dr. Ruth M. Gschwind and Prof. Dr. Hendrik Zipse

To be submitted

A) Conductivity and Electrophilicty measurements were performed by Veronika Burger. All theoretical calculations were performed by Veronika Burger. The manuscript was mainly written by Veronika Burger and Maximilian Franta. B) DOSY NMR measurements were performed by Maximilian Franta. C) Dr. Armin Ofial contributed with interpretation of data, writing and proof-reading of the manuscirpt D) Prof. Dr. Ruth M. Gschwind contributed to conceptualization of the project, design of experiments, interpretation of data, writing and proof-reading of the manuscript and provided funding. E) Prof. Dr. Hendrik Zipse contributed to conceptualization of the project, design of experiments, interpretation of data, writing and proof-reading of the manuscript and provided funding.

Text and Figures may differ from the original manuscript.

4.1. Abstract

Free ions in apolar organic solvents are expected to be highly reactive. However, the formation of unreactive ion pairs at concentrations relevant for synthesis has prevented the success of this concept so far. On the example of highly nucleophilic pyridinamide phosphonium salts in dichloromethane we show that asymmetric aggregation offers a solution to this general problem. A combination of conductivity, diffusion-ordered NMR (DOSY), and kinetic measurements utilizing an ionic strength-controlled benzhydrylium ion methodology enables us to uniquely link insight about the number of ions with their aggregation/association state and nucleophilicity. This approach reveals that pyridinamide tetraphenylphosphonium salts aggregate in dichloromethane solution asymmetrically to a sandwich-type cation (composed of cations and anions in a 2:1 ratio) and a free anion. The nucleophilicity of this free anion exceeds that of the well-established reference nucleophile 9-azajulolidine (TCAP) by a factor of 38. Based on these results we suggest that asymmetric aggregation in apolar organic solvents might be a general pathway to boost the reactivity of anionic nucleophiles.

4.2. Introduction

Lewis basic pyridines, such as 4-(dimethylamino)pyridine (DMAP, **1**)[1] or the more reactive 9-azajulolidine (TCAP, **2**),[2] are frequently used catalysts for group transfer reactions such as acylations,[3-6] esterifications,[4,6] alkylations,[7] and silylations (Scheme 4.1).[8,9] The nucleophilicity of these catalysts has, together with other donor-substituted pyridines, been quantified using Mayr's benzhydrylium ion method.[10–13] Even higher nucleophilicities and possibly also higher catalytic activities in Lewis base-mediated reactions may be expected for anionic Lewis bases. Given that anionic reagents unavoidably require a counter-cation, such salts tend to form ion pairs when dissolved in organic solvents of low polarity, such as dichloromethane.[14,15] This ion clustering has beneficially been used in ion pair catalysis,[16-18] which extends from classical cationic phase-transfer (PT) catalysis[19] to applications in asymmetric synthesis.[16,20-22] Recently, the Zipse group introduced Lewis basic pyridinamide ion pair catalysts, which outperformed TCAP and other neutral organocatalysts in selected catalytic benchmark reactions.[23,24]

The pyridinamide phosphonium salts (such as **3a** and **4a** in Scheme 4.1) investigated so far show the general usefulness of the concept of anionic nucleophilic organocatalysis, whose development tails that of neutral systems.[25-27] In order to minimize ion pairing effects, most kinetic studies aiming at the quantification of the reactivity of anionic nucleophiles are performed in highly polar solvents (water, DMSO, etc.), often in combination with crown ether additives to further reduce the interactions between metal counter-ions and the reacting anion.[28] In solvents of low polarity, the intrinsic nucleophilicity of a free anion should be by far higher. However, the reactivity of anions is expected to depend on ion pair formation, which gives rise to non-linear effects and, thus, complicates systematic kinetic studies in apolar organic solvents (dichloromethane (DCM), THF, toluene etc.) commonly employed in organocatalysis.

In order to elucidate the underlying principles responsible for the high nucleophilicity of ion pairs such as **3a** and **4a**, we report here a combination of conductivity measurements, diffusion-ordered NMR (DOSY) measurements at very low concentrations, and photometric kinetic measurements by utilizing an ionic strength-controlled benzhydrylium methodology. This combination of physicochemical methods is expected to be generally

applicable to ion pair chemistry and catalysis and may help to uncover the full potential of this field.

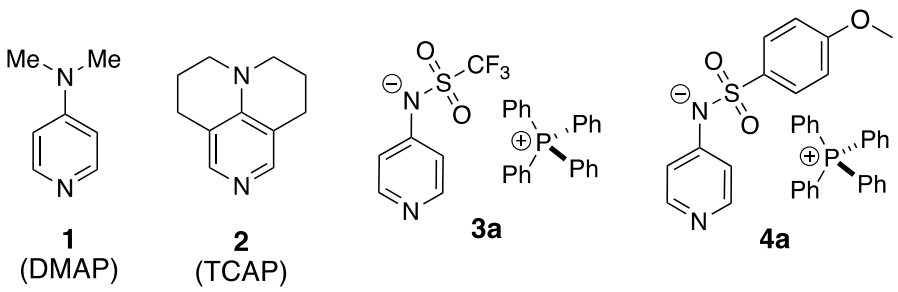

Scheme 4.1 Structures of neutral organocatalysts DMAP (1) and TCAP (2), and of pyridinamide ion pair catalyst 3a.

4.3. Results and Discussion

4.3.1. Conductivity

Conductivity measurements have frequently been employed to quantify ion pairing effects.[29-32] This method was therefore applied to determine the association of the cationic and anionic components of phosphonium salt **3a** selected here as a reference system in DCM and acetonitrile (MeCN). In both solvents **3a** is expected to be more reactive towards electrophiles than DMAP (**1**). Conductivity measurements were performed for concentrations ranging from 0.02 mM to 1.0 mM as this appears to represent the onset of ion pair formation from free ions. At low electrolyte concentrations and for the case of non-interacting ions the experimentally determined conductivity κ depends on the specific molar conductivity Λ_m and the ion concentration [A] as expressed in Equation (1).

$$\kappa = \Lambda_m[A] \qquad (1)$$

In the polar aprotic solvent MeCN the ions of **3a** are well stabilized and exist mainly as free ions as indicated by a nearly perfect linear increase of conductivity with [**3a**]. In the less polar solvent DCM the situation is more complex and two different domains can be seen in Figure 4.1B: (a) At low **3a** concentrations (region I, blue background) the conductivity κ correlates linearly with [**3a**] and (b) a non-linear part II at higher concentrations of **3a** (see Figure 4.1B beige background). While linear region I is assumed to represent the behavior of free anions (**3**) and cations (**a**), two ion association models were tested for non-linear region II. The first corresponds to the formation of ion pair **3a** (purple box in Figure 4.1A), while the second model involves formation of "sandwich cation" **a3a** together with free anion **3** (grey box in Figure 4.1A). The latter model was originally proposed to account for the properties of tetraalkyl ammonium salts in apolar solution,[33] and subsequently employed for a variety of systems in organic solvents.[34-37] In order to compare both models on equal footing, the respective equilibrium constants K_{IP} and K_{CAC} are defined relative to two equivalents each of free cation **a** and free anion **3**.

The 1:1 ion pair model retains the specific molar conductivity Λ_m derived from the linear region I and adds the effects of reducing the number of conducting species through

formation of overall neutral (and thus inactive) ion pairs **3a**. Fitting this model to the observed conductivities up to an overall concentration of 1.0 mM yields ion pair formation constant K_{IP} = 6.86 × 10^5 M^{-2} with good accuracy. The second model involves formation of sandwich cation **a3a** together with one equivalent of free anion **3** (grey box in Figure 4.1A), again combined with the specific molar conductivity Λ_m value obtained from linear region I. This model fits the observed conductivity values in the region up to 1.0 mM with sandwich association constant K_{CAC} = 6.38 × 10^6 M^{-2} with equally good accuracy. This is also true for a third model involving formation of sandwich anion **3a3** (blue box in Figure 4.1A), whose optimized association constant is actually identical at K_{ACA} = 6.38 × 10^6 M^{-2}. The measured conductivity values together with the model predictions are depicted in Figure 4.1B (grey line for the **a3a** sandwich model, blue line for the **3a3** sandwich model, and purple dotted line for the 1:1 ion pair), which illustrates that all models fit the experimental conductivity curve perfectly well as indicated by largely similar RMSE values of RMSE(K_{CAC}) = 0.17, RMSE(K_{ACA}) = 0.17, and RMSE(K_{IP})= 0.30, respectively.

4.3.2. DOSY NMR

Since conductivity measurements alone cannot provide direct information on the size of the contributing ions, DOSY-NMR measurements of **3a** were performed in DCM-d_2 for concentrations ranging from 0.001 mM to 1.0 mM (see Figure 4.1C). To enable DOSY measurements at these low concentrations, a 600 MHz spectrometer with a helium cryo probe and measurement times up to 12 h per sample were employed. The DOSY results were compared to calculated volumes of cation **a** (362 $Å^3$), anion **3** (215 $Å^3$), and contact ion pair **3a** (570 $Å^3$), which are based on the van der Waals cavities employed in the SMD continuum solvation model at the SMD(DCM)/B3LYP-D3/6-31+G(d) level of theory and indicated through the horizontal dashed lines in Figure 4.1C. At [**3a**] = 0.005 mM as the lowest concentration accessible for DOSY measurements we determined volumes of 367 $Å^3$ for cation **a** and 192 $Å^3$ for anion **3**, both of which agree closely with the SMD-derived volumes volumes for cation **a** and anion **3**. At any concentration of **3a** > 0.005 mM

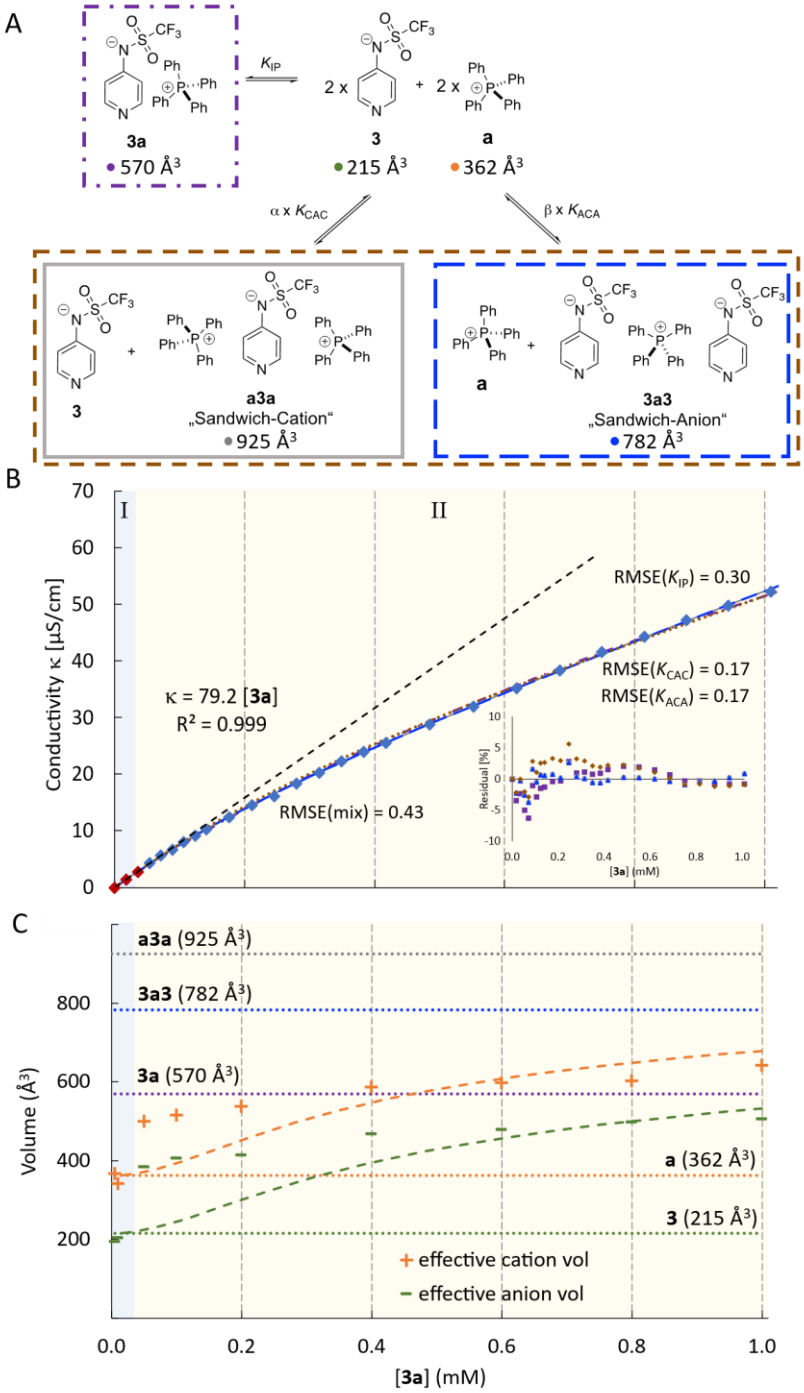

Figure 4.1 (A) 1:1 ion pair 3a, sandwich cation a3a, and sandwich anion 3a3 as potential association models for anion 3 and cation a together with SMD-derived molecular volumes; (B) conductivity profile for 3a in DCM fits to the calculated conductivity data for the 1:1 association model (purple dotted/dashed line), and the two sandwich association models (grey and blue line); (C) DOSY-derived ion volumes [Å³] compared to SMD-derived volumes (dashed horizontal lines) for single anion 3, single cation a, ion pair 3a, cation sandwich a3a, and anion sandwich 3a3.

Considerably larger cation and anion volumes were observed already in region I. In the 1:1 association model shown in the purple box in Figure 4.1A, the volumes of both species are expected to converge to the SMD-derived value of 570 Å^3 for the 1:1 ion pair

3a. Instead, we persistently detected substantially different effective volumes for cation **a** and anion **3** also at higher concentrations (region II), and also note that the DOSY-derived volume for cation **a** exceeds that calculated for the 1:1 ion pair **3a**.

This latter observation can be rationalized with the sandwich ion models, where the DOSY-derived cation volume is expected to approach that of the **a3a** sandwich cation of 925 Å^3. Combining the SMD-derived molecular volumes of ions with the equilibrium constants obtained from conductivity measurements allows us to predict concentration-dependent effective cation and anion volumes. These are shown in Figure 4.1C as a green line for anion and an orange line for cation volumes. Comparing experimentally derived with theoretically predicted volumes shows these to coincide quite well between 0.4 mM and 1.0 mM for the cation sandwich model.[38] In contrast, the 1:1 model predicts volumes for both ions which are significantly lower as the experimental values (by more than 200 Å^3 for the cation and >100 Å^3 for the anion, see SI). This is also true for the **3a3** anion sandwich model that predicts larger anion than cation volumes. The agreement between experimentally determined DOSY volumes and model predictions can be further improved by combining the two limiting sandwich models considered here. In practice this requires optimization of the two scaling factors α and β shown in Figure 4.1A such that the agreement with the conductivity data and the DOSY volumes is optimized. Best agreement for ion pair **3a** is found for α = 0.44 and β = 0.21, while the mixing coefficients are different for ion pair **4a** with α = 0.12 and β = 0.61 (see SI). The performance of these "mixed sandwich" models is quite satisfactory in concentration region II, but less so in region I with tis rapid increase of ion volumes with salt concentration. It is an intriguing aspect of the formation of sandwich cation **a3a** that it generates one equivalent of free anion **3** as the counterion. This may, in part, be due to the hydrogen bonding (and thus anion-stabilizing) properties of DCM.[39] The concentration of free anion **3** will quite obviously impact the efficiency of pyridinamide-anion based catalytic systems, where free anion **3** is expected to account for most of the observed activity.

4.3.3. Kinetics

To characterize the nucleophilic reactivity of ion pairs **3a** and **4a** we used Mayr‘s benzhydrylium ion method. This methodology has repeatedly demonstrated its utility to describe the reactivity of a wide range of carbon-, nitrogen, oxygen-, sulfur-, and phosphor-based nucleophiles in different solvents,[40] including DMAP (**1**) and TCAP

(**2**).[10,11,40] In short, the benzhydrylium ion method involves the photometric monitoring of the reactions of colored benzhydrylium salts, such as **5a**–**5c** (Table 4.1) whose electrophilic reactivities are characterized by the solvent-independent parameters *E*, with nucleophiles used in excess concentration to achieve kinetics under pseudo-first order conditions. The first-order rate constants k_{obs} (s^{-1}) can then be obtained by fitting a mono-exponential decay function to the decreasing absorption of **5** during the reaction with **3**. The conductivity measurements had shown that ion pairs **3a** and **4a** fully dissociate into anions and cations when dissolved in MeCN. Accordingly, a linear increase of pseudo-first order rate constants k_{obs} with nucleophile concentrations [**3**] (or [**3a**]) was observed in the kinetics of reactions of **3a** with **5** [Equation (2)].

$$k_{obs} = k_2[\mathbf{3}] \tag{2}$$

$$\log k_2 = s_N(N + E) \tag{3}$$

Equation (2) thus yields the second-order rate constants k_2 (M^{-1} s^{-1}) for the reactions of **3** with **5a**-**5c** in acetonitrile (Table 4.1). The rate constants k_2 for **3** are approx. three times larger than those for analogous reactions of **5** with DMAP (**1**) and quite similar to those for reactions with TCAP (**2**). Analyzing the kinetic data with the Mayr-Patz Equation (3) yields the nucleophilicity N = 16.38 (s_N = 0.60) of **3** in MeCN. Following exactly the same approach for ion pair **4a** yields N(**4a**) = 17.28 (s_N = 0.65), in full agreement with the results obtained for these two systems in selected catalytic transformations.[23]

The kinetics of reactions of **3a** with the reference electrophiles **5** in DCM solution, however, showed a more complex dependence of k_{obs} on [**3a**] in the concentration range from 0.01 to 1.0 mM (blue diamonds in Figure 4.2). In analogy to the conductivity measurements, an initial region I with linear k_{obs} vs. $[\mathbf{3a}]_0$ relation was observed (Figure 4.2, blue background, experimental values marked in red). At higher [**3a**] values this is followed by non-linear region II (beige background in Figure 4.2), where the observed rate constants deviate negatively from the linear correlation extrapolated from region I. The degree of deviation reflects the fraction of anion **3** captured in the (presumably) unreactive sandwich cation **a3a** and the (possibly also) less reactive sandwich anion **3a3**.

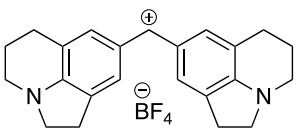

$(lil)_2CH^+$ (**5a**)
E = -10.04

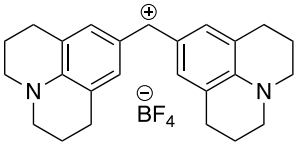

$(jul)_2CH^+$ (**5b**)
E = -9.45

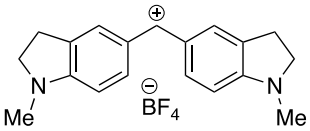

$(ind)_2CH^+$ (**5c**)
E = -8.76

Table 4.1 Second-order rate constants k_2 for the reactions of DMAP (1), TCAP (2), and pyridinamide salts 3a and 4a with reference electrophiles 5a, 5b, and 5c in MeCN (at 20 °C) analyzed by equation (3) to give the nucleophile-specific reactivity parameters N (and s_N).

Cat	k_2 [M^{-1} s^{-1}] *N* (s_N)			*N* (s_N)
	5a	**5b**	**5c**	
1[a]	2.11×10^3	5.30×10^3	1.29×10^4	15.51 (0.62)[e]
2[b]	6.30×10^3	–	4.17×10^4	15.60 (0.68)[e]
3[c]	7.16×10^3	1.53×10^4	4.13×10^4	16.38 (0.60)
4[d]	5.11×10^4	1.36×10^5	3.47×10^5	17.28 (0.65)

[a] Second-order rate constants k_2 from ref. [10]. [b] Second-order rate constants k_2 from ref. [11]. [c] Assuming that [3] = $[3a]_0$. [d] Assuming that [4] = $[4a]_0$. [e] Additional k_2 values from refs. [10,11] were used to determine N (and s_N).

Analysis of the kinetic data in region I (0.01 – 0.03 mM) is straightforward as conductivity measurements in combination with the sandwich association models indicate almost complete (> 97%) dissociation into separate ions **3** and **a**, that is [**3**] = $[\mathbf{3a}]_0$. Application of eq. (2) then yields k_2(**5a**) = 1.84×10^6 M^{-1} s^{-1} as indicated by the dotted line in Figure 4.2.

In synthetic applications, the concentration of ion pair catalysts is usually 1.0 mM or higher, which is far into the non-linear region II. Increasing ion concentrations may impact the reaction rates not only through shifting the association equilibrium towards a higher fraction of ion aggregates, but also through non-specific polarity effects. To assess the influence of the high salt concentration on the solvent polarity, we determined Reichardt's $E_T(30)$ values in DCM solutions with increasing concentrations of pyridinamide salt **3a** and additive $Ph_4P^+BF_4^-$ (**6**). We observed insignificant changes of the $E_T(30)$ values even at total salt concentrations of up to 6.0 mM (see SI). We conclude, therefore, that addition of **6** to a reaction mixture of **3a** and **5a-c** does not change the overall polarity of the solvent system and only affects the position of the ion pairing equilibrium shown in Figure 4.2, where higher concentrations of Ph_4P^+ (= **a**) give rise to an increase of [**a3a**]. To further investigate the effect of the $Ph_4P^+BF_4^-$ (**6**) additive, the ion volumes of selected **3a** + **6** mixtures were determined by DOSY measurements. The DOSY experiments show that the volumes of the cation and anion determined for **3a** + **6** mixtures at an ionic strength of *I* = 1.0 mM are in the same region as the volumes obtained for a pure **3a** solution at

[**3a**] = 1.0 mM (for details see SI). The kinetics of the reaction of **3a** + **5a** were subsequently studied at constant ionic strength (*I*) of *I* = 1.0 mM as this represents the highest concentration of **3a** in this study. At [**3a**] < 1.0 mM, the ionic strength of the DCM solution was adjusted by addition of **6** such that in each kinetic measurement the condition [**3a**] + [**6**] + [**5a**] = 1.0 mM is fulfilled.

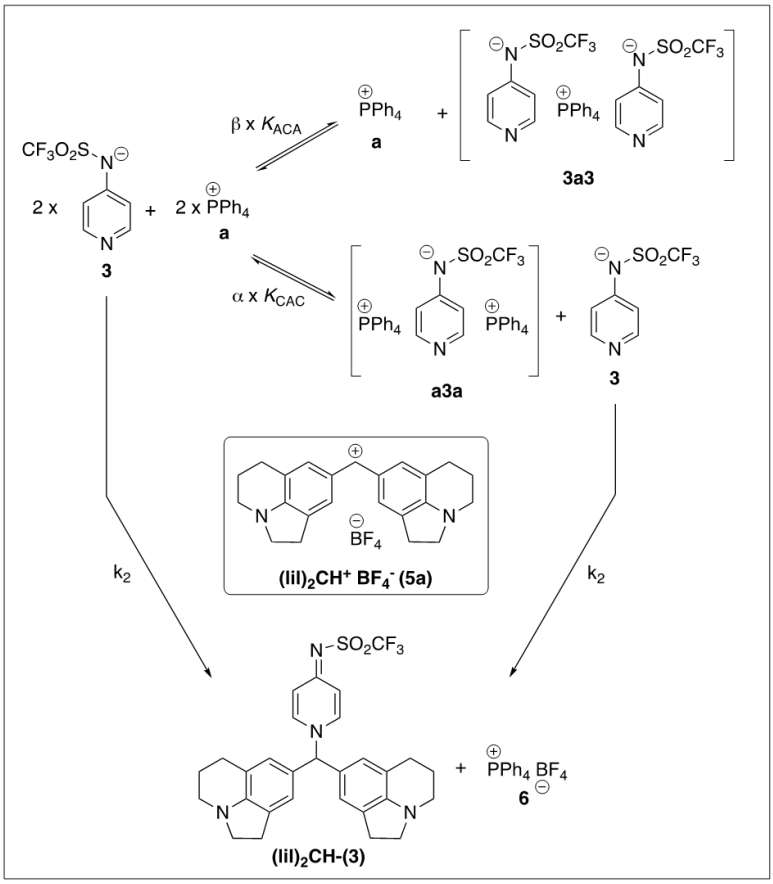

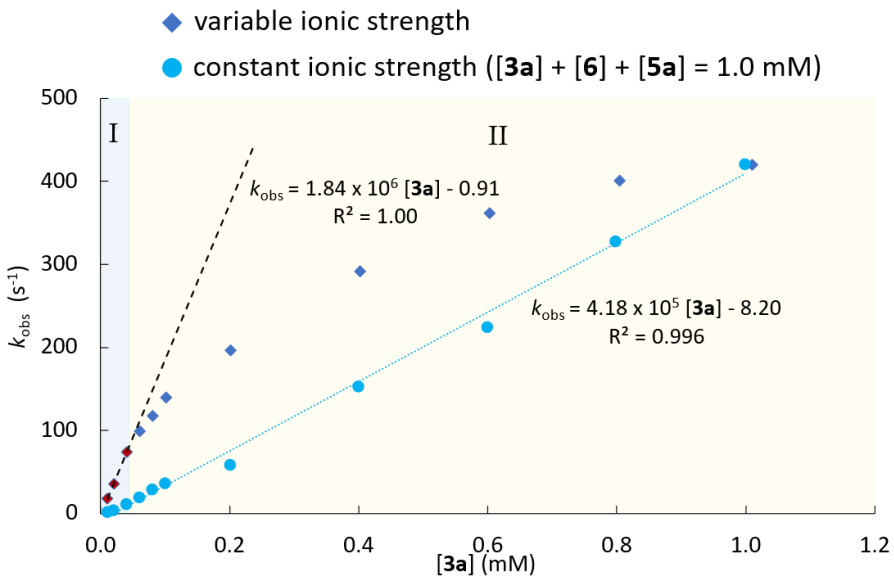

Figure 4.2 (A) Benzhydrylium ion reaction applied for the quantification of nucleophilicities. (B) Correlation of k_{obs} for the reaction of 5a with 3a for salt concentrations [3a] from 0.01 – 1.0 mM in DCM at 20°C (blue diamonds), and in the presence of additive PPh_4BF_4 (6) (turquoise dots).

By maintaining I = 1.0 mM, the rate constants k_{obs} for **3a** + **5a** reactions in DCM correlated linearly with [**3a**] in the entire concentration range from 0.01 to 1.0 mM (turquoise points in Figure 4.2). When we account for the fact that variable fractions of anion **3** are caught

in unreactive sandwich cation **a3a** (and to a smaller extend also in anion sandwich **3a3**), and also consider the effect of additive **6** on [Ph_4P^+], we obtain k_2(**5a**) = 5.38 × 10^5 M^{-1} s^{-1} for the reaction of **3** with **5a**, which is by a factor of 3.5 smaller than k_2 obtained in the low-concentration region (Table 4.2). Analogous kinetic measurements at I = 1.0 mM were performed for reactions of **3a** with the more reactive benzhydryl salts **5b** and **5c** (Table 4.2).

Table 4.2 Second-order rate constants k_2 of the reactions of DMAP (1), TCAP (2), and pyridinamide salt 3a with the reference electrophiles 5a, 5b, and 5c in DCM (at 20 °C).

Cat	k_2 [M^{-1} s^{-1}]		
	5a	**5b**	**5a**
1[a]	6.45 × 10^3	**1**[a]	6.45 × 10^3
2[b]	1.42 × 10^4	**2**[b]	1.42 × 10^4
3[c]	1.84 × 10^6 (LC)	**3**[c]	1.84 × 10^6 (LC)
3[d]	5.42 × 10^5 (mix)	**3**[d]	5.42 × 10^5 (mix)
4[e]	1.69 × 10^6 (mix)	**4**[e]	1.69 × 10^6 (mix)

[a] Second-order rate constants k_2 from ref. [10a]. [b] This work, see Supporting Information for details of the kinetic experiments. [c] Determined at [3] < 0.03 mM, that is, in the low concentration (LC) region I (Figure 4.2), by assuming [3] = $[3a]_0$. [d] Determined over a concentration range [3a] = 0.1 to 0.3 mM at constant ionic strength I = 1.0 mM (kept by addition of salt 6) by assuming a mixed sandwich association model which generates a3a as the counter-cation of the nucleophilic anion 3. [e] Determined over a concentration range [3a] = 0.04 to 0.1 mM at constant ionic strength I = 1.0 mM (kept by addition of salt 6) by assuming a mixed sandwich association model.

In DCM as the solvent, we note a moderate increase in the bimolecular rate constants k_2 when going from DMAP (**1**) to TCAP (**2**), but a significantly larger increase of the k_2 values for **3a** (Table 4.2). The k_2 values for reaction of **3a** with **5a**-**5c** in DCM in the low concentration (LC) region I (as defined in Figure 4.2) exceed those for **2** by approx. two orders of magnitude. Analyzing the LC kinetic data by the Mayr-Patz equation (3) gives N = 17.78 (s_N = 0.81) for **3a**. Rate constants k_2 for reactions of **3** with all three benzhydryl cations **5a**-**5c** decrease slightly (by a factor of 3.5-4.5) under conditions of constant ion strength (I = 1.0 mM). The resulting N-parameter for **3** is, however, hardly changed at N = 17.88 (s_N = 0.73). Following the same mode of analysis for ion pair **4a** under reactions conditions where I = 1.0 mM, we find that anion **4** exceeds the nucleophilicity of **3** by a factor of 3.0±0.5 in its reaction with benzhydryl cations **5a**-**5c** as is also reflected in the respective N-parameter of N(**4**) = 19.63 (s_N = 0.65).

These measurements thus establish **3a** and **4a** as potent and exceedingly nucleophilic pyridine derivatives in solvents of low polarity (Figure 4.3). That **4a** is more nucleophilic than **3a** is in full agreement with the results for selected organocatalytic transformations performed in $CDCl_3$ as the solvent.[23] The combined methodology developed here thus

allows for a quantitative assessment of catalyst nucleophilicity at synthetically relevant concentrations.

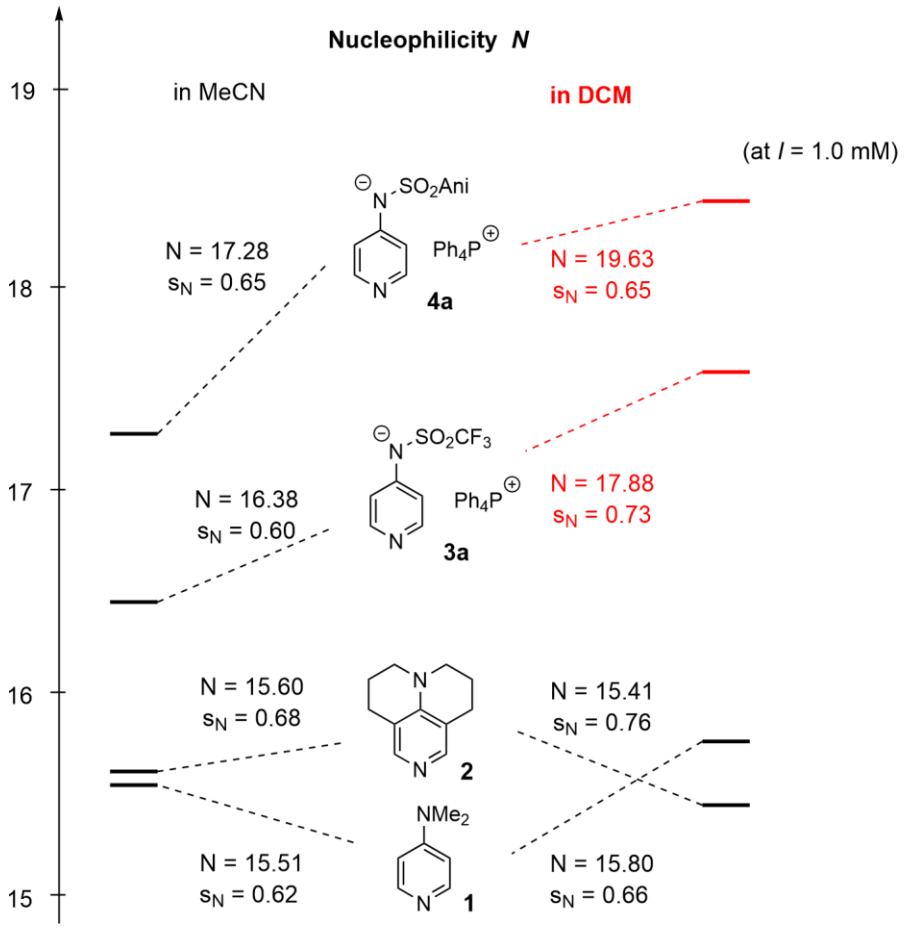

Figure 4.3 Mayr nucleophilicities N (and s_N) of DMAP (1), TCAP (2), and the pyridinamide anion 3 and 4 in MeCN and DCM.

4.4. Conclusion

Employing a combination of conductivity and DOSY measurements, we have deciphered the asymmetric association behavior of pyridinamide ion pair **3a** in the apolar solvent DCM. Through the combination of well soluble anions with less soluble cations, sandwich cation complexes of the general type of cation/anion/cation are formed, leaving a free anion to act as highly reactive nucleophile. This association competes favorably with alternative sandwich anion species and thus overcomes the drawback of ionic compounds associating into poorly reactive 1:1 adducts in apolar solvents. Without the combination of conductivity and DOSY measurements this result could not have been achieved since conductivity alone does not give insight into the type of charged species that are being measured. The reactivity of the super-nucleophilic anions was quantified with the benzhydrylium ion method, which facilitates the comparison of **3a** and **4a** with neutral nucleophilic catalysts, such as DMAP or TCAP. In DCM, we were able to evaluate kinetic data not only at low ion pair concentrations, but also at synthetically relevant higher concentrations by keeping the ionic strength constant throughout the measurement to prevent the interference of ion association. The direct comparison of k_2 values for reactions with cationic reference electrophiles reveals nucleophilicity values of pyridinamide anions **3** and **4** (at high concentration) that are 39 and 90 times higher than that of TCAP (**2**). One might expect that the higher nucleophilicity of **3** and **4** in comparison to neutral nucleophilic catalysts, which was determined by using cationic reference electrophiles, may not be comparably effective for reactions with neutral electrophiles (typically used substrates in acylations, alkylations, or esterifications) in low polarity media (toluene, alkanes, THF, Et_2O). However, recent results showed that a significant fraction of the superior reactivity of pyridinamide anions is also found in reactions with neutral substrates.[19,34]

4.5. References

[1] a) L. M. Litvinenko, A. I. Kirichenko, Dokl. Akad. Nauk. SSSR **1967**, 176, 97; b) W. Steglich, G. Höfle, Angew. Chem. Int. Ed. **1969**, 8, 981–981.

[2] M. R. Heinrich, H. S. Klisa, H. Mayr, W. Steglich, H. Zipse, Angew. Chem Int. Ed. **2003**, 42, 4826–4828.

[3] W. Steglich, G. Höfle, Tetrahedron Lett. **1970**, 4727–4730.

[4] A. Hassner, V. Alexanian, Tetrahedron Lett. **1978**, 4475–4478.

[5] G. Höfle, W. Steglich, H. Vorbrüggen, Angew. Chem. Int. Ed. **1978**, 17, 569–583.

[6] B. Neises, W. Steglich, Angew. Chem. Int. Ed. **1978**, 17, 522–524.

[7] S. K. Chaudhary, O. Hernandez, Tetrahedron Lett. **1979**, 20, 95–98.

[8] P. Patschinski, C. Zhang, H. Zipse, J. Org. Chem. **2014**, 79, 8348–8357.

[9] S. K. Chaudhary, O. Hernandez, Tetrahedron Lett. **1979**, 20, 99–102.

[10] For the nucleophilic reactivity of DMAP (1) in MeCN, see: (a) F. Brotzel, B. Kempf, T. Singer, H. Zipse, H. Mayr, Chem. Eur. J. **2007**, 13, 336–345. (b) for supplementary kinetic data and revised *N* (and s_N) parameters for DMAP (**1**), see: T. A. Nigst, J. Ammer, H. Mayr, J. Phys. Chem. A **2012**, 116, 8494–8499.

[11] R. Tandon, T. Unzner, T. A. Nigst, N. De Rycke, P. Mayer, B. Wendt, O. R. P. David, H. Zipse, Chem. Eur. J. **2013**, 19, 6435–6442.

[12] H. Mayr, Tetrahedron 2015, 71, 5095–5111.

[13] Lakhdar, S. in *Lewis Base Catalysis in Organic Synthesis*, First Ed. (Eds.: E. Vedejs, S. E. Denmark), Wiley-VCH, Weinheim, **2016**, Chapt. 4, pp. 85-116.

[14] Y. Marcus, G. Hefter, Chem. Rev. **2006**, 106, 4585–4621.

[15] C. Reichardt, Solvents and Solvent Effects in Organic Chemistry (3rd ed.), VCH, Weinheim, **2003**, Chapt. 5.5.5.

[16] K. Brak, E. N. Jacobsen, Angew. Chem. Int. Ed. **2013**, 52, 534–561.

[17] a) M. Waser, J. Novacek, K. Gratzer, in Coop. Catal., Wiley, **2015**, pp. 197–226. b) J. Otevrel, M. Waser, in Asymmetric Organocatalysis, Wiley, **2023**, pp. 71–120.

[18] X. Ye, C.-H. Tan, Chem. Sci. **2021**, 12, 533–539.

[19] S. Shirakawa, K. Maruoka, Angew. Chem. Int. Ed. **2013**, 52, 4312–4348.

[20] C. Merten, C. H. Pollok, S. Liao, B. List, Angew. Chem. Int. Ed. **2015**, 54, 8841–8845.

[21] M. Mahlau, B. List, Angew. Chem. Int. Ed. **2013**, 52, 518–533.

[22] R. J. Phipps, G. L. Hamilton, F. D. Toste, Nat. Chem. **2012**, 4, 603–614.

[23] J. Helberg, T. Ampßler, H. Zipse, J. Org. Chem. **2020**, 85, 5390–5402.

[24] S. H. Dempsey, A. Lovstedt. S. R. Kass, J. Org. Chem. **2023**, 88, 10525–10538.

[25] H. J. A. Dale, G. R. Hodges, G. C. Lloyd-Jones, J. Am. Chem. Soc. **2023**, 145, 18126–18140.

[26] X. Yang, V. B. Birman, Org. Lett. **2009**, 11, 1499–1502.

[27] D. J. M. Lyons, C. Empel, D. P. Pace, A. H. Dinh, B. K. Mai, R. M. Koenigs, T. V. Nguyen, ACS Catal. **2020**, 10, 12596–12606.

[28] C. L. Liotta, H. P. Harris, J. Am. Chem. Soc. **1974**, 96, 2250–2252.

[29] L. Coury, Current Sep. **1999**, 3, 91–96.

[30] M. Mizuhata, Electrochemistry **2022**, 90, 1–12.

[31] L. Martínez, Quim. Nova **2018**, 41, 814–817.

[32] R. Schneider, H. Mayr, P. H. Plesch, Ber. Bunsenges. Phys. Chem. **1987**, 91, 1369–1374.

[33] The triple ion sandwich model has first been proposed in: R. M. Fuoss, C. A. Kraus, J. Am. Chem. Soc. **1933**, 55, 2387-2399.

[34] J. Jiang, K. P. N. G. Dennis, Acc. Chem. Res. **2009**, 42, 79–88.

[35] M. Hojo, H. Moriyama, J. Solution Chem. **1996**, 25, 681–694.

[36] M. Hojo, T. Ueda, T. Inoue, M. Ike, M. Kobayashi, H. Nakai, J. Phys. Chem. B **2007**, 111, 1759–1768.

[37] F. Zhu, W. Zhang, H. Liu, X. Wang, Y. Zhou, C. Fang, Y. Zhang, Spectrochim. Acta - Part A Mol. Biomol. Spectrosc. **2020**, 224, 117308.

[38] Note: At concentrations lower than 0.4 mM the experimental values deviate considerably from the theoretical curve. This shows that the equilibrium between free ions and sandwich ion cannot be described by a simple model. However, the concentration limits of DOSY prevent further refinements.

[39] C. A. Hunter, Angew. Chem. Int. Ed. **2004**, 43, 5310–5324.

[40] H. Mayr, A. Ofial, „Database of Nucleophilicities and Electrophilicities“, can be found under https://www.cup.lmu.de/oc/mayr/reaktionsdatenbank2/, 2015.

4.6. Supporting Information

4.6.1. NMR Spectroscopy

Diffusion ordered NMR spectroscopy (DOSY) experiments were performed using a Bruker® Avance III 600 MHz operating at 600.25 MHz for protons, equipped with a 5-mm high-resolution TCI cryoprobe and with pulsed gradient units, capable of producing magnetic field pulsed gradients in the z-direction of 0.64 $T.m^{-1}$. All measurements were performed at 298 K. Temperature was certified by internal NMR calibration samples from Bruker®. NMR Data was processed, evaluated, and plotted with TopSpin 3.2 software. Further analysis of the measurements was performed with Microsoft Excel (Version 16.0.10359.20023 64 Bit).

4.6.1.1. Sample Preparation for NMR Spectroscopy

For the sample preparation 1.0 mL stock solutions with a concentration of 1/5 mM were prepared of ion pair **3a** in freshly distilled deuterated solvents (CD_2Cl_2, CD_3CN). These stock solutions were then diluted to the respective concentrations. Thereafter the stock solution was put in an ultrasonic bath for 1 minute before it was used. Before the addition of the stock solutions, the NMR tubes were evacuated and flushed with Argon three times. Then the stock solution was added to the NMR tube under Argon flow. Tetramethyl silane (TMS) was added as a reference by withdrawing 0.5 mL from the atmosphere of the TMS bottle, just above the surface of the liquid. Afterwards, the NMR tube was sealed and again put in an ultrasonic bath for 1 minute before use.

4.6.1.2. Diffusion Ordered Spectroscopy (DOSY)

All DOSY measurements were performed with the convection suppressing DSTE (double stimulated echo) pulse sequence developed by Jerschow and Müller in a pseudo 2D mode.[1] Therefore, TMS was added to the sample and used as reference for the ^1H chemical shifts and for temperature as well as the viscosity of the solvent. For the measurement a set of 4 dummy scans and 32 scans was used for samples with concentration ≥ 0.5 mM of the ion pair. A set of 4 dummy scans and 64 scans were used for samples with concentrations ≥ 0.1 mM of the ion pair. A set of 4 dummy scans and 256 scans was used for samples with less than 0.05 mM of the ion pair. A relaxation delay of 3.5 s was used for all samples. The diffusion time delay was set to 40 ms and

the gradient pulse lengths (p30, SINE.100 pulse shape) were optimized for each species to give a sigmoidal signal decay for varying gradient strengths between 5% and 95%. Optimal pulse lengths of 1.12 – 1.3 ms were used at 298 K for TMS and ion pairs. For each species, twenty spectra with linear varying gradient strength from 5% to 95% were measured. Thereby, no line broadening occurred for increased gradient strengths. For integration the corresponding signals of **3a** were used except if there was an overlap with another signal (see Figure S4.1).

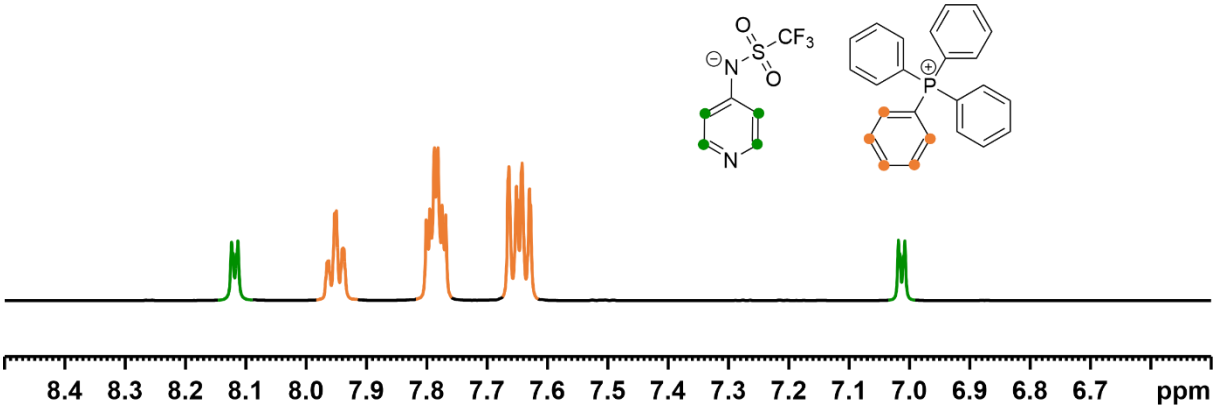

Figure S4.1 Signals used for DOSY evaluation of 3a. Anion signals are marked in green, cation signals are marked in orange. All corresponding signals were used for DOSY evaluation and averaged for each ion.

In general, the transformation of diffusion coefficients into hydrodynamic radii via the Stejskal-Tanner equation is applicable for neutral molecules. In the case of ions, the additional electrostatic interactions between counter ions should be included and are expected to reduce the mobility of the ions at higher concentrations. In this manuscript extremely low concentrations of ions between 0.001 mM and 1.0 mM are applied, therefore the electrostatic interactions should be negligible. Indeed, DOSY/Steijskal-Tanner/Stokes-Einstein approach for measurements at extremely low concentrations were in good agreement with the calculated volumes of the free ions. Furthermore, upon concentration increase the DOSY data don't show any direct correlation to the concentration but a concentration dependence which in combination with the conductivity data and the nucleophilicity data is only consistent with the sandwich formation (see main text). In addition, for the interpretation mainly the relative values of cations and anions i.e. the offset is important, and this shouldn't be affected by the electrostatic interactions. Therefore, the signal intensities of these groups in the DOSY spectra were classically analyzed as a function of the gradient strength by the in Bruker TopSpin 3.2 included software T1/T2 relaxation package by employing the Stejskal-Tanner equation.[2] Based

on the obtained translational diffusion coefficients, the hydrodynamic radii of the analytes r_H were estimated following the Stokes-Einstein equation (S1), with D_i = self-diffusion coefficient k = Boltzmann constant, T = temperature, η = viscosity of the sample, c = correcting factor, F = shape factor:[3]

$$D_i = \frac{kT}{Fc\pi\eta r_H} \tag{S1}$$

The shape factor F was set to 1 for a spherical shape. The semi-empirical modification by Chen (S2) was used to calculate the correction factor c. Therefore, a from literature known value for the radius of the corresponding solvent was used ($r_{CD_2Cl_2}$ = 2.46 Å[4], r_{CD_3CN} = 2.86 Å[5]).[6]

$$c_{Chen} = \frac{6F}{1 + 0.695\,(\frac{r_{solv}}{r_{ref}})^{2.234}} \tag{S2}$$

Viscosity calibration of the derived D_i values was performed with literature known values for the radii of TMS (r_{ref} = 2.96 Å, calculated from hard-sphere increments[5]) and the experimentally determined diffusion coefficient D_{ref} of TMS, which is determined individually for each sample.

$$\eta\ [kg/ms] = \frac{kT\ (1 + 0.695\ \left(\frac{r_{solv}}{r_{ref}}\right)^{2.234})}{6\pi D_{ref}\ r_{ref}} \tag{S3}$$

After including all correction and calibration equations in the Stokes equation (S1), the equation was rearranged for the hydrodynamic radii r_H (S4). For easier imagination, the corresponding volumes V_A were calculated with the assumption of a spherical shape.

$$D = \frac{kT\ (1 + 0.695\ \left(\frac{r_{solv}}{r_{ref}}\right)^{2.234})}{6\pi\eta r_H} \tag{S4}$$

The experimental self-diffusion coefficients D_i, the viscosity corrected hydrodynamic radii r_H and the resulting volumes V_A of all samples are depicted in Table S4.1 and Table S4.2. TMS was used as viscosity reference in each sample separately with the variation in its experimental diffusion coefficients reflecting the different viscosities depending on the ion pair concentration (see Table S4.1-4.3). The average D_i values were derived by using all baseline separated signals that were referring to the same species. As stated above the

hydrodynamic values and the volumes are viscosity corrected and therefore the only values, which can be directly compared with each other.

Table S4.1 Experimental self-diffusion coefficients D_i, viscosity corrected hydrodynamic radii r_H and resulting volumes V_A of ion pair 3a in varying concentrations. TMS was used as viscosity reference for the experimental self-diffusion coefficients D_i to allow for a comparison of hydrodynamic radii r_H and resulting volumes V_A. The corresponding self-diffusion coefficients D_i of TMS are given for each sample. Entry 1-17: SW = 22 Hz, O1P = 10.0 ppm, gradient strength 5-95% linear. Samples were measured at room temperature.

Sample	Solvent	Species inside sample	Concen-tration (mM)	Diffusion coefficient D_i ($m^2.s^{-1}$)	Standard deviation D_i ($m^2.s^{-1}$)	Hydrodynamic radius r_H (Å)	Volume V_A (Å^3)	R^2
1	CD_2Cl_2	**3a** Anion **3a** Cation TMS	0.005 0.005	1.81×10^{-9} 1.33×10^{-9} 2.47×10^{-9}	5.52×10^{-11} 1.30×10^{-11}	3.59 4.44	192 367	0.992 0.997
2	CD_2Cl_2	**3a** Anion **3a** Cation TMS	0.01 0.01	1.66×10^{-9} 1.29×10^{-9} 2.31×10^{-9}	2.56×10^{-11} 8.22×10^{-12}	3.64 4.34	203 342	0.998 0.998
3	CD_2Cl_2	**3a** Anion **3a** Cation TMS	0.05 0.05	1.32×10^{-9} 1.18×10^{-9} 2.49×10^{-9}	1.21×10^{-11} 3.69×10^{-12}	4.51 4.93	383 500	0.999 0.999
4	CD_2Cl_2	**3a** Anion **3a** Cation TMS	0.1 0.1	1.29×10^{-9} 1.16×10^{-9} 2.49×10^{-9}	7.59×10^{-11} 2.44×10^{-12}	4.59 4.97	405 515	0.999 0.999
5	CD_2Cl_2	**3a** Anion **3a** Cation TMS	0.2 0.2	1.26×10^{-9} 1.13×10^{-9} 2.46×10^{-9}	6.54×10^{-12} 1.22×10^{-12}	4.62 5.04	413 537	0.999 0.999
6	CD_2Cl_2	**3a** Anion **3a** Cation TMS	0.4 0.4	1.21×10^{-9} 1.10×10^{-9} 2.49×10^{-9}	5.13×10^{-12} 1.08×10^{-12}	4.81 5.19	466 587	0.999 0.999
7	CD_2Cl_2	**3a** Anion **3a** Cation TMS	0.6 0.6	1.19×10^{-9} 1.08×10^{-9} 2.47×10^{-9}	4.48×10^{-12} 2.16×10^{-12}	4.84 5.23	477 598	0.999 0.999
8	CD_2Cl_2	**3a** Anion **3a** Cation TMS	0.8 0.8	1.17×10^{-9} 1.08×10^{-9} 2.48×10^{-9}	5.75×10^{-12} 2.50×10^{-12}	4.92 5.24	497 603	0.999 0.999
9	CD_2Cl_2	**3a** Anion **3a** Cation TMS	1.0 1.0	1.20×10^{-9} 1.07×10^{-9} 2.49×10^{-9}	4.51×10^{-12} 5.09×10^{-12}	4.85 5.32	477 629	0.999 0.999
10	CD_2Cl_2	**3a** Anion **3a** Cation TMS	1.0 1.0	1.18×10^{-9} 1.07×10^{-9} 2.52×10^{-9}	5.22×10^{-12} 1.38×10^{-12}	4.98 5.36	517 645	0.999 0.999
11	CD_2Cl_2	**3a** Anion **3a** Cation TMS	1.0 1.0	1.19×10^{-9} 1.07×10^{-9} 2.51×10^{-9}	5.39×10^{-12} 3.89×10^{-12}	4.92 5.36	497 643	0.999 0.999
12	CD_2Cl_2	**3a** Anion **3a** Cation TMS	1.0 1.0	1.18×10^{-9} 1.08×10^{-9} 2.55×10^{-9}	4.96×10^{-12} 4.53×10^{-12}	5.01 5.37	527 649	0.999 0.999
13	CD_2Cl_2	**3a** Anion **3a** Cation TMS	2.0 2.0	1.31×10^{-9} 1.14×10^{-9} 2.72×10^{-9}	7.98×10^{-11} 3.74×10^{-11}	4.85 5.42	478 667	0.998 0.997
14	CD_2Cl_2	**3a** Anion **3a** Cation TMS	3.0 3.0	1.11×10^{-9} 1.01×10^{-9} 2.52×10^{-9}	1.83×10^{-11} 9.89×10^{-12}	5.19 5.61	587 739	0.999 0.999
15	CD_2Cl_2	**3a** Anion **3a** Cation TMS	5.0 5.0	1.06×10^{-9} 1.02×10^{-9} 2.47×10^{-9}	6.93×10^{-10} 9.42×10^{-12}	5.47 5.52	687 703	0.999 0.999

16	CD_3CN	**3a** Anion **3a** Cation TMS	0.5 0.5	1.89×10^{-9} 1.69×10^{-9} 3.23×10^{-9}	1.03×10^{-13} 2.05×10^{-10}	4.33 4.79	340 461	0.998 0.999
17	CD_3CN	**3a** Anion **3a** Cation TMS	5.0 5.0	2.09×10^{-9} 1.51×10^{-9} 3.43×10^{-9}	9.12×10^{-11} 6.09×10^{-12}	4.21 5.48	313 689	0.999 0.999

Table S4.2. Experimental self-diffusion coefficients D_i, viscosity corrected hydrodynamic radii r_H and resulting volumes V_A of ion pair 4a in varying concentrations. TMS was used as viscosity reference for the experimental self-diffusion coefficients D_i to allow for a comparison of hydrodynamic radii r_H and resulting volumes V_A. The corresponding self-diffusion coefficients D_i of TMS are given for each sample. Entry 18-26: SW = 22 Hz, O1P = 10.0 ppm, gradient strength 5-95% linear. Samples were measured at room temperature.

Sample	Solvent	Species inside sample	Concen-tration (mM)	Diffusion coefficient D_i ($m^2.s^{-1}$)	Standard deviation D_i ($m^2.s^{-1}$)	Hydrodynamic radius r_H (Å)	Volume V_A (Å^3)	R^2
18	CD_2Cl_2	**4a** Anion **4a** Cation TMS	0.005 0.005	1.41×10^{-9} 1.22×10^{-9} 2.36×10^{-9}	1.79×10^{-10} 1.27×10^{-11}	4.13 4.59	296 404	0.996 0.998
19	CD_2Cl_2	**4a** Anion **4a** Cation TMS	0.01 0.01	1.37×10^{-9} 1.24×10^{-9} 2.58×10^{-9}	1.62×10^{-9} 8.24×10^{-11}	4.49 4.87	379 482	0.987 0.998
20	CD_2Cl_2	**4a** Anion **4a** Cation TMS	0.05 0.05	1.17×10^{-9} 1.17×10^{-9} 2.53×10^{-9}	1.14×10^{-10} 3.43×10^{-12}	5.00 5.02	525 529	0.998 0.999
21	CD_2Cl_2	**4a** Anion **4a** Cation TMS	0.1 0.1	1.09×10^{-9} 1.14×10^{-9} 2.52×10^{-9}	1.18×10^{-11} 3.03×10^{-12}	5.29 5.09	619 553	0.999 0.999
22	CD_2Cl_2	**4a** Anion **4a** Cation TMS	0.2 0.2	1.06×10^{-9} 1.11×10^{-9} 2.53×10^{-9}	3.94×10^{-12} 2.75×10^{-12}	5.44 5.24	672 602	0.999 0.999
23	CD_2Cl_2	**4a** Anion **4a** Cation TMS	0.4 0.4	1.02×10^{-9} 1.08×10^{-9} 2.48×10^{-9}	4.74×10^{-12} 2.87×10^{-12}	5.49 5.28	692 615	0.999 0.999
24	CD_2Cl_2	**4a** Anion **4a** Cation TMS	0.6 0.6	1.00×10^{-9} 1.05×10^{-9} 2.49×10^{-9}	2.99×10^{-1} 2.64×10^{-12}	5.58 5.38	729 653	0.999 0.999
25	CD_2Cl_2	**4a** Anion **4a** Cation TMS	0.8 0.8	9.90×10^{-10} 1.04×10^{-9} 2.52×10^{-9}	2.11×10^{-12} 3.87×10^{-12}	5.71 5.50	778 698	0.999 0.999
26	CD_2Cl_2	**4a** Anion **4a** Cation TMS	1.0 1.0	9.84×10^{-10} 1.03×10^{-9} 2.49×10^{-9}	4.43×10^{-12} 2.92×10^{-11}	5.67 5.46	765 682	0.999 0.994

Table S4.3. Experimental self-diffusion coefficients D_i, viscosity corrected hydrodynamic radii r_H and resulting volumes V_A of ion pair 3a/4b while fixing the overall ion concentrations at 1.0 mM. PPh_4BF_4 was chosen as additive (Add) to keep the ion concentration at 1.0 mM. The ratio of 3a/Add is given in percentage. TMS was used as viscosity reference for the experimental self-diffusion coefficients D_i to allow for a comparison of hydrodynamic radii r_H and resulting volumes V_A. The corresponding self-diffusion coefficients D_i of TMS are given for each sample. Entry 27-32: SW = 22 Hz, O1P = 10.0 ppm, gradient strength 5-95% linear. Samples were measured at room temperature.

Sample	Solvent	Species inside sample	Concen-tration (mM)	Diffusion coefficient D_i ($m^2.s^{-1}$)	Standard deviation D_i ($m^2.s^{-1}$)	Hydrodynamic radius r_H (Å)	Volume V_A (Å^3)	R^2
27	CD_2Cl_2	**3a** Anion **3a** Cation TMS	1.0 1.0	20% **3a** 80% Add	1.16×10^{-9} 1.07×10^{-9} 2.49×10^{-9}	1.78×10^{-11} 1.09×10^{-11}	4.98 5.32	519 631
28	CD_2Cl_2	**3a** Anion **3a** Cation TMS	1.0 1.0	50% **3a** 50% Add	1.21×10^{-9} 1.09×10^{-9} 2.62×10^{-9}	3.35×10^{-11} 1.23×10^{-11}	5.03 5.44	528 673
29	CD_2Cl_2	**3a** Anion **3a** Cation TMS	1.0 1.0	80% **3a** 20% Add	1.13×10^{-9} 1.04×10^{-9} 2.46×10^{-9}	3.16×10^{-12} 6.97×10^{-12}	5.03 5.39	535 656
30	CD_2Cl_2	**4a** Anion **4a** Cation TMS	1.0 1.0	20% **4a** 80% Add	1.15×10^{-10} 1.07×10^{-9} 2.59×10^{-9}	7.39×10^{-11} 3.81×10^{-12}	5.16 5.50	576 698
31	CD_2Cl_2	**4a** Anion **4a** Cation TMS	1.0 1.0	50% **4a** 50% Add	1.01×10^{-9} 1.06×10^{-9} 2.50×10^{-9}	1.20×10^{-10} 2.20×10^{-12}	5.57 5.36	725 646
32	CD_2Cl_2	**4a** Anion **4a** Cation TMS	1.0 1.0	80% **4a** 20% Add	1.00×10^{-9} 1.06×10^{-9} 2.56×10^{-9}	2.27×10^{-12} 1.51×10^{-12}	5.71 5.46	780 680

4.6.1.3. CAC Sandwich-Model

The resulting DOSY volumes for **3a** of Table S4.1 were plotted against the used concentration for both cation and anion (see Figure S4.2). First, for the lowest concentration 0.005 mM and 0.01 mM we were able to determine volumes close to the ones which were calculated for the free ions (cation: 362 Å^3 and anion: 215 Å^3, for calculation see Table S4.4). In a 1:1 association model, as the concentration is increased, the volumes of both ions should rise and gradually converge until they are identical at higher concentrations. Thereby, the anion volume would have to grow more rapidly with higher concentrations than the cation volume to result in an equal volume, as expected for a 1:1 aggregation.

Despite a clear increase of the volumes for both the cation a as well as of the anion **3** can at concentration higher than 0.01 mM, a large offset between the cation **a** and the anion **3** volume is observed. Notably, the cation **a** volume increases more than the anion **3** volume leading to an increasing offset between the two, which is the reverse of the expected behavior for a 1:1 model. These observations are in contrast to the initially assumed 1:1 association model the volumes of anion and cation should converge and approach 570 Å^3 for a monomeric ion pair **3a**. Additionally, in the concentration range of 0.4-1.0 mM a stagnation of the cation volume can be seen at a volume that even significantly exceeds the calculated volume for the 1:1 monomeric ion pair **3a** (649 Å^3 versus 570 Å^3). All these observations led to the assumption of another species that must be involved.

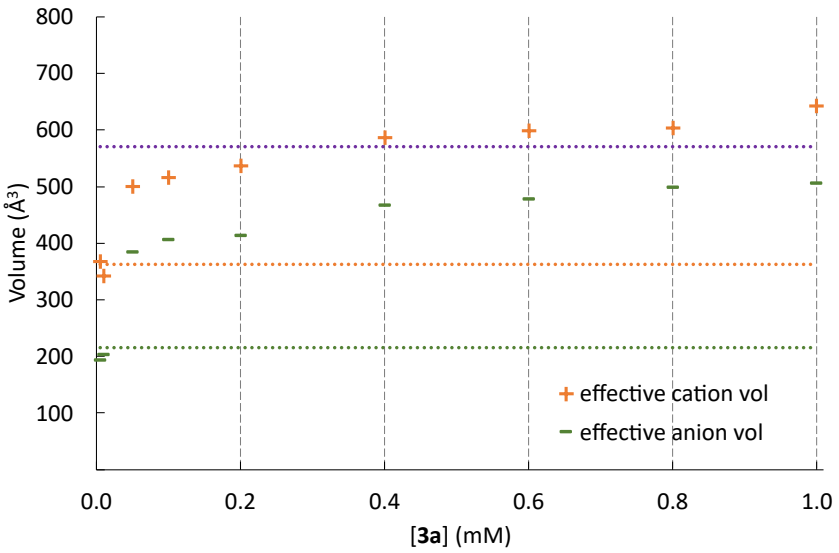

Figure S4.2. All sample concentrations with the corresponding calculated volumes based on DOSY for the cation and anion of 3a are displayed. The purple dotted line indicates the calculated volume for the 1:1 monomeric ion pair. The orange dotted line indicates the calculated volume for the free cation. The green dotted line indicates the calculated volume for the free anion. DOSY derived cation volumes are displayed as orange "+" symbols and anion volumes as green "-" symbols.

To explain this deviation, we established a "sandwich association" model. In this model two cations **a** and one anion **3** form a "sandwich-cation" **a3a** (calculated volume of 925 Å^3, for calculation see Table S4.4) with an additional free anion **3** (calculated volume of 215 Å^3, for calculation see below). With this sandwich cation the increasing offset between cation **a** and anion **3** upon ion pair formation can be explained. The significantly smaller increase of the volume of anion **3** is in agreement with the additional free anion reducing the averaged DOSY volume. In addition, the significantly higher volumes of 642 Å^3 at higher concentrations can be explained by the formation of CAC cations which are included in the average volume of all cation species derived by DOSY. Furthermore, solvation effects were considered. According to the study of Hunter[7] DCM is a better hydrogen donor than acceptor (H-bond donor: α=1.9, H-bond acceptor: β=1.1). Therefore, the anion **3** should be better dissolved than the cation **a** in DCM. This agrees with the sandwich model assuming that an aggregated cation reduces the solvent-cation interactions. Furthermore, a considerable amount of free dissolved anion **3** will be in solution which is in accordance with the Hunter parameters.

In addition, the theoretical volumes of both free ions, the 1:1 monomeric ion pair **3a** as well as the sandwich model were calculated. These calculations were performed based on the van der Waals cavity used in the SMD solvation model at the B3LYP-D3/6-31+G(d) level of theory (see Table S4.4).

Table S4.4. Calculated volumes of all proposed species based on the van der Waals cavity used in the SMD solvation model at the B3LYP-D3/6-31+G(d) level of theory.

Species	Volume (Å³)
Anion **3**	215
Anion **4**	285
Cation **a**	362
1:1 ion pair **3a**	570
Cation sandwich **a3a**	925
Anion sandwich **3a3**	782
1:1 ion pair **4a**	641
Cation sandwich **a4a**	995
Anion sandwich **4a4**	920

Based on these values we set up a two variable equation system which only considers an equilibrium between free ions (**3**/**a**) and the sandwich model **a3a**+**3** (S5). Using the calculated volumes of the free ions and the average measured volume of the cation in the concentration range between 0.4-1.0 mM leads to a ratio of 68:32 of free ions to sandwich cation/free anion.

$$\mathrm{vol_{cat}} = \frac{[\mathrm{C}]}{[\mathrm{IP}]_{\mathrm{tot}}} \times 362 + \left(\frac{2 \times [\mathrm{CAC}]}{[\mathrm{IP}]_{\mathrm{tot}}}\right) \times 925 \qquad \text{(S5a)}$$

$$\mathrm{vol_{an}} = \frac{[\mathrm{A}]}{[\mathrm{IP}]_{\mathrm{tot}}} \times 215 + \left(\frac{[\mathrm{CAC}]}{[\mathrm{IP}]_{\mathrm{tot}}}\right) \times 925 \qquad \text{(S5b)}$$

Besides this assumption, we also set up a three variable equation system which considers an equilibrium between free ions (**3**/**a**), monomeric 1:1 ion pair **3a** and the sandwich model **a3a**+**3** (S6). Due to this system being a three variable two equation system, a clear ratio cannot be determined only based on DOSY. Nevertheless, various solutions are possible for this model (e. g. 20% free cation, 34% sandwich cation, 46% 1:1 ion pair). Hence, both models are fitting to the observed volumes while the 3 point-model system is slightly closer to the observed volumes.

$$(2 * (362 * x + 2 * 925 * y + 570 * z))/3 = 642 \qquad \text{(S6a)}$$

$$(2 * (215 * x + 925 * y + 215 * y + 570 * z))/3 = 505 \qquad \text{(S6b)}$$

The population of the free anion and free cation at a given overall salt concentration was calculated with the aid of the conductivity data. Based on the calculated populations of the respective free ion, the theoretical DOSY volumes were simulated (see Figure S4.3).

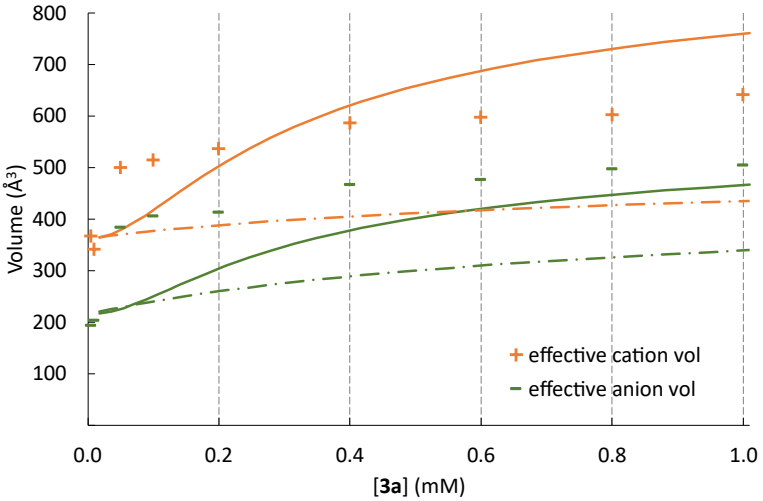

Figure S4.3. All sample concentrations with the corresponding calculated volumes based on DOSY for the cation and anion of 3a are displayed. Cation volumes are displayed as orange "+" symbols. Anion volumes are displayed as green "-"symbols. The calculated trend for the 1:1 model is indicated as an orange dotted-dashed line for the cation. The calculated trend for the cation sandwich model is indicated as an orange line for the cation. The calculated trend for the 1:1 model is indicated as a green dotted-dashed line for the anion. The calculated trend for the cation sandwich model is indicated as a green line for the anion.

For both ions, the calculated trend for a 1:1 ion aggregation model leads to far lower volumes than observed by the DOSY model with discrepancies of up to 250 Å^3 (see Figure S4.3). In contrast, by the addition of the sandwich cation the calculated curves fit far better to the observed trends in volume (see Figure S4.3-4.7). Hence, the volumes cannot be explained by a single 1:1 aggregation but other species like in the sandwich model must be considered.

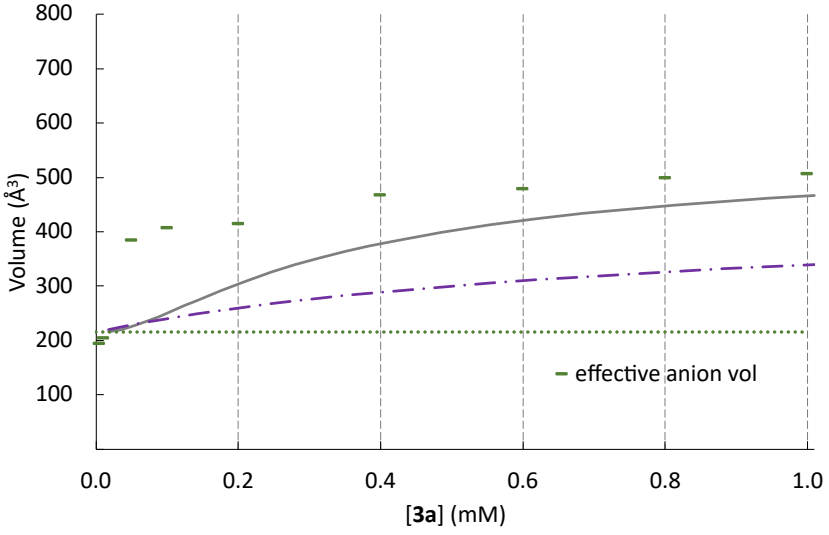

Figure S4.4. All sample concentrations with the corresponding calculated volumes based on DOSY for the anion of 3a are displayed. Anion volumes are displayed as green "-"symbols. The calculated trend for the 1:1 model is indicated as a purple dotted-dashed line for the anion. The calculated

trend for the cationic sandwich model is indicated as a grey line for the anion. The free anion volume is marked as a light green dotted line.

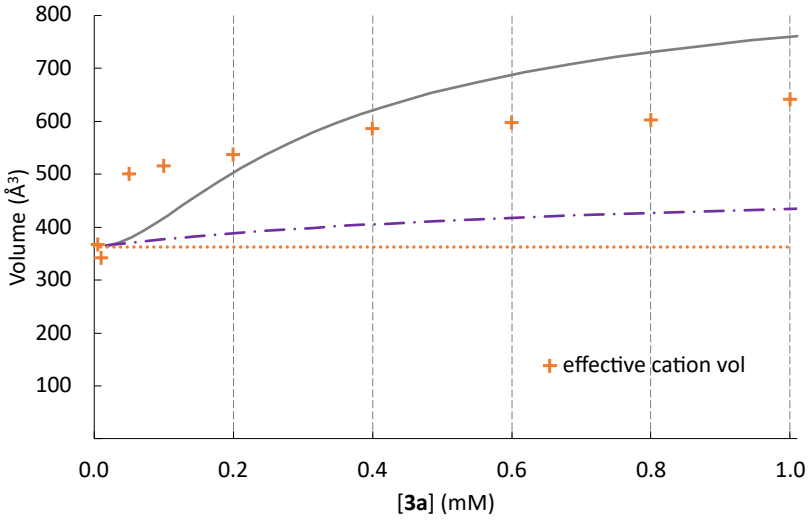

Figure S4.5. All sample concentrations with the corresponding calculated volumes based on DOSY for the cation of 3a are displayed. Cation volumes are displayed as orange "+" symbols. The calculated trend for the 1:1 model is indicated as an purple dotted-dashed line for the cation. The calculated trend for the cationic sandwich model is indicated as an grey line for the cation. The free cation volume is marked as a light orange dotted line.

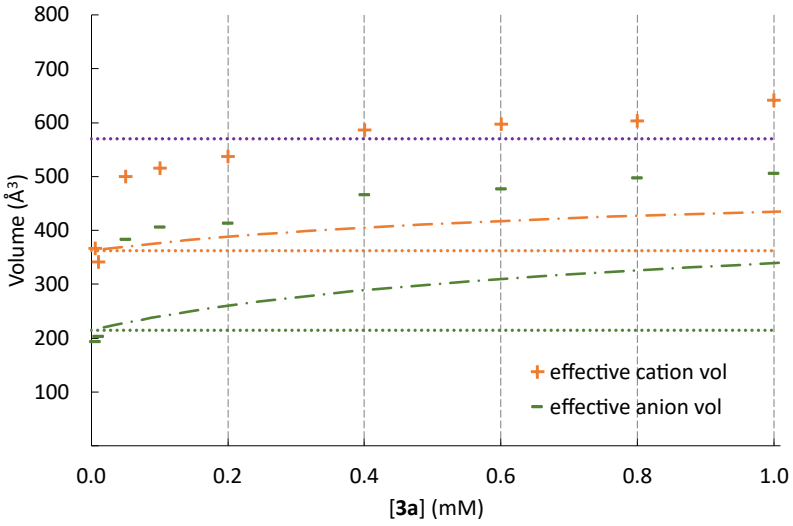

Figure S4.6. All sample concentrations with the corresponding calculated volumes based on DOSY for the cation and anion of 3a are displayed. Cation volumes are displayed as orange "+" symbols. Anion volumes are displayed as green "-"symbols. The purple dotted line indicates the calculated volume for the 1:1 monomeric ion pair. The orange dotted line indicates the calculated volume for the free cation. The green dotted line indicates the calculated volume for the free anion. In addition, the calculated trends for an assumed 1:1 aggregation model are included as dash-dotted orange and green lines for the cation and anion respectively.

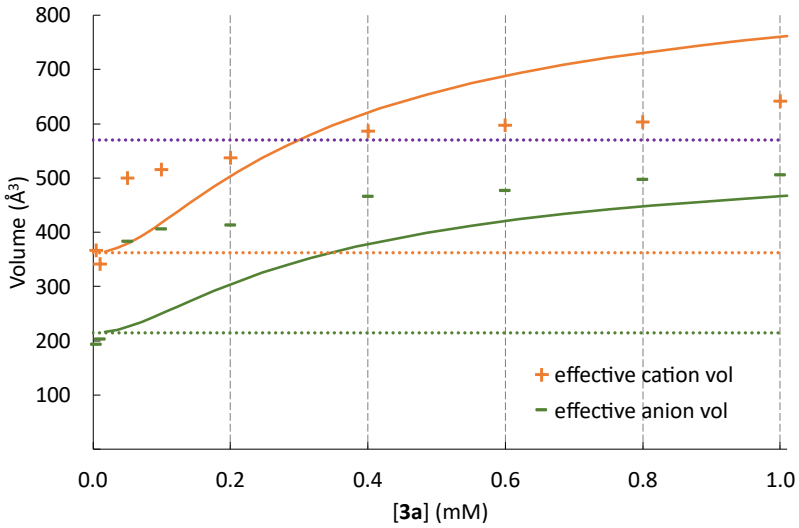

Figure S4.7. All sample concentrations with the corresponding calculated volumes based on DOSY for the cation and anion of 3a are displayed. Cation volumes are displayed as orange "+" symbols. Anion volumes are displayed as green "–" symbols. The purple dotted line indicates the calculated volume for the 1:1 monomeric ion pair. The orange dotted line indicates the calculated volume for the free cation. The green dotted line indicates the calculated volume for the free anion. In addition, the calculated trends for the proposed sandwich model are included as orange and green lines for the cation and anion respectively.

4.6.1.4. ACA Sandwich-Model

Furthermore, when plotting the DOSY volumes for **4a** against the concentration a different trend is observed which is also indicating the presence of another species. Here, contrary to **3a** the anion **4** volume is increasing significantly more than the cation **a** volume while increasing the concentration up to the point that the anion **4** volume surpasses the cation **a** volume. Again, at a concentration of 0.005 mM the volumes determined for cation **a** (403 Å^3) and anion **4** (296 Å^3) are close to the calculated volumes of the free ions (cation: 360 Å^3 and anion: 285 Å^3, for calculation see Table S4.2). Upon increasing the concentration both the volumes of anion **4** and cation **a** increase but the anion **4** volume increases more in comparison to the cation **a**. This leads to a crossing point of cation **a** and anion **4** at a concentration of 0.05 mM were both volumes are nearly identical before the anion **4** volume surpasses the volume of the cation **a** (**4**: 765 Å^3; **a**: 682 Å^3). Regardless of the different increase in volume of both ions, the calculated volume for a 1:1 ion pair **4a** (641 Å^3) is exceeded for both anion **4** as well as cation **a** (see S4.8). These observed results cannot be explained by a 1:1 ion pair nor by a CAC sandwich formation. Thus, for this ion pair a different aggregate has to be formed.

Due to the contrary observed trends for the ion volumes, a different higher aggregate must be responsible for this observation. Considering the formation of the CAC sandwich for **3a** a similar higher aggregate in form of an ACA sandwich is likely for **4a** including two anions **4** and one cation **a** (**4a4**) with a free cation **a**. This ACA sandwich model correlates with all observations. First, the increase of the anion **4** volume above the cation **a** volume and the resulting crossing point can be explained due to the formed higher aggregate which includes two anions **a**. In addition, this model also gives an explanation for the cation **a** volume exceeding the calculated volume of the 1:1 ion pair **4a** as the respective DOSY volumes display an average of all cation **a** species within the sample.

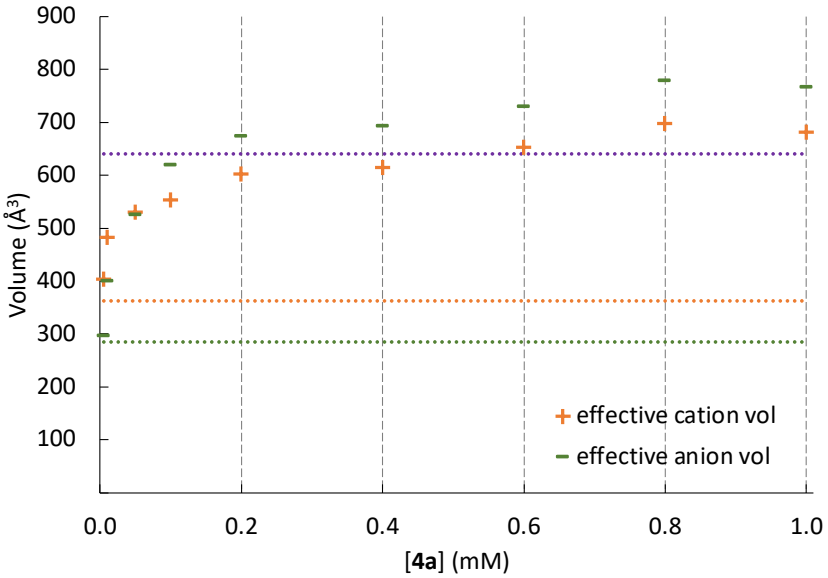

Figure S4.8. All sample concentrations with the corresponding calculated volumes based on DOSY for the cation and anion of 4a are displayed. Cation a volumes are displayed as orange "+" symbols. Anion 4 volumes are displayed as green "-"symbols. The calculated volume for the 1:1 ion pair 4a is indicated as a purple dotted. The calculated volume for the free cation a is indicated as an orange dotted. The calculated volume for the free anion 4 is indicated as a green dotted.

Additionally, experiments with a fixed cation concentration at 1.0 mM were performed. Three different ion pair **4a** concentrations (0.2 mM, 0.5 mM, 0.8 mM) were investigated using additive **5** to maintain the ion concentration at 1.0 mM. Here, for an ACA sandwich model the volume of the anion should decrease with increasing additive fraction as the ACA sandwich is less likely formed. Indeed, with increasing fraction of the additive the volume of the anion significantly decreases (780 Å^3 to 576 Å^3) while the cation volume nearly stays the same (680 Å^3 698 Å^3) again leading to a crossing point in which the cation volume exceeds the anion volume (see Figure S4.9). Thus, these experiments also support the ACA sandwich model.

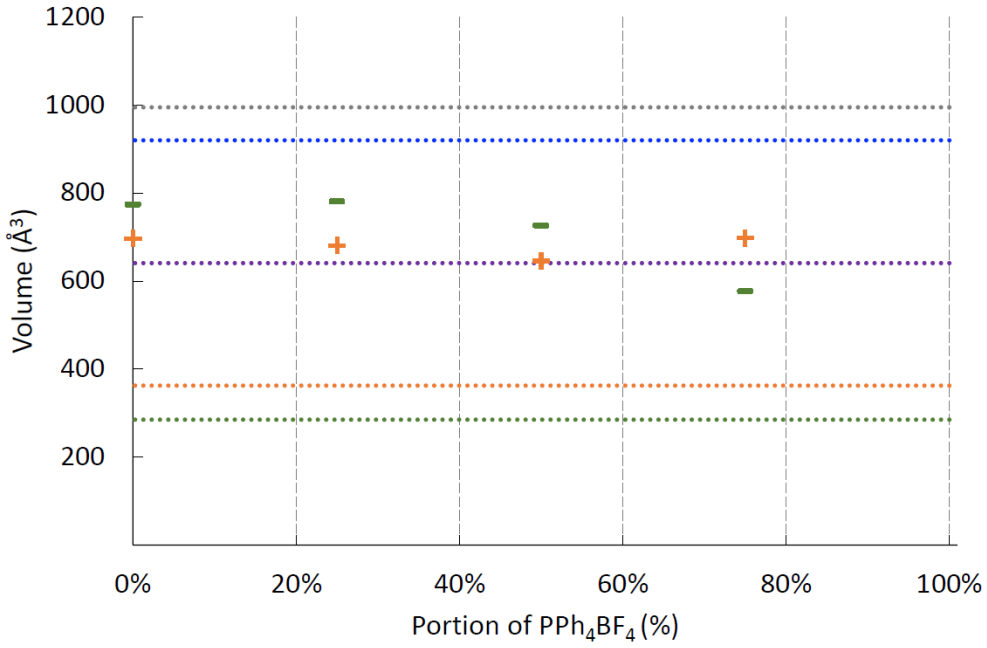

Figure S4.9. Measured cation and anion volumes for 4a/additive 5 mixtures with increasing additive 5 amount. Cation a volumes are displayed as orange "+" symbols. Anion 4 volumes are displayed as green "-"symbols. The calculated volume for the 1:1 ion pair 4a is indicated as a purple dotted. The calculated volume for the free cation a is indicated as an orange dotted. The calculated volume for the free anion 4 is indicated as a green dotted line. The calculated volume for cation sandwich a4a is indicated as a grey dotted line. The calculated volume for anion sandwich 4a4 is indicated as a blue dotted line.

Furthermore, computations were conducted including the CAC sandwich model, the ACA sandwich model, the 1:1 ion pair formation model and a mixed model (CAC, ACA, IP). The calculations of these four models were compared to the DOSY data (see Figure S4.10-4.12). Here, the ACA sandwich model and the mixed model showed the best correlation to the DOSY data. In contrast, the CAC sandwich model differed the most. Thus, the computations also support an ACA model, but a mixed model is likely in which all species coexist with the ACA sandwich being the most populated.

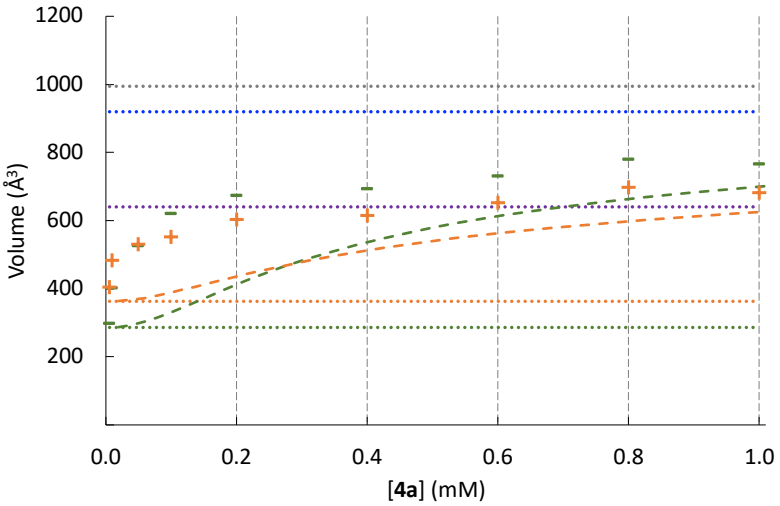

Figure S4.10. All sample concentrations with the corresponding calculated volumes based on DOSY for the cation and anion of 4a are displayed. Cation a volumes are displayed as orange "+" symbols. Anion 4 volumes are displayed as green "-"symbols. The calculated volume for the 1:1 ion pair 4a is indicated as a purple dotted. The calculated volume for the free cation a is indicated as an orange dotted. The calculated volume for the free anion 4 is indicated as a green dotted. The calculated volume for the CAC sandwich a4a is indicated as a grey dotted. The calculated volume for the ACA sandwich 4a4 is indicated as a blue dotted. The orange long dash line displays the calculated volumes for the cation a with the mixed model. The green long dash line displays the calculated volumes for the anion 4 with the mixed model.

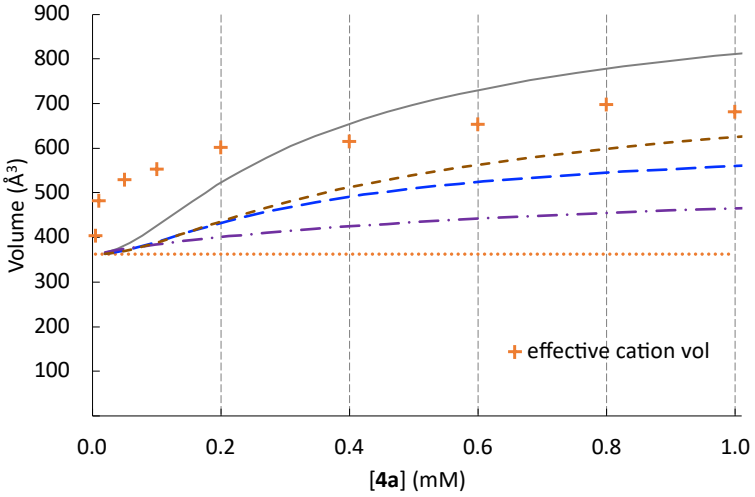

Figure S4.11. All sample concentrations with the corresponding calculated volumes based on DOSY for cation a. Cation a volumes are displayed as orange "+" symbols. The calculated volume for the free cation a is indicated as an orange dotted. The brown shortly dashed line displays the calculated volumes for the cation a with the mixed model. The blue longish dashed line displays the calculated volumes for the cation a with the ACA sandwich model. The orange line displays the calculated volumes for the cation a with the CAC sandwich model. The purple shortly dotted-dashed line displays the calculated volumes for the cation a with the IP sandwich model.

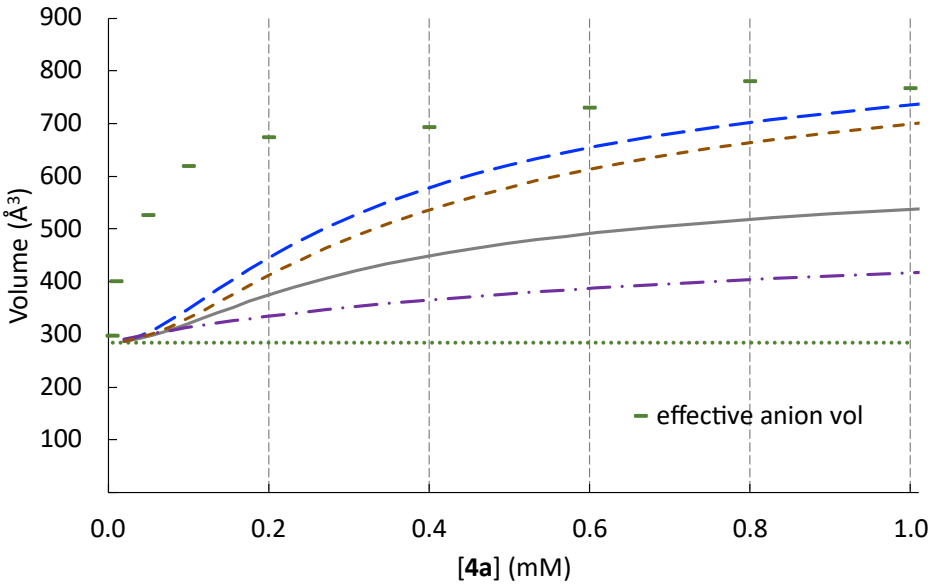

Figure S4.12. All sample concentrations with the corresponding calculated volumes based on DOSY for anion 4. Anion 4 volumes are displayed as green "-" symbols. The calculated volume for the free anion 4 is indicated as a green dotted. The brown longish dash line displays the calculated volumes for the anion 4 with the mixed model. The blue shortly dash line displays the calculated volumes for the anion 4 with the ACA sandwich model. The green line displays the calculated volumes for the anion 4 with the CAC sandwich model. The purple dashed-dotted line displays the calculated volumes for the anion 4 with the IP sandwich model.

4.6.1.5. Importance of the Ultrasonic Bath during NMR Sample Preparation

During initial investigations the NMR samples were prepared without using an ultrasonic bath. DOSY measurements of these samples showed high volumes for both cation and anion even at very low concentrations of **3a** (see Figure S4.13, Table S4.1). For a concentration of 0.001 mM volumes similar to the calculated free ions were determined for both cation **a** (392 Å^3) and anion **3** (239 Å^3). However, starting from 0.00166 mM a sudden increase of the cation volume to 528 Å^3 was observed. In addition, the derived volumes in a concentration range of 0.2 – 1.0 mM were varying significantly, especially for anion **3**.

Considering that the samples were prepared by diluting a stock solution starting from a concentration of 1.0 – 5.0 mM **3a**, we assumed that some ion pair aggregates formed at this concentration remain even after dilution. Hence, the resulting volume was depending on the starting concentration of the stock solutions, explaining the variance in the concentration range of 0.2 – 1.0 mM as well as the high volumes at low concentrations.

Indeed, repeating the measurements with a sample preparation that includes an ultrasonic bath during dilution solved both problems (see Figure S4.3). Thus, for a valid interpretation of the DOSY results for these pyridinamide ion pairs the usage of an ultrasonic bath for the preparation of samples is essential.

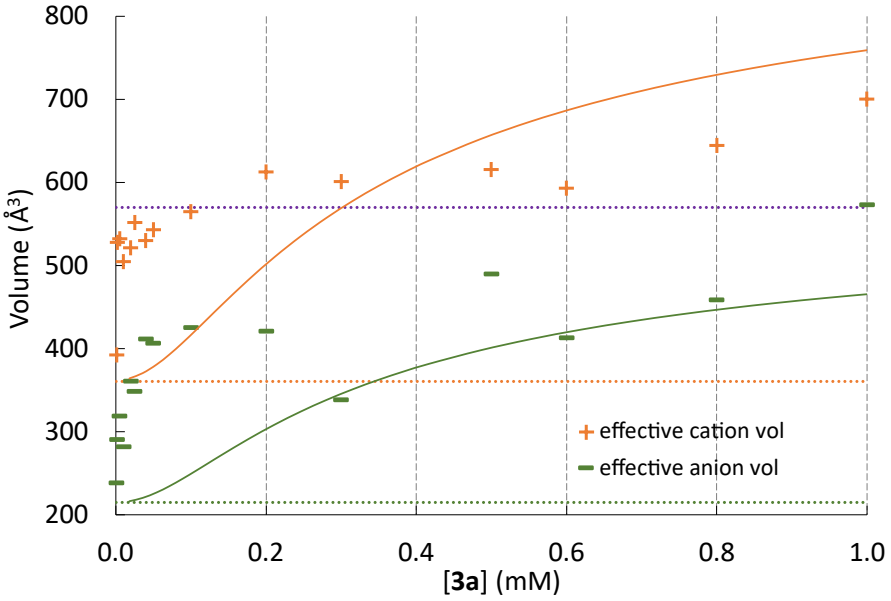

Figure S4.13. All sample concentrations with the corresponding calculated volumes based on DOSY for the cation and anion of 3a are displayed when preparing samples without an ultrasonic bath. Cation volumes are displayed as orange "+" symbols. Anion volumes are displayed as green "-" symbols. The purple dotted line indicates the calculated volume for the 1:1 monomeric ion pair 3a. The orange dotted line indicates the calculated volume for the cation a. The green dotted line indicates the calculated volume for the anion 3. In addition, the calculated trends for the proposed cation sandwich model are included as orange and green lines for the cation and anion respectively.

Table S4.5. Experimental self-diffusion coefficients D_i, viscosity corrected hydrodynamic radii r_H and resulting volumes V_A of ion pair 3a when preparing the samples without an ultrasonic bath. TMS was used as viscosity reference for the experimental self-diffusion coefficients D_i to allow for a comparison of hydrodynamic radii r_H and resulting volumes V_A. The corresponding self-diffusion coefficients D_i of TMS are given for each sample. Entry 1-15: SW = 22 Hz, O1P = 10.0 ppm, gradient strength 5-95% linear. Samples were measured at room temperature.

Sample	Solvent	Species inside sample	Concen-tration (mM)	Diffusion coefficient D_i ($m^2.s^{-1}$)	Standard deviation D_i ($m^2.s^{-1}$)	Hydrodynamic radius r_H (Å)	Volume V_A (Å^3)	R^2
1	CD_2Cl_2	**3a** Anion **3a** Cation TMS	0.001 0.001	1.65 x 10^{-9} 1.31 x 10^{-9} 2.49 x 10^{-9}	2.08E-11 4.33E-11	3.85 4.54	239 392	0.997 0.999
2	CD_2Cl_2	**3a** Anion **3a** Cation TMS	0.00166 0.00166	1.53 x 10^{-9} 1.17 x 10^{-9} 2.54 x 10^{-9}	1.94E-11 4.13E-11	4.11 5.01	290 528	0.995 0.999
3	CD_2Cl_2	**3a** Anion **3a** Cation TMS	0.005 0.005	1.47 x 10^{-9} 1.17 x 10^{-9} 2.55 x 10^{-9}	6.37E-11 1.86E-11	4.24 5.03	319 532	0.995 0.999
4	CD_2Cl_2	**3a** Anion **3a** Cation TMS	0.01 0.01	1.56 x 10^{-9} 1.20 x 10^{-9} 2.55 x 10^{-9}	1.76E-11 3.63E-11	4.07 4.94	282 505	0.996 0.999
5	CD_2Cl_2	**3a** Anion **3a** Cation TMS	0.02 0.02	1.37 x 10^{-9} 1.17 x 10^{-9} 3.50 x 10^{-9}	1.49E-12 1.06E-11	4.41 4.99	360 521	0.993 0.999
6	CD_2Cl_2	**3a** Anion **3a** Cation TMS	0.025 0.025	1.41 x 10^{-9} 1.15 x 10^{-9} 2.53 x 10^{-9}	8.62E-11 7.14E-12	4.37 5.09	349 552	0.988 0.998
7	CD_2Cl_2	**3a** Anion **3a** Cation TMS	0.04 0.04	1.28 x 10^{-9} 1.14 x 10^{-9} 2.48 x 10^{-9}	1.80E-11 5.93E-12	4.61 5.02	411 530	0.995 0.999
8	CD_2Cl_2	**3a** Anion **3a** Cation TMS	0.05 0.05	1.27 x 10^{-9} 1.13 x 10^{-9} 2.46 x 10^{-9}	1.22E-10 9.88E-12	4.59 5.06	406 543	0.999 0.999
9	CD_2Cl_2	**3a** Anion **3a** Cation TMS	0.1 0.1	1.29 x 10^{-9} 1.14 x 10^{-9} 2.54 x 10^{-9}	1.09E-10 2.85E-11	4.66 5.13	425 565	0.999 0.999
10	CD_2Cl_2	**3a** Anion **3a** Cation TMS	0.2 0.2	1.30 x 10^{-9} 1.11 x 10^{-9} 2.56 x 10^{-9}	7.57E-11 1.47E-11	4.65 5.27	421 613	0.999 0.999
11	CD_2Cl_2	**3a** Anion **3a** Cation TMS	0.3 0.3	1.45 x 10^{-9} 1.13 x 10^{-9} 2.59 x 10^{-9}	5.53E-11 2.13E-11	4.32 5.24	338 601	0.998 0.999
12	CD_2Cl_2	**3a** Anion **3a** Cation TMS	0.5 0.5	1.21 x 10^{-9} 1.09 x 10^{-9} 2.53 x 10^{-9}	5.40E-12 1.12E-11	4.89 5.28	490 616	0.999 0.999
13	CD_2Cl_2	**3a** Anion **3a** Cation TMS	0.6 0.6	1.30 x 10^{-9} 1.11 x 10^{-9} 2.53 x 10^{-9}	7.70E-11 2.60E-11	4.62 5.21	413 593	0.999 0.999
14	CD_2Cl_2	**3a** Anion **3a** Cation TMS	0.8 0.8	1.24 x 10^{-9} 1.07 x 10^{-9} 2.52 x 10^{-9}	3.98E-11 1.05E-11	4.78 5.36	459 645	0.999 0.999
15	CD_2Cl_2	**3a** Anion **3a** Cation TMS	1.0 1.0	1.13 x 10^{-9} 1.04 x 10^{-9} 2.53 x 10^{-9}	8.36E-11 2.71E-11	5.15 5.51	573 700	0.999 0.999

4.6.2. Acknowledgments

This work was funded by the Deutsche Forschungsgemeinschaft (DFG, German Research Foundation) – 426795949 through the Research Training Group (RTG) 2620 “Ion Pair Effects in Molecular Reactivity”. The authors are thankful to Dr. Robert J. Mayer for help with the conductivity measurements and Nathalie Hampel for the synthesis of 6a-6c.

4.6.3. References

[1] A. Jerschow, N. Müller, Macromolecules **1998**, 31, 6573–6578.

[2] E. O. Stejskal, J. E. Tanner, J. Chem. Phys. **1965**, 42, 288–292.

[3] A. Macchioni, G. Ciancaleoni, C. Zuccaccia, D. Zuccaccia, Chem. Soc. Rev. **2008**, 37, 479–489.

[4] D. Zuccaccia, A. Macchioni, Organometallics **2005**, 24, 3476–3486.

[5] D. Ben-Amotz, K. G. Willis, **1993**, I, 7736–7742.

[6] H. C. Chen, S. H. Chen, J. Phys. Chem. **1984**, 88, 5118–5121.

[7] C. A. Hunter, Angew. Chem. Int. Ed. **2004**, 43, 5310–5324.

4.7. Additional Findings

4.7.1. Model Systems

After elucidating the aggregation behavior for two pyridinamide based ion pair catalysts, we aimed to explore if these findings are transferable to other pyridinamide based ion pair catalysts which could be used for catalyst design. Therefore, Veronika Burger synthesized four additional pyridinamide ion pair catalyst (see Figure A4.1). Catalysts **1a**-**d** were selected for modulation of the cation. Catalyst **2b** and **4b** were selected for the modulation of the anion. Additionally, solvent effects were investigated for dichloromethane (DCM), chloroform, tetrahydrofuran and acetonitrile. Again the combination of conductivity, nucleophilicity and DOSY was used to gather information about the aggregation trends. Veronika Burger performed conductivity and nucleophilicity measurements as described in the publication shown above (chapter 4), which are referred to in the following evaluation of the additional DOSY measurements.

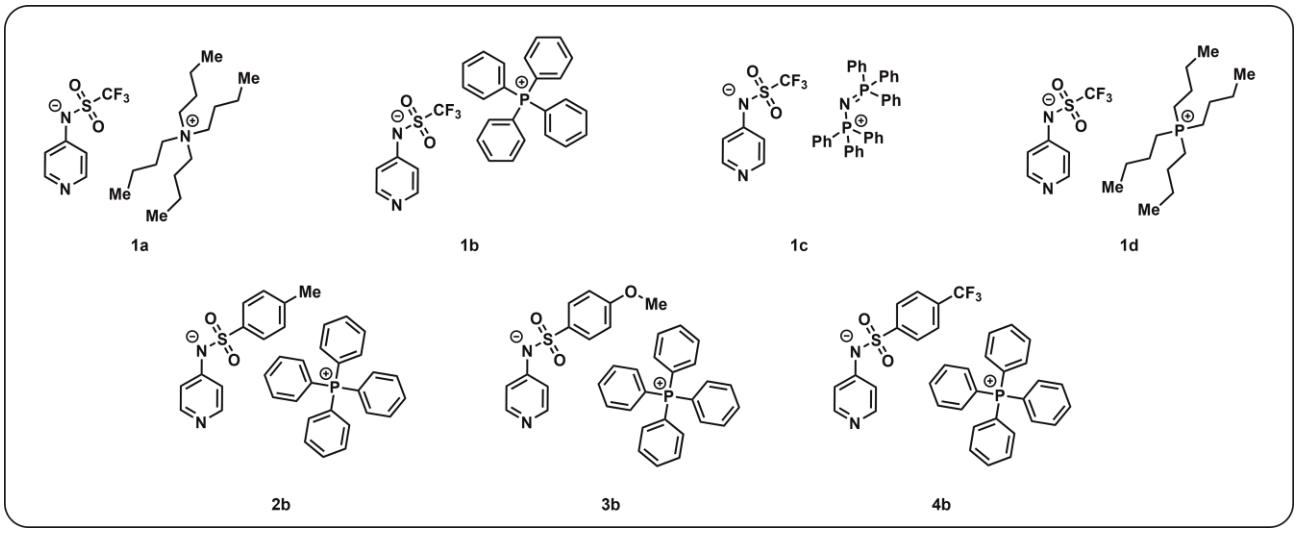

Figure A 4.1 Overview of the selected pyridinamide based ion pair catalysts.

4.7.2. Aggregation Trends

To elucidate the aggregation trends of ion pairs **1a-d**, **2b**, **3b** and **4b** in CD_2Cl_2, samples with a concentration range of 0.05 mM to 5.0 mM of the respective ion pair were investigated by DOSY measurements. Based on our prior study (see Chapter 4.1-4.4), two aggregation types were observed. On the one hand a cation sandwich aggregation (CAC) with a free anion for **1b** and on the other hand an anionic sandwich aggregation (ACA) with a free cation for **3b**. These two association types were further investigated with the additional ion pair catalysts. Especially, the cation and anion influence on the formation of the CAC/ACA sandwich were studied to establish design principles for future pyridinamide ion pair catalysts.

Here, a clear trend was observed for the preference of either CAC or ACA sandwich model. The concentration-DOSY plots of ion pair catalysts **1a**, **1c** and **1d** showed a similar curve as detected for **1b** (see Figure A4.2 - 4.4, **1b** for comparison see chapter 4.6.1.3). For all three catalysts, the cation volume increases more relative to the anion volume with rising concentration. Simultaneously, the anion volume does not exceed the cation volume at any point which would be the case for an ACA aggregation. Hence, for all investigated ion pairs containing anion **1** the CAC model is the predominant association type.

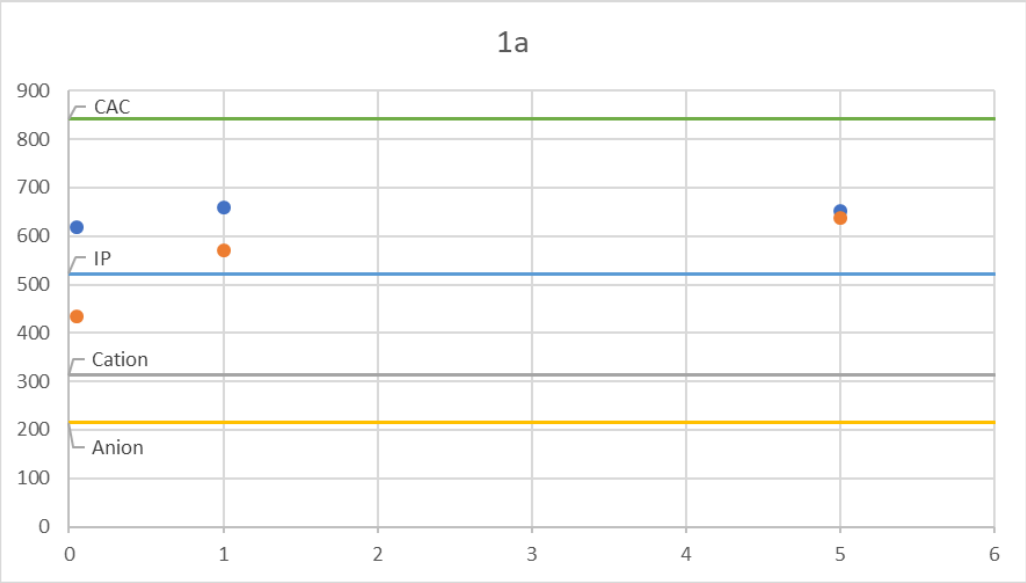

Figure A 4.2 Plot of concentration against DOSY derived volumes for 1a in CD_cCl_2. Calculated values for free anion/cation, 1:1 ion pair (IP) and CAC are depicted. Cation a is displayed as blue dots, Anion 1 is displayed as orange dots.

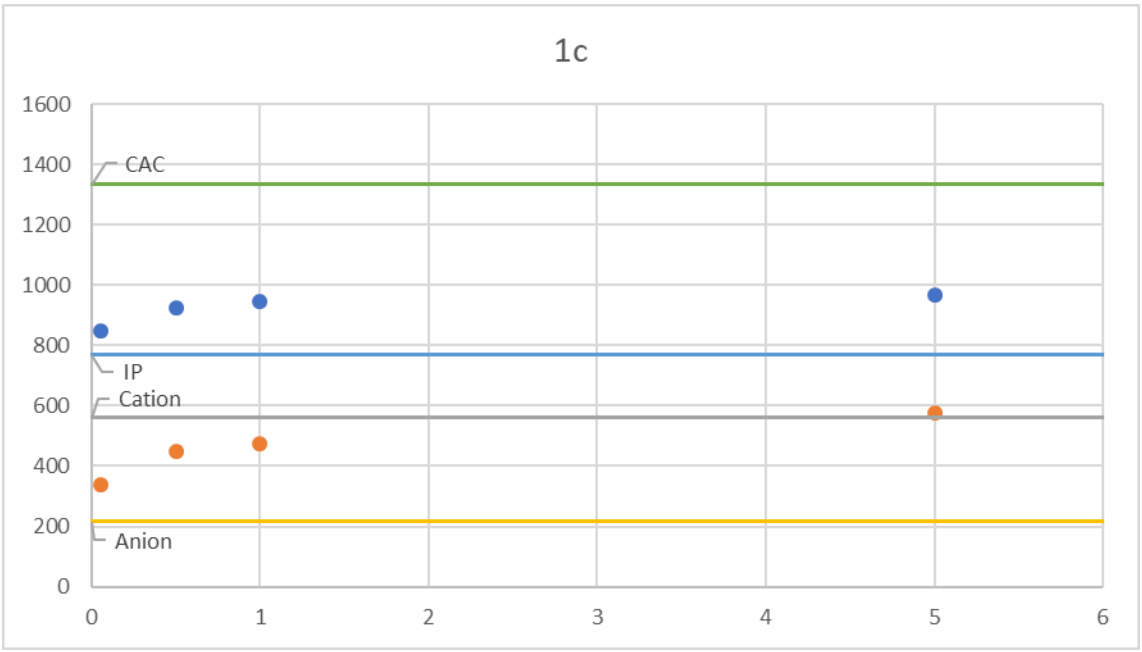

Figure A 4.3 Plot of concentration against DOSY derived volumes for 1c in CD_cCl_2. Calculated values for free anion/cation, 1:1 ion pair (IP) and CAC are depicted. Cation c is displayed as blue dots, Anion 1 is displayed as orange dots.

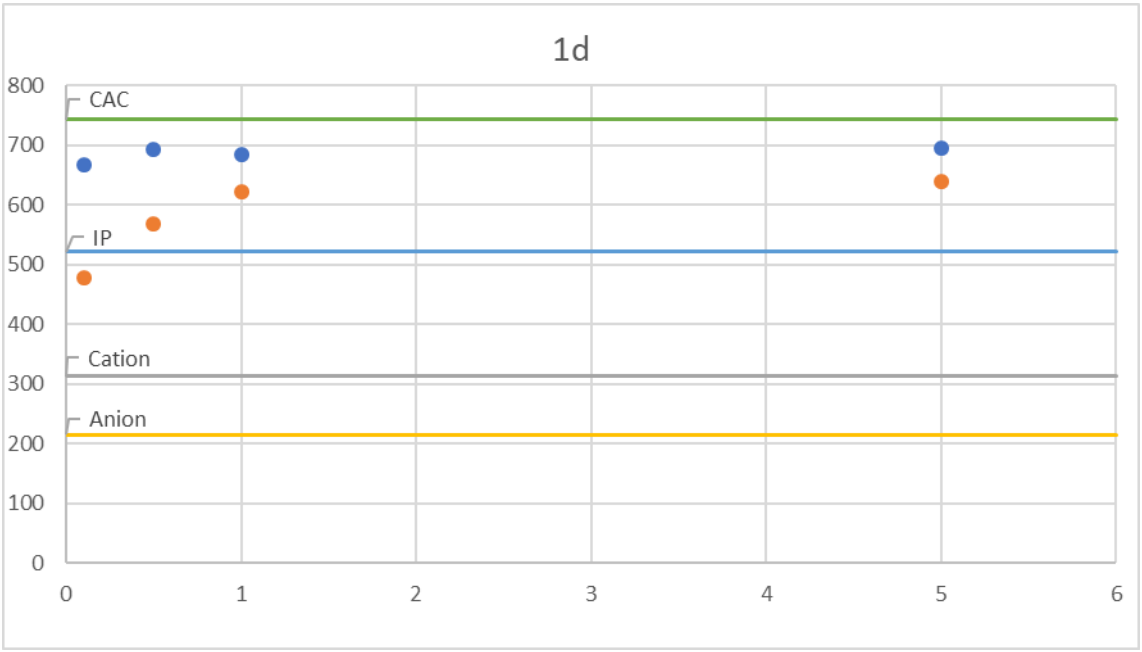

Figure A 4.4 Plot of concentration against DOSY derived volumes for 1d in CD_cCl_2. Calculated values for free anion/cation, 1:1 ion pair (IP) and CAC are depicted. Cation d is displayed as blue dots, Anion 1 is displayed as orange dots.

Contrary, changing the anion to **2** or **4** leads to a similar observation as for **3b** in prior studies (see Figure A4.5 - 4.6, **3b** for comparison see chapter 4.6.1.4). Here, a crossing point in which the anion volume exceeds the cation volume is observed, clearly indicating the formation of the sandwich anion ACA. This behavior is also observed at higher concentration (5.0 mM).

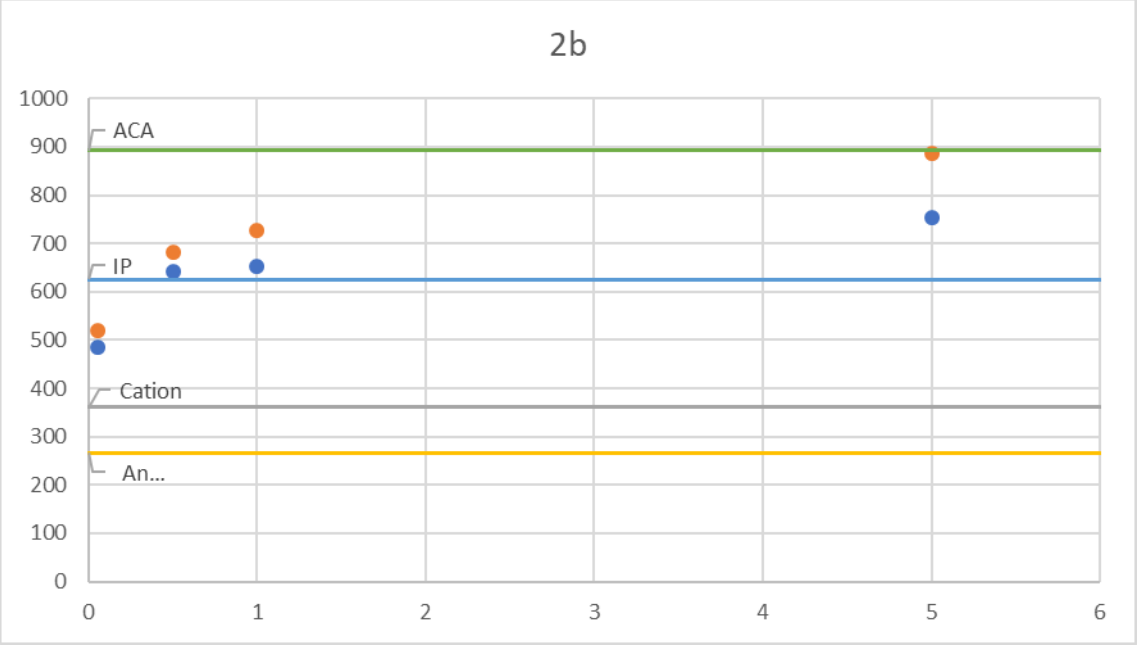

Figure A 4.5 Plot of concentration against DOSY derived volumes for 2b in CD_2Cl_2. Calculated values for free anion/cation, 1:1 ion pair (IP) and CAC are depicted. Cation b is displayed as blue dots, Anion 2 is displayed as orange dots.

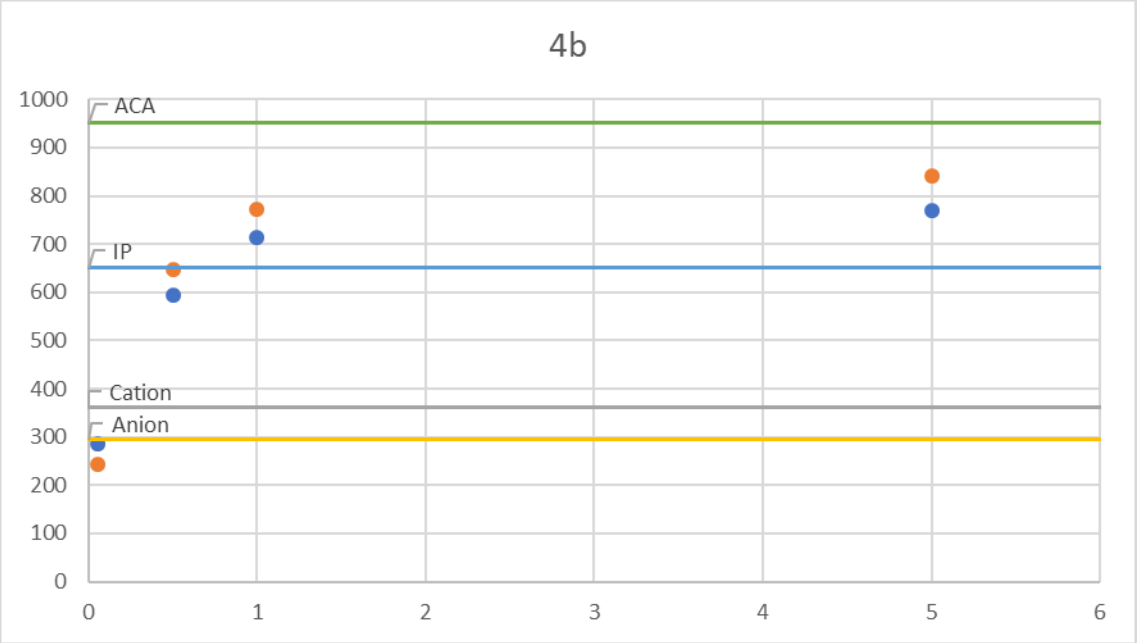

Figure A 4.6 Plot of concentration against DOSY derived volumes for 4b in CD_2Cl_2. Calculated values for free anion/cation, 1:1 ion pair (IP) and CAC are depicted. Cation b is displayed as blue dots, Anion 4 is displayed as orange dots.

Thus, for both association types CAC and ACA a clear distinction is observed between **1a**-**d** and **2**-**4b**. Based on DOSY observations, the preference of either ACA or CAC sandwich association seems to be depending on the anion. Especially, larger anions such as **2**, **3** and **4** with their extended sulfonamide group seem to favor the ACA over the CAC sandwich association. Hence, these observations could be applied for future pyridinamide ion pair catalyst designs.

***Table A 4.1** Experimental self-diffusion coefficients D_i, viscosity corrected hydrodynamic radii r_H and resulting volumes V_A of the ion pair 1a in varying concentrations. TMS was used as viscosity reference for the experimental self-diffusion coefficients D_i to allow for a comparison of hydrodynamic radii r_H and resulting volumes V_A. The corresponding self-diffusion coefficients D_i of TMS are given for each sample. Entry 1-3: SW = 22 Hz, O1P = 10.0 ppm, gradient strength 5-95% linear. Samples were measured at room temperature.*

Sample	Solvent	Species inside sample	Concentration [mM]	Diffusion coefficient D_i [$m^2.s^{-1}$]	Hydrodynamic radius r_H [Å]	Volume V_A [$Å^3$]	R^2
1	CD_2Cl_2	**1a** Anion **1a** Cation TMS	0.05 0.05	1.30×10^{-9} 1.11×10^{-9} 2.58×10^{-9}	4.70 5.32	434 630	0.999 0.997
2	CD_2Cl_2	**1a** Anion **1a** Cation TMS	1.0 1.0	1.14×10^{-9} 1.07×10^{-9} 2.55×10^{-9}	5.15 5.4	571 660	0.998 0.998
3	CD_2Cl_2	**1a** Anion **1a** Cation TMS	5.0 5.0	1.05×10^{-9} 1.04×10^{-9} 2.46×10^{-9}	5.34 5.34	640 651	0.999 0.999

***Table A 4.2** Experimental self-diffusion coefficients D_i, viscosity corrected hydrodynamic radii r_H and resulting volumes V_A of the ion pair 1c in varying concentrations. TMS was used as viscosity reference for the experimental self-diffusion coefficients D_i to allow for a comparison of hydrodynamic radii r_H and resulting volumes V_A. The corresponding self-diffusion coefficients D_i of TMS are given for each sample. Entry 4-7: SW = 22 Hz, O1P = 10.0 ppm, gradient strength 5-95% linear. Samples were measured at room temperature.*

Sample	Solvent	Species inside sample	Concentration [mM]	Diffusion coefficient D_i [$m^2.s^{-1}$]	Hydrodynamic radius r_H [Å]	Volume V_A [$Å^3$]	R^2
4	CD_2Cl_2	**1c** Anion **1c** Cation TMS	0.05 0.05	1.45×10^{-9} 9.82×10^{-10} 2.59×10^{-9}	4.32 5.88	337 850	0.998 0.999
5	CD_2Cl_2	**1c** Anion **1c** Cation TMS	0.5 0.5	1.25×10^{-9} 9.24×10^{-10} 2.52×10^{-9}	4.74 6.05	447 927	0.998 0.999
6	CD_2Cl_2	**1c** Anion **1c** Cation TMS	1.0 1.0	1.22×10^{-9} 9.18×10^{-10} 2.52×10^{-9}	4.83 6.09	473 944	0.999 0.999
7	CD_2Cl_2	**1c** Anion **1c** Cation TMS	5.0 5.0	1.11×10^{-9} 8.99×10^{-10} 2.49×10^{-9}	5.16 6.14	577 969	0.999 0.999

***Table A 4.3** Experimental self-diffusion coefficients D_i, viscosity corrected hydrodynamic radii r_H and resulting volumes V_A of the ion pair 1d in varying concentrations. TMS was used as viscosity reference for the experimental self-diffusion coefficients D_i to allow for a comparison of hydrodynamic radii r_H and resulting volumes V_A. The corresponding self-diffusion coefficients D_i of TMS are given for each sample. Entry 8-12: SW = 22 Hz, O1P = 10.0 ppm, gradient strength 5-95% linear. Samples were measured at room temperature.*

Sample	Solvent	Species inside sample	Concentration [mM]	Diffusion coefficient D_i [$m^2.s^{-1}$]	Hydrodynamic radius r_H [Å]	Volume V_A [$Å^3$]	R^2
8	CD_2Cl_2	**1d** Anion **1d** Cation TMS	0.05 0.05	1.00×10^{-9} 1.03×10^{-9} 2.63×10^{-9}	5.85 5.71	497 603	0.999 0.999
9	CD_2Cl_2	**1d** Anion **1d** Cation TMS	0.1 0.1	1.24×10^{-9} 1.08×10^{-9} 2.58×10^{-9}	4.85 5.42	479 668	0.998 0.999
10	CD_2Cl_2	**1d** Anion **1d** Cation TMS	0.5 0.5	1.15×10^{-9} 1.06×10^{-9} 2.57×10^{-9}	5.14 5.49	569 694	0.999 0.999
11	CD_2Cl_2	**1d** Anion **1d** Cation TMS	1.0 1.0	1.09×10^{-9} 1.05×10^{-9} 2.53×10^{-9}	5.29 5.47	621 684	0.999 0.999
12	CD_2Cl_2	**1d** Anion **1d** Cation TMS	5.0 5.0	1.04×10^{-9} 1.01×10^{-9} 2.45×10^{-9}	5.34 5.50	639 696	0.999 0.999

***Table A 4.4** Experimental self-diffusion coefficients D_i, viscosity corrected hydrodynamic radii r_H and resulting volumes V_A of the ion pair 2b in varying concentrations. TMS was used as viscosity reference for the experimental self-diffusion coefficients D_i to allow for a comparison of hydrodynamic radii r_H and resulting volumes V_A. The corresponding self-diffusion coefficients D_i of TMS are given for each sample. Entry 13-16: SW = 22 Hz, O1P = 10.0 ppm, gradient strength 5-95% linear. Samples were measured at room temperature.*

Sample	Solvent	Species inside sample	Concentration [mM]	Diffusion coefficient D_i [$m^2.s^{-1}$]	Hydrodynamic radius r_H [Å]	Volume V_A [$Å^3$]	R^2
13	CD_2Cl_2	**2b** Anion **2b** Cation TMS	0.05 0.05	1.18×10^{-9} 1.22×10^{-9} 2.54×10^{-9}	4.99 4.87	519 485	0.999 0.997
14	CD_2Cl_2	**2b** Anion **2b** Cation TMS	0.5 0.5	1.04×10^{-9} 1.06×10^{-9} 2.50×10^{-9}	5.46 5.36	681 643	0.999 0.999
15	CD_2Cl_2	**2b** Anion **2b** Cation TMS	1.0 1.0	1.00×10^{-9} 1.05×10^{-9} 2.49×10^{-9}	5.58 4.38	727 652	0.999 0.999
16	CD_2Cl_2	**2b** Anion **2b** Cation TMS	5.0 5.0	9.31×10^{-10} 9.95×10^{-10} 2.50×10^{-9}	5.96 5.64	888 753	0.999 0.999

***Table A4.5** Experimental self-diffusion coefficients D_i, viscosity corrected hydrodynamic radii r_H and resulting volumes V_A of the ion pair 4b in varying concentrations. TMS was used as viscosity reference for the experimental self-diffusion coefficients D_i to allow for a comparison of hydrodynamic radii r_H and resulting volumes V_A. The corresponding self-diffusion coefficients D_i of TMS are given for each sample. Entry 17-20: SW = 22 Hz, O1P = 10.0 ppm, gradient strength 5-95% linear. Samples were measured at room temperature.*

Sample	Solvent	Species inside sample	Concentration [mM]	Diffusion coefficient D_i [$m^2.s^{-1}$]	Hydrodynamic radius r_H [Å]	Volume V_A [$Å^3$]	R^2
17	CD_2Cl_2	**4b** Anion **4b** Cation TMS	0.05 0.05	1.19×10^{-9} 1.10×10^{-9} 1.81×10^{-9}	3.87 4.09	243 286	0.999 0.999
18	CD_2Cl_2	**4b** Anion **4b** Cation TMS	0.5 0.5	1.03×10^{-9} 1.06×10^{-9} 2.42×10^{-9}	5.36 5.21	646 594	0.999 0.999
19	CD_2Cl_2	**4b** Anion **4b** Cation TMS	1.0 1.0	1.01×10^{-9} 1.04×10^{-9} 2.55×10^{-9}	5.69 5.54	772 714	0.999 0.999
20	CD_2Cl_2	**4b** Anion **4b** Cation TMS	5.0 5.0	9.66×10^{-10} 1.00×10^{-9} 2.54×10^{-9}	5.86 5.68	841 769	0.999 0.999

4.7.3. Solvent Effects

Additionally, the influence of four solvents (CD_2Cl_2, $CDCl_3$, THF-d_8, CD_3CN) on the ion association of **1b** was investigated by DOSY screening (see Table A4.6). In $CDCl_3$ identical DOSY values for cation and anion are already observed at 0.05 mM, indicating a 1:1 ion pair aggregation. As described in chapter 4, in CD_2Cl_2 nearly identical values for both ions are detected at 5.0 mM. In CD_3CN no approximation of the diffusion values of cation and anion was observed up to 5 mM indicating mainly free ions. In summary, the DOSY data confirm the conductivity measurements for weakly coordinating solvents (ion pair formation in the order: $CD_3CN < CD_2Cl_2 < CDCl_3$).

For THF-d_8, deviations in the diffusion coefficients between the anion and cation persist up to a concentration of 5.0 mM. However, the measured volume of the cation at 0.05 mM is by far larger than the calculated volume for cation **b**. Our hypothesis for this observation is that the cation interacts with THF-d_8 leading to a solvent shell which influences the diffusion coefficient and hence the calculated volume. Therefore, no clear interpretation based solely on DOSY is feasible and further studies must be conducted to investigate this phenomenon.

***Table A 4.6** Experimental self-diffusion coefficients D_i, viscosity corrected hydrodynamic radii r_H and resulting volumes V_A of the ion pairs in varying concentrations and solvents ($CDCl_3$, CD_3CN, THF-d_8). TMS was used as viscosity reference for the experimental self-diffusion coefficients D_i to allow for a comparison of hydrodynamic radii r_H and resulting volumes V_A. The corresponding self-diffusion coefficients D_i of TMS are given for each sample. Entry 21-28: SW = 22 Hz, O1P = 10.0 ppm, gradient strength 5-95% linear. Samples were measured at room temperature.*

Sample	Solvent	Species inside sample	Concentration [mM]	Diffusion coefficient D_i [$m^2.s^{-1}$]	Hydrodynamic radius r_H [Å]	Volume V_A [$Å^3$]
21	$CDCl_3$	**1b** Anion	0.05	7.59e-10	6.13	963
		1b Cation	0.05	7.59e-10	6.13	963
		TMS		2.19e-09	-	-
22	$CDCl_3$	**1b** Anion	0.1	8.03e-10	5.89	857
		1b Cation	0.1	7.91e-10	5.96	886
		TMS		2.2e-09	-	-
23	$CDCl_3$	**1b** Anion	5.0	9.1e-10	5.74	791
		1b Cation	5.0	9.1e-10	5.74	791
		TMS		2.42e-09	-	-
24	CD_3CN	**1b** Anion	0.05	1.89e-09	4.33	340
		1b Cation	0.05	1.69e-09	4.79	461
		TMS		3.23e-09	-	-
25	CD_3CN	**1b** Anion	5.0	2.09e-09	4.21	313
		1b Cation	5.0	1.51e-09	5.48	689
		TMS		3.43e-09	-	-
26	THF-d_8	**1b** Anion	0.05	1.41e-09	4.05	278
		1b Cation	0.05	9.57e-10	5.30	622
		TMS		2.33e-09	-	-
27	THF-d_8	**1b** Anion	1.0	1.11e-0	4.94	505
		1b Cation	1.0	9.5e-10	5.58	727
		TMS		2.35e-09	-	-
28	THF- d_8	**1b** Anion	5.0	9.28e-10	5.62	742
		1b Cation	5.0	8.45e-10	6.06	934
		TMS		2.31e-09	-	-

4.7.4. NMR Spectroscopy

NMR spectrometer

Ion pairs **1a**, **1c**, **1d**, **2b**, **4b** in CD_2Cl_2: Diffusion ordered NMR spectroscopy (DOSY) experiments were performed using a Bruker® Avance III 600 MHz operating at 600.25 MHz for protons, equipped with a 5-mm high-resolution TCI cryoprobe and with pulsed gradient units, capable of producing magnetic field pulsed gradients in the z-direction of 0.64 $T.m^{-1}$. All measurements were performed at 298 K. Temperature was certified by internal NMR calibration samples from Bruker®. NMR Data was processed, evaluated, and plotted with TopSpin 3.2 software. Further analysis of the measurements was performed with Microsoft Excel (Version 16.0.10359.20023 64 Bit). For the measurements a set of 4 dummy scans and 32 scans was used for samples with concentration ≥ 0.5 mM of the ion pair. A set of 4 dummy scans and 64 scans were used for samples with concentrations ≥ 0.1 mM of the ion pair. A set of 4 dummy scans and 256 scans was used for samples with less than 0.05 mM of the ion pair.

Solvent screening of **1b**: DOSY experiments were performed on Bruker Avance III HD 600 MHz spectrometer, equipped with a 5 mm CPPBBO BB-1H/19F. All measurements were performed at 298 K and temperature was controlled by BVT 3000. NMR Data was processed, evaluated, and plotted with TopSpin 3.2 software. Further analysis of the measurements was performed with Microsoft Excel (Version 16.0.10359.20023 64 Bit). For the screening a set of 4 dummy scans and 16-64 scans was used.

Diffusion-Ordered Spectroscopy (DOSY)

Sample preparation was conducted as described in chapter 4.6.1.1. DOSY evaluation and calculation was performed as described in chapter 4.6.1.2.

For the semi-empirical modification by Chen, a from literature known value for the radius of the corresponding solvent was used ($r_{CD_2Cl_2}$ = 2.46 Å[1], r_{CDCl_3} = 2.65 Å[1], $r_{THF\text{-}d_8}$ = 2.72 Å[2], r_{CD_3CN} = 2.86 Å[2]).[3]

4.7.5. References

[1] D. Zuccaccia, A. Macchioni, *Organometallics* **2005**, *24*, 3476–3486.

[2] D. Ben-amotz, K. G. Willis, **1993**, *I*, 7736–7742.

[3] H. C. Chen, S. H. Chen, *J. Phys. Chem.* **1984**, *88*, 5118–5121.

5. Conclusion

In the last decades, ion pairs in catalysis have facilitated a range of transformations with reactivities and selectivities that were previously unthinkable of. Just recently, pyridinamide based ion pair catalysts were discovered which outperform pioneer organocatalysts in their field. On the other hand, the BINOL-derived chiral phosphoric acids represent a long-lasting success story in organocatalysis with continuous advancements persisting even to the present day. Due to their significant achievements, ion pairs became of huge interest for mechanistic studies. Especially, the aggregation trends and resulting structures are a focus of such investigations due to their impact on the reaction outcome. Therefore, in this thesis the mechanism of the CPA-catalyzed transfer hydrogenation of imines was further investigated regarding potential secondary pathways and later reaction intermediates. These new revelations should lead to a better general understanding of CPAs and could be used for reaction design. In addition, pyridinamide based ion pairs are studied in regard of their aggregation to give first mechanistic insights into this new catalyst class.

In chapter two, the first experimental structural and conformational analysis of the ternary complex of chiral phosphoric acids (CPAs) was conducted. Additionaly, the experimental access of the ternary complex was also transferred to a study of London-Dispersion interactions and their influence on stereoselectivity.[1] This was possible by utilizing a Hantzsch Ester derivate with improved solubility, even at the required 180 K for the detection of hydrogen bonds by NMR spectroscopy. NMR investigations revealed an extensive structural and conformational space. Notably, besides the ternary complex, a yet unknown [3:3] dimeric species consisting of two ternary complexes was discovered. This complex has not been considered in prior theoretical calculations, but its potential influence on reaction outcomes and prediction models cannot be excluded. Furthermore, the 2:1:1 ternary complex of the dimeric species was identified for the first time by NMR spectroscopy. This finding confirmed the proposed structural arrangement, where the HE binds to one CPA and the imine binds to the second CPA within the dimer. In addition,

[1] J. Gramüller, M. Franta, R. M. Gschwind, *J. Am. Chem. Soc.* **2022**, *144*, 19861–19871.

theoretical calculations were performed to obtain conformers of the 1:1:1 ternary complex of CPAs, which were analyzed by NMR data. For the analysis of the conformers, Bio-NMR pulse sequences were applied to small molecules to provide in-depth data, necessary for a conformational analysis. Thereby, three distinct conformers for the ternary complexes were revealed and validated by NMR spectroscopy. Two of these conformers could lead to a reactive transition state, with the lowest energy conformer closely resembling the previously calculated transition states, providing experimental evidence of the transition states for the first time. Consequently, NMR investigations revealed a broad structural and confromational space indicating that the 3,3'-substituents of the CPAs do not hinder structural freedom in late reaction intermediates. Furthermore, this study provided easy access to the ternary complexes of CPAs which enables further studies in regard of a possible correlation between late intermediates and stereoselectivity.

In chapter three, the CPA catalyzed transfer hydrogenation of imines was investigated for a potential dimeric pathway similar to the transfer hydrogenation of quinolines. Low temperature NMR investigations revealed a hydrogen bond bridged CPA/CPA/imine dimer and in combination with DFT calculations structural insights and cooperativity effects were revealed. Furthermore, NMR studies revealed that dimer formation is favored when combining opposite electronic properties on CPA and substrate. Despite NMR studies proving the existence of a dimeric 2:1 species at 180 K, no change in stereoselectivity was observed when varying catalyst loading, temperature or total concentration. Thus, the with quinolines observed dimeric pathway is no general feature of CPA catalysis but has to be considered depending on the substrate.

In chapter four, DOSY measurements were key to understand the reactivity of pyridinamide ion pair catalysts. Initially, the formation of unreactive 1:1 ion pairs in solution was assumed which would lead to a significant reduction in reactivity. However, the data of conductivity measurments did not align with a 1:1 ion pair model. Consequently, DOSY experiments were conducted revealing an aggregation of two cations and one anion (CAC) or two anions and one cation (ACA) into a so-called “sandwich”-complex. For the CAC complex, this asymmetric association results in the release of a highly reactive anion which would explain the observed conductivity data. On the other hand, the ACA sandwich itself seems to be be highly reactive, as the pyridinamide-based ion pairs remain highly reactive despite the formation of this

sandwich complex. Noteably, screening 7 ion pairs demonstrated that the formation of either CAC or ACA can be controlled by the size of the ions, paving the way for model design of this catalyst class. Therefore, DOSY results were key to correctly interpret the data provided by conducitivity and nucleophilicity measurements and demonstrated the influence of higher ionic aggregates on the reactivity of this catalyst class. Furthermore, the combination of nucleophilicity, conductometric, calculations and DOSY measurements allowed unprecedent insights into ion pair formation and also showcased its general potential for future mechanistic studies.

In summary, it was shown that higher aggregates are a common feature in ion pair catalysis and in some cases have a severe impact on the reaction outcome. In CPA studies, an approach for accessing and simplifying the study of late reaction intermediates was established. First in-depth insights of the ternary complex of CPAs were achieved, which revealed a broad structural and conformational space. Thus, demonstrating that the sterically demanding 3,3´-substituent do not lead to a limited structural arrangement. In addition, the with quinolines observed dimeric species was also identified by NMR spectroscopy with imines. However, the same effect in *ee* as with quinolines was not observed, ruling out a dimeric pathway as a general feature in CPA catalysis and suggesting it is instead a substrate dependent feature. In addition, in the field of pyridinamide catalysts, “sandwich”-complexes were detected which is responsible for the high reactivities of this catalyst class and showcased the relevance of higher aggregates in ion pair catalysis.

6. Eidesstattliche Versicherung

(1) Ich erkläre hiermit an Eides statt, dass ich die vorliegende Arbeit ohne unzulässige Hilfe Dritter und ohne Benutzung anderer als der angegebenen Hilfsmittel angefertigt habe; die aus anderen Quellen direkt oder indirekt übernommenen Daten und Konzepte sind unter Angabe des Literaturzitats gekennzeichnet.

(2) Bei der Auswahl und Auswertung folgenden Materials haben mir die zu Beginn des jeweiligen Kapitels aufgeführten Personen in der jeweils beschriebenen Weise unentgeltlich geholfen.

(3) Weitere Personen waren an der inhaltlich-materiellen Herstellung der vorliegenden Arbeit nicht beteiligt. Insbesondere habe ich hierfür nicht die entgeltliche Hilfe eines Promotionsberaters oder anderer Personen in Anspruch genommen. Niemand hat von mir weder unmittelbar noch mittelbar geldwerte Leistungen für Arbeiten erhalten, die im Zusammenhang mit dem Inhalt der vorgelegten Dissertation stehen.

(4) Die Arbeit wurde bisher weder im In- noch im Ausland in gleicher oder ähnlicher Form einer anderen Prüfungsbehörde vorgelegt.

Regensburg den 30.07.2024 _____

Maximilian Franta